AD-A073 746 CALIFORNIA INST OF TECH PASADENA GRADUATE AERONAUTIC--ETC F/G 20/4
CHEMICAL REACTIONS IN TURBULENT MIXING.(U)
JUL 79 H W LIEPMANN, G L BROWN, P E DIMOTAKIS F44620-76-C-0046
UNCLASSIFIED GALCIT-151 AFOSR-TR-79-0952 NL

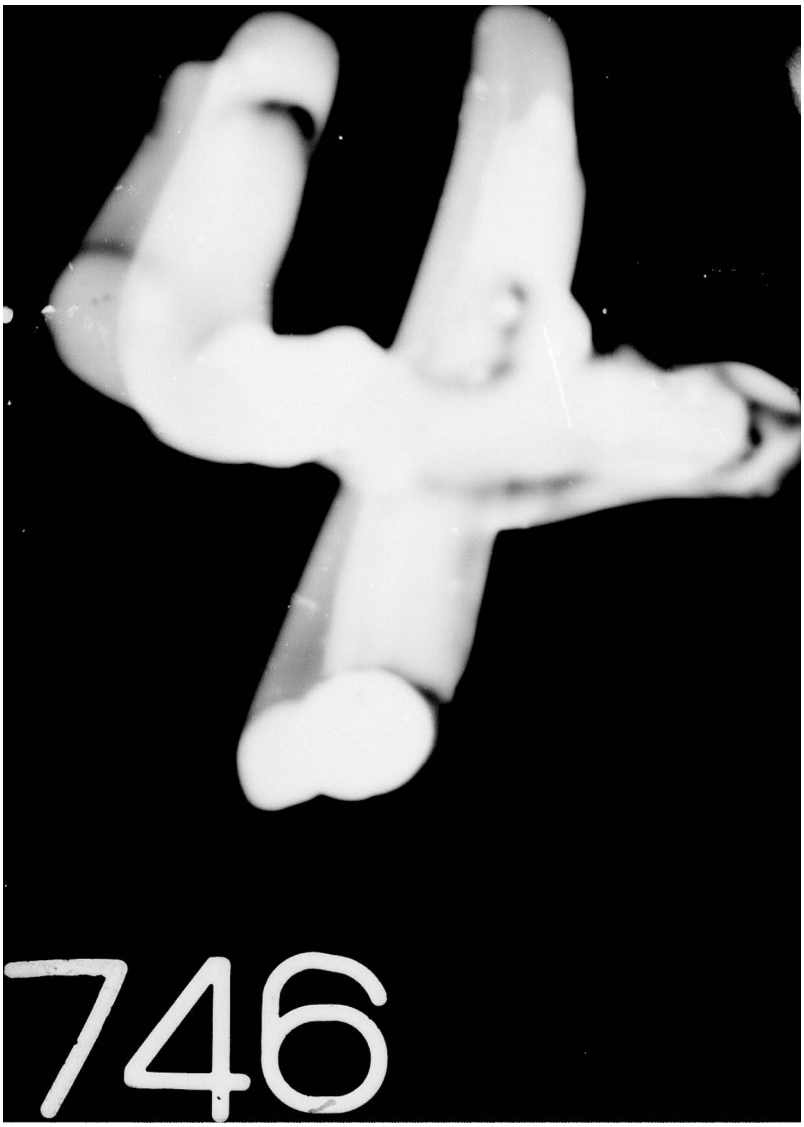
746

GRADUATE AERONAUTICAL LABORATORIES

CALIFORNIA INSTITUTE OF TECHNOLOGY

LEVEL II

FINAL TECHNICAL REPORT

CHEMICAL REACTIONS IN TURBULENT MIXING

AFOSR Contract No. F44620-76-C-0046

1 December 1975 - 14 April 1979

Firestone Flight Sciences Laboratory

Guggenheim Aeronautical Laboratory

Karman Laboratory of Fluid Mechanics and Jet Propulsion

Pasadena

(10)

FINAL TECHNICAL REPORT

CHEMICAL REACTIONS IN TURBULENT MIXING

AFOSR Contract No. F44620-76-C-0046

1 December 1975 - 14 April 1979

by

Principal Investigator

H.W. Liepmann

Co-investigators

G.L. Brown, P.E. Dimotakis, F.E. Marble

A. Roshko and P.G. Saffman

Graduate Aeronautical Laboratories

California Institute of Technology

Pasadena, California

157 700

ABSTRACT

The more important results and developments achieved as a direct result of this contract are as follows:

A model for the calculation of turbulent flows was constructed which incorporates effects of Reynolds stress relaxation and the generation or destruction of turbulent energy by rotation. The model was verified by comparison with experiment. It was then used to predict the properties of isolated turbulent vortices and applied to the turbulent mixing layer, in particular to the formation and interaction of the organized structure in the mixing layer. An alternative approach to the mixing layer in which it is modelled by a rolling-up vortex sheet between fluids of different density has also been formulated.

Calculations of strained flame elements for use in the coherent flame model of H_2, F combustion showed that only at very high strain rates was sufficient vibrational nonequilibrium produced to be of interest for a chemical laser. This result is reflected in the fact that only in the early portion of the jet, where strain rates are a maximum, does this vibrational nonequilibrium occur.

Experimental results were obtained in a new facility and by a new technique, for the amount of reaction product obtained between two chemically reacting aqueous streams. Results at high and low Reynolds number showed the dependence of the mixing on Reynolds number and Schmidt number. A transition Reynolds number region was found and the nature of the generation of small scale motions which dominate the formation of reaction product was explored.

A new facility to explore energetic reactions with substantial heat release has been designed, is being built, and should be used for the

first measurements in the summer of 1979. The design problems were formidable but the facility is unique and offers the prospect of obtaining new and very important data with which to compare existing models. As a result of the design, the range of problems and parameters that can be studied in the facility and the possibilities for the development and application of new instrumentation and diagnostics are very great.

State-of-the-art, very high speed and precise laser Doppler velocity measurements were completed under this contract. The acquired expertise will find application in the turbulent combustion experiments. It has already been applied with considerable success up to a Mach number of 2.2. The extension of two-point velocity measurements has now been made and a multipoint multichannel LDV system has been designed and is nearing completion.

A laser induced fluorescence technique was developed and successfully applied to the observation of turbulent mixing in a water jet. It allowed the direct observation of a concentration field to the smallest turbulent scales. Both direct photographic techniques and imaging of a line on a 1024 detector Reticon array have been used to obtain the data. Image processing will give quantitative measurements of the concentration field and potentially an inferred velocity field.

II. INTRODUCTION

The general aim of the research carried out under this contract was a combined attack, both experimental and theoretical, on the problem of trying to predict and understand chemically reacting turbulent flows. This major contract made it possible to focus a wide diversity of interest and expertise at Caltech on the problem. As a result, four separate but overlapping tasks were identified and described in the first proposal, two concerned with predictive models and two with experiments.

Section III is a summary of the progress made in each of these tasks. Section IV lists the publications derived from this research and also lists the seminars, presented papers and invited lectures given by GALCIT faculty, research fellows and students on the work. Section V is an appendix which includes details of the research referred to in each Task summary but may not yet be available as a final publication in the open literature.

This research was sponsored by the Air Force Office of Scientific Research (AFSC) and the Air Force Weapons Laboratory (AFSC), United States Air Force.

III. GENERAL SUMMARY

TASK I. A Study of Turbulence Models and Applications

Principal Investigator

P. G. Saffman

The problem of developing a turbulent model that would allow the quantitative examination of the interaction or organized turbulent structures was considered. One of the main features of the large eddies is the presence of mean vorticity or mean solid body rotation. To deal with their interaction, it is necessary to have a turbulence model which has been demonstrated to be effective in the presence of rotation. Two important physical effects need to be taken into account. First, there is the generation or destruction of turbulent energy by rotation and, second, there is the relaxation effect of the Reynolds stresses in following the rotation of the principal axes of strain.

A model was developed which appeared to contain the essential physics of turbulence in rotating fluids and tested by comparison with the experimental data on turbulent flow in the gap between rotating cylinders. The model was then applied to determine the structure of an isolated turbulent vortex and the coalescence of turbulent large scale structures in the turbulent mixing layer. In the first application, the existence of a similarity structure for the decaying turbulent vortex was demonstrated with an inner laminar core whose size is inversely proportional to the Reynolds number. In the second application, a turbulent time-dependent spatially-homogeneous mixing layer was calculated from the model equations. A small disturbance with wavelength equal to that of the most unstable disturbance of the associated Orr-Sommerfeld problem was imposed and followed to finite amplitude. This temporally developing

mixing layer, instead of the spatially developing one, was considered for reasons of computational cost. The growth of the disturbance into two noticeable eddies which then coalesced was followed. It was concluded that turbulence models can be constructed which will allow the description of the interaction and coalescence of organized structures.

Work was also started on an alternative formulation of the mixing layer in which it is modelled by a rolling-up vortex sheet. The equations of motion of the vortex sheet have been formulated as a singular, non-linear integro-differential equation. The mathematical problems association with this equation are, however, severe.

TASK II. The Coherent Flame Sheet Model for Turbulent Chemical Reactions

Principal Investigator

F. E. Marble

In order to adapt the coherent flame model to the H-F chemical laser, an extension of the theory was demanded that developed into a more serious task than had been anticipated. Before beginning the analysis of turbulent jet structure, calculations of laminar diffusion flames under various rates of strain were required. This was accomplished through use of the Blottner code, obtained from TRW and the Defense and Space Systems Group, and reworked for the computing facilities at Caltech. In order to achieve the degree of vibrational inversion that we considered appropriate, it was necessary to strain the flame at rates far in excess of other computations we have made. Strain rates of 10^6 sec^{-1} showed a first indication of non-equilibrium vibrational states while strain rates of 10^7 sec^{-1} achieved a large degree of total inversion. This strain rate was accompanied by a distinct change in the laminar flame structure.

Where the strain rate was generally less than 10^5 sec^{-1}, the flame behaved very accurately as if the reaction rate was infinitely fast, at least so far as the reactant consumption rates are concerned. Thus the reactant consumption in this range was $\sim\sqrt{D\epsilon}$ where D is the appropriate binary diffusion coefficient and ϵ is the strain rate. The numerical calculation gave the factor of proportionality and its dependence upon reactant concentration. The strain rate, entering only in the manner shown, demonstrated that the consumption rate was controlled by

diffusion and totally insensitive to chemical rates. On the other hand, when the strain rate was greater than 10^5 sec^{-1}, the reactant consumption varied as $\epsilon^{-\frac{1}{2}}$. Examination of the results showed that the flame was chemically limited in this range and that the chemically active zone filled the entire flame thickness. It was then clear that the proper form of the reactant consumption rate for large values of ϵ was $\sim \frac{1}{\tau_c}\sqrt{D/\epsilon}$ where $\sqrt{D/\epsilon}$ is proportional to the thickness of the reaction zone and τ_c is a chemical time. For the entire range of strain rates, the reactant consumption rate is

$$\sim \frac{\sqrt{D\epsilon}}{1+\tau_c\epsilon}$$

which behaves as $\sqrt{D\epsilon}$ for strain rates $\epsilon \ll 1/\tau_c$ and as $(1/\tau_c)\sqrt{D/\epsilon}$ for $\epsilon \gg 1/\tau_c$.

To accomodate this more complex burning law, the entire integral formulation was reworked. This extended model was used in the study of a circular jet of hydrogen issuing into a background of stationary atomic fluorine. Calculations were made of the distributions of flame surface area chemical species, and vibrational states of HF at several values of z/d along the jet axis. The calculations were done also for two values of $\frac{W_0\tau_c}{d}$, where W_0 is the initial jet velocity emitted from a nozzle of diameter d. This parameter essentially determines the quantity $\tau_c\epsilon$ and hence, according to the above relationship for the reactant consumption rate, accentuates the type of flame structure that leads to non-equilibrium of the vibrational states of HF.

This work is covered in detail in Appendix C which will be available as a GALCIT Technical Report.

TASK III. Dilute and Energetic Chemical Reactions in Turbulent Flow

Principal Investigators:

A. Roshko and G. L. Brown (since October 1978)

A. Isothermal Chemical Reactions in Turbulent Flow

The blow-down water channel facility was utilized fully during the present reporting period for several investigations of turbulent free shear layers and wakes. The principal experimental techniques made use of the visible (red) reaction product which is produced when the reactants phenolphthalein and sodium hydroxide mix chemically in the turbulent mixing region. Flow photographs and movies were used to obtain information about the large- and small-scale structure of the flows and a light absorption technique was used to infer the instantaneous amount of visible product.

The main results of the past year's research are as follows:

1) At high Reynolds number (Re) the mixing in the shear layer is independent of Re and, based on a comparison with previous measurements of Konrad in a gaseous flow, at most only weakly dependent on Schmidt number ($Sc \equiv \frac{\nu}{\mathcal{D}}$).

2) At low Re the mixing is a strong function of Sc.

3) A transition region exists in which small scale, three-dimensional motions are introduced and develop in the layer. They are superimposed on the large, quasi-two-dimensional vortex structures. These small scale motions generate a very large reaction interface area and strain rate, thereby permitting the mixing rate to be as large as the entrainment rate of fresh reactant into the shear layer. The transition appears to be determined mainly by the initial conditions of the shear layer rather than by the large scale Reynolds number. The parameters

which seem to best characterize the transition are the development distance x/θ_1 based on the initial momentum thickness and the Reynolds number $\frac{U_1 \theta_1}{\nu}$ of the boundary layer on the high speed side.

4) The wakes from a blunt and from a sharp trailing edge of the splitter plate were also found to exhibit a mixing transition across which the aqueous mixing increases by an order of magnitude or more. Again the physical explanation is in the emergence of small scale motions in the transition region. At large Re, the wake mixing is likewise independent of Re.

Reference

Konrad, J.H. "An Experimental Investigation of Mixing in Two-Dimensional Turbulent Shear Flows with Applications to Diffusion Limited Chemical Reactions", Ph.D. Thesis, 1977, California Institute of Technology.

B. Energetic Chemical Reaction in Turbulent Flow

Work on the overall design and fabrication of this facility continued. The major recent work has been in the final design of the upstream contraction, test section, and downstream gas cooling, scrubbing and collecting region. Construction is presently underway at the Caltech Central Engineering Shop. The major concerns have been material compatibility with Fluorine, compatibility with corrosive and high-temperature HF, machining costs and overall safety. Safety remains a prime concern as both Fluorine (F_2) and the reactant product Hydrogen Fluroide (HF) are highly corrosive and extremely toxic.

The main results of the past year's work are as follows:

1) The apparatus has been moved to what was formerly the "Clean Air Car Laboratory" from its former location in the Guggenheim penthouse. The major reasons for this move are (i) availability and (ii) preferable, particularly from the safety standpoint as this location is much more accessible, affords more room for working and allows more isolation in terms of the exhaust gas containment. Since the experiment is to be performed here in the heart of Caltech, containment is considered one of our strongest safety requirements because of the toxicity of the F_2 and HF and their low threshold limits (0.1 ppm for F_2; 3 ppm for HF). The pipe link that joins the high pressure supply to the reactant holding tanks has also been completed.

2) The two adjustable metering valves have been built. Each is made of a 316 stainless steel housing into which the reactant gas enters and then chokes through a series of 8 rectangular slots which are milled into a Monel tube. The choked area is variable by means of a movable stainless steel piston. With 100 psi (6.9×10^5 N/m^2) inlet pressure

the mass flow rate is continuously adjustable up to 1.5 kg of Nitrogen per second.

3) A modularized design for the test section has been adopted. It consists of a series of sections linked together in the downstream direction. Each section has been optimized in terms of our three requirements of material compatibility, cost and safety.

(a) The contraction section: overall 27 x 46½ x 9½ inches (69 x 118 x 24 cm). This part contains the settling chamber, screens for turbulence management, splitter plate and the contraction. Stainless steel was found to be excessively expensive and somewhat questionable as to its stability in the presence of rapidly flowing F_2 (approx. 100 m/s). The final design, presently under construction, uses TFE Teflon sheet for containment of the flowing F_2 and aluminum jig plate for overall structural integrity. The Teflon is bonded to the inner surface of the aluminum plate using PR-1730BT, a Viton-based adhesive, which is the only such material that we have found that is stable in both stationary and flowing gaseous F_2. (These tests were performed by C. Moran at JPL as part of their compatiblity studies.)

The final design has been commented upon by groups working with F_2 at TRW and JPL. It appears to be entirely satisfactory and construction should be relatively fast and much less expensive than it would have been in stainless steel.

(b) The test section: Overall 14 x 26 x 10 inches (36 x 66 x 25 cm). The main reaction occurs at this station and stainless steel has been used for compatibility reasons. It consists of a 316 stainless steel box framework with easily removable glass sidewalls for accessibility. Clear-through visibility allows for optical studies (shadowgraph,

schlieren, LDV) of the mixing layer in the sideview. The top and bottom walls are also of glass and allow for similar study of the planform of the mixing layer. A traverse mechanism platform can be substitute for the top and bottom walls, while accessibility remains through the sidewalls. Some parts of the traverse mechanism will be subjected to hot HF attack and those parts have been made replaceable. Provision has also been made for film cooling of the sidewalls by injecting cool Nitrogen at the beginning of the mixing layer. Etching of the glass by the HF and thermal shock due to heat release are considered the major problems and film cooling may be required only in the maximum heat release cases (temperature rise of 1000° C).

Drawings for this section are complete and construction will begin immediately upon completion of the contraction section.

(c) The diffuser/afterburner section: This divergent section allows the reaction to go to completion before the exhaust gases are discharged downstream into the exhaust gas section.

(d) The exhaust gas section: The design problems associated with collecting or processing the hot and highly toxic exhaust gas in a built-up environment like Caltech are formidable. Because of the large flow rates associated with this facility, processing of the hot exhaust gases on the fly and discharge to the atmosphere were initially considered as impractical because of the extremely low concentration of exhausted HF or F_2 which could be considered. In particular, packed absorber beds commonly used in chemical laser or rocket engine work are totally unsatisfactory because of size, pressure drop and time to reach steady state conditions. Some typical magnitudes for the present facility are as follows:

mass flow rate on one side of layer	~ 1 kg/sec
maximum molar concentration of F_2	~ 5%
maximum temperature rise	~ 1000° C
initial volume (2 reactant tanks) at 100 psi (6.9×10^5 N/m^2)	~ 30 ft^3 (.85 m^3)
typical heat release	~ 10^6 J/s
final volume at ~ 1000° C and 1 atmosphere pressure	~ 800 ft^3 (22.6 m^3)

Collecting 800 ft^3 of corrosive and toxic gas at 1000° C, and then subsequently scrubbing presents a substantial problem. A heat exchanger and gas containment gas were designed for the facility and appeared to be a possible solution. The design is briefly described below. More recently, however, after discussions with J. Ortwerth and using some results on HF/F_2 scrubbing obtained at the Boeing Research Laboratory, it has been decided to replace the heat exchanger and gas containment bag by a system in which 5% sodium hydroxide solution is sprayed in a fogjet into the exhaust gas to cool it to about 100° C and partially neutralize the HF and F_2. The final volume to be handled will now be significantly reduced and probably no more than 300 ft^3 (8.5 m^3). The exhaust gas and carryover spray are then caught in a large teflon bag and subsequently scrubbed and discharged to the atmosphere, this latter process occurring at a much slower rate. Some additional work remains to be done on the caustic spray system before the design is complete.

(1) Heat exchanger and gas containment bag: This design was pursued at some length because of its many intrinsic advantages. It will not now be built, however, and has been superseded by the

scrubbing system outlined above. The exchanger was designed to remove approximately 10^6 J/sec for four seconds using a thermal mass concept. Fifteen laminar flow elements, each consisting of many closely spaced stainless steel plates precooled with liquid nitrogen, would reduce the exhaust gas temperature to typically 100° C. This exhaust gas is then trapped in a large stainless steel, very thin sheet, bag of a metal bellows design (10 ft by 10 ft). A teflon bag was not used so that the system would be failsafe. As before, the trapped gas would then be neutralized at a slower rate.

(2) Gas feed system: Finally, the supply lines and valves for transferring F_2 from the high pressure supply bottles to the reactant tanks remains to be built. We have had useful inputs from JPL on this design and forsee no major problems here.

TASK IV. Advanced Instrumentation and Measurement Techniques Development

Principal Investigators:

P. E. Dimotakis and H. W. Liepmann

A. Laser Doppler Velocimetry

1) High speed flow measurement. The experiments, data reduction and analysis on turbulent boundary layer measurements of mean u, v, u', v', and u'v' in high speed, high Reynolds number turbulent boundary layers were completed during the contract period. Preliminary results were presented at the Third International Workshop on Laser Velocimetry, at Purdue University in July 1978 (see Appendix D). The final results will be published as an AEDC report, under whose sponsorship the work began. A pre-print of the report, by Dimotakis, Collins, and Lang is appended (Appendix E). We believe these measurements constitute the state-of-the-art in precision high speed laser Doppler velocimetry, which also specifically address the difficulties in making measurements in the vicinity of solid boundaries (walls).

In these measurements, a flow Mach number range of 0.1 to 2.2 was covered in two different facilities (GALCIT Merrill Wind Tunnel at $M \sim 0.1$ and the 20" JPL Supersonic Wind Tunnel for the higher speed flows). As a result of our measurements, we were able to show conclusively that the discrepancies that had arisen in the past in high speed flow measurements of the Reynolds stress in the vicinity of walls were unrelated to compressibility effects, as opposed to what had originally been claimed. We were also in a position to make investigations into the nature of turbulent transport in the vicinity of the viscous sublayer which, even though it is usually only a small fraction of the

turbulent boundary layer thickness (typically ~ 0.001 boundary layer thicknesses at high Reynolds number), can have significant effects that extend over the lower 20% of the turbulent boundary layer.

2) Multipoint, multichannel laser Doppler velocimetry. The design and fabrication of the electronic components of the multipoint, multichannel laser Doppler velocimetry system is proceeding satisfactorily even if a little behind the schedule we had hoped would have been possible. The design is by now complete and the effort is presently expended in the fabrication and assembly in a manner that will render the manufacture of additional channels as inexpensive as possible.

To this end, computer aided design and computer aided manufacturing (CAD/CAM) techniques have been used wherever practical. In particular the special purpose wire wrap/printed circuit boards, on which the system is being assembled, were designed on the computer, which also computed and stored the coordinates for the 7,000 holes that had to be drilled and generated the artwork on a digital plotter. The resulting plots were then used to generate the negatives used to etch the printed circuit boards. Reduced copies of the resulting board etch pattern are included in Appendix F. The drilling was subsequently done by using the computer to feed the stored coordinates of the holes to a digital 3-axis positioning table on which a precision 45,000 RPM drill motor (fitted with tungsten carbide drills) was mounted.

As of this writing, the high speed analog front end signal processing circuitry for four channels has been fabricated. We anticipate that the first measurements using the new system will be realized during the current calendar year and that it will be available in time

to be used in the high heat release combustion facility presently under construction.

Concurrently with the design and fabrication of the multichannel system, we were able to measure at the same time the velocity at two points in a high Reynolds number, two-dimensional shear layer. This was possible through a modification of the existing processor that allowed the signals from two optical channels to be time multiplexed into a single digital processor, thereby essentially measuring the selected velocity component at two points in the flow simultaneously. The results are summarized in a paper submitted to the AIAA Journal for publication. A pre-print of this paper by Koochesfahani, Catherasoo, Dimotakis, Gharib and Lang is appended. The measurements and resulting new conclusions, that were made possible by our ability to monitor velocity at one additional point in the flow, suggest to us that our efforts at truly multipoint measurements should yield a wealth of new information about turbulence.

B. Laser Induced Fluorescence.

One of the most rewarding parts of the research under this task has been the development of the Laser Induced Fluorescence (LIF) technique. This has allowed the positive identification of the concentration field of one of two aqueous mixing species that is labeled in terms of a dye that can be selectively excited to fluoresce by a laser illuminated field (beam, sheet or volume). The technique not only allows flow visualization under conditions that are inaccessible by conventional flow visualization techniques, but also allows quantitative measurements to be made since the fluorescence intensity emitted from a point in the flow is linearly dependent on the concentration of the fluorescing dye and the local intensity of the laser field.

As of this writing, two methods of acquiring data that result from this technique have been used. The first method utilizes the laser as a sheet illumination source and records the data photographically by focusing the plane illuminated by the laser on the image plane of a 35 mm camera. Examples of data recorded in this fashion appear on Figures 2a, 6, 7, 8, and 9 of Appendix H. The second method utilizes the laser as a line illumination source (beam) and images the illuminated line on a linear charged coupled device (CCD) detector array of 128 or 1024 detectors that are electronically scanned at high speed to produce a sequence of synchronous voltages that are proportional to the light intensity incident on the corresponding detector. These voltages are then used to modulate the intensity of a cathode ray tube beam which is driven by a raster scan pattern synchronously with the electronic scanning of the detector array. The resulting pattern on the CRT screen is then photographed to produce an image corresponding to the concentration of the labeled mixing species on the illuminated line as a function of time.

Examples of data recorded in this manner appear on Figures 4 and 5 of Appendix H.

Several important discoveries were made possible by this new flow diagnostic method. It was possible to determine, for example, that entrainment of irrotational fluid into the turbulent region of a jet was by means of a mechanism not significantly different from the mechanism that was found in the two-dimensional shear layer. In particular, it was found that entrainment does not proceed as the result of a diffusive process of a turbulent - non-turbulent interface, but rather as a result of the induced velocity as a result of the large structures that are also found in the turbulent jet. Secondly, it was established that, at least in the case of water (high Schmidt number), it was possible to find unmixed reservoir fluid all the way to the axis of the jet, contrary to the conventionally accepted ideas in this matter. Thirdly, it was also established that the notions of intermittency and a turbulent region that is separated from the non-turbulent region by an interface that is topologically relatively simple are of questionable validity. Lastly, evidence was found that the structures in the turbulent jet grow in size by a mechanism akin in many ways to the coalescence process that is dominant in the two-dimensional shear layer. These are important observations because they suggest that the organization of turbulence that was found to exist in the two-dimensional shear layer may also be found in other turbulent shear flows. This leads us to hypothesize that all turbulent shear flows are organized to a lesser or greater extent, depending on the topology of the geometry, in a hierarchy of flows that places the organized wake of the circular cylinder on top.

It should be emphasized that all these conclusions were made possible by the fact that the data that result from the Laser Induced Fluorescence measurements are field measurements as opposed to point measurements. The information regarding the structure of the various flow patterns that were observed would simply not have been available by measurements on fewer dimensions. A preliminary report of some of the early conclusions is included in the form of Appendix H.

C. Acoustical Imaging

Transmission of sound waves through a given flow field can be utilized to extract information about the flow. Since a temperature change is the principal cause in changing the speed of sound, transmission imaging was demonstrated by using a steady plume as the object. A heater was mounted at the bottom of a water tank, while two piezoelectric probes were rigidly connected and traversed through the tank (Fig. 1). A pulse generator triggered a function generator to generate 3 MHz sine-wave bursts of about 50 msec duration, which were fed into the transmitter probe. The receiving probe picked up the sound bursts, which were then amplified, bandpass filtered and averaged. The plotter recorded this signal, which is a measure of the transmitted sound amplitude, as a function of the traverse position. Figure 2 shows such a plot while Figure 3 shows the actual temperature variation through the plume as measured with a thermocouple. As expected from ordinary shadowgraphy, the acoustic trace shows the second derivative of the thermocouple trace, where the amplitude decrease in the center is due to the deflection of the center rays out from the center.

In order to investigate unsteady flows, an acoustical sensing array, comprised of 100 piezoelectric elements in a line, has been designed and fabricated. Each element measures .035" x 0.5" to give a total length of 3.5". Since utilizing sound waves give the opportunity to measure also the phase of the signal directly, processing electronics are under design to extract amplitude and phase from the incoming signal, which will then be recorded in digital form on tape as a function of time. The recording speed is designed to be 500 frames/sec. The unique feature to have

amplitude and phase available at the same time allows one to obtain various images from the same recording, e.g., amplitude only images and phase only images. It is also possible to apply various numerical reconstruction techniques like Fresnel Transforming, which require the knowledge of both amplitude and phase.

It is planned to apply this technique in a gas flow using sound frequencies of about 350 kHz. Since the speed of sound is a strong function of the temperature only, an acoustical image can give complementary information to the optical image. Another application is a flow situation, where light is too sensitive, like in the HF mixing layer facility.

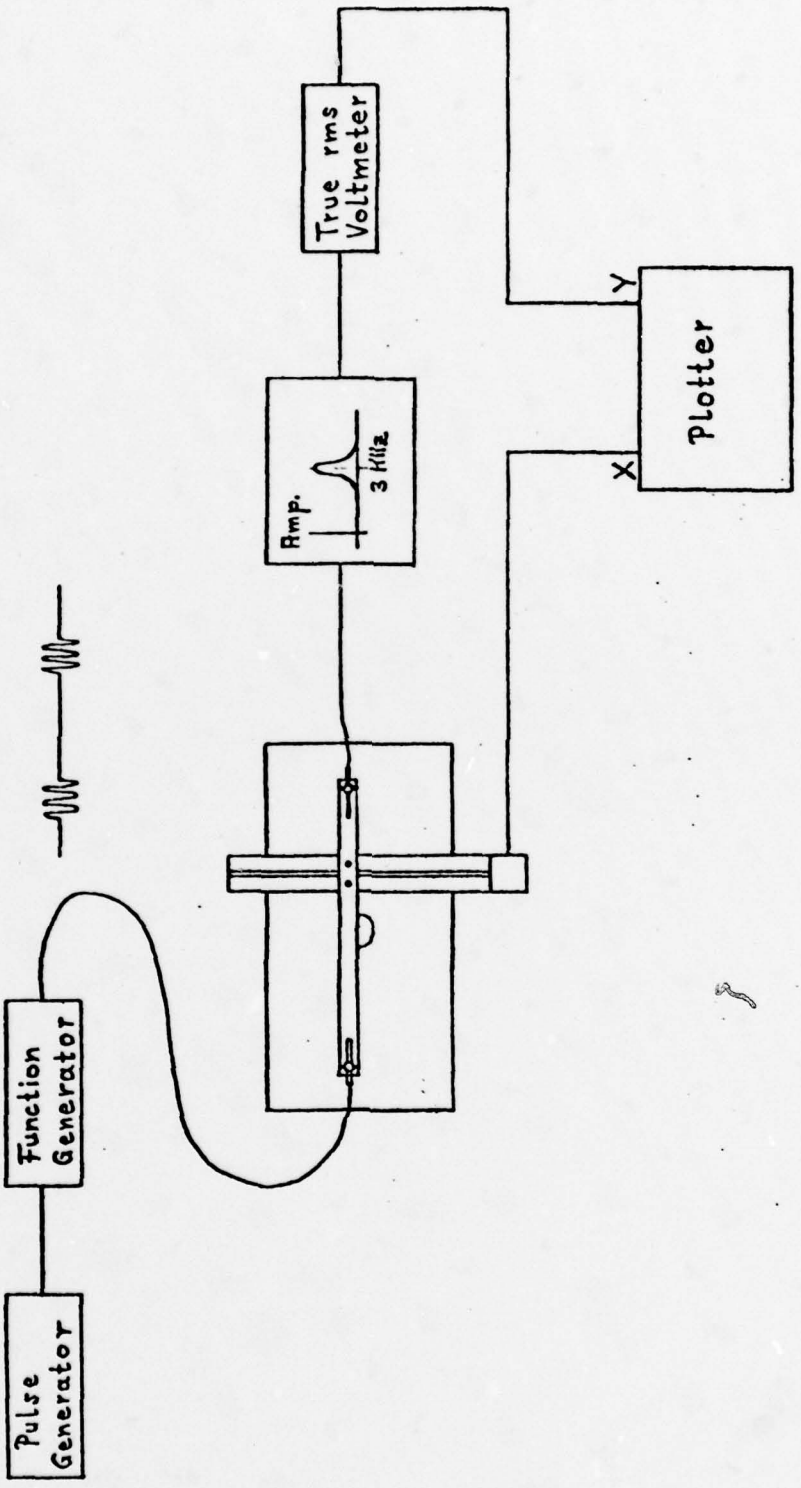

Figure 1. SCHEMATIC

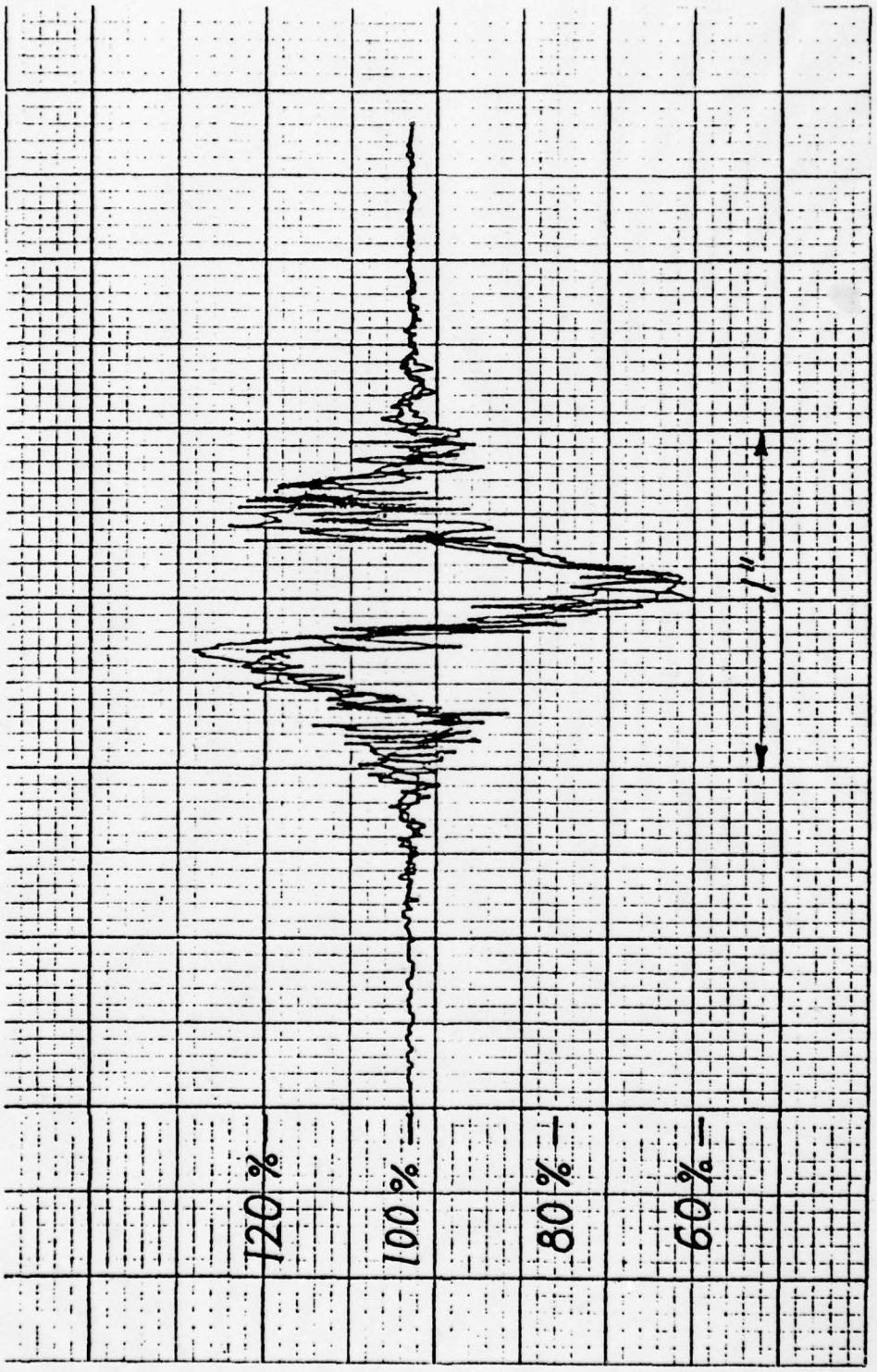

Figure 2. ACOUSTIC AMPLITUDE TRANSMISSION IMAGE OF PLUME AT 15 W

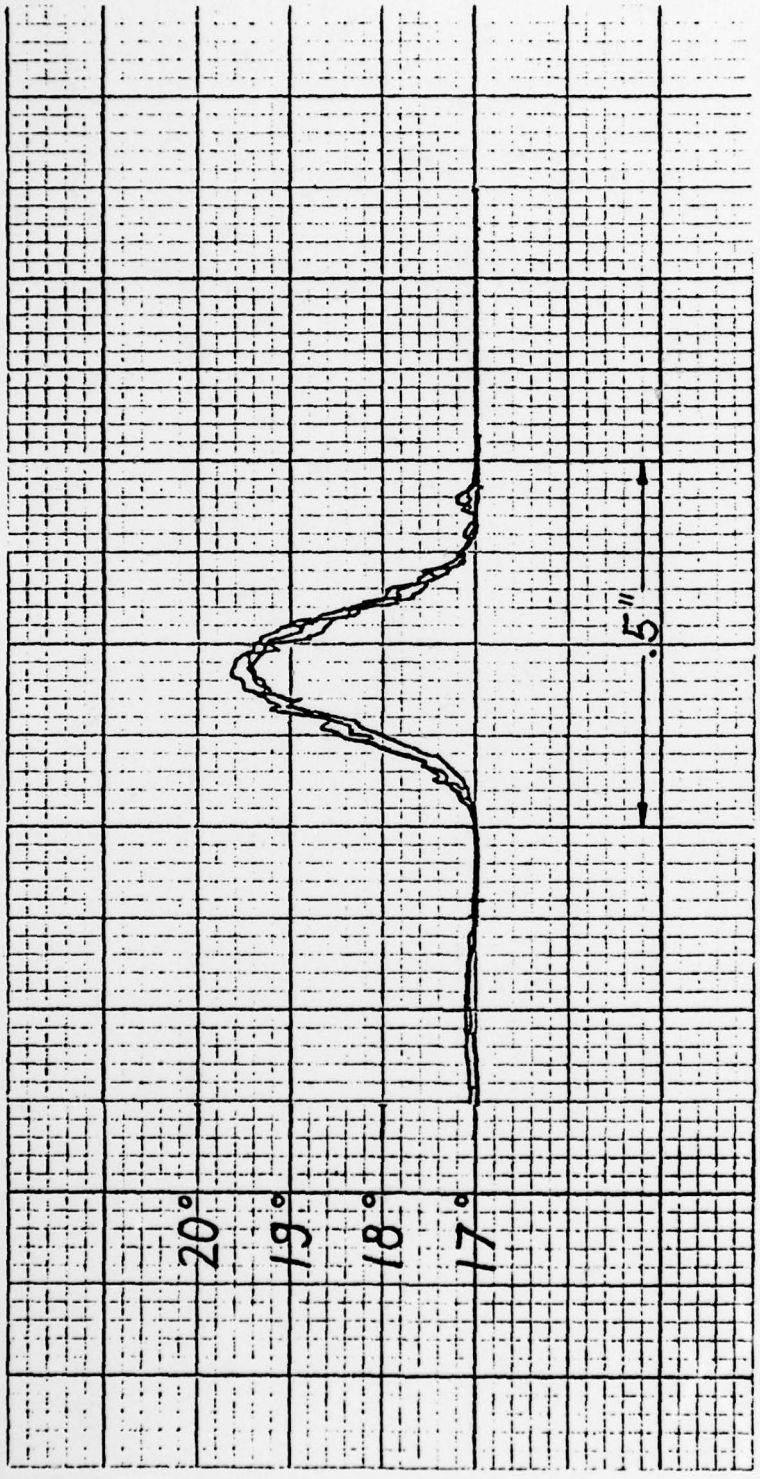

Figure 3. TEMPERATURE DISTRIBUTION THROUGH PLUME AT 15 W

SECTION V

PUBLICATIONS

1. R.E. Breidenthal, J.E. Broadwell and A. Roshko, "A Chemically Reacting Turbulent Shear Layer," 30th Anniversary Meeting, Am. Phys. Soc., Div. of Fluid Dynamics, November 22, 1977.

2. D.D. Knight and P.G. Saffman, "Turbulence Model Predictions for Flows with Significant Mean Streamline Curvature." AIAA Paper 78-258, January 1978.

3. R.E. Breidenthal, J.E. Broadwell, and A. Roshko, "Turbulent Shear Layer between Chemically Reacting Streams," Eighth U.S. National Congress of Theoretical and Applied Mechanics, June 1978.

4. D.D. Knight, "Model Equation Predictions of the Coalescence of Vortices in the Turbulent Mixing Layer," Eighth U.S. National Congress of Theoretical and Applied Mechanics, June 1978.

5. P.E. Dimotakis, D.J. Collins, and D.B. Lang, "Laser Doppler Velocity Measurements in Subsonic, Transonic and Supersonic Turbulent Boundary Layers." Third Intl. Workshop on Laser Velocimetry, Purdue University, July 11-13, 1978.

6. R.E. Breidenthal, "A Chemically Reacting Turbulent Shear Layer." Ph.D. Thesis, California Institute of Technology, November 1978.

7. P.E. Dimotakis, R.C. Lye, and R.D. Morrison, "Laser Induced Fluorescence and Particle Streak Measurements in Round Turbulent Jets." Bull. Am. Phys. Soc. 23 (8), 994, November 1978.

8. R.E. Breidenthal, "A Chemically Reacting Turbulent Wake." Bull. Am. Phys. Soc. 23 (8), 1010, November 1978.

9. P.E. Dimotakis, M.M. Koochesfahani, C.J. Catherasoo, M. Gharib, and D.B. Lang, "Two-point LDV Measurements in a Plane Mixing Layer." Bull. Am. Phys. Soc. 23 (8) 1007, November 1978. Also submitted for publication to AIAA Journal.

10. R.E. Breidenthal, "Chemically Reacting, Turbulent Shear Layer." AIAA Journal 17, pp. 310-311, March 1979.

11. L. Bernal, R.E. Breidenthal, G.L. Brown, J.H. Konrad, and A. Roshko. "On the Development of Three Dimensional Small Scales in Turbulent Mixing Layers." Second Symposium on Turbulent Shear Flows, Imperial College, London, July 1979.

SEMINARS, INVITED LECTURES, AND PRESENTATIONS

R.E. Breidenthal

McDonnell Douglas Research Labs	Mar. 6, 1978
General Electric Research Center	Mar. 27, 1978
University of Texas	June 7, 1978
Sandia Laboratory - Livermore	Jan. 12, 1979
The Boeing Company - Seattle	Mar. 9, 1979

P.E. Dimotakis

Massachusetts Institute of Technology	Nov. 28, 1977
" " "	Apr. 20, 1978
Purdue University	July 7, 1978
Princeton University	Apr. 26, 1979
Courant Institute of Mathematics, NYU	Apr. 27, 1979

F.E. Marble

Annual Thermo-Fluids Lecture Series University of Arizona, Tucson	Mar. 5-8, 1979

A. Roshko

Stanford University	Mar. 14, 1978
General Motors Research Labs	Apr. 10, 1978
McGill University	Apr. 12, 1978
Midwest Mechanics Seminar Series:	
Illinois Institute of Technology	Sept.20, 1978
University of Illinois	Sept.21, 1978
Purdue University	Sept.22, 1978
University of Michigan	Apr. 2, 1979
Michigan State University	Apr. 3, 1979
University of Wisconsin	Apr. 5, 1979
University of Minnesota	Apr. 6, 1979

P.G. Saffman

Symposium on Turbulence, Berlin	Sept. 1977
University of Iowa	Oct. 1978

APPENDICES*

A. D.D. Knight, "On the Approximate Motion of Vorticity-Bearing Eddies in a Perfect Fluid in Three Dimensions."

B. D.D. Knight, "Numerical Investigation of the Coalescence of Large Scale Structures in the Turbulent Mixing Layer."

C. F.E. Marble, J.E. Broadwell, O.P. Norton, and M.V. Subbaiah, "The Turbulent Chemical Reaction of a Hydrogen Jet Discharged into Fluorine." GALCIT Technical Report, July 1979.

D. P.E. Dimotakis, D.J. Collins and D.B. Lang, "Laser-Doppler Measurements in Subsonic, Transonic and Supersonic Turbulent Boundary Layers." Third International Workshop on Laser Doppler Velocimetry, Purdue University, July 11-13, 1978.

E. P.E. Dimotakis, D.J. Collins and D.B. Lang, "Measurements in the Turbulent Boundary Layer at Constant Pressure in Subsonic and Supersonic Flow. Part II: Laser-Doppler Velocity Measurements." To be published as an AEDC report.

F. Reduced copies of computer generated printed circuit board etch patterns for multi-channel laser Doppler velocimetry processing system.

G. M.M. Koochesfahani, C.J. Catherasoo, P.E. Dimotakis, M. Gharib and D.B. Lang, "Two-point LDV Measurements in a Plane Mixing Layer."

H. R.C. Lye, "Laser Induced Fluorescence Measurements in the Turbulent Jet." Senior thesis, California Institute of Technology, May 1978 (advisor, P.E. Dimotakis).

*Material not readily available in the open literature reporting work under this contract is included in this appendices.

NUMERICAL INVESTIGATION OF THE COALESCENCE OF LARGE SCALE STRUCTURES IN THE TURBULENT MIXING LAYER

D. D. Knight

I. Introduction

During the past twenty-five years, considerable attention has been devoted to the phenomenon of the large-scale structures ("eddies") in turbulent shear flows. The early work of Townsend[1,2] and his colleagues emphasized the importance of the large eddies in the dynamics of turbulent flows. Recently, Brown and Roshko[3] discovered the remarkable coherence of the large eddies in a two-dimensional turbulent mixing layer. Additional evidence of coherent structures has been found in a wide variety of turbulent shear flows, including the two-dimensional wake,[4] boundary layer,[5] and axi-symmetric jet.[6] These results have led to new theories as to the role of the eddies in the phenomena of entrainment,[7,8] mixing,[9] combustion and pollutant formation.[10]

The purpose of this research is to investigate the ability of turbulence models (in particular, the model equations of Saffman[11,12]) to describe the features of the large-scale structures in the incompressible homogeneous turbulent mixing layer. Specific attention is focused on the process of amalgamation ("pairing") of large scale eddies.

II. Definition of Problem

The problem under consideration is the two-dimensional temporally-developing turbulent mixing layer, indicated in Figure 1a. The mixing layer is formed by two parallel streams of infinite extent in the x-direction. The flow is statistically unsteady, since the width of the mixing region grows in time. In contrast, the typical experimental configuration is the spatially developing mixing layer formed by two semi-infinite parallel streams, as indicated in Figure 1b. The flow is statistically steady, and the mixing width grows linearly downstream.

The temporally-developing mixing layer is considered for reasons of computational cost. In this configuration, the mean convective velocity of the eddies is approximately zero, thereby allowing the use of a fixed computational domain whose streamwise extent is twice the eddy size (for the case of a single

"pairing"). In the spatially developing mixing layer, the mean convective velocity is approximately $(U_1 + U_2)/2$, thereby requiring a computational domain whose streamwise extent is several times the typical eddy size in order to consider a similar amalgamation.

There is no precise transformation between the temporally- and spatially-developing cases. Qualitatively, however, the configurations are similar if related by the Galilean transformation

$$x' = \tfrac{1}{2}(U_1 + U_2)t \tag{1}$$

The freestream velocity U_∞ in the temporally developing case is thus defined as

$$U_\infty = \tfrac{1}{2}(U_1 - U_2) \tag{2}$$

The turbulent motion is assumed to consist of a combination of large-scale coherent motion and fine-scale random fluctuations. Considering the instantaneous streamwise velocity, $U(x,y,z,t)$, a conditional average $\langle U \rangle$, denoted by u for simplicity, is defined by

$$u = \langle U \rangle \equiv \frac{1}{T_o} \int_{t - \frac{T_o}{2}}^{t + \frac{T_o}{2}} U dt \tag{3}$$

where T_o is defined by:

time scale of random motion $\ll T_o \ll$ time scale of coherent motion.

Based on the experimental data,[3] the conditionally-averaged ("coherent") motion is assumed to be two-dimensional and unsteady. The instantaneous streamwise velocity is thus

$$U = u + u''$$

where u'' represents the fine-scale random fluctuations. Similarly, the instantaneous velocities in the y and z directions are defined by

$$V = v + v''$$

$$W = w + w''$$

where in the present case $w = 0$.

The conditionally-averaged conservation equations are

$$\text{Momentum:}\quad \frac{\partial u_i}{\partial t} + u_j \frac{\partial u_i}{\partial x_j} = -\frac{\partial p}{\partial x_i} + \frac{\partial}{\partial x_j}\left(-\langle u_i'' u_j''\rangle\right) + \nu \frac{\partial^2 u_i}{\partial x_j^2} \tag{4}$$

$$\text{Mass:}\quad \frac{\partial u_i}{\partial x_i} = 0 \tag{5}$$

where $u_1 = u$, $u_2 = v$, $x_1 = x$, $x_2 = y$ and ν is the kinematic viscosity. The turbulence model equations of Saffman[11,12] provide additional rate equations for the "fine-scale Reynolds stresses" $\langle u_i'' u_j''\rangle$, thereby yielding a closure of the equations of motion. For purposes of brevity the model equations are not presented here; complete details are given in references 11 and 12.

The initial profiles for the velocity, pressure and fine-scale Reynolds stresses are taken to be the similarity solution of the equations of motion, wherein there is no streamwise (i.e., x) variation (e.g., $u = U_\infty f(\eta)$, where $\eta = y/U_\infty t_o$ is the similarity independent variable and t_o is an arbitrary initial time). In addition, a perturbation is added to the velocity and pressure field. The perturbation is the sum of two contributions: 1) the (approximately) most unstable eigenfunction (harmonic) corresponding to an inviscid (Raleigh) stability analysis of the initial velocity profile, and 2) the first subharmonic [i.e., the eigenfunction whose wavelength is twice that of the disturbance in 1)]. The relative phase of the two contributions is chosen to yield an initial vorticity field which is symmetric upon reflection through an origin located at the center of the computational region. The pair of eddies which initially develop, therefore, have the same "strength," as discussed later. The kinetic energy of the initial perturbation, equi-partitioned between harmonic and subharmonic, is taken to be 4% of the initial kinetic energy defect of the mixing layer. The initial Reynolds

based on the velocity difference ($2U_\infty$), velocity-profile maximum slope thickness and kinematic viscosity is 480.

The boundary conditions assume periodicity in x over the length of the computational domain which is equal to the wavelength of the first subharmonic. Freestream boundary conditions are taken at sufficiently large $|y|$ where $u = U_\infty$ and all fine-scale Reynolds stresses vanish.

III. Results

Mean Flow Properties

The mean velocity $\bar{u}$ in the streamwise direction, denoted by U, is defined as

$$U = \bar{u} \equiv \frac{1}{L} \int_0^L u dx \tag{6}$$

where L = length of computational domain. The velocity-profile maximum slope thickness $\delta_\omega(t)$ ("vorticity thickness") is defined by

$$\delta_\omega = \frac{2U_\infty}{\left.\frac{\partial U}{\partial y}\right|_{max}} \tag{7}$$

Using equations (1) and (2), the computed results yield a growth rate given by

$$\frac{d\delta_\omega}{dx'} = 0.24 \frac{(U_1 - U_2)}{(U_1 + U_2)}$$

The experimental best-fit indicated by Brown and Roshko[3] is

$$\frac{d\delta_\omega}{dx'} = 0.18 \frac{(U_1 - U_2)}{(U_1 + U_2)}$$

although the numerical coefficient is dependent upon the state of the boundary layer at the end of the splitter plate[13] with values varying from 0.16 in the experiment of Liepmann and Laufer[14] to 0.24 in the results of Wygnanski and Fiedler.[15] In view of the only approximate similarity between the temporally and

spatially developing mixing layers, the agreement with experiment is reasonable.

In Figure 2, the mean velocity profile U(y,t) is shown as a function of y/θ, where θ is the momentum thickness defined in the usual fashion.[8] In this figure, the time t has been non-dimensionalized using U_∞ and the initial half-width* of the mixing layer, with t = 0 implying the initial conditions. It is apparent that the mean velocity profile has remained self-similar despite substantial growth in the coherent perturbations. In particular, define the coherent perturbation kinetic energy by

$$E_{coh} = \frac{1}{L} \int_{-\infty}^{\infty} \int_{0}^{L} \tfrac{1}{2}(u'^2 + v'^2) dx dy \tag{8}$$

where u' and v' are given by

$$u' = u - U, \quad v' = v \tag{9}$$

and define the mean kinetic energy defect by

$$E_{mean} = \int_{-\infty}^{\infty} \tfrac{1}{2}(U_\infty^2 - U^2) dy \tag{10}$$

As indicated above, the initial coherent perturbation kinetic energy is 4% of the initial E_{mean}. At t= 10, however, the coherent perturbation kinetic energy is 23% of the current mean kinetic energy defect. The self-similarity of the mean velocity is in agreement with experiment.[1]

---

*The initial half-width is defined as the value of y for which $U = .99U_\infty$ for the initial velocity profile.

Large Scale Structure

The evolution and interaction of a pair of large-scale eddies is indicated in Figures 3a through 3i. Each figure is a contour plot* at a particular time of the conditionally-averaged vorticity ζ where $\zeta = \frac{\partial v}{\partial x} - \frac{\partial u}{\partial y}$. Selected numerical values of the vorticity are shown, where the vorticity has been non-dimensionalized using U_∞ and the initial half-width of the mixing layer. As indicated earlier, the particular choice of the relative phase of the harmonic and subharmonic yields initially two eddies whose maximum absolute vorticity is identical (Figure 3a).

The vorticity contour plots clearly indicated the growth, interaction and eventual amalgamation or "pairing" of the two eddies. The features are qualitatively similar to the experimental dye photographs of Winant and Browand,[8] and the experimental vorticity contour plots of the large-scale structures of Browand and Weidman.[16] In particular, the correlation coefficient of the large-scale perturbations** at $t = 8$ (see Figure 3d) is greater than 0.9 for $-1.3 < y/\theta < 1.3$. This is in agreement with the experimental result of Browand and Weidman[16] who found the correlation coefficient of the large structures to be greater than 0.9 for $-2 \leq y/\theta \leq 2$ at a stage in the vortex pairing where the vorticity contours display a strong resemblance to Figure 3d.***

---

*The contour plots were produced on a line printer. The algorithm employed divided the vorticity at a particular time into a fixed number of equal increments between its minimum and maximum values. The projection of these levels onto the x-y plane were printed alternately as characters and blanks. The result is more precisely a "level" plot, rather than a contour plot; for example, the dark region at the center of the eddies in Figure 3a corresponds to $-1.68 < \zeta < -1.58$, and the immediately surrounding blank annular region corresponds to $-1.58 < \zeta < -1.47$. For purposes of simplicity, the numerical values indicated in Figures 3a to 3i are the mid-range values (i.e., -1.63, -1.52, ..., for the above case).

**Defined by $T = -\overline{u'v'}/\{\overline{u'^2}\ \overline{v'^2}\}^{\frac{1}{2}}$. Note definitions of equations (6) and (9).

***This is Stage II of Browand and Weidman[16] (Figure 6b). In comparing the figures, due account must be given to the differences in definition of direction of mean flow.

The qualitative features of fluid entrainment by the large-scale structures have been examined by inclusion of a passive scalar (i.e., diffusion) equation. The initial passive scalar (e.g., fluid "dye") profile was located slightly above the mixing layer with a uniform concentration in x and a Gaussian distribution in y. The "dye" concentration at suceeding times is indicated in Figures 4a through 4i, where three arbitrary fixed levels of concentration have been plotted with increasing darkness in order to give a qualitative visual impression of the dye concentration. At early times, both the diffusion of the dye by fine scale turbulence and the convection by the large-scale structures is apparent. As the eddies amalgamate, a large fraction of the dye-bearing fluid is entrained into the mixing layer, and the region of maximum concentration eventually coincides with the final amalgamated eddy. It is interesting that the dyed fluid appears to be swept across the mixing region before eventually appearing as a concentrated eddy-like structure.

IV. Conclusions

The dynamical evolution of the large-scale structures in the temporally-developing mixing layer have been studied numerically using the turbulence model equations of Saffman. Preliminary results indicate quantitative agreement with mean growth rate and self-similarity of the mean velocity profile. The results display the observed phenomena of "pairing" of large-scale structures in qualitative agreement with experiment. Further work is currently being pursued to provide more detailed comparison of the features of the large-scale interactions.

VI. References

1. Townsend, A. A., The Structure of Turbulent Shear Flow, Cambridge University Press, 1956.

2. Townsend, A. A., "The Mechanism of Entrainment in Free Turbulent Flows," J. of Fluid Mechanics, 26, 1966, 689-715.

3. Brown, G., and Roshko, A., "On Density Effects and Large Structure in Turbulent Mixing Layers," J. of Fluid Mechanics, 64, 1974, 775-816.

4. Papailiou, D., and Lykoudis, P., "Turbulent Vortex Streets and the Mechanism of the Turbulent Wake," J. of Fluid Mechanics, 62, 1974, 11-31.

5. Kline, S. J., et al, "The Structure of Turbulent Boundary Layers," J. Fluid Mechanics, 30, 1967, 741-773.

6. Higuchi, H., "An Experimental Investigation on Axi-Symmetric Turbulent Wakes with Zero Momentum Defect," Ph.D. Thesis, Calif. Inst. of Technology, 1976.

7. Dimotakis, P. E., and Brown, G. L., "The Mixing-Layer at High Reynolds Number. Large Structure Dynamics and Entrainment," J. of Fluid Mechanics, 78, 1976, 535-560.

8. Winant, C. D., and Browand, F. K., "Vortex Pairing: The Mechanism of Turbulent Mixing-Layer Growth at Moderate Reynolds Number," J. of Fluid Mechanics, 63, 1974, 237-255.

9. Konrad, J. H., "An Experimental Investigation of Mixing in Two-Dimensional Turbulent Shear Flows with Applications to Diffusion-Limited Chemical Reactions," Project Squid Technical Report CIT-8-PU, December 1976.

10. Yule, A. J., Chigier, N. A., and Thompson, D., "Coherent Structures in Combustion," Symposium on Turbulent Shear Flows, April 18-20, 1977, University Park, Pennsylvania.

11. Saffman, P. G., "Development of a Complete Model for Calculation of Turbulent Shear Flows," in Statistical Mechanics and Dynamical Systems and Papers from the 1976 Duke Turbulence Conference, W.K. Allard, et al, editors, Duke Univ., Math. Dept., 1976.

12. Knight, D. D. and Saffman, P. G., "Turbulence Model Predictions for Flows with Significant Mean Streamline Curvature," AIAA Paper 78-258, AIAA 16th Aerospace Sciences Meeting, 1978.

13. Batt, R. G., "Some Measurements of the Effect of Tripping the Two-Dimensional Shear Layer," AIAA J., 13, 2, 1975, 245-247.

14. Liepmann, H., and Laufer, J., "Investigations of Free Turbulent Mixing," Report 1257, NACA, 1947.

15. Wygnanski, I., and Fiedler, H. E., "The Two-Dimensional Mixing Region," J. of Fluid Mechanics, 41, 2, 1970, 327-361.

16. Browand, F., and Weidman, P., "Large Scales in the Developing Mixing Layer," J. of Fluid Mechanics, 76, 1, 1976, 127-144.

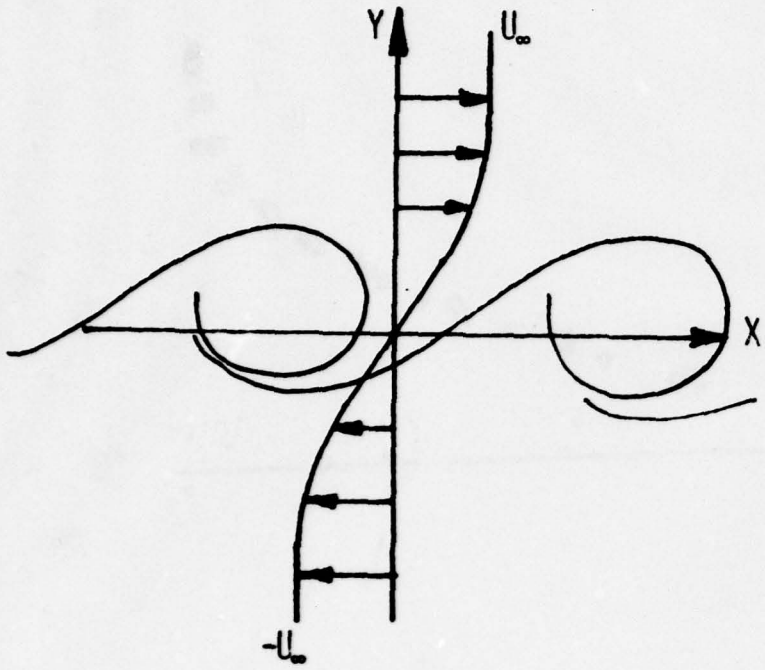

Figure 1a: THEORETICAL CASE
Temporally-Developing

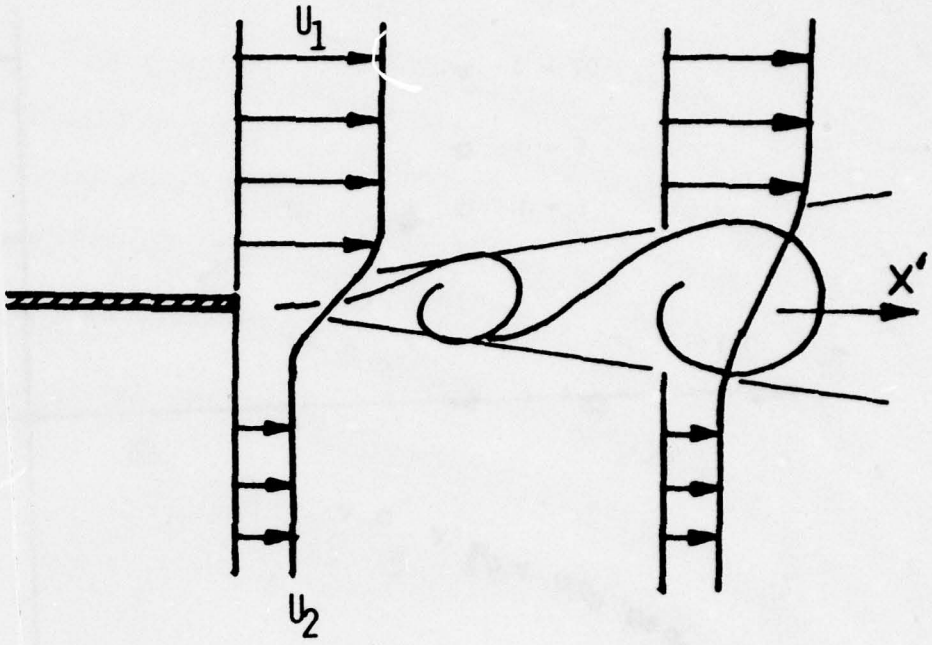

Figure 1b: EXPERIMENTAL CASE
Spatially-Developing

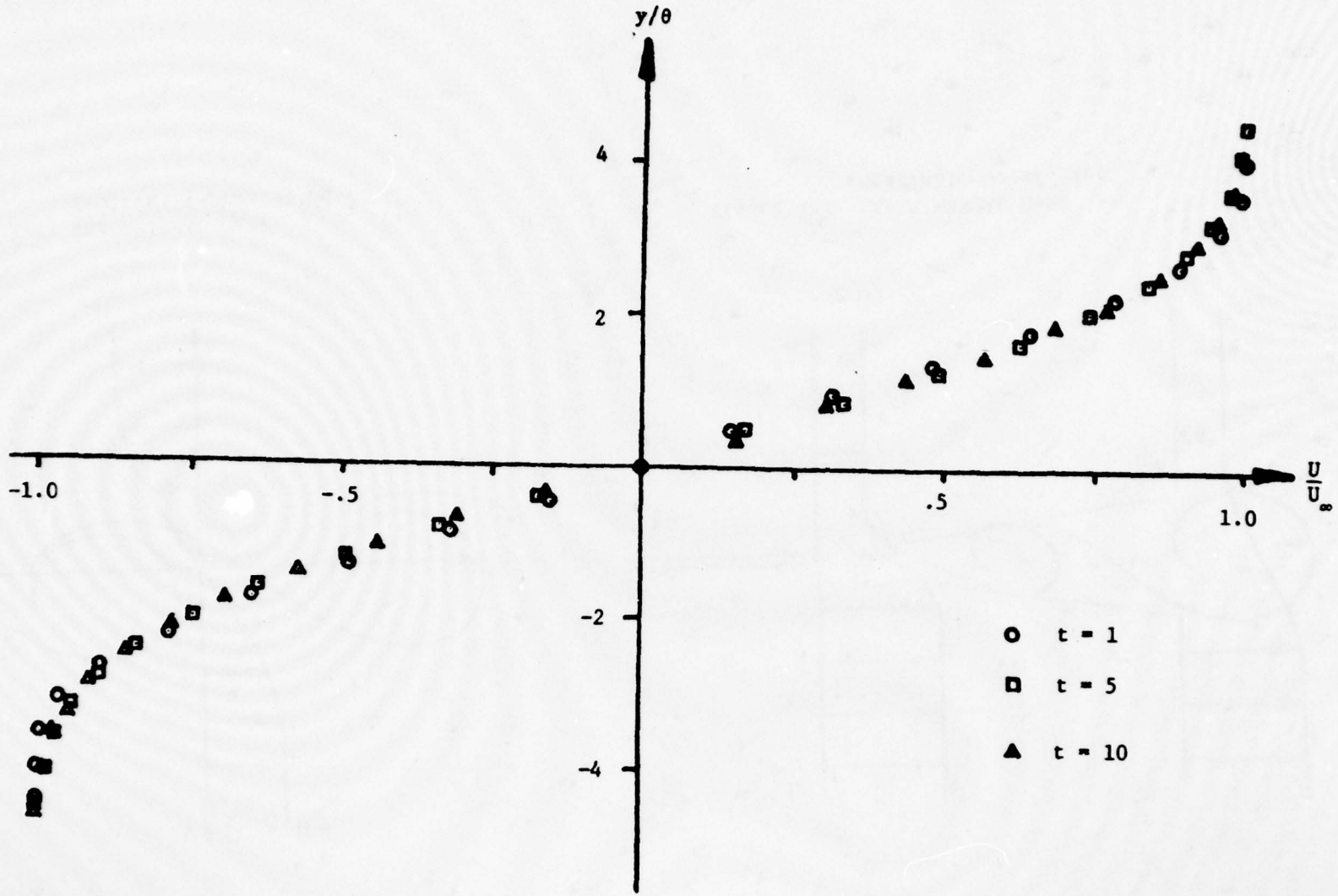

Figure 2: MEAN VELOCITY PROFILE AT SEVERAL STAGES DURING THE EDDY PAIRING

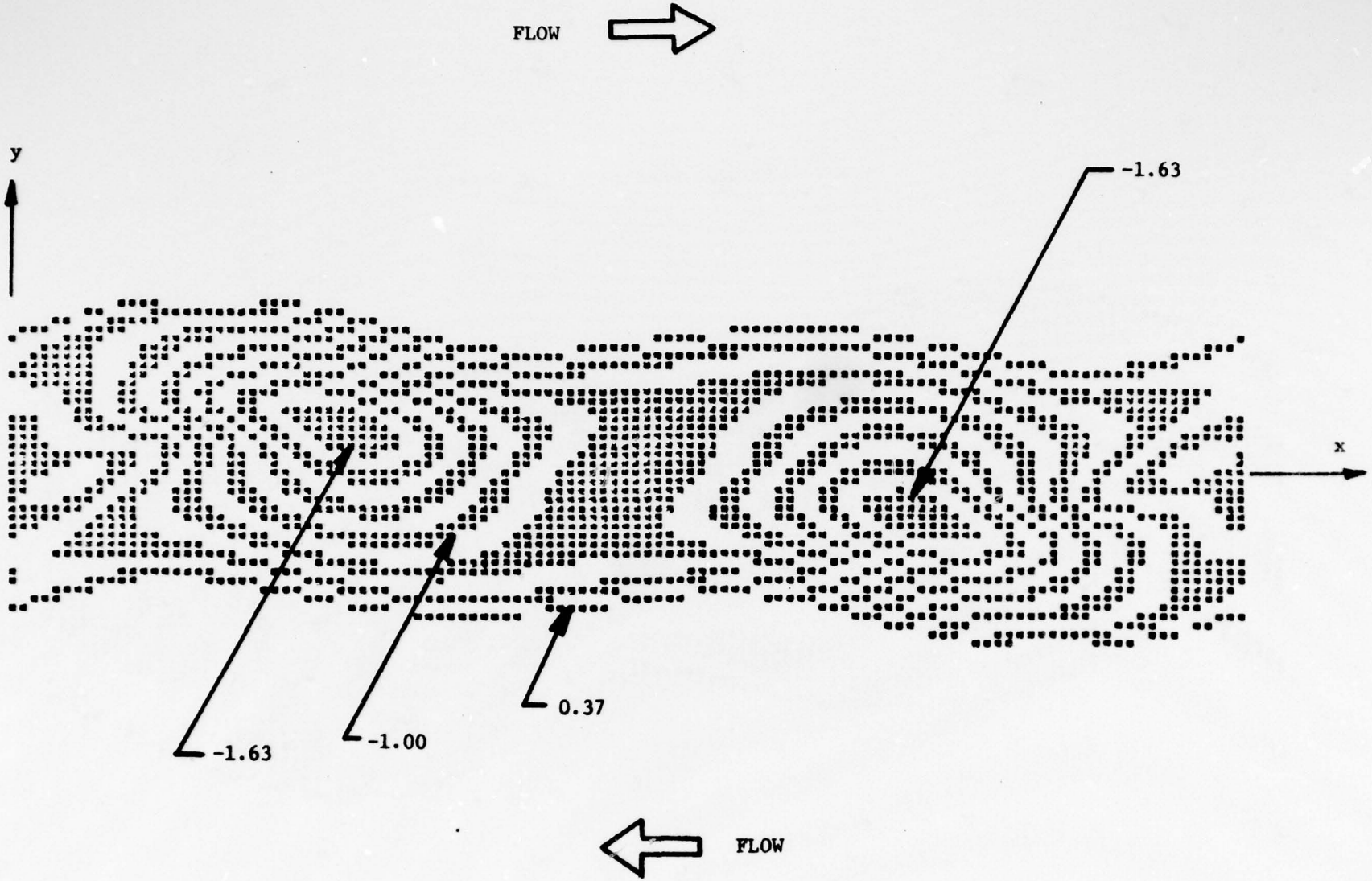

Figure 3a: VORTICITY CONTOURS: t = 2
Values of vorticity are shown. The top and bottom row of asterisks indicate vertical extent of the computational domain.

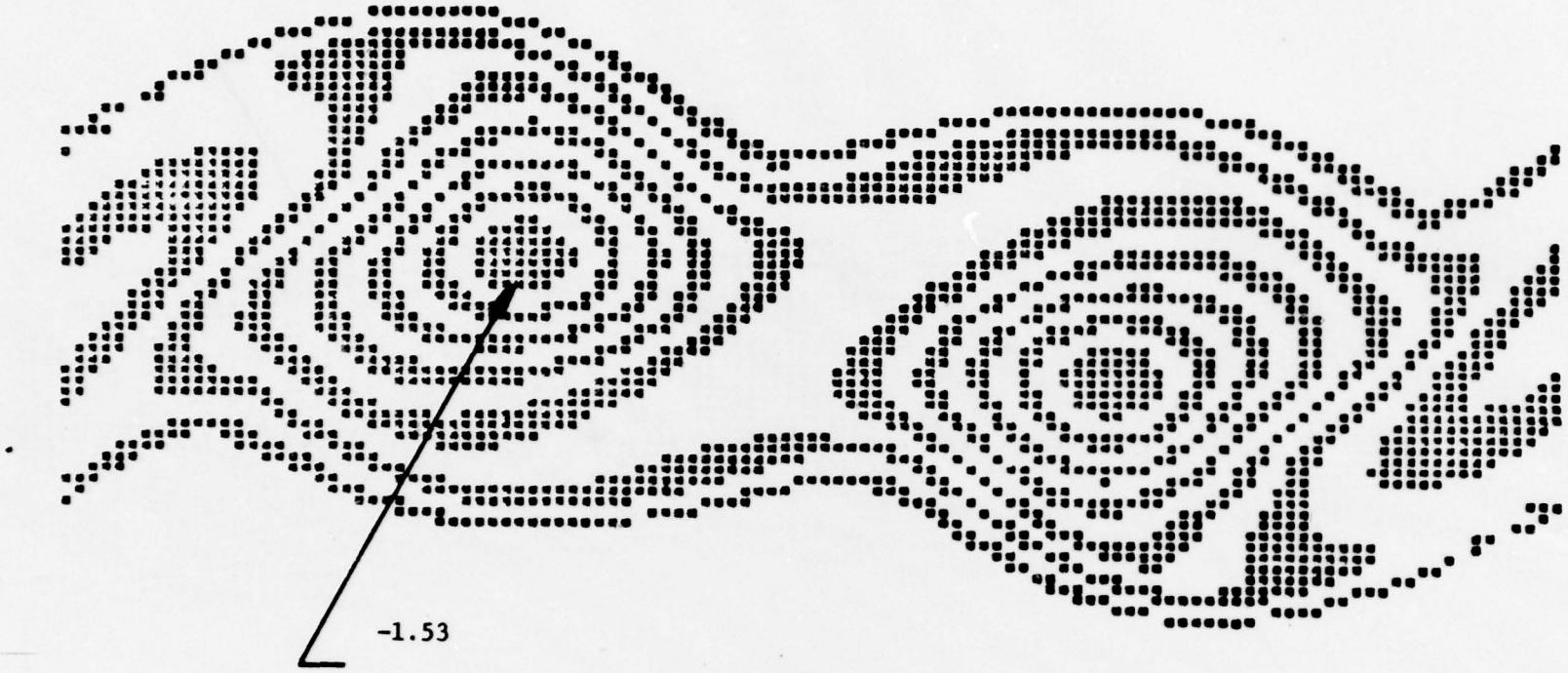

Figure 3b: VORTICITY CONTOUR: t = 4

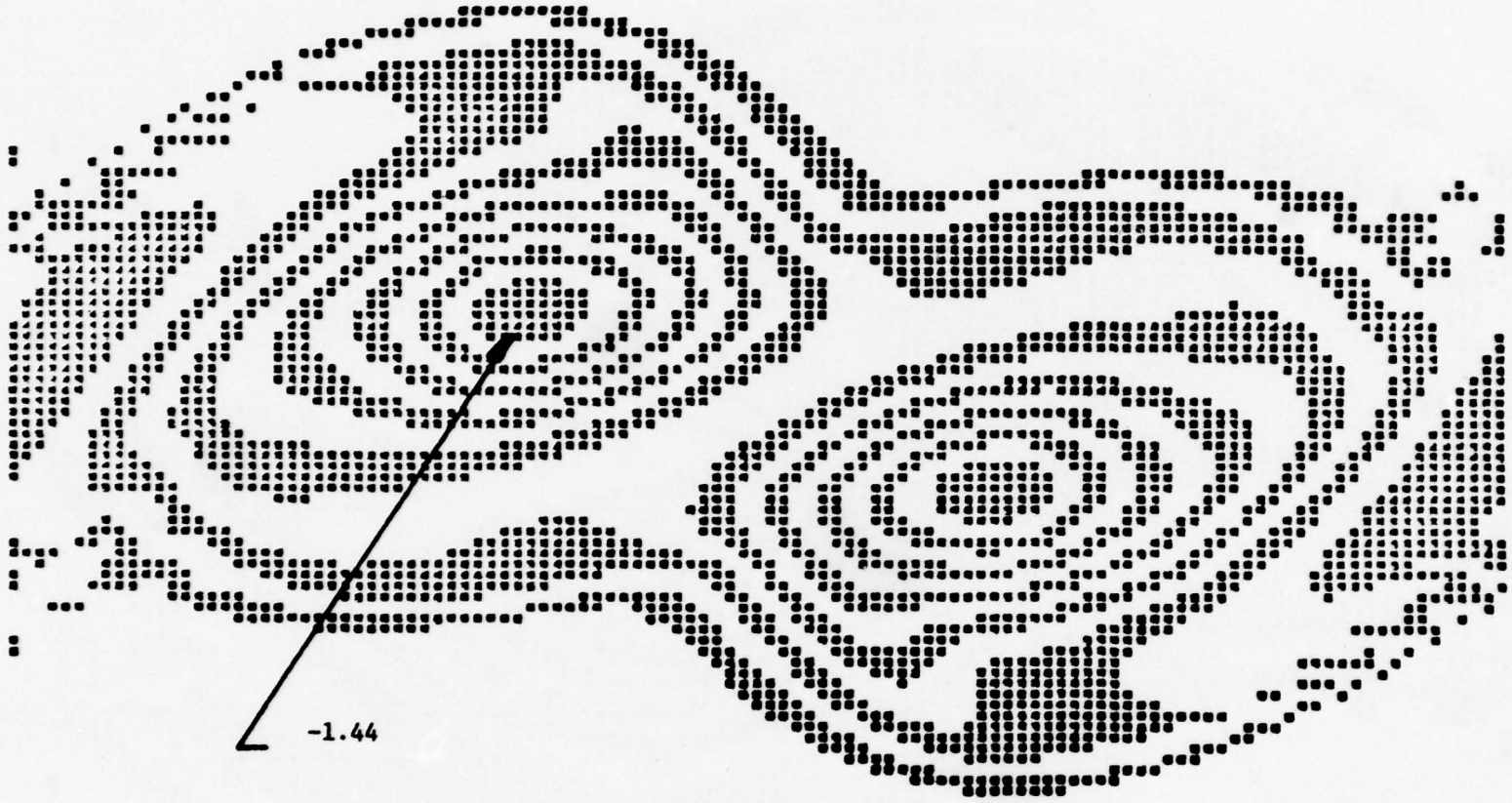

Figure 3c: VORTICITY CONTOUR: t = 6

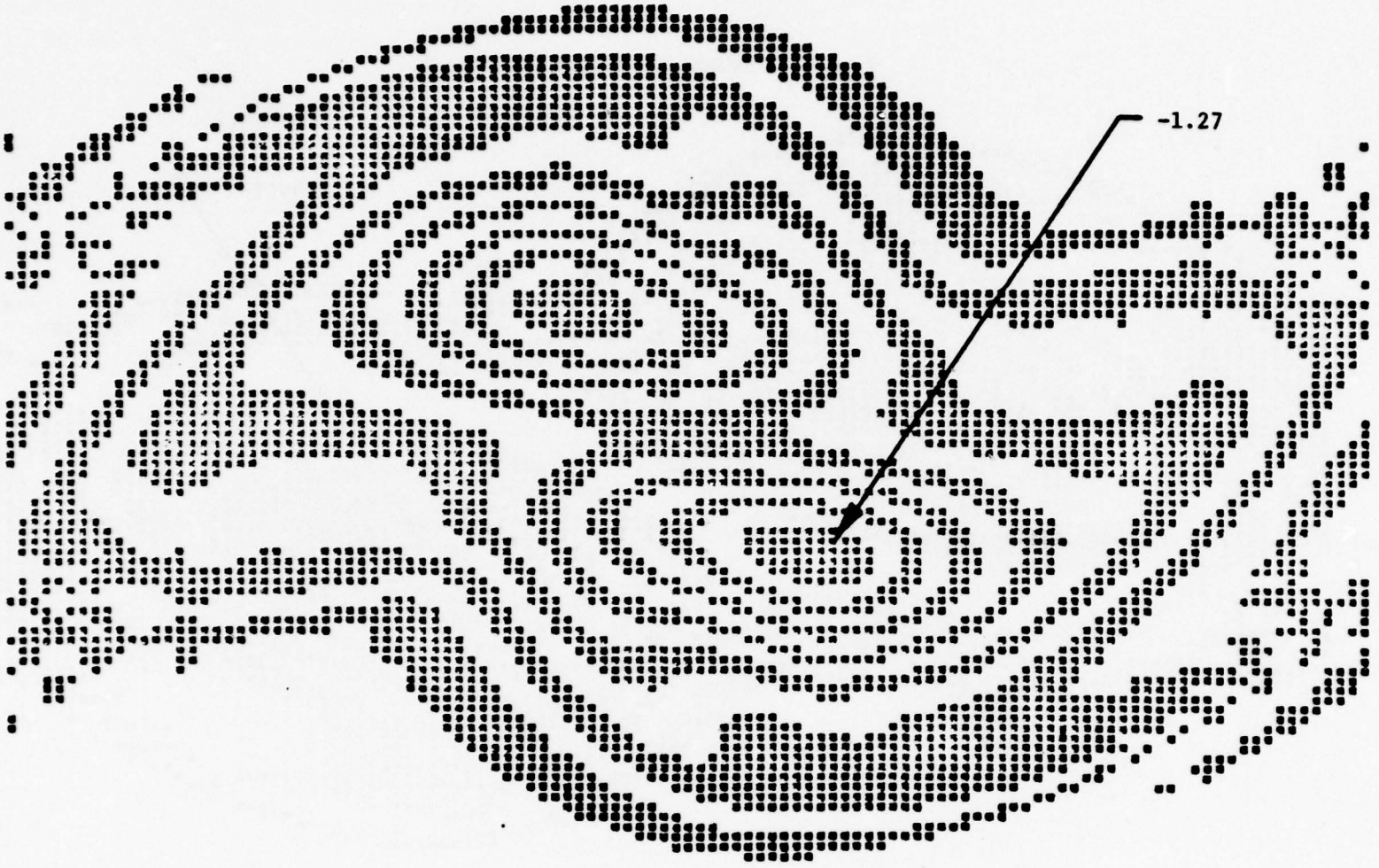

Figure 3d: VORTICITY CONTOUR: t = 8

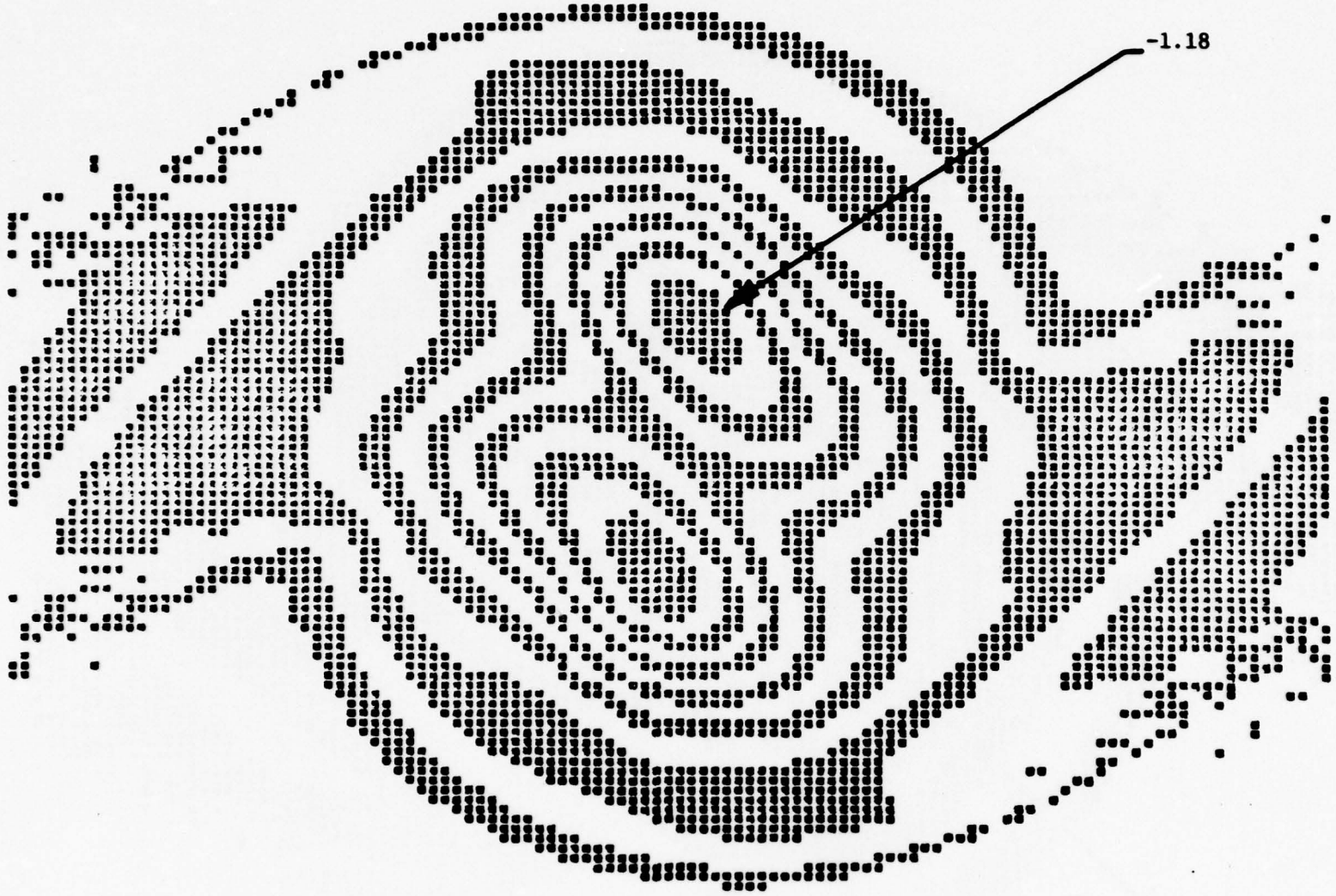

Figure 3e: VORTICITY CONTOUR: t = 10

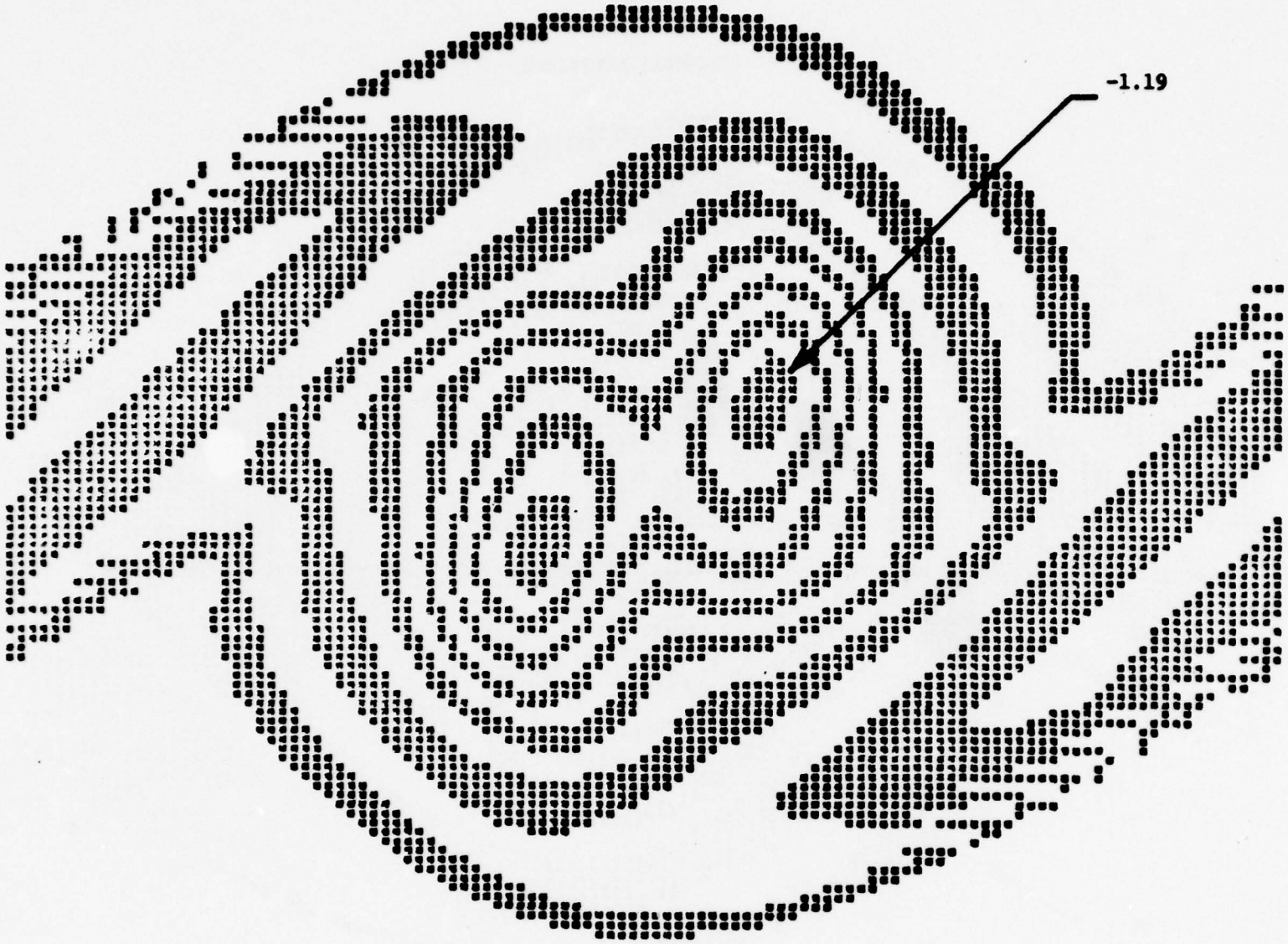

Figure 3f: VORTICITY CONTOUR: t = 12

Figure 3g: VORTICITY CONTOUR: t = 14

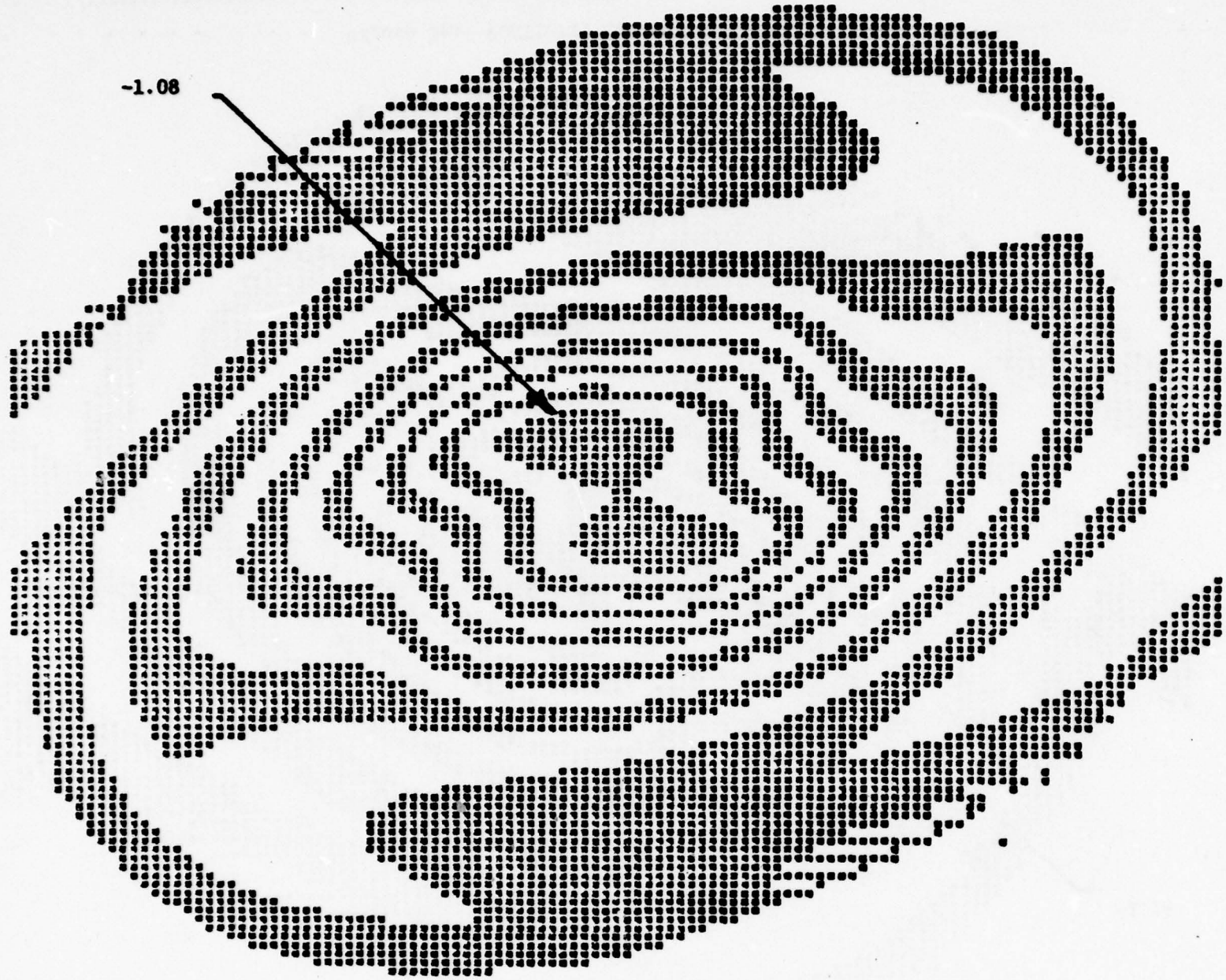

Figure 3h: VORTICITY CONTOUR: t = 16

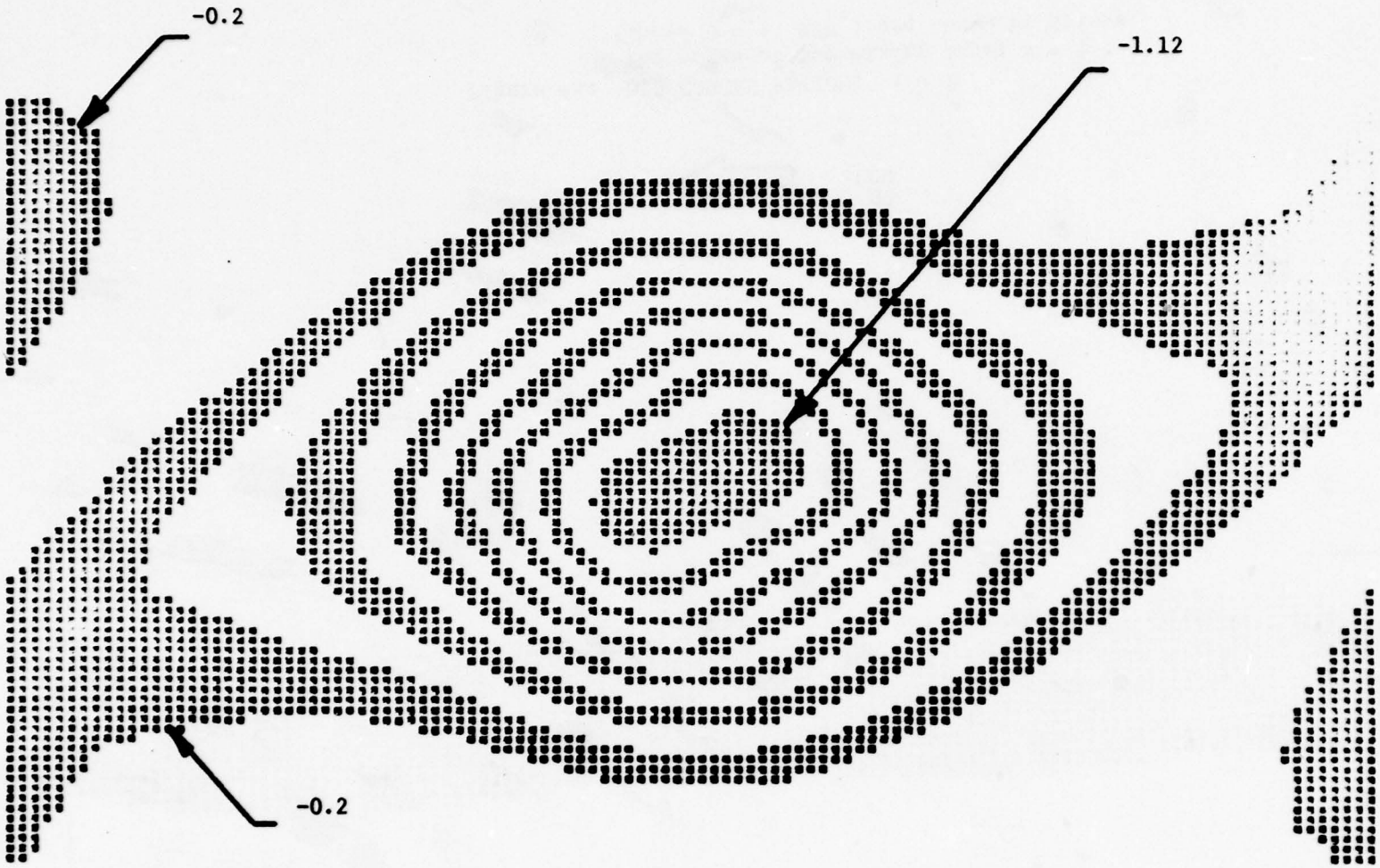

Figure 31: VORTICITY CONTOUR: t = 19

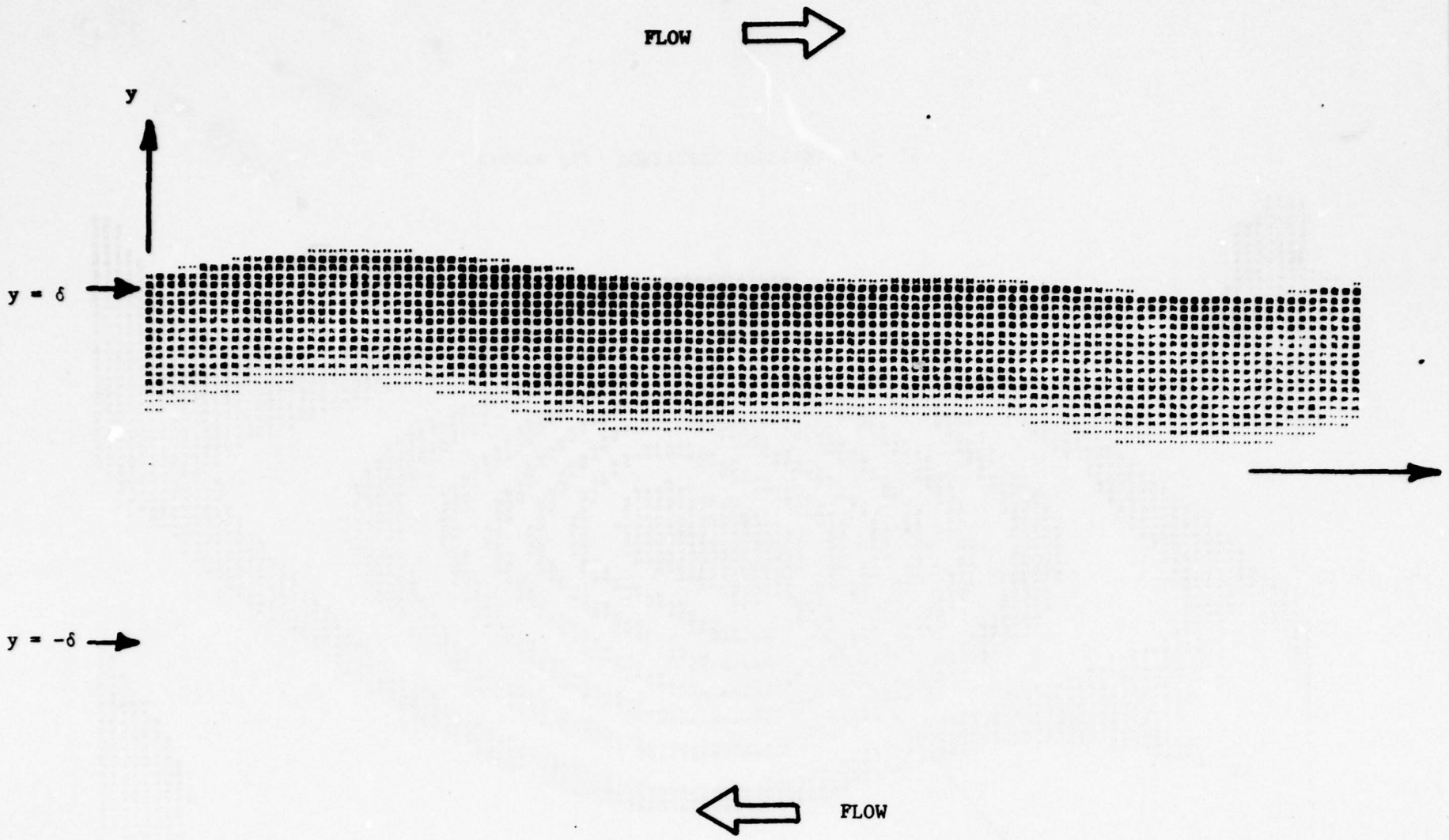

Figure 4a: DYE CONCENTRATION: t = 2
The edges of the mixing layer $y = \pm \delta$ (where $U = \pm .99U_\infty$) are shown by arrows.

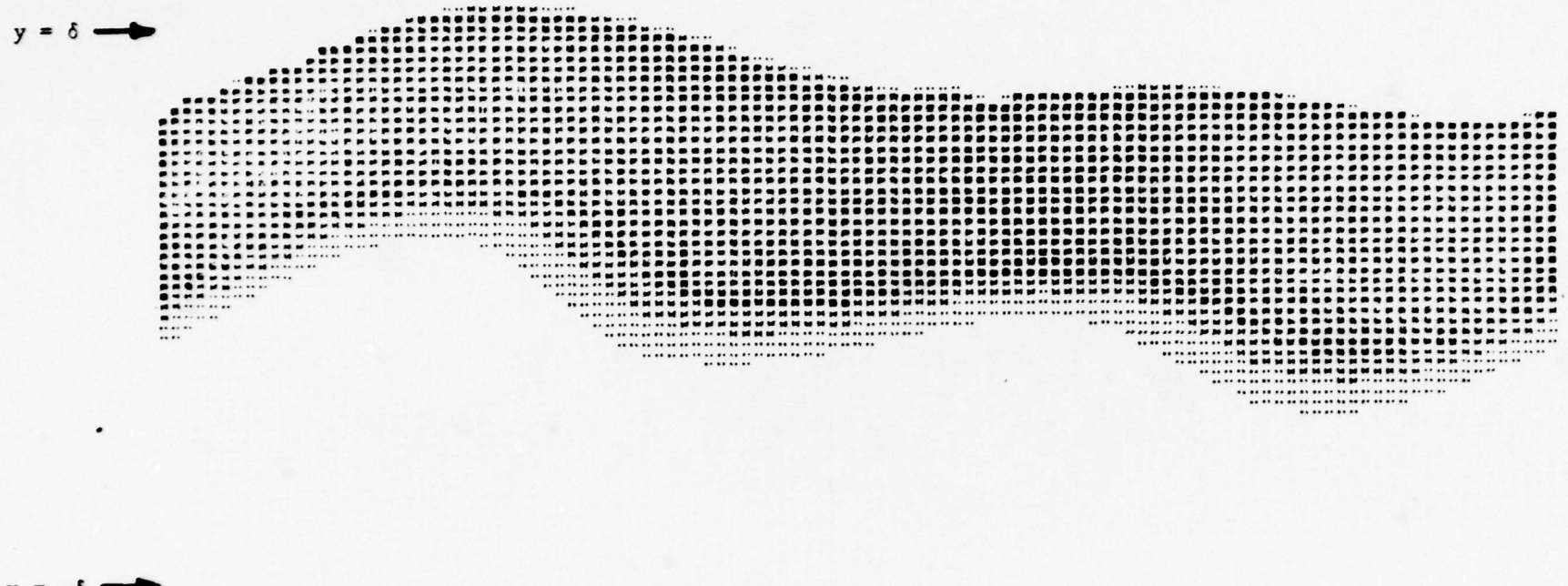

Figure 4b: DYE CONCENTRATION: t = 4

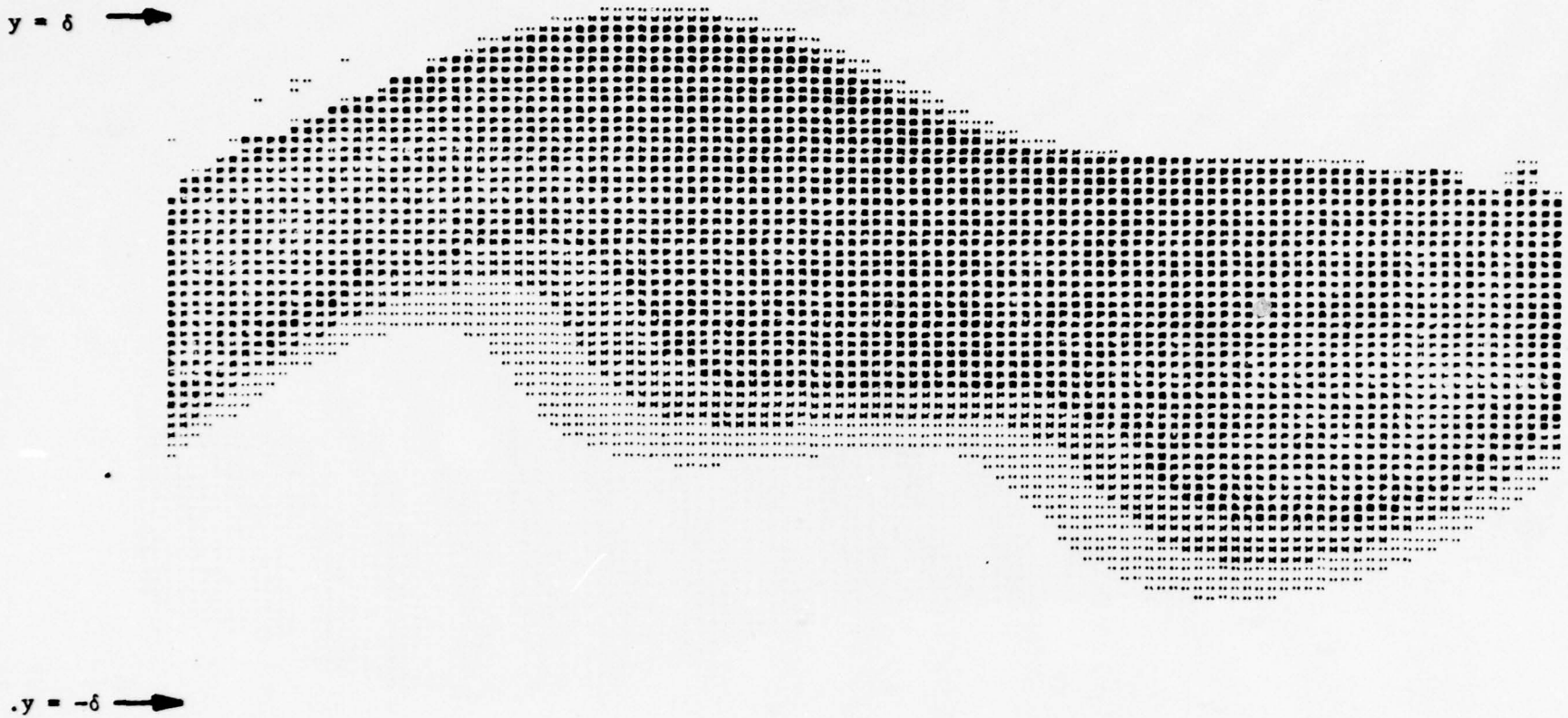

Figure 4c: DYE CONCENTRATION: t = 6

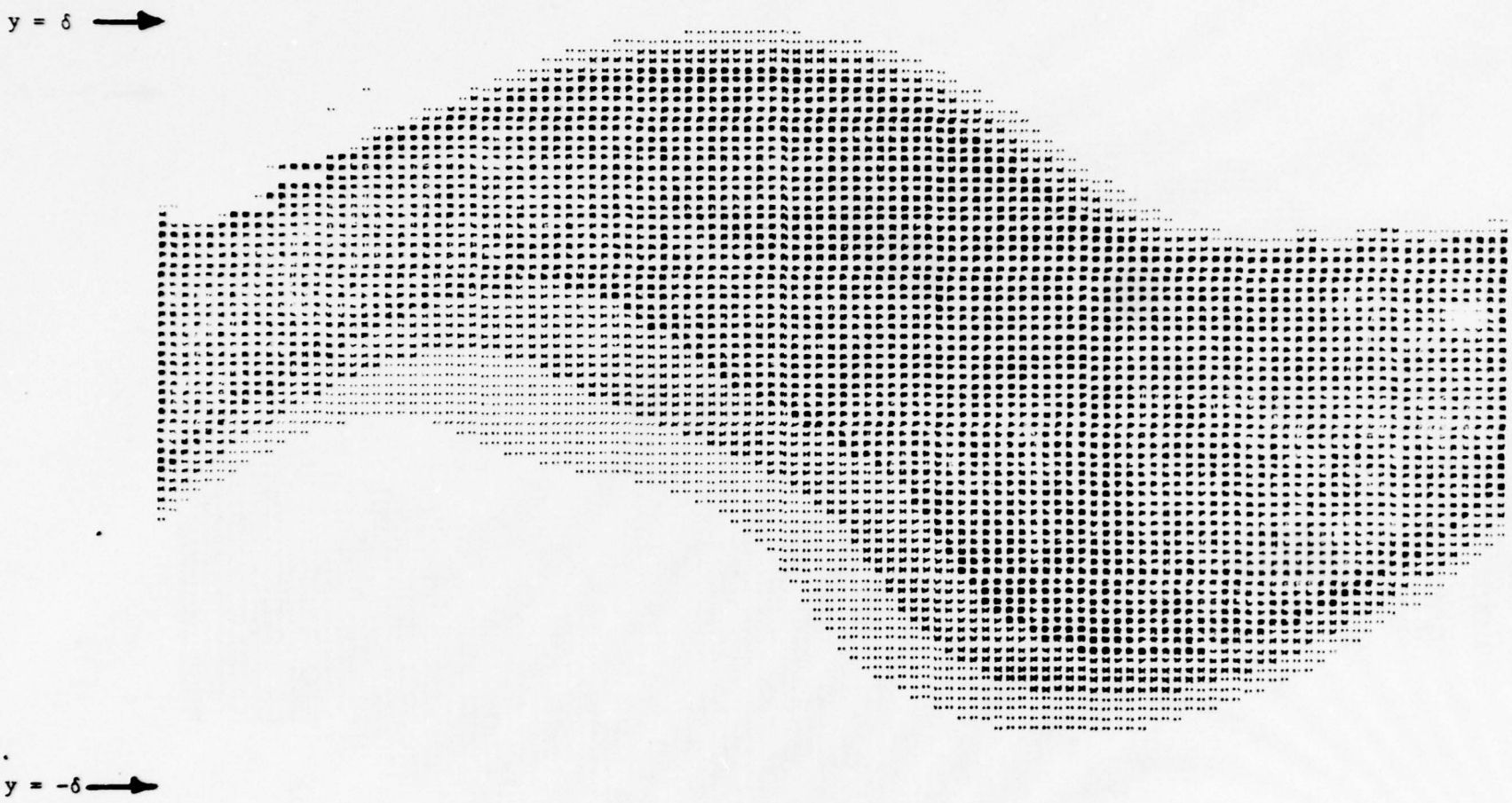

Figure 4d: DYE CONCENTRATION: t = 8

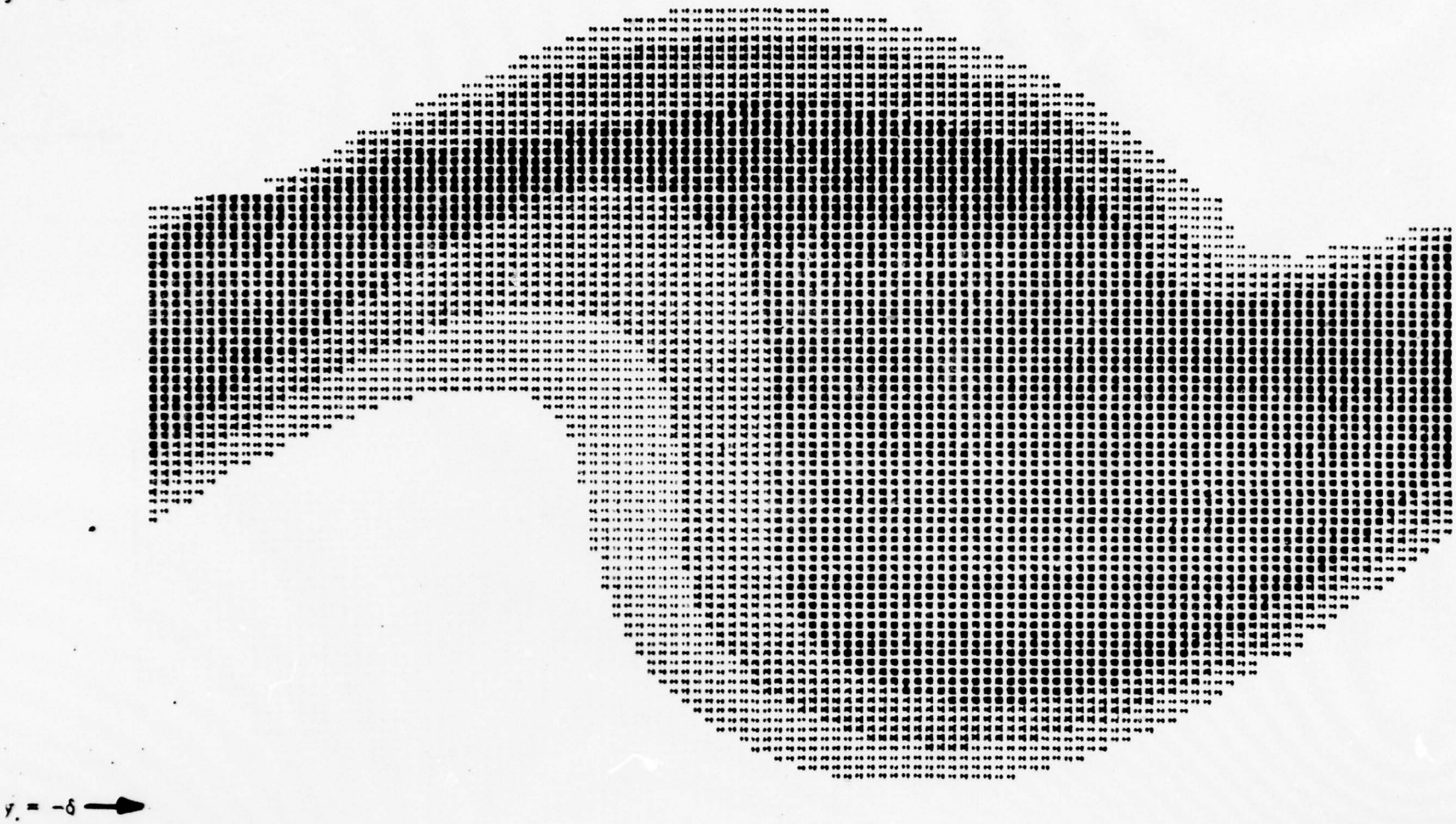

Figure 4e: DYE CONCENTRATION: t = 10

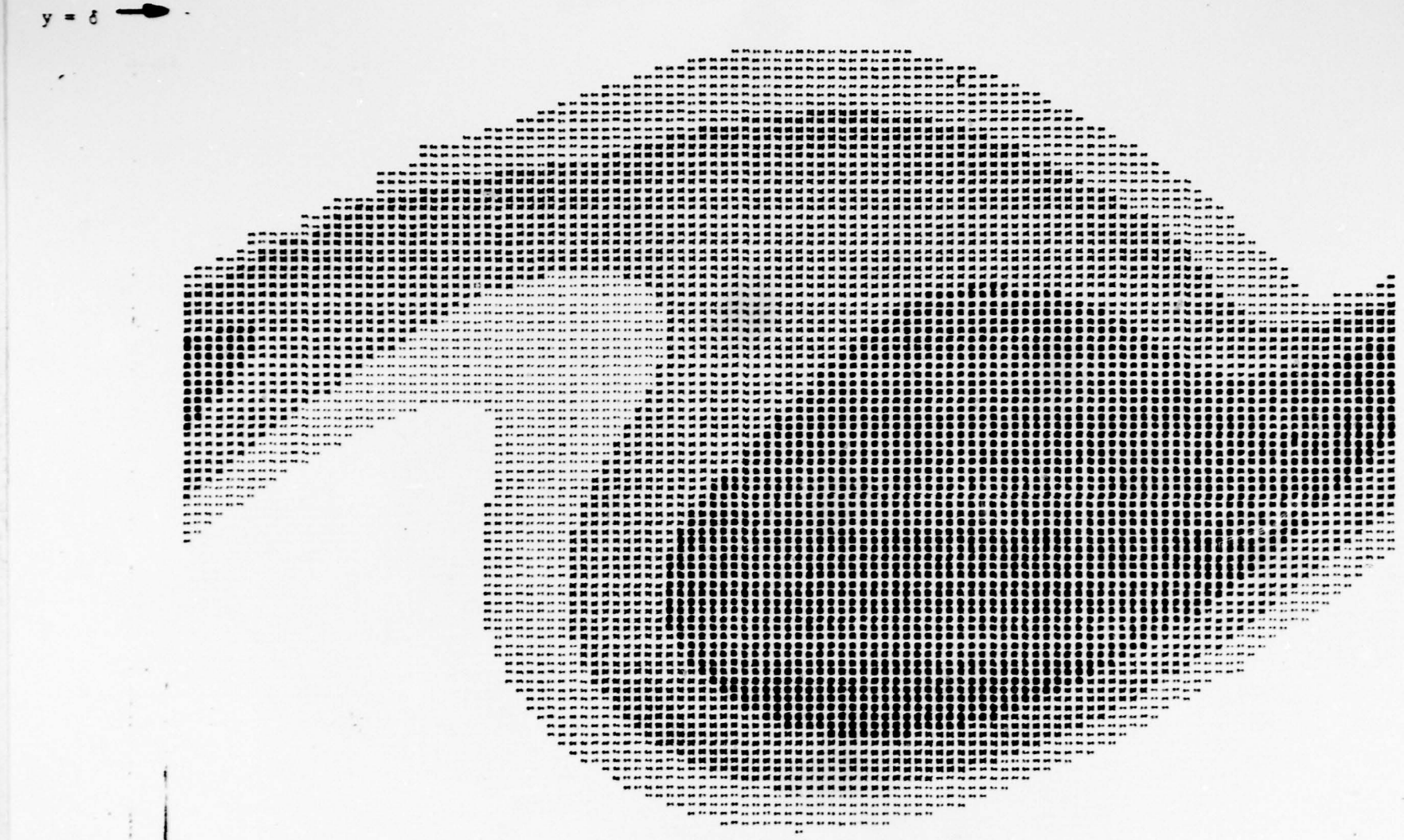

Figure 4f: DYE CONCENTRATION: t = 12

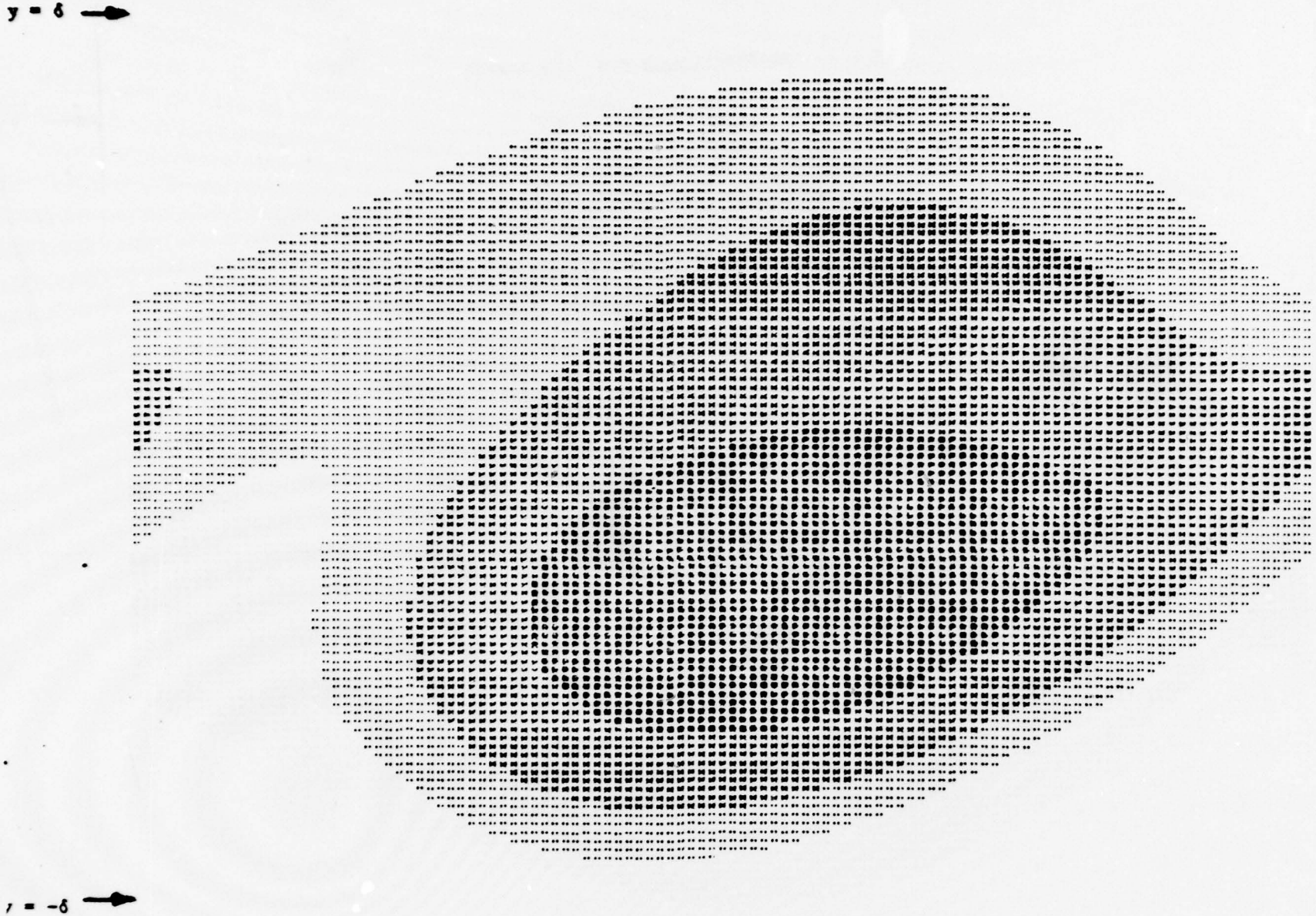

Figure 4g: DYE CONCENTRATION: t = 14

y = δ

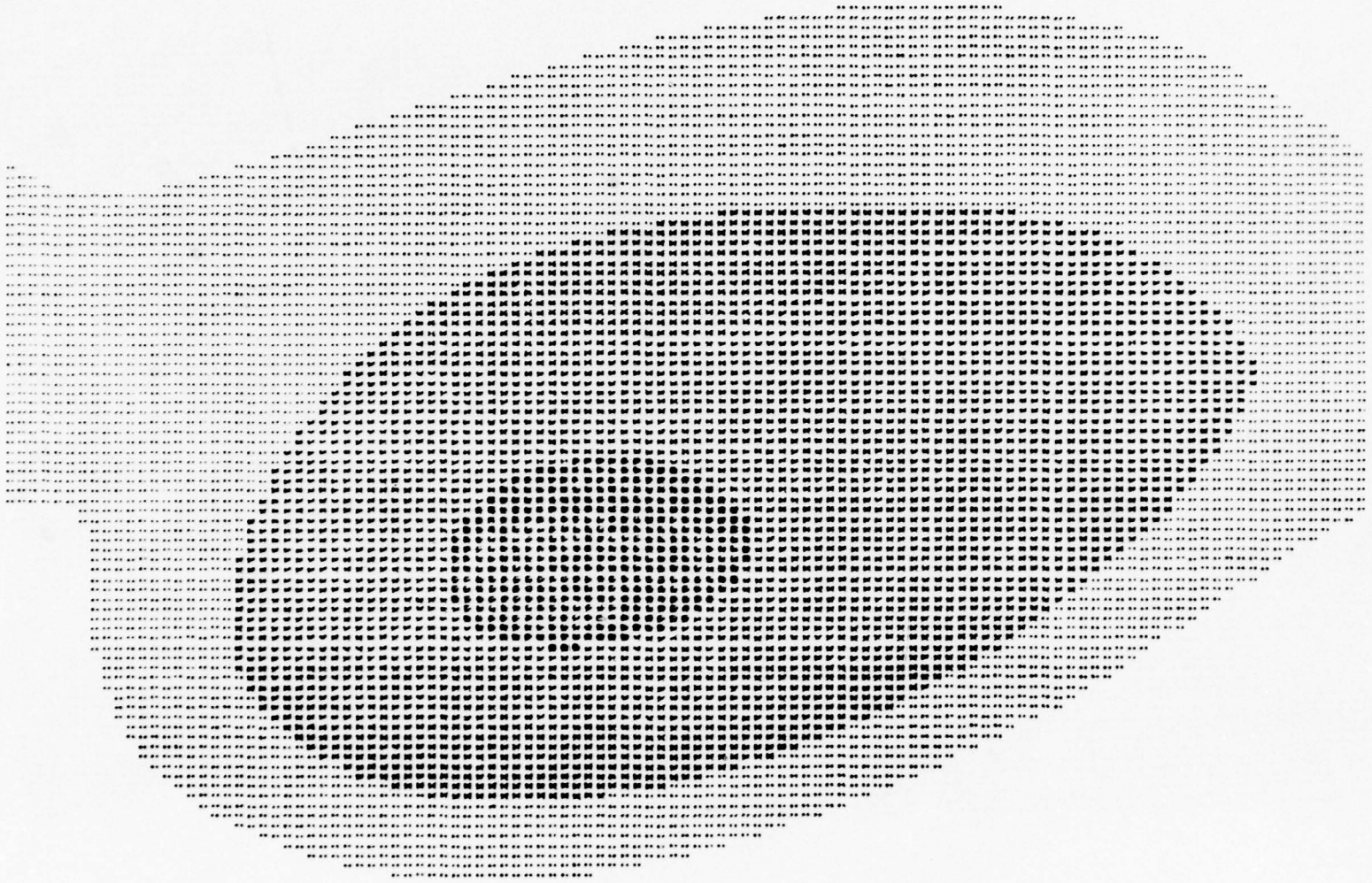

y = -δ

Figure 4h: DYE CONCENTRATION: t = 16

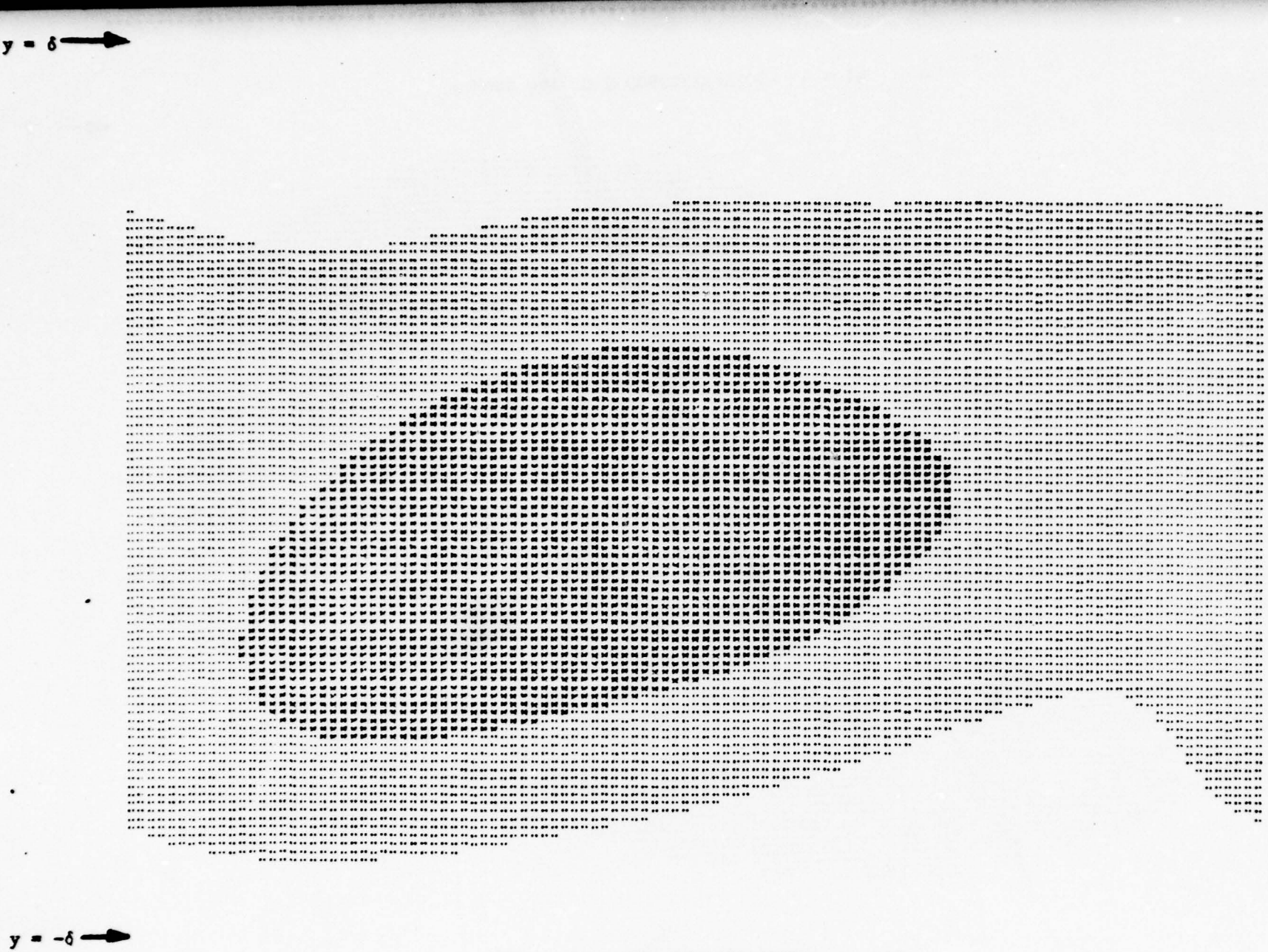

Figure 41: DYE CONCENTRATION: t = 19

On the Approximate Motion of Vorticity-Bearing Eddies in a Perfect Fluid in Three Dimensions

by

Doyle D. Knight
Applied Mathematics Department
California Institute of Technology
Pasadena, California 91125

The approximate equations of motion of a dilute collection of vorticity-bearing eddies in an unbounded perfect fluid in three dimensions are derived. The planar interaction of a pair of eddies is considered numerically for two initial configurations. Application to a deterministic model of the large eddies in a turbulent shear layer is discussed.

I. Introduction

The past several years have seen a resurgence of interest in the role of the "large eddies" in turbulent flows. First utilized extensively by Townsend in his research on turbulent shear flows (Townsend 1956), the concept of the large eddies has recently been the subject of considerable research (for a brief review, see Roshko (1976)).

The present results are a first step in an approximate deterministic model of the large eddies in a turbulent flow.

The "large eddies" are viewed as simply-connected regions or "blobs" of fluid with non-zero vorticity in an otherwise perfect fluid in three-dimensions. They form a dynamical system, whose approximate equations of motion are described below. The effects of viscosity (i.e., entrainment) and generation are currently under study.

II. Formulation of Problem

We consider a collection of simply-connected regions of non-zero vorticity (the "large eddies") in an otherwise perfect fluid in three-dimensions. For simplicity, we assume that the flow is unbounded, at rest at infinity, and contains no sources, sinks or body forces. (For further discussion, see IV).

As the fluid is assumed perfect, Kelvin's theorem allows that vortex tubes move with the flow, and thus the volume of rotational fluid comprising each eddy remains constant. We define the center of mass $\underset{\sim}{R}^i$ of the i^{th} eddy with volume V_i in the usual fashion,

$$\underset{\sim}{R}^i = V_i^{-1} \int_{V_i} \underset{\sim}{x}\, dV \qquad (1)$$

where $\underset{\sim}{x}$ is the position vector. It is straightforward to show that

$$V_i \frac{d\underset{\sim}{R}^i}{dt} = \underset{\sim}{I}^i + \int_{\partial V_i} \varphi \, \underset{\sim}{n} \, dS \tag{2}$$

where

$\underset{\sim}{I}^i$ = Impulse of i^{th} eddy = $\frac{1}{2}\int_{V_i} \underset{\sim}{x} \wedge \underset{\sim}{\omega} \, dV$

$\underset{\sim}{\omega}$ = vorticity = curl $\underset{\sim}{u}$

$\underset{\sim}{u}$ = velocity

φ = velocity potential

$\hat{n}$ = outward normal on surface of i^{th} eddy

As the fluid is assumed unbounded and at rest at infinity, the velocity field can be expressed as

$$\underset{\sim}{u}(\underset{\sim}{x}, t) = -\frac{1}{4\pi} \int_{\text{All space}} \frac{(\underset{\sim}{x} - \underset{\sim}{x}') \wedge \underset{\sim}{\omega}(\underset{\sim}{x}', t) dV(\underset{\sim}{x}')}{|\underset{\sim}{x} - \underset{\sim}{x}'|^3} \tag{3}$$

At some point within the i^{th} eddy, it is convenient to represent the velocity as a sum of two terms,

$$\underset{\sim}{u}(\underset{\sim}{x}, t) = \underset{\sim}{u}_E + \underset{\sim}{u}_I$$

where $\underset{\sim}{u}_E(\underset{\sim}{x}, t)$ is the contribution due to the presence of the eddies exterior to the i^{th} eddy (i.e., the volume integral in (3) is divided into the region exterior and the region interior to the i^{th} eddy). It is then possible to derive the dynamical result (Saffman, 1971)†

$$\frac{d\underset{\sim}{I}^i}{dt} = \int_{V_i} \underset{\sim}{u}_E \wedge \underset{\sim}{\omega} \, dV. \tag{4}$$

---

† Professor Saffman has noted that the essential idea of equation (4) is evident in Betz (1933).

The system of equations (2) and (4) provide the framework for an approximate description of the motion of the eddies.

III. Approximate Equations of Motion

We first consider the equation for the impulse (4). By utilizing the fact that in the vicinity of the i^{th} eddy $\underset{\sim}{u}_E$ may be expressed as the gradient of a scalar, and expanding $\underset{\sim}{u}_E$ in a Taylor's series about the center of mass of the i^{th} eddy, we can obtain after some manipulation

$$\frac{d\underset{\sim}{I}^i}{dt} \cong - A(t)\underset{\sim}{I}^i \tag{5}$$

where $A(t)$ is a second order tensor given by

$$A(t) = \text{grad } \underset{\sim}{u}_E(\underset{\sim}{R}^i(t), t)$$

and contributions from higher order terms in the Taylor series expansion are ignored. The velocity field at the center of mass of the i^{th} eddy due to the presence of all other eddies (i.e., $\underset{\sim}{u}_E(\underset{\sim}{R}^i(t), t)$) can be expressed using the asymptotic form (Batchelor, 1970),

$$\underset{\sim}{u}_E(\underset{\sim}{R}^i(t), t) \sim \frac{1}{4\pi} \sum_{\substack{j=1 \\ j\neq i}}^{N} \text{grad}\left\{ \underset{\sim}{I}^j(t) \cdot \text{grad}\left(\frac{1}{|\underset{\sim}{x} - \underset{\sim}{R}^j(t)|}\right)\right\}\Bigg|_{\underset{\sim}{x} = \underset{\sim}{R}^i(t)} \tag{6}$$

where the summation omits the i^{th} eddy.

It is possible to give a physical interpretation of the term on the right side of equation (5), analogous to the "vortex stretching" effect in the vorticity equation (Batchelor, 1970). The quantity $- A(t)\underset{\sim}{I}^i$ represents the negative of the product of two terms: 1) The magnitude of the impulse (i.e., $|\underset{\sim}{I}^i|$), and 2) The relative rate of change of an infinitesimal material line element

vector at $\underset{\sim}{R}^i$ (connecting two points along the direction of $\underset{\sim}{I}^i$) due to the irrotational straining field induced by the other eddies (i.e., $\underset{\sim}{u}_E(\underset{\sim}{R}^i(t), t)$).

We next consider the equation for the center of mass (2). We divide the velocity potential in the surface integral over the i^{th} eddy into two contributions, arising from the vorticity exterior and interior to the i^{th} eddy:

$$\varphi = \varphi_E + \varphi_I$$

where $\underset{\sim}{u}_E = \text{grad } \varphi_E$. We then obtain

$$\int_{\partial V_i} \varphi_E \hat{n} ds = \int_{V_i} \underset{\sim}{u}_E dV \cong \underset{\sim}{u}_E(\underset{\sim}{R}^i(t), t) V^i$$

where higher order (quadratic) terms arising from the Taylor series expansion of $\underset{\sim}{u}_E$ are omitted. Utilizing the asymptotic expansion for φ_I, we obtain

$$\int_{\partial V_i} \varphi_I \hat{n} ds \cong -\frac{1}{3} \underset{\sim}{I}^i$$

where higher order terms arising from the non-spherical nature of the i^{th} eddy surface are omitted. The result is

$$V_i \frac{d\underset{\sim}{R}^i}{dt} \cong \frac{2}{3} \underset{\sim}{I}^i + V_i \underset{\sim}{u}_E(\underset{\sim}{R}^i(t), t) \qquad (7)$$

where $\underset{\sim}{u}_E$ is given by (6).

For a collection of N eddies in an unbounded quiescent fluid, equations (5) and (7) represent a closed set of 6N equations for the vectoral quantities $\underset{\sim}{R}^i$, $\underset{\sim}{I}^i$, i = 1, N. There is in addition the global requirement that the total impulse be conserved. This condition can be easily shown to follow from equations (5), (6) and (7) for N = 1 or 2, and it is expected that it can be shown for arbitrary N.

It is trivial to verify that equations (5) and (7) reduce to the exact description of a single Hill spherical vortex in an unbounded flow, i.e.,

$$\frac{d\underset{\sim}{I}}{dt} = 0$$

$$V\frac{d\underset{\sim}{R}}{dt} = \frac{2}{3}\underset{\sim}{I}$$

The basic assumption inherent in the above approximations is that the collection of eddies is "dilute", i.e., that their average separation is much larger than their typical size.

III. Interaction of Two Eddies

For the purpose of providing a simple qualitative picture, the two-dimensional interaction of two eddies of equal volume was considered. The governing equations were solved numerically using a fourth-order Runge-Kutta scheme (Isaacson and Keller, 1966). The accuracy of the method was verified by computing the behavior with the impulse of one of the eddies set identically to zero. The motion of the "eddy" with zero impulse is equivalent to that of a fluid parcel in irrotational flow about a sphere, thus providing a check on the numerics.

Figure 1 shows the motion of a pair of eddies whose impulses at $t = 0$ were equal in magnitude and opposite in sign, directed along the x-axis (i.e., horixontal). The positions of the eddies are shown at equal time increments, beginning with $t = 0$. A notable feature is the development of a component of impulse in the vertical direction by each eddy, as evidenced by the inclined trajectories at large time. As the total impulse is conserved, the final vertical velocities are of equal magnitude and opposite sign.

An altogether different behavior is indicated in Figure 2, which shows the motion of two eddies whose initial impulses were

+1 and +3, directed along the +x-axis. Again, the effect of the straining field produced by one eddy on the other is evident in the development of a component of impulse in the vertical direction. By use of a Galilean transformation, the initial velocities of the eddies (though not the impulses) in Figure 2 can be made approximately equivalent to those of Figure 1, and the straining field experienced by, for example, eddy #1 is qualitatively similar in both figures. The observed difference between the two cases in direction of vertical motion of eddy #1 at large time can thus be seen to result from the difference in orientation of its impulse (see equation (5)).

IV. Extensions

The eddy model as described above is as yet incomplete. Some of the additional effects which require incorporation are indicated below.

a. Entrainment. The model, being inviscid, provides no means for entrainment of irrotational fluid by the large eddies. The turbulent entrainment process must be modeled, as it is the basic growth mechanism of a turbulent shear layer.

b. Generation. For turbulent boundary layers on smooth surfaces, the mechanism by which the vorticity generated at the surface is 'ejected' into the boundary layer is a complicated phenomena (see; for example, Kline et al, 1967). This generation cycle for the eddies requires additional modeling.

There are additional questions of interest, in particular,

the possibility of extending the approximate equations of motion by considering higher order terms, thereby introducing tensor descriptions of the vorticity distribution within each eddy.

V. Bibliography

Batchelor, G.K., 1970. An Introduction to Fluid Dynamics, Cambridge University Press.

Betz, A., 1933. "Behavior of Vortex Systems," NACA TM 713, National Advisory Committee for Aeronautics.

Isaacson, E. and Keller, H.B., 1966. Analysis of Numerical Methods, John Wiley & Sons.

Kline, S.J., Reynolds, W.C., Schraub, F.A., and Runstadler, P.W., 1967. "The Structure of Turbulent Boundary Layers," J. of Fluid Mechanics, 30, 4, 741-773.

Roshko, A., 1976. "Structure of Turbulent Shear Flows: A New Look", Dryden Lecture, AIAA 14th Aerospace Sciences Meeting, Washington, D.C.

Saffman, P.G., 1971. Lectures in Vortex Motion, California Institute of Technology, Pasadena, California.

Townsend, A., 1956. Structure of Turbulent Shear Flow, Cambridge Univ. Press.

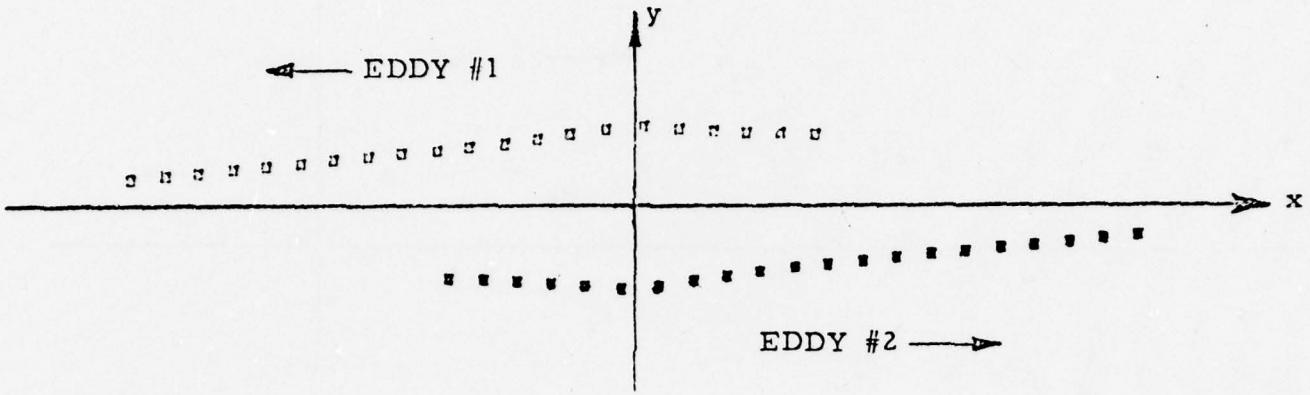

Initial impulse: $\underset{\sim}{I}^1 = (- 1, 0)$

$\underset{\sim}{I}^2 = (+ 1, 0)$

Figure 1: Motion of pair of eddies whose impulses are of opposite sign. Positions of each eddy are shown at equal time increments.

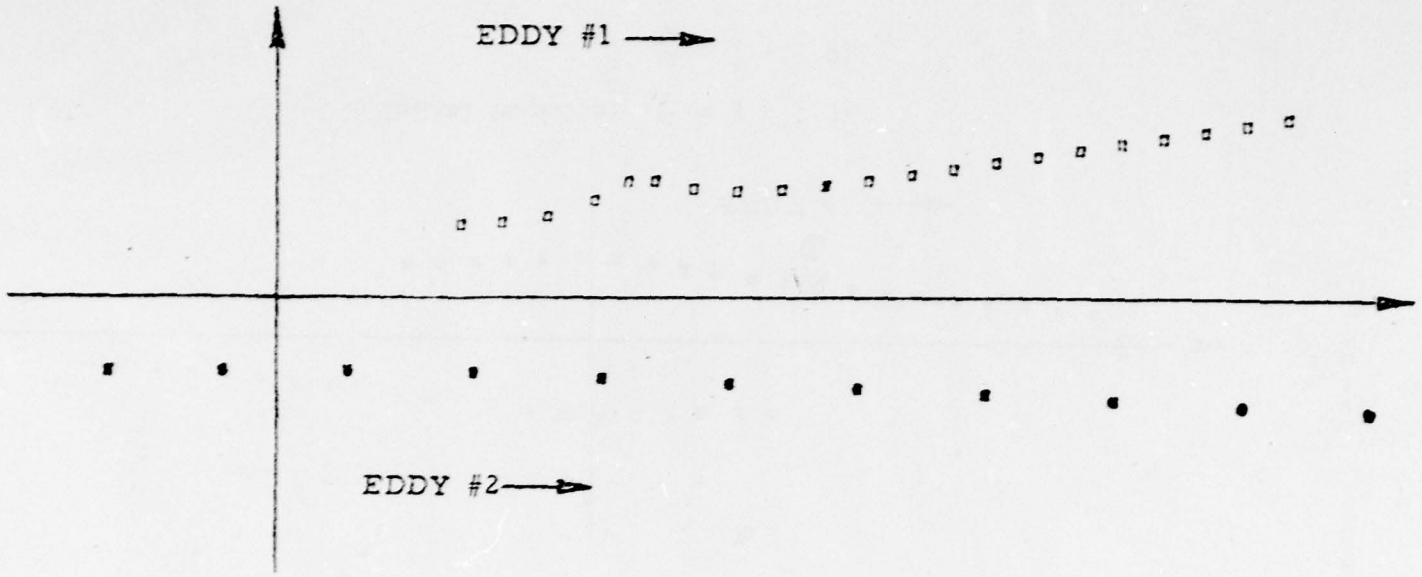

Initial Impulse: $\underset{\sim}{I}^1 = (1, 0)$

$\underset{\sim}{I}^2 = (3, 0)$

Figure 2: Motion of pair of eddies whose impulses are of same sign. Positions of each eddy are shown at equal time increments.

THE TURBULENT CHEMICAL REACTION OF A HYDROGEN JET DISCHARGED INTO FLUORINE

Frank E. Marble, J.E. Broadwell,
O.P. Norton, M.V. Subbaiah

ABSTRACT

The coherent flame model for turbulent chemical reactions describes the flame structure in terms of a distribution of laminar flame elements, each of which retains a flame-like behavior while it is being stretched in its own plane and transported by the turbulent field. In its simplest form, which is employed here, it should describe fast chemical reactions in the early stages of mixing with some accuracy.

In the present work this model is applied to the turbulent hydrogen-fluorine reaction with reference to the H-F laser. Because the non-equilibrium distribution of vibrational states of the HF molecule is central to the laser problem, flame strain rates ε must be considered such that $\varepsilon \tau_c >> 1$ where τ_c is the relevant chemical time. This requirement necessitates modification to the consumption rate of reactants that is utilized in the model. For these high strain rates, the flame is no longer diffusion controlled with a relatively small zone of chemical reaction. Rather, the chemistry occupies the entire diffusion zone. The model has been modified to accommodate this new description of reactant consumption and the mechanics of calculating the distribution of vibrationally existed states has been developed.

Because the description of the turbulent jet and the chemistry of the hydrogen-fluorine reaction are fixed, the only parameters

required to define the problem are the initial states of the hydrogen and fluorine streams and the value of $W_o \tau_c / d$ (sometimes referred to as a Damköhler number) where W_o is the initial velocity of the jet issuing from a port of diameter d, and τ_c is a characteristic chemical time of the reaction. Detailed distribution of the HF product species and the corresponding populations of vibrational states have been calculated for two values of $W_o \tau_c / d$. These results are given at distances of 2, 7 and 15 jet diameters downstream of the port. At similar locations within the jet, the larger value of $W_o \tau_c / d$ tends to accentuate the non-equilibrium population of vibrational states. The effect of distance along the jet is more complex. It is shown that the combined effects of flame surface density and strain rate produce a maximum in the vibrational population non-equilibirum that occurs several diameters downstream of the jet origin.

1. INTRODUCTION

The coherent flame front model[1] is a description of fast chemical reactions in turbulent flow in which the reactions are assumed confined to thin flame surfaces. The turbulent flame structure then consists of a distribution of these surface elements. The model describes the manner in which the flame elements are stretched and the distribution is dispersed by the turbulent motion, as well as the mechanism by which neighboring flame surfaces consume the intervening reactant and annihilate each other. A considerable advantage of the coherent flame model is that it effectively separates the detailed structure of the laminar flames from the fluid mechanics so that systems with complex chemical reactions may be treated nearly as easily as simple ones.

The work described here treats a turbulent combustion process associated with the hydrogen-fluorine CW laser. The geometry of the problem consists of a circular jet of hydrogen gas discharging into a stationary field of atomic fluorine. Both gases are diluted with helium. Although this configuration differs somewhat from that which occurs in practical lasers, it serves to illustrate the mechanics of applying the coherent flame model in a situation where the assumptions of the model are quite closely satisfied.

The central issue is the determination of the degree to which the vibrational degrees of freedom for the HF molecule differ, during the turbulent combustion process, from their normal equilibrium distribution as well as the distribution of these states over the jet flame. The complexity of the chemistry required to describe even a somewhat simplified model of the process demonstrates quite clearly the

advantages that accrue to the coherent flame description.

The present application of the flame sheet theory differs in one essential way from the previous developments, references 1, 2. In earlier applications we have employed the quasi-steady strained diffusion flame result that, for a diffusion-controlled flame, the reactant consumption rate per unit flame area is proportional to $\sqrt{D\varepsilon}$ where D is the coefficient of molecular diffusion and ε is the strain rate (sec^{-1}) in the plane of the flame surface. In this circumstance the actual region of chemical reaction is thin in comparison with the thickness of the diffusion zones. In other words, the characteristic chemical time τ_c is short in comparison with the value of ε^{-1}; hence $\varepsilon\tau_c << 1$. But it is almost evident that in order to disturb the normal distribution of HF vibrational states, the fluid dynamical time must be short compared with the relevant chemical time, so that $\varepsilon\tau_c >> 1$. When this circumstance prevails, the reactant consumption is no longer diffusion controlled and, indeed, the entire diffusion zone is chemically active. Then the reactant consumption rate is proportional to the thickness of the diffusion zone, $\sqrt{D/\varepsilon}$ divided by the chemical time, or $\frac{1}{\tau_c}\sqrt{D/\varepsilon}$. Thus a local reactant consumption law has been introduced that encompasses both the diffusion controlled and chemically controlled flame. The same law is appropriate to describing the distribution of vibrationally excited states.

2. THE FLAME STRUCTURE MODEL

To make this turbulent flame picture quantitative, define the flame surface density Σ to be the flame surface area per unit volume; the dimensions of the flame surface are very large in comparison with its thickness. The local flame surface density is altered by: 1) production resulting from fluid straining motions, 2) turbulent transport, and 3) flame annihilation, in which neighboring flame surfaces consume the intervening fuel or oxidizer.

The structure of the flame surface elements is dominated by the straining motion in the plane of the flame. Then if $\varepsilon \sim 1/\text{time}$ is the straining rate and $D \sim (\text{length})^2/\text{time}$ is the molecular diffusion coefficient, the flame thickness is $\sim\sqrt{D/\varepsilon}$ and consumes reactants at a rate $\sim\sqrt{D\varepsilon}$ per unit flame surface area.

Now when the straining rate is very high so that $\varepsilon \tau_c >> 1$ where τ_c is a characteristic chemical reaction time, the reactant consumption rate is proportional to the thickness of the diffusion zones of the flame, because it is within this layer that the reactants are molecularly mixed. Then the reactant consumption is $\sim \frac{1}{\tau_c}\sqrt{D/\varepsilon}$. The representation of the law which encompasses both diffusion controlled and chemically controlled reactant consumption is

$$\frac{\sqrt{D\varepsilon}}{1+\varepsilon\tau_c} \qquad (1)$$

When the flame surface density Σ and the strain rate ϵ are known locally, the reactant consumption rates within this region are known also because they are fixed by the flame structure. The actual flame structure may be determined to any degree of approximation between the simplest, where the chemical reaction rates are very rapid so that the reactant consumption is controlled by molecular diffusion, to the detailed structure involving the complete chemistry with appropriate rates. The flame structure with finite rates requires numerical calculation but, because it is a steady one-dimensional problem, the actual calculations may be accomplished with relative ease.

The appropriate form of the equation describing the flame surface density may be deduced from first principles by considering the distortion and migration of surface elements, fixed to the fluid, in a turbulent medium.[3] Here, it will be sufficient to motivate the form by physical reasoning and then to suggest the manner in which the various terms scale with features of the flowfield and the chemistry of the flame structure. Now in a fluid with mean velocity components U_i, the expression

$$\frac{D\Sigma}{Dt} \equiv \frac{\partial \Sigma}{\partial t} + U_j \frac{\partial \Sigma}{\partial x_j} \tag{2}$$

gives the change in flame density following a mean fluid element. According to our model described earlier, this change may be written in the following form

$$\frac{D\Sigma}{Dt} = \text{turbulent diffusion of flame elements into the region}$$

$$+ \text{ increase in flame surface element area by turbulent straining motions}$$

- reduction in flame surface resulting from local consumption of the reactants.

In these calculations, the turbulent diffusion of flame surface will be described using a turbulent diffusivity and the assumption that the turbulent fluctuation velocities are large in comparison with diffusion velocities, familiar from usual treatments of turbulent heat and mass transport. Thus, if we denote $\mathcal{D}$ the diffusion coefficient that arises in the description of momentum exchange, the turbulent diffusion term applicable to the treatment of the turbulent circular jet is

$$\frac{1}{r}\frac{\partial}{\partial r}\left(r\mathcal{D}\frac{\partial \Sigma}{\partial r}\right)$$

where the appropriate boundary layer approximation has been made. The rate of increase of an element of flame surface area is proportional to the strain rate in the turbulent fluctuations. Under the assumption that this strain rate is proportional to the rate of strain in the mean motions, the rate of increase in flame surface density is thus proportional to the product of the strain rate of mean motion and the local flame density. Thus we take the second term on the right equal to

$$\varepsilon\Sigma = \alpha\left|\frac{\partial W}{\partial r}\right|\Sigma$$

where, again, we have written the term in the form appropriate to the circular jet, W being the velocity component of the mean motion in the direction of the symmetry axis.

The process by which flame surface is removed from the field is best pictured by considering two neighboring laminar diffusion flame fronts parallel to each other and containing one constituent, say, fuel, between them. As the motion progresses, the intervening fuel is consumed and both elements of flame surface are extinguished.

A similar process takes place if the intervening constituent is the oxidizer. To make the mechanism quantitative, we note that fraction of local volume occupied by fuel is proportional to the concentration K_1 of fuel. Moreover, the rates of reactant consumption by an element of laminar flame are presumed known from detailed calculations of that flame structure. If we call V_1 the volume rate of consumption of fuel per unit flame area, the rate at which volume occupied by fuel is being consumed is $V_1 \Sigma$ so that the fractional rate of fuel consumption in a unit volume of space is $V_1 \Sigma / K_1$. Thus, if the flame surface area is nearly uniformly distributed over the region, this expression gives also the fraction of flame surface that is annihilated so that the flame surface area reduction due to fuel consumption is

$$\left(\frac{V_1 \Sigma}{K_1} \right) \Sigma = \frac{V_1}{K_1} \Sigma^2$$

In a completely similar manner, we may reason that the flame surface area reduction due to consumption of oxidizer is proportional to

$$\frac{V_2}{K_2} \Sigma^2$$

and because in a given region, the surface is being reduced by either the exhaustion of fuel or oxidizer, but not both, the two expressions will be considered additive.

If now we collect the various terms that have been discussed, it is possible to write in detail the conservation equation for flame surface density

$$U \frac{\partial \Sigma}{\partial r} + W \frac{\partial \Sigma}{\partial z} = \pm \frac{\partial}{\partial r} \left(r B \frac{\partial \Sigma}{\partial r} \right) + \alpha \left| \frac{\partial W}{\partial r} \right| \Sigma - \lambda \frac{V_1}{K_1} \Sigma^2 - \lambda \frac{V_2}{K_2} \Sigma^2 \qquad (3)$$

The form of equation has been chosen to be that appropriate for the analysis of the circular jet.

The conservation equations for the individual reactants are conventional except for the terms describing the reactant consumption by chemical reaction. These will be given in terms of the flame surface density and the reactant consumption for a unit flame surface supplied by one-dimensional flame calculations. For the fast overall chemical reaction, we need consider only three constituents, the fuel K_1, the oxidizer K_2, and the product K_3, related by the fact that the sum of mass fractions is unity

$$K_1 + K_2 + K_3 = 1 \tag{4}$$

so that only two of these K_1 and K_2, need be calculated. The detailed chemistry, in contrast to the overall reaction between fuel and oxidizer, is contained within the one-dimensional flame structure.

The consumption rate of fuel per unit volume is simply the product of the effective influx velocity V_1, the flame surface density Σ_1, and the mass fraction K_1^* of fuel in the fuel-containing component in the unmixed state. The conservation equation for fuel may be written down directly as

$$U\frac{\partial K_1}{\partial r} + W\frac{\partial K_1}{\partial z} = \frac{1}{r}\frac{\partial}{\partial r}\left(r\mathcal{D}\frac{\partial K_1}{\partial r}\right) - K_1^* V_1 \Sigma_1 \tag{5}$$

Similarly, the conservation equation for the oxidizer component is

$$U\frac{\partial K_2}{\partial r} + W\frac{\partial K_2}{\partial z} = \frac{1}{r}\frac{\partial}{\partial r}\left(r\mathcal{D}\frac{\partial K_2}{\partial r}\right) - K_2^* V_2 \Sigma_1 \tag{6}$$

It remains to define the consumption rates V_1 and V_2 for the fuel and oxidizer components. Regardless of whether these quantities are defined through use of infinitely fast reaction rates or by detailed calculation of the one-dimensional flame structure, they depend upon the reactant concentrations on each side of the flame, κ_1^* and κ_2^*, and the local strain rate $\mathcal{E}$ of the mean flow. It is this latter item which couples the local diffusion flame structure to the gasdynamic structure.

3. THE TURBULENT CIRCULAR FUEL JET

The detailed solution for a turbulent flame structure described in the manner outlined in the previous section requires a turbulence model for the mean flow and, because there is a choice of turbulence model to be used, it is preferable to go directly to the problem of interest rather than describe the procedure in general. For the problem of the circular fuel jet, we shall choose the elementary model utilizing a scalar turbulent diffusivity. Furthermore, we shall, in the interests of simplicity, neglect the change of mean gas density associated with the chemical reactions. This restriction in no way implies that the density change is a negligible factor. Rather the use of a turbulence model for flows of non-uniform density introduces a degree of uncertainty of its own which makes it additionally difficult to judge the merits of the flame model.

Under these restrictions, the gasdynamic field is described by the equations

$$\frac{1}{r}\frac{\partial}{\partial r}(rU) + \frac{\partial W}{\partial z} = 0 \tag{7}$$

$$U\frac{\partial W}{\partial r} + W\frac{\partial W}{\partial z} = \frac{1}{r}\frac{\partial}{\partial r}\left(r\frac{\tau_{rz}}{\rho}\right) \tag{8}$$

where the pressure of the far field has been assumed constant. Using the eddy-diffusivity model for the turbulent shear stress τ_{rz}, we write

$$\frac{\tau_{rz}}{\rho} = \mathfrak{D}\frac{\partial W}{\partial r} \tag{9}$$

where $\mathfrak{D}$ is the turbulent analogue to the kinematic viscosity. The customary difficulty arises here in the choice, rather than the deter-

mination, of the eddy diffusivity. For the circular jet, however, the choice is made simpler by the fact that the jet momentum, which is conserved along the direction of flow, has the dimension of (velocity)^2 x (length)^2. And because $\mathcal{D}$ has the dimension of (length) x (velocity), there being no other characteristic dimensions in the problem, it is evident that the turbulent diffusivity is proportional to the square root of the jet momentum, and hence is a constant.

It is possible to find a similarity solution for the turbulent jet, or more properly for a point momentum source. To carry this out, it proves convenient to introduce a modified radial dimension

$$\eta = \sqrt{\frac{3}{8}} \left(\frac{\sqrt{\mu}}{\mathcal{D}} \right) \frac{r}{z} \tag{10}$$

where μ is the constant jet momentum flux

$$\mu = \int_0^\infty W^2 r dr \tag{11}$$

The stream function ψ, with the usual properties that $U = -\frac{1}{r}\frac{\partial \psi}{\partial z}$, $W = \frac{1}{r}\frac{\partial \psi}{\partial r}$, may then be written in the form

$$\psi = \mathcal{D} z F(\eta) \tag{12}$$

Substitution into the momentum equation, Equation 8, yields the ordinary differential equation for $F(\eta)$

$$-\left\{ \frac{1}{\eta} FF'' + \frac{1}{\eta} F'F' - \frac{1}{\eta^2} FF' \right\} = \frac{d}{d\eta} \left(F'' - \frac{1}{\eta} F' \right)$$

which may be integrated once to give

$$-\frac{1}{\eta} FF' = F'' - \frac{1}{\eta} F' \tag{13}$$

the constant of integration being zero because $\frac{1}{\eta}F'$ and F'' vanish for large η. Fortunately, the solution for Equation 13 may be written simply as

$$F(\eta) = \frac{\eta^2}{1+\frac{1}{4}\eta^2} \tag{14}$$

which satisfies the requirement that the stream function vanish on the symmetry axis, $\eta = 0$, and satisfies identically the momentum conservation relation, Equation 11, as

$$\frac{3}{8}\int_0^\infty \left(\frac{F'}{\eta}\right)^2 \eta\, d\eta = 1 \tag{15}$$

The velocity components of the mean flowfield are then

$$W = \frac{3}{8}\frac{\mu}{\rho}\frac{1}{x}\left(\frac{F'}{\eta}\right)$$

$$= \frac{3}{8}\frac{\mu}{\rho}\frac{1}{x}\frac{1}{(1+\frac{1}{4}\eta^2)^2} \tag{16}$$

and

$$U = -\sqrt{\frac{3}{8}\mu}\,\frac{1}{x}\left(\frac{F}{\eta} - F'\right)$$

$$= \sqrt{\frac{3}{8}\mu}\,\frac{1}{x}\,\frac{\eta\left(1-\frac{1}{4}\eta^2\right)^2}{\left(1+\frac{1}{4}\eta^2\right)^2} \tag{17}$$

Now explicit solution of the flame density and reactant conservation relations require a quantitative form for the reactant consumption rates. If the chemistry were actually of infinitely fast rate and if the mutual reactants were uncontaminated by products of combustion, the values of V_1 and V_2 appearing in Equations 5 and 6 could be written

$$K_1'' V_1 = \beta_1 \sqrt{D\varepsilon} \quad ; \quad K_2'' V_2 = \beta_2 \sqrt{D\varepsilon} \tag{18}$$

where D is the coefficient of molecular diffusion, $\varepsilon \propto \left|\frac{\partial W}{\partial r}\right|$ is proportional to the turbulent strain rate, and β_1, β_2 are constants for a given chemical system, depending upon the reaction stoichiometry and the amount of diluent accompanying the reacting species in the unmixed

gas streams. Numerical calculations of strained laminar diffusion flames, which will be described subsequently, showed that strain rates between $10^3 sec^{-1}$ and $10^7 sec^{-1}$ were required to achieve a large alteration in the distribution of vibrational states of H-F. These high strain rates were accompanied by a distinct change in the laminar flame structure.

When the strain rate was less than $10^5 sec^{-1}$ the reactant consumption rate behaved as if the chemistry were infinitely fast. In this range the reactant consumption rate is $\sim\sqrt{D\varepsilon}$ where D is the appropriate binary diffusion coefficient. When the strain rate was greater than $10^5 sec^{-1}$, the reactant consumption varied as $\varepsilon^{-1/2}$, the results showing that the reactant consumption rate was chemically limited and that the chemically active zone filled the entire flame thickness. It was clear then that the proper expression for the reactant consumption rate at large strain rates is

$$\frac{1}{\tau_c}\sqrt{D/\varepsilon} \tag{19}$$

where $\sqrt{D/\varepsilon}$ is proportional to the flame thickness and τ_c is a chemical time.

For the entire range of strain rates the reactant consumption per unit flame area is

$$\kappa_i'' V_i = \beta_i \frac{\sqrt{D\varepsilon}}{1 + \tau_c \varepsilon} \tag{20}$$

where $\beta_i = \beta_1, \beta_2$ depending upon whether we are considering the consumption of hydrogen or fluorine atoms. This gives a rate $\beta_i\sqrt{D\varepsilon}$ for strain rates $\varepsilon\tau_c << 1$ and $(\beta_i/\tau_c)\sqrt{D/\varepsilon}$ for larger strain rates $\varepsilon\tau_c >> 1$. The equations for reactant consumption and flame density may then be written

$$U\frac{\partial K_1}{\partial r} + W\frac{\partial K_1}{\partial z} = \frac{1}{r}\frac{\partial}{\partial r}\left(r\mathcal{D}\frac{\partial K_1}{\partial r}\right) - \beta_1\frac{\sqrt{D\mathcal{E}}}{1+\mathcal{J}_c\mathcal{E}}\mathcal{E} \tag{21}$$

$$U\frac{\partial K_2}{\partial r} + W\frac{\partial K_2}{\partial z} = \frac{1}{r}\frac{\partial}{\partial r}\left(r\mathcal{D}\frac{\partial K_2}{\partial r}\right) - \beta_2\frac{\sqrt{D\mathcal{E}}}{1+\mathcal{J}_c\mathcal{E}}\mathcal{E} \tag{22}$$

$$U\frac{\partial \mathcal{E}}{\partial r} + W\frac{\partial \mathcal{E}}{\partial z} = \frac{1}{r}\frac{\partial}{\partial r}\left(r\mathcal{D}\frac{\partial \mathcal{E}}{\partial r}\right) - \lambda\beta_1\frac{\sqrt{D\mathcal{E}}}{1+\mathcal{J}_c\mathcal{E}}\frac{\mathcal{E}^2}{K_1 K_2} \tag{23}$$

$$K_1 + K_2 + K_3 = 1 \tag{24}$$

When the chemistry is fast, as it is in this case, it is convenient to use a linear combination of K_1 and K_3 that satisfies a homogeneous diffusion equation. Such a combination is $K_1 + \frac{1}{1+\beta_2/\beta_1}K_3 \equiv J$ and because a diffusion flame with fast chemistry utilizes fuel and oxidizer in the stoichiometric ratio φ, the quantity $\beta_2/\beta_1 = \varphi$ and

$$J = K_1 + \frac{1}{1+\varphi}K_3 \tag{25}$$

Thus J(r, z) satisfies

$$U\frac{\partial J}{\partial r} + W\frac{\partial J}{\partial z} = \frac{1}{r}\frac{\partial}{\partial r}\left(r\mathcal{D}J\right) \tag{26}$$

with the conditions $J(\infty, z) = 0$ and hence, comparing Equations 26, 8, and 9, it is clear that $J(r,z) \sim W(r,z)$. The constant of proportionality between J and W is found by noting that if the actual flow of fuel injected into the stream is γ, then the flow of the product formed is $(1+\varphi)\gamma$ for large values of z where the reaction is complete and $K_1 = 0$. Then the integrated flux of the product is, as $z \to \infty$

$$\int_0^\infty K_3 W r\,dr = \gamma(1+\varphi) \tag{27}$$

and because integration of Equation 26 shows that $\int_0^\infty JWr\,dr$ is conserved along the z direction, it follows that

$$\int_0^\infty J W r dr = \gamma \tag{28}$$

Because J is proportional to W, the integral is the same as evaluated to ensure conservation of momentum with z and hence it follows, comparing Equations 11 and 28, that

$$J = \frac{\gamma}{\mu} W = \frac{3}{\theta} \frac{\gamma}{\rho} \frac{1}{z} \left(\frac{F'}{\eta}\right) \tag{29}$$

We have then the algebraic relation

$$K_1 + \frac{1}{1+\varphi} K_3 = \frac{3}{\theta} \frac{\gamma}{\rho} \frac{1}{z} \left(\frac{F'}{\eta}\right) \tag{30}$$

in addition to the relation Equation 24 and, as a consequence, we need only work with a single species conservation Equation 21.

In order to make this identification between J(r, z) and W(r, z), it has been necessary to introduce the volume flow rate γ as well as the momentum μ of the jet. These two quantities may be used to characterize the jet velocity

$$\text{velocity} \sim \mu/\gamma \tag{31}$$

and the characteristic dimension of the jet,

$$\text{length} \sim \gamma/\sqrt{\mu} \tag{32}$$

where, in fact, the length $\frac{\gamma}{\sqrt{\mu}} = \sqrt{\pi} R$, where R is the initial radius of a jet with uniform velocity.

4. THE STRAINED LAMINAR HYDROGEN-FLUORINE FLAME

To complete the detailed description of the model, we require the numerical solution for the strained hydrogen-fluorine flame which determine the flame structure, including the distribution of vibrationally excited states, and the reactant consumption rates. Results of this type can be obtained analytically when the chemistry is simple but in the present case in which the vibrational populations result from a complex interaction of chemical kinetics and molecular diffusion, a numerical calculation is necessary. These were made with the Blottner boundary layer computer program modified so as to apply to the laminar diffusion flame[4]. The boundary layer equations and the numerical scheme employed in their solution are described in references 5 and 6. The program modifications together with a comparison of results with experimentally determined HF vibrational population profiles are given in reference 7. The following brief description of the computer program is taken from the latter reference.

The physical situation is sketched in Figure 1. Two-dimensional streams of hydrogen and fluorine (diluted with helium) flowing from opposite sides of a splitter plate interdiffuse and react to form the laminar flame sheet, in which the various vibrational levels of hydrogen fluoride, HF(v), are produced. When the free stream reactant concentration are uniform and the stream velocities are constant and equal to W_∞ , the flame is equivalent to the "standard" time dependent diffusion flame (with z/W_∞ replaced by t); the strained flame is generated when W_∞ is caused to increase linearly with z.

If the chemistry is simple and the reaction rate fast, it is

straight-forward to prove[8] that the structure and reactant consumption rates of a flame experiencing a strain rate ϵ are identical to those of an unstrained time dependent flame at the time $t = 1/2\epsilon$. A few comparisons of our numerical results for H_2-F flames in the two cases indicated that the two solutions are similar when the same transformation of independent variable is made. Consequently, the shorter time dependent computation was used to obtain the results described in the following.

The Blottner program, which solves the standard boundary layer conservation equations, was designed especially to treat many chemical species and chemical reactions and to allow multi-component diffusion. In the present case, the kinetic system consisted of the "pumping" reactions:

$$H_2 + F \longrightarrow HF(v) + H \quad ; \quad v = 1, 2, 3 \tag{33}$$

together with equations describing the important deactivational effects of H, H_2 F as well as HF itself. The set of reaction equations together with the associated rate coefficients are given subsequently.

The temperature dependence of the species viscosities are program inputs. The other transport processes were treated with the simplifying assumption that the Prandtl and Lewis numbers were constant at unity.

Both reactant streams were at 300°K and 5 torr. The fuel stream composition was: hydrogen, $2.67 \cdot 10^{-8}$ g mole/cm^3, helium $2.47 \cdot 10^{-7}$ g mole/cm^3. The composition of the oxidizer was atomic fluorine, $2.67 \cdot 10^{-8}$ g mole/cm^3, helium $2.47 \cdot 10^{-7}$ g mole/cm^3.

The program outputs consist of various property profiles of temperature and concentration for instance, and of H_2 and F consumption

rates. The dependence of the latter on strain rate, ε , is shown in Figure 2. As the arguments presented in earlier sections lead us to expect, the consumption rates at large values of the strain vary like $\varepsilon^{-1/2}$ and at low values like $\varepsilon^{1/2}$. Equation 20, given previously,

$$K_i^* V_i = \beta_i \frac{\sqrt{D\varepsilon}}{1 + \tau_c \varepsilon} \tag{20}$$

is a fit to the curve in Figure 2. The numerical constants required for our work are

$$\beta_i = 4.60$$

$$\tau_c = 5.95 \times 10^{-6} \text{ sec} \tag{34}$$

The vibrationally excited and ground state populations within the flame structure depend, as do the reactant consumption rates, upon the rate of strain. These populations, in the form of integrated mass (g moles) per unit flame area are shown in Figure 3. We note the large departures from equilibrium at the high strain rates, indeed total inversions exist for $\varepsilon > 10^5 \text{ sec}^{-1}$. Empirical approximation to the results in Figure 3 that are convenient for the turbulent jet analysis are given in Section 6.

The "complete" chemical reaction system for the H_2 - F_2 reaction as presented in reference 8 consists of some 100 chemical reactions. For given ranges of temperature and concentration, many of these reactions have negligible influence on the HF vibrational populations and need not be considered. For purposes of the present investigation it was decided that the important excited state pumping and deactivational processes were contained in the eighteen equations given in Table 1. Also shown are the coefficients in the expression for the forward and backward reaction rate coefficients which are of

the form:

$$k_f = C_0 T^{C_2} \exp(-1000\, C_1/T)$$

$$k_b = D_0 T^{D_2} \exp(-1000\, D_1/T)$$

The symbol M represents the HF molecule in any state.

	C_o	C_1	C_2	D_o	D_1	D_2
$F + H_2 \rightarrow HF^1 + H$	2.70×10^{13}	0.8051	0.0	9.78×10^{12}	10.97	0.152
$F + H_2 \rightarrow HF^2 + H$	8.85×10^{13}	0.8051	0.0	3.22×10^{13}	5.535	0.152
$F + H_2 \rightarrow HF^3 + H$	4.30×10^{13}	0.8051	0.0	1.55×10^{13}	0.3044	0.152
$HF^3 + M \rightarrow HF^2 + M$	3.00×10^{14}	0.0	-0.800	3.00×10^{14}	5.211	-0.800
$HF^2 + M \rightarrow HF^1 + M$	2.00×10^{14}	0.0	-0.800	2.00×10^{14}	5.452	-0.800
$HF^1 + M \rightarrow HF^0 + M$	1.00×10^{14}	0.0	-0.800	1.00×10^{14}	5.700	-0.800
$HF^1 + H \rightarrow HF^0 + H$	9.10×10^{13}	0.5898	-0.275	9.10×10^{13}	6.290	-0.275
$HF^2 + H \rightarrow HF^1 + H$	4.36×10^{12}	0.3633	0.201	4.36×10^{12}	5.816	0.201
$HF^2 + H \rightarrow HF^0 + H$	4.26×10^{13}	0.4509	-0.084	4.26×10^{13}	11.60	-0.084
$HF^3 + H \rightarrow HF^2 + H$	3.71×10^{13}	0.4474	-0.090	3.71×10^{13}	5.695	-0.090
$HF^3 + H \rightarrow HF^1 + H$	2.82×10^{13}	0.3397	-0.078	2.82×10^{13}	11.00	-0.078
$HF^3 + H \rightarrow HF^0 + H$	3.88×10^{13}	0.3829	-0.063	3.88×10^{13}	16.75	-0.063
$HF^3 + H_2 \rightarrow HF^2 + H_2$	2.90×10^{8}	0.7714	1.500	1.45×10^{7}	0.000	1.500
$HF^2 + H_2 \rightarrow HF^1 + H_2$	2.00×10^{8}	0.5304	1.500	1.00×10^{7}	0.000	1.500
$HF^1 + H_2 \rightarrow HF^0 + H_2$	1.50×10^{8}	0.2828	1.500	7.50×10^{6}	0.000	1.500
$HF^3 + F \rightarrow HF^2 + F$	1.50×10^{10}	0.5535	1.000	1.50×10^{10}	5.765	1.000
$HF^2 + F \rightarrow HF^1 + F$	1.50×10^{10}	0.5535	1.000	1.50×10^{10}	6.006	1.000
$HF^1 + F \rightarrow HF^0 + F$	1.50×10^{10}	0.5535	1.000	1.50×10^{10}	6.253	1.000

M Includes HF^0, HF^1, HF^2, and HF^3

Table 1.

5. INTEGRAL FORMULATION OF HYDROGEN JET IN FLUORINE

To treat the jet of hydrogen issuing into a stationary background of fluorine atoms, consider equations 21, 23 and 30. If there were no reactions and if the flame straining were negligible ($\alpha = 0$), then the problem would possess similarity solutions of the form $\kappa_1 \sim \frac{1}{z} k_1(\eta)$ and $\mathcal{E} \sim \frac{1}{z} \sigma(\eta)$. There is a certain advantage in writing these quantities in that form, as

$$\kappa_1 = \frac{3}{\theta} \frac{r}{D} \frac{1}{z} k_1(\eta, z) \tag{35}$$

and

$$\mathcal{E} = \frac{3}{\theta} \left(\frac{\sqrt{\mu}}{\alpha D}\right)^{1/2} \frac{1}{\beta_1 z} \sigma(\eta, z) \tag{36}$$

Now because we shall use an integral technique to obtain our final result, it is convenient to rewrite Equations 21 and 23 in similarity variables and integrate them over the flame cross section. Introducing the similarity coordinates, η and z, we have

$$\frac{\sqrt{\frac{3}{\theta}\mu}}{\theta} \frac{1}{z} \frac{\partial}{\partial \eta}(rU\kappa_1) + \frac{\partial}{\partial z}(rW\kappa_1) - \frac{1}{z}\frac{\partial}{\partial \eta}(r\eta W\kappa_1) + \frac{1}{z}(rW\kappa_1)$$
$$= \frac{\sqrt{\frac{3}{\theta}\mu}}{\theta} \frac{1}{z} \frac{\partial}{\partial \eta}\left(r\theta \frac{\partial \kappa_1}{\partial \eta}\right) - \beta_1 \frac{\sqrt{\alpha D \left|\frac{\partial W}{\partial r}\right|}}{1 + \alpha \tau_c \left|\frac{\partial W}{\partial r}\right|} r\mathcal{E} \tag{37}$$

and

$$\frac{\sqrt{\frac{3}{\theta}\mu}}{\theta} \frac{1}{z} \frac{\partial}{\partial \eta}(rU\mathcal{E}_1) + \frac{\partial}{\partial z}(rW\mathcal{E}_1) - \frac{1}{z}\frac{\partial}{\partial \eta}(r\eta W\mathcal{E}_1) + \frac{1}{z}(rW\mathcal{E}_1)$$
$$= \frac{\sqrt{\frac{3}{\theta}\mu}}{\theta} \frac{1}{z} \frac{\partial}{\partial \eta}\left(r\theta \frac{\partial \mathcal{E}_1}{\partial r}\right) + \alpha\left|\frac{\partial W}{\partial r}\right| - \lambda\beta_1 \frac{\sqrt{\alpha D \left|\frac{\partial W}{\partial r}\right|}}{1 + \alpha \tau_c \left|\frac{\partial W}{\partial r}\right|} \left(\frac{r\mathcal{E}_1^2}{\kappa_1 \kappa_2}\right) \tag{38}$$

Integrate these from $\eta = 0$ to $\eta = \infty$ and take account of the behavior of κ_1 and $\mathcal{E}$ for large radii. We then have from Equation 37

$$\frac{d}{dz}\int_0^\infty \left(\frac{F'}{\eta}\right) k_1(\eta, z)\, \eta\, d\eta = \left(\frac{3}{\theta}\right)^{3/4} \int_0^\infty \frac{\sqrt{\frac{d}{d\eta}\left(-\frac{F'}{\eta}\right)}}{1 + \frac{\tau_c}{\beta_1}\frac{d}{d\eta}\left(-\frac{F'}{\eta}\right)} \sigma(\eta, z)\, \eta\, d\eta \tag{39}$$

where we have used a new variable for distance along the axis,

$$\xi = \frac{\theta}{3}\frac{\mathcal{D}}{\gamma} z \tag{40}$$

and introduced a Damköhler number

$$\mathcal{J} = \sqrt{\frac{\theta}{3}}\,\alpha\,\frac{(\mu)^{3/2}}{\gamma^2}\,\mathcal{J}_c \tag{41}$$

Treating the flame density relation in the same manner

$$\frac{d}{d\xi}\int_0^\infty \left(\frac{F'}{\eta}\right)\sigma(\eta,\xi)\,d\eta = \left(\frac{3}{8}\right)^{1/2}\frac{\alpha\sqrt{\mu}}{\mathcal{D}}\,\frac{1}{\xi}\int_0^\infty \frac{d}{d\eta}\left(-\frac{F'}{\eta}\right)\sigma(\eta,\xi)\,\eta\,d\eta$$

$$-\lambda\left(\frac{3}{8}\right)^{3/4}\int_0^\infty \frac{\sqrt{\frac{d}{d\eta}\left(-\frac{F'}{\eta}\right)}}{1+\frac{\gamma}{\xi^2}\frac{d}{d\eta}\left(-\frac{F'}{\eta}\right)}\;\frac{\sigma^2(\eta,\xi)}{k_1 K_2}\,\eta\,d\eta \tag{42}$$

where in this notation

$$K_2 = 1 - \frac{1}{\xi}\left((1+\varphi)\frac{F'}{\eta} - \varphi k_1\right) \tag{43}$$

To complete the solution using the integral technique, it is required to select profile shapes for the mass fraction distribution and for the flame surface density. These are chosen specifically in the following form:

$$k_1(\eta,\xi) = \left(\frac{F'}{\eta}\right)\left(1 - f(\xi)\right) \tag{44}$$

$$K_2(\eta,\xi) = 1 - \left(\frac{F'}{\eta}\right)\frac{1}{\xi}\left(1+\varphi f(\xi)\right) \tag{45}$$

$$\sigma(\eta,\xi) = \left(\frac{F'}{\eta}\right) h(\xi)\left(1-f(\xi)\right)\left[1-\left(\frac{F'}{\eta}\right)\frac{1}{\xi}\left(1+\varphi f(\xi)\right)\right] \tag{46}$$

where $f(\xi)$ and $h(\xi)$, unknown functions of distance along the axis, will be determined through the integral relations, Equations 39 and 42. This choice posesses several features in its favor:

a) They are exact when there is no chemical reaction.

b) They satisfy exactly the conditions given by Equation 30 among species mass fractions.

c) They satisfy the appropriate boundary conditions at the symmetry axis and at distances remote from the axis.

d) The flame surface density vanishes, as it must physically, where either the fuel or oxidizer reactants vanish.

Now the value of $F(\eta) = \eta^2/(1+\frac{1}{4}\eta^2)$, Equation 14, is the exact solution for the stream function in the jet problem utilizing the turbulent diffusivity formulation. Utilizing this and the representations for $k_1(\eta,\xi)$, $K_2(\eta,\xi)$, $S(\eta,\xi)$ given in Equations 44, 45, and 46, the integrations indicated in the integral relations, Equations 39 and 42, may be carried out. The integrals are of three classes: (i) those which may be evaluated directly, (ii) those which may be reduced to an integral of $(1+\frac{1}{4}\eta^2)^{-n}$ and have the value

$$\int_0^\infty \frac{d\eta}{(1+\frac{1}{4}\eta^2)^n} = \pi \prod_{j=1}^{n-1} \left(\frac{2(n-j)-1}{2(n-j)} \right) \tag{47}$$

and (iii) those of the form

$$I_n = \int_0^\infty \left(\frac{F'}{\eta}\right)^n \frac{\sqrt{\frac{d}{d\eta}\left(-\frac{F'}{\eta}\right)}}{1+\frac{\gamma}{\xi^2}\frac{d}{d\eta}\left(-\frac{F'}{\eta}\right)}\, d\eta \tag{48}$$

This last class may, after a transformation, be written in the form

$$I_n(\xi;\gamma) = \int_0^1 \frac{x^{2n+3/4}(1-x)^{1/4}}{1+\frac{4\gamma}{\xi^2}x^{3/2}(1-x)^{1/2}}\, dx \tag{49}$$

which is suitable for numerical integration.

Now if we utilize these results in the integral relations,

Equations 39 and 42 , for the hydrogen concentration and the flame density respectively, then these become respectively

$$\frac{d}{d\xi}(1-f) = -\left(\frac{3}{\beta}\right)^{7/4} h(\xi)(1-f)\left\{ I_0(\xi;\tau) - \frac{1+\varphi f}{\xi} I_1(\xi,\tau) \right\} \quad (50)$$

and

$$\frac{d}{d\xi}\left\{ h(\xi)(1-f)\left[1 - \frac{b}{5}\left(\frac{1+\varphi f}{\xi}\right)\right]\right\}$$

$$= \frac{\alpha\sqrt{\mu}}{\beta}\left(\frac{3}{\beta}\right)^{3/2}(1.96350)\left(\frac{1}{\xi}\right)h(\xi)(1-f)\left[1 - \frac{21}{20}\left(\frac{1+\varphi f}{\xi}\right)\right]$$

$$- \lambda\left(\frac{3}{\beta}\right)^{7/4} h^2(\xi)(1-f)\left\{ I_0(\xi;\tau) - \left(\frac{1+\varphi f}{\xi}\right) I_1(\xi;\tau)\right\}$$

(51)

These are to be integrated from $\xi \cong 2$, the virtual origin of the jet being at $\xi = 0$, to an arbitrary value of ξ ; the initial values of $f(\xi_0) = 0$ and $h(\xi_0) = h_0$, where h_0 gives a measure of the amount of flame surface that is present at the start of calculation. Physically, the initial value of $h(\xi_0)$ is related to an ignition process which the turbulent flame model does not, of course, describe. It is to be expected that varying the initial value h_0 will have a significant effect upon the structure of the flame $\xi \cong \xi_0$ but a much smaller effect away from the origin. The values of φ and $\frac{\sqrt{\mu}}{\beta}$ are fixed by the reactants and by the turbulence model, respectively. The values of α and λ , on the other hand, are numerical constants which are universal in the sense that they do not depend upon stoichiometry, momentum flux, or geometrical size of the hydrogen jet.

6. DISTRIBUTION OF REACTION PRODUCTS

The results that are desired from our calculations are the distribution of the product HF molecule within the jet and the distribution of this product over the vibrational states that are important in the laser operation.

First, the distribution of HF mass fraction follows from the hydrogen mass fraction, which we have just determined

$$K_1(\eta,\xi) = \frac{1}{\xi}\left(\frac{F'}{\eta}\right)(1-f) \tag{52}$$

and the general integral, Equation 30. From there we find immediately

$$\frac{1}{\xi}(1-f)\left(\frac{F'}{\eta}\right) + \frac{1}{1+\varphi}K_3 = \frac{1}{\xi}\left(\frac{F'}{\eta}\right)$$

from which we deduce

$$K_3 = (1+\varphi)\left(\frac{f}{\xi}\right)\left(\frac{F'}{\eta}\right)$$

$$= 2(1+\varphi)\frac{1}{(1+\frac{1}{4}\eta^2)^2}\left(\frac{f}{\xi}\right) \tag{53}$$

This result may be utilized directly to compute distribution of the HF product within the jet.

The vibrationally excited states of HF are somewhat more difficult to calculate because they exist only within the active flame structure and the populations of the individual states depends upon the strain rate. Referring to figure 3, the integrated mass of HF in the ground state and in each of the first three excited states are shown as functions of strain rate. These are reasonably well represented in the form

$$S^{(i)} = S_\infty^{(i)} e^{-\delta^{(i)}\left(\varepsilon \eta_\infty^{(i)} - 1\right)^2} \tag{54}$$

where $S^{(i)}$ is mass of $HF_v^{(i)}$ per unit area of flame surface, $S_*^{(i)}$ is the maximum value of this quantity. $\tau_*^{(i)}$ is the characteristic time (reciprocal of strain rate) at which this maximum occurs and $\delta^{(i)}$ is a constant giving the breadth of the distribution. As discussed in section 4, these numbers follow from the calculations of figure 3,

	v = 0	v = 1	v = 2	v = 3
$S_*^{(i)}$	2×10^{-9}	7×10^{-10}	5×10^{-10}	10^{-10}
$\delta^{(i)}$	7.46×10^{-6}	4.38×10^{-5}	2.46×10^{-4}	1.38×10^{-3}
$\tau_*^{(i)}/\tau_c$	25	10	4.17	1.67

Table 2. Constants for Representation of Distribution of Vibrational States, Eq. 54

Now to evaluate the distribution of states, explicit calculations of strain rate and the actual flame surface density are required. The strain rate then becomes

$$\alpha \left| \frac{\partial w}{\partial r} \right| = \alpha \sqrt{\frac{\theta}{3}} \left(\frac{\mu \sqrt{\mu}}{r^2} \right) \frac{1}{\delta^2} \left(\frac{2\eta}{(1 + \frac{1}{4}\eta^2)^3} \right) \tag{55}$$

and recalling the definition of τ from Equation 41,

$$\varepsilon \gamma_c = 2 \frac{\gamma}{\delta^2} \frac{\eta}{(1 + \frac{1}{4}\eta^2)^3} \tag{56}$$

and hence the quantity $\varepsilon \gamma_*^{(i)}$ required for the evaluation of $S^{(i)}$ is

$$\varepsilon \gamma_*^{(i)} = (\varepsilon \gamma_c) \left(\frac{\gamma_*^{(i)}}{\gamma_c} \right) \tag{57}$$

where the second factor is given in Table 1.

The distribution of vibrational states, $C_v^{(i)}$, is then

$$C_v^{(i)} = S^{(i)} \Sigma \tag{58}$$

AD-A073 746 CALIFORNIA INST OF TECH PASADENA GRADUATE AERONAUTIC--ETC F/G 20/4
CHEMICAL REACTIONS IN TURBULENT MIXING.(U)
JUL 79 H W LIEPMANN, G L BROWN, P E DIMOTAKIS F44620-76-C-0046
UNCLASSIFIED GALCIT-151 AFOSR-TR-79-0952 NL

2 OF 4
AD A073 746

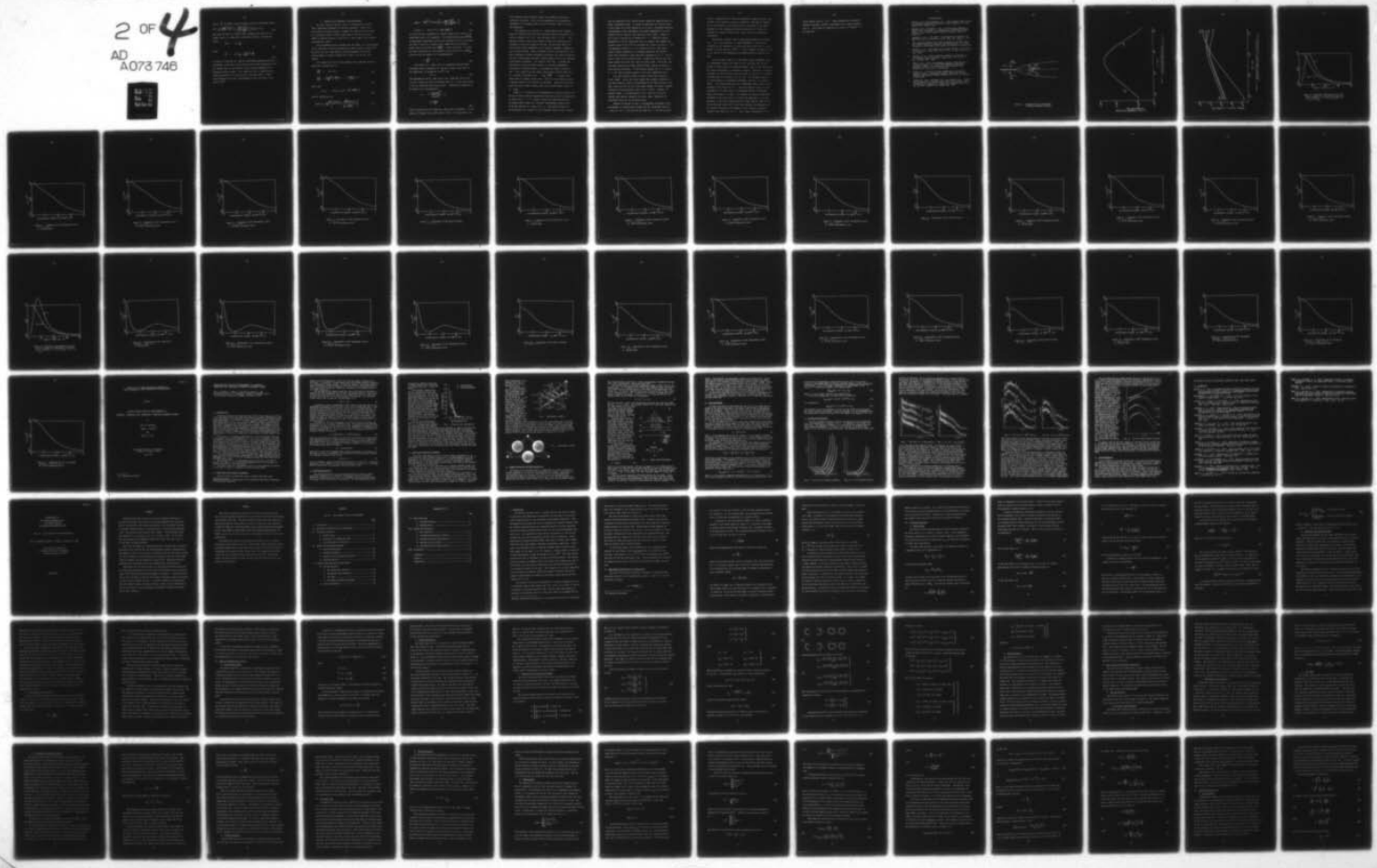

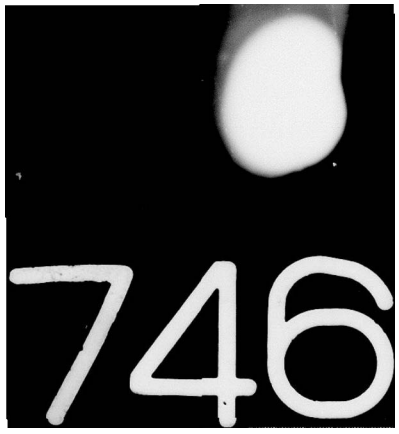
746

where Σ, the flame surface density, may be conveniently written

$$\Sigma = \frac{1}{\beta_1}\left(\frac{\sqrt{\mu}}{\alpha D}\right)^{1/2}\frac{\rho}{r}\left(\frac{1-\frac{1+\varphi_f}{s}\left(\frac{F'}{\eta}\right)}{1-\frac{1}{s}\left(\frac{1+\varphi_f}{s}\right)}\right)\left(\frac{F'}{\eta}\right)\frac{1}{s}\,Y(\xi) \tag{59}$$

The value of $Y(\xi)$ has already been calculated and hence it is a simple matter to compute the normalized densities of vibrational states,

$$\tilde{C}^{(i)} = S^{(i)}\tilde{\Sigma} \tag{60}$$

where

$$\tilde{\Sigma} \equiv \Sigma \Big/ \frac{1}{\beta_1}\left(\frac{\sqrt{\mu}}{\alpha D}\right)^{\frac{1}{2}}\frac{\rho}{r} \tag{61}$$

It should be noted that although the normalized population densities are convenient, in that they remove some of the system parameters from the results, they do not provide a direct scaling analysis for the hydrogen fluorine system. The reason for this is simply that the system parameters are involved also in the parameter τ, which enters Equation 56 for the representation of $\varepsilon\gamma_c$ and hence in the values of $S^{(i)}$.

7. RESULTS OF SPECIFIC CALCULATIONS

We shall show two specific cases of a hydrogen jet reacting with a stationary atmosphere of fluorine molecules. These were made with the specific purpose to explore the behavior of the model for a particular kinetic scheme rather than to describe the distribution of chemical species in the jet for a wide range of jet momenta and geometric scales.

The calculations divide naturally into two steps: (i) Determination of the centerline reactant concentration and flame surface density, $f(\xi)$ and $h(\xi)$ and (ii) Determination of the distribution of chemical species within the flame element and, hence, over the jet cross section.

The solution for the first step follows from equations 50 and 51 which are rewritten here as

$$\frac{df}{d\xi} = A(\xi;\tau) \tag{62}$$

$$\frac{dY}{d\xi} = \left(\frac{\alpha\sqrt{\mu}}{\mathcal{D}}\right)\frac{B(\xi)}{\xi}Y - \lambda\,\frac{C(\xi;\tau)}{1-f}\,Y^2 \tag{63}$$

where now

$$Y(\xi) = h(\xi)(1-f)\left[1 - \frac{b}{s}\left(\frac{1+\varphi f}{\xi}\right)\right] \tag{64}$$

and the coefficients are

$$A(\xi;\tau) = \left(\frac{3}{8}\right)^{7/4}\left\{\frac{I_0(\xi;\tau) - \frac{1+\varphi f}{\xi}I_1(\xi;\tau)}{1 - \frac{b}{s}\left(\frac{1+\varphi f}{\xi}\right)}\right\} \tag{65}$$

$$B(\xi) = \left(\frac{3}{8}\right)^{3/2} (1.96350) \left\{ \frac{1 - \frac{21}{20}\left(\frac{1+\varphi_f}{5}\right)}{1 - \frac{6}{5}\left(\frac{1+\varphi_f}{5}\right)} \right\} \tag{66}$$

$$C(\xi;\tau) = A(\xi;\tau) \Big/ \left[1 - \frac{6}{5}\left(\frac{1+\varphi_f}{5}\right) \right] \tag{67}$$

To carry out this calculation we require values for the several constants that arise in the equations. The dimensionless group $\sqrt{\mu}/\rho$ is determined empirically by the known structure of the non-reacting jet and α is universal constant which relates the local turbulent strain rate to the strain rate $\left|\frac{\partial W}{\partial r}\right|$ of the mean flow. In fixing the value of α from jet measurements it is as easy to fix $\alpha\sqrt{\mu}/\rho$ directly, and this appears to be approximately

$$\alpha \frac{\sqrt{\mu}}{\rho} = 5 \tag{68}$$

The value of λ, which occurs in connection with the flame shortening terms of Equation 63, has been chosen on the basis of the experiments of Hawthorne et al[9] to be

$$\lambda = 2 \tag{69}$$

The integrals I_0 and I_1, that occur in the coefficient $A(\xi;\tau)$ and $C(\xi;\tau)$ contain the ratio of chemical time τ_c, to the time defined by the jet momentum and flow, μ and r. Referring to Equation 41, the value of τ is proportional to

$$\tau \sim \alpha \frac{(W_0^2 d^2)^{3/2}}{(W_0 d^2)^2} \tau_c$$

$$= \alpha \frac{W_0 \tau_c}{d} \tag{70}$$

where W_0 and d are the initial jet velocity and jet diameter. As the value of τ changes from small values ($\sim \xi_0^2$) to large values, the

local diffusion flame elements change from diffusion controlled to chemistry controlled. And from the standpoint of non-equilibrium populations of vibrational states of HF, the larger values of γ favor non-equilibrium.

The solutions for (1-f) and Y, proportional to the centerline values of hydrogen mass fractions and flame density respectively, are shown in Figure 4 for $\gamma = 5$ and in Figure 10 for $\gamma = 20$. The general character of the flame density is that the straining process dominates in the early portion of the jet, increasing the flame density until the flame annihilation terms become important, stopping the rise in flame density. After a distance of 10-12 port diameters, the flame straining and flame annihilation processes are nearly in balance, but lead to the gradual decrease in flame surface area as the hydrogen concentration diminishes. The effect of $W_o \tau_c / d$ is evident and shows that for large γ values, Figure 10, the flame annihilation mechanism is somewhat slower in retarding the growth in flame surface. This results from the higher strain rates involved which lead to a reactant consumption rate $\sim \frac{1}{\tau_c} \sqrt{D/\epsilon}$, giving lower values than for smaller strain rates. Thus the active flame occupies a smaller fraction of the volume for $W_o \tau_c / d$ large and hence postpones the peak in flame density until it has reached larger values of $\xi \sim z/d$.

Figure 5 - 9 summarize the distribution of reaction products over the jet for three distances downstream from the jet port corresponding to values of $\xi = 2, 7, 15$. Figure 5 gives the radial distribution of the ground state, Figure 5a, and three vibrationally excited states of the HF molecule at a value of $\xi = 2$. The general features of the distribution are similar for all vibrational states but the concentra-

tion, as indicated on the vertical scale, shows the rapid decrease for higher vibrational levels. It should be noted that the vertical scales of each figure have been adjusted so as to give a reasonable geometric representation of the distribution; the actual magnitudes of the populations must be obtained with reference to the scales. Figures 6 and 7 show a similar set of results at $\xi = 7$. While the relative populations of the HF vibrational levels is changed only slightly, the absolute values of the $C^{(i)}$ are increased by a factor of nearly 3. The corresponding results for $\xi = 15$, given in 8 and 9, show again a similar relative population of vibrational states but the absolute values have declined to about half their magnitude at $\xi = 2$. This behavior, which was described earlier, results from the fact that both flame density and strain rate enter the final result. The strain rate decreases along the jet length while the flame density increases at first and then decreases. In the present example for $\mathcal{T} = 5$, Figures 4 - 9, the flame density variation is the more significant factor.

Two other features should be kept in mind when looking at these results. First, the actual volume that contains molecules in any state along the radius is proportional to the radius and hence the high values near the jet axis carry little weight, the volume weighted maximum occurring between values of $\eta = 1$ and 2. Second, the physical radius r is proportional to ηx and hence increases linearly with distance along the jet which, again, influences the distribution along the jet discussed above.

Figures 10 through 15 give a corresponding description of the distribution of hydrogen, flame density and HF vibrational states for a value $\mathcal{T} = 20$, in contrast with the value of $\mathcal{T} = 5$ for the previous

series. Inasmuch as the chemical parameters remain the same, this increase in the value of $\mathcal{J}$ may be considered, referring to Equation 70, as an increase in jet velocity and/or a decrease in jet radius. Because it is the comparison with the series for $\mathcal{J} = 5$ that is of interest, the specific details of the curves will not be discussed extensively.

One feature, however, that is particularly apparent in Figures 11a - 11d, is the alteration of radial distribution. This feature results from the dependence of strain rate upon radius and is accentuated for larger values of $\mathcal{J}/\xi^2$. Thus it appears in Figure 11 for $\xi = 2$ but not in the distributions at larger distances along the jet axis.

For the larger value of $\mathcal{J}$, the flame surface annihilation rate is considerably reduced over that at $\mathcal{J} = 5$ and hence the net production of flame surface is somewhat larger. But, on the other hand, the actual consumption of reactants is reduced. This fact is reflected in Figure 12 where the mass fraction of HF is shown to be somewhat less than that for the slower $(\mathcal{J} = 5)$ jet. The integrated species in various degrees of vibrational excitation, however, is somewhat larger. This demonstrates that the considerable flame surface manufactured in the range $2 \leq \xi \leq 7$ must wait until the strain rate has diminished to the point where the integrated density of vibrational states (see Figure 3) is high. This tendency to delay the diffusional thickening of the flame sheet, and hence the appearance of reaction products, is one of the unusual effects of high velocity, high $\mathcal{J}$ jets. By the time the value of $\xi = 15$ has been reached, the populations of the excited vibrational levels appear to have returned reasonably closely to the values for $\mathcal{J} = 5$. This relative independence of $\mathcal{J}$

would indicate that for $\xi = 15$, both examples have reached a diffusion controlled reactant consumption rate, weakly dependent upon γ . This would be expected in as much as $47/(15)^2 < 1$ for both jets.

REFERENCES

1. Marble, F.E. and Broadwell, J.E., "The Coherent Flame Model for Turbulent Chemical Reactions," Project SQUID Tech. Rpt. TRW-9-PU, January 1977.

2. Marble, F.E., Broadwell, J.E., "A Theoretical Analysis of Nitric Oxide Production in a Methane-Air Turbulent Diffusion Flame," U.S. Environmental Protection Agency, Report No. April 1979.

3. Batchelor, G.K., "The Effect of Homogeneous Turbulence on Material Lines and Surfaces," Proc. Roy. Soc. A213, p. 349.

4. The computer program was made available by the TRW Space and Defense Systems Group and was reworked for use by the Computing Center Staff at the California Institute of Technology.

5. Blottner, F.G., "Nonequilibrium Laminar Boundary Layer Flow of Ionized Air," AIAA Jour. Vol. 2, No. 11, pp. 1921-1927, Nov. 1964.

6. Blottner, F.G., "Finite Difference Methods of Solutions of the Boundary Layer Equation," AIAA Jour. Vol. 8, No. 2, pp. 193-205, Feb. 1970.

7. Witte, A.B., et al, "Aerodynamic Reactive Flow Studies of the H_2/F_2 Laser - II," Air Force Weapons Laboratory Technical Report No. AFWL-TR-74-78, February 1974. Kirtland Air Force Base, New Mexico.

8. Cohen, N., "A Review of Rate Coefficients in the H_2-F_2 Chemical Laser - Supplement (1977)," Space and Missile Systems Organization, Report SAMSO-TR-78-41, Los Angeles, 8 June 1978.

9. Hawthorne, W.R., Weddell, D.S., and Hottel, H.C., "Mixing and Combustion in Turbulent Gas Jets," Proceedings, Third Symposium on Combustion, Flame and Explosion Phenomena, pp. 266-288, Williams and Wilkins pub. 1949.

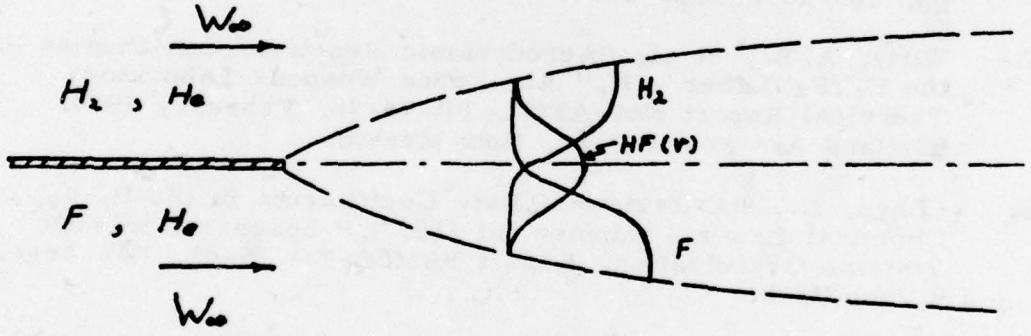

Figure 1. Configuration for Calculation of Strained Diffusion Flames.

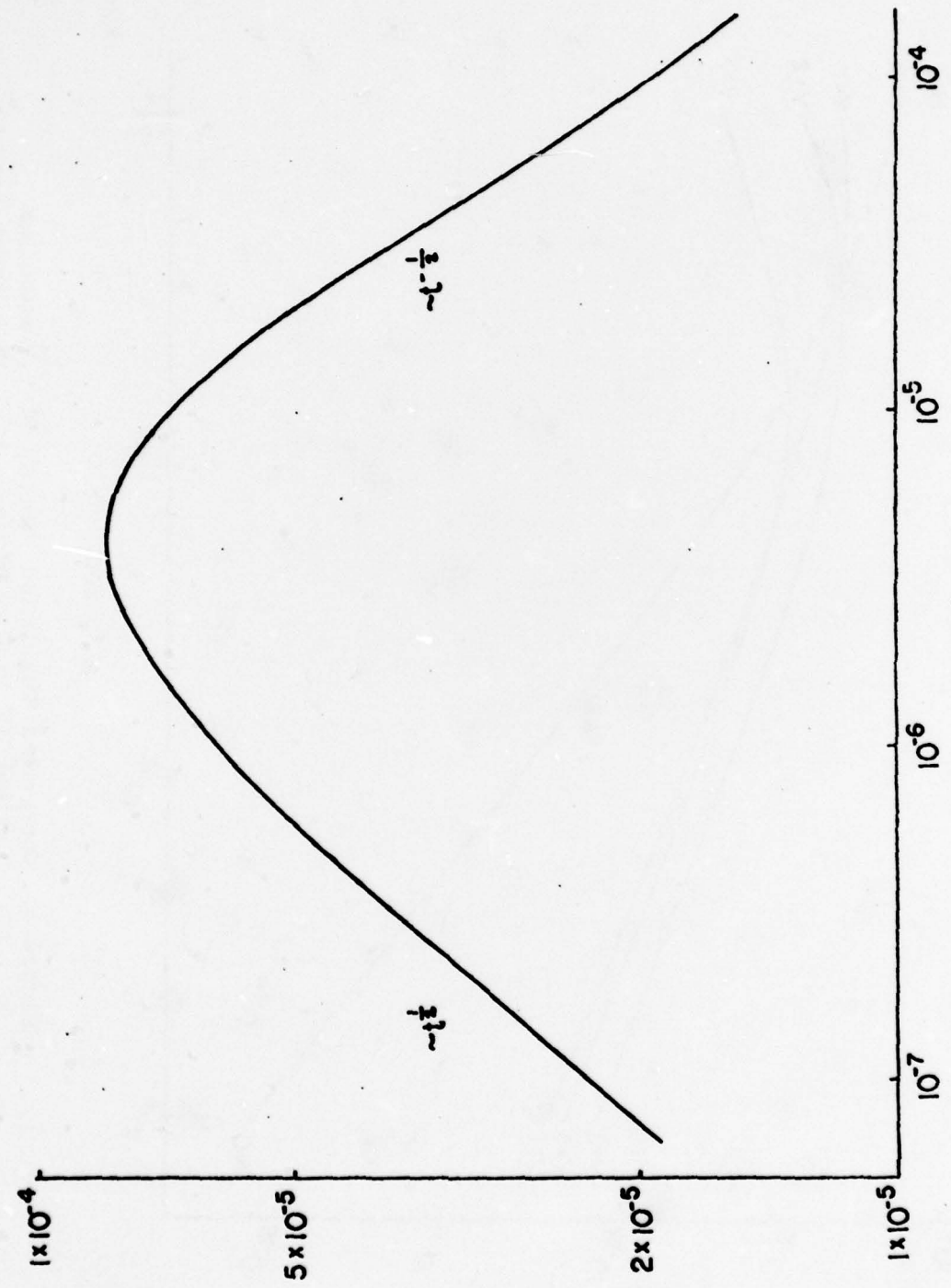

Figure 2. Reactant Consumption Rate for H_2-F Diffusion Flames Strained at Rate ϵ.

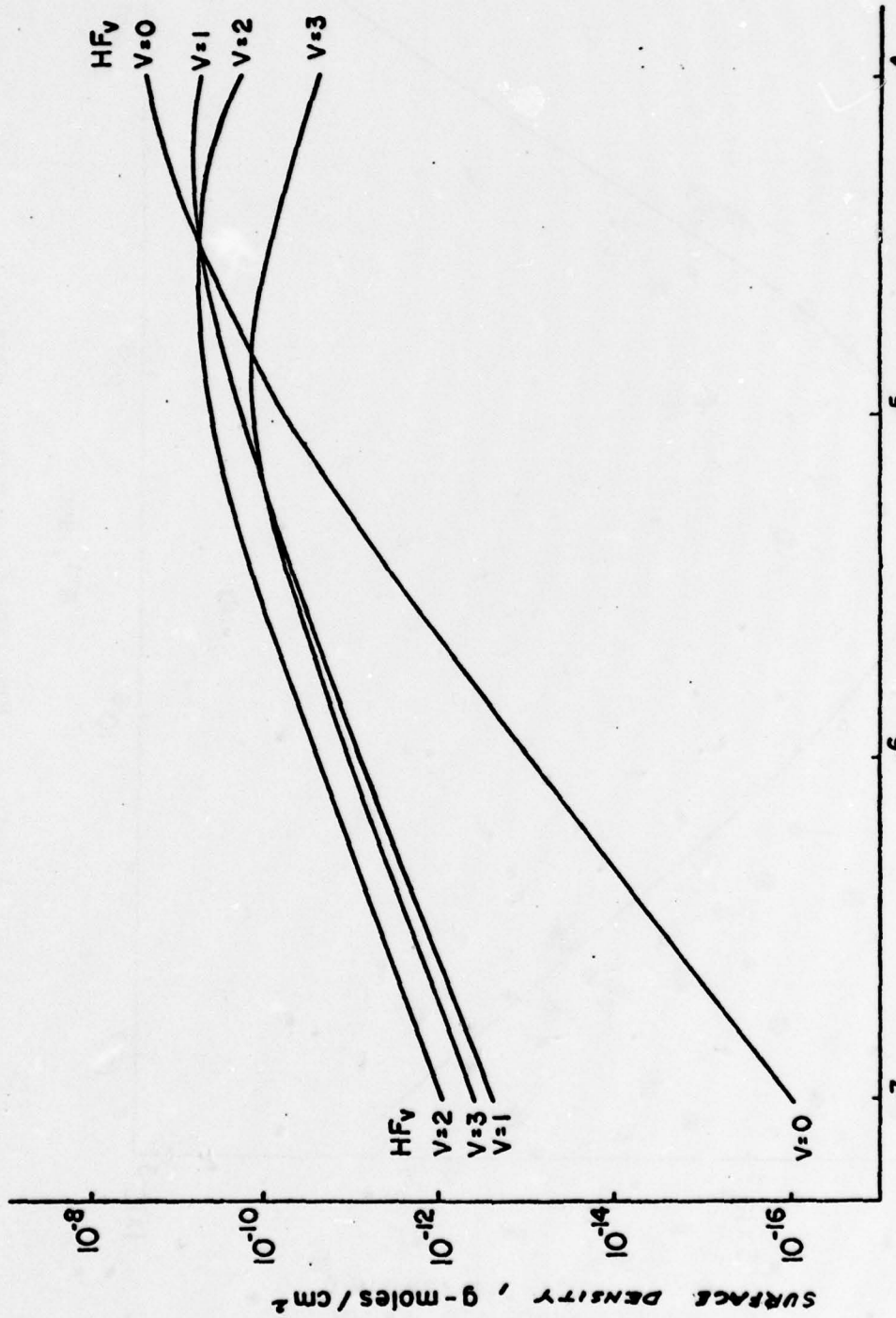

Figure 3. Integrated Population Density of Vibrationally Excited HF in Unit Surface Area of Strained Flame.

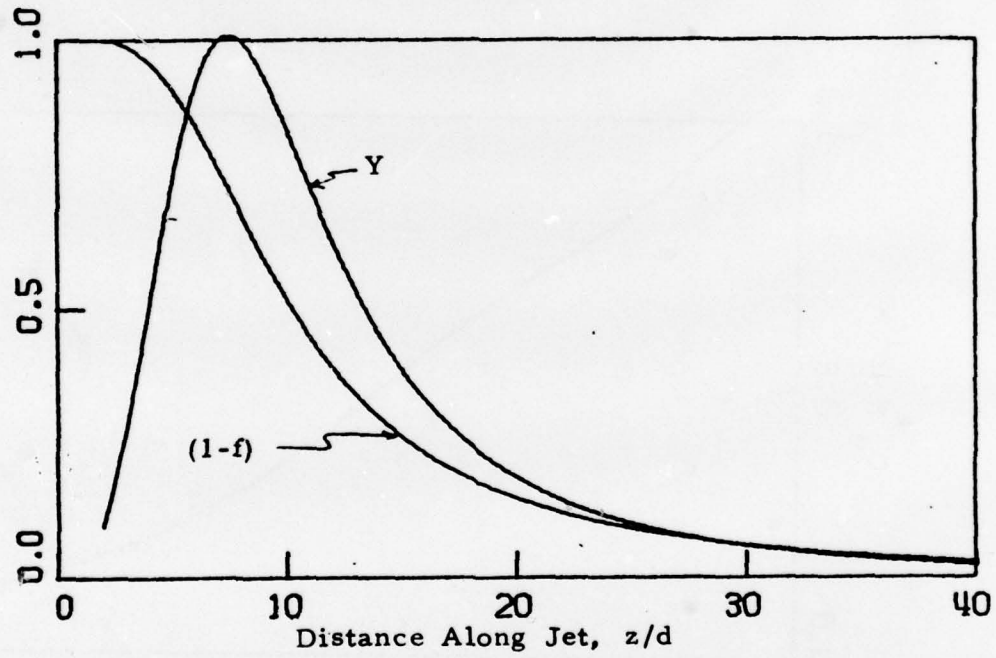

Figure 4. Hydrogen Concentration (1-f) and Flame Density (Y) Along Axis of Hydrogen Jet in Fluorine. $\varphi = 2.0$, $\alpha\sqrt{\mu}/\beta = 5$, $\lambda = 2$, $\tau = 5.0$.

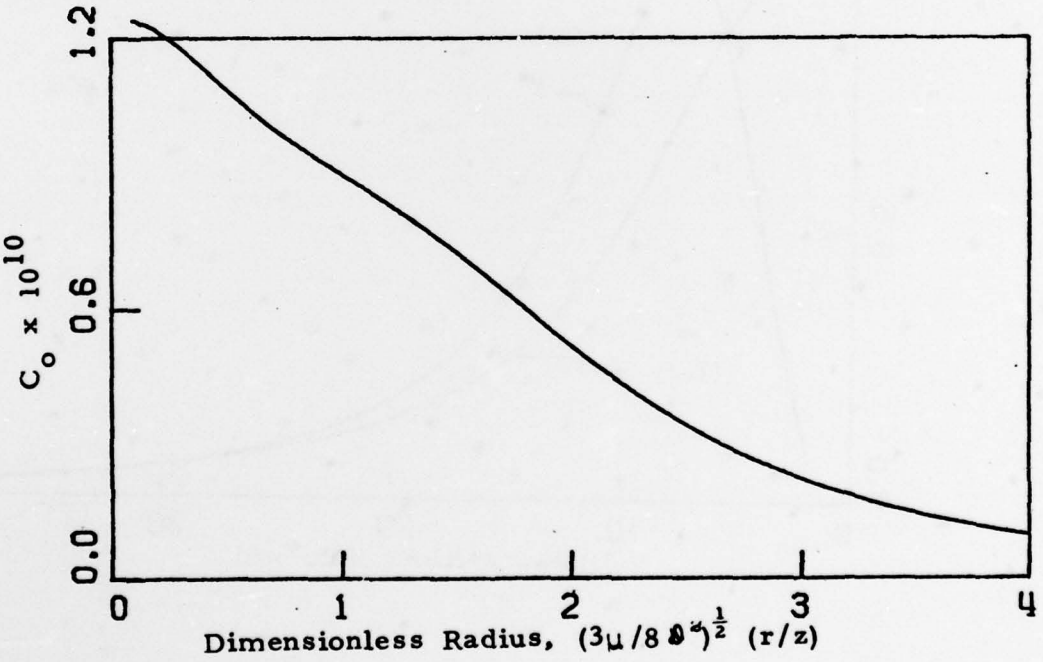

Figure 5. Population of HF Vibrational Level;
$\tau = 5$, $\zeta = 2$.
a) Ground State

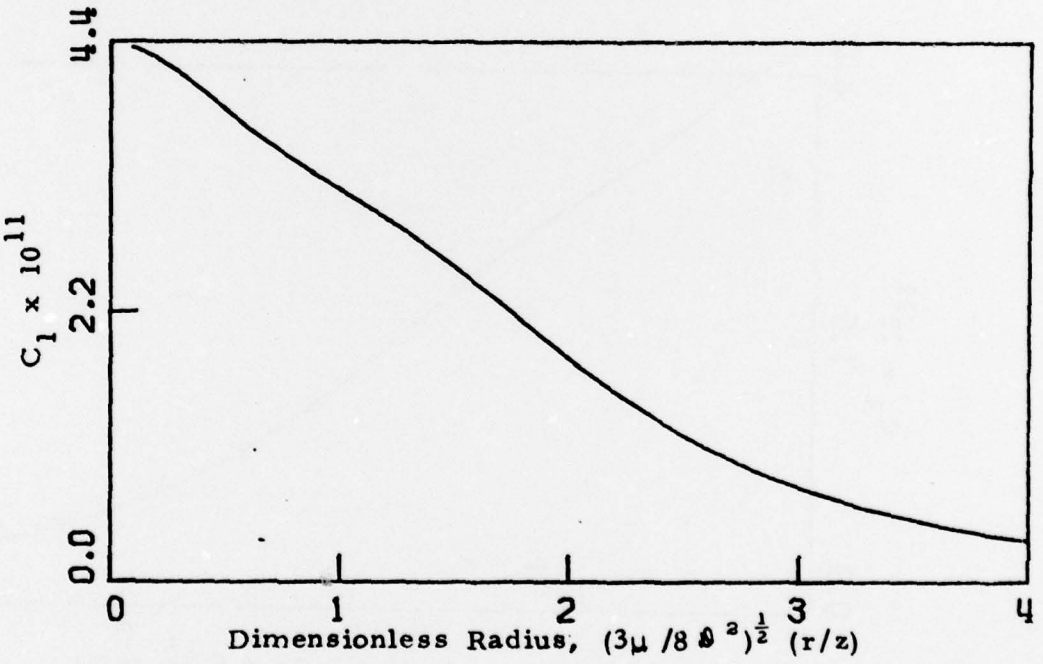

Figure 5. . Population of HF Vibrational Level;
$\tau = 5$, $\zeta = 2$.
b) First Vibrational Level

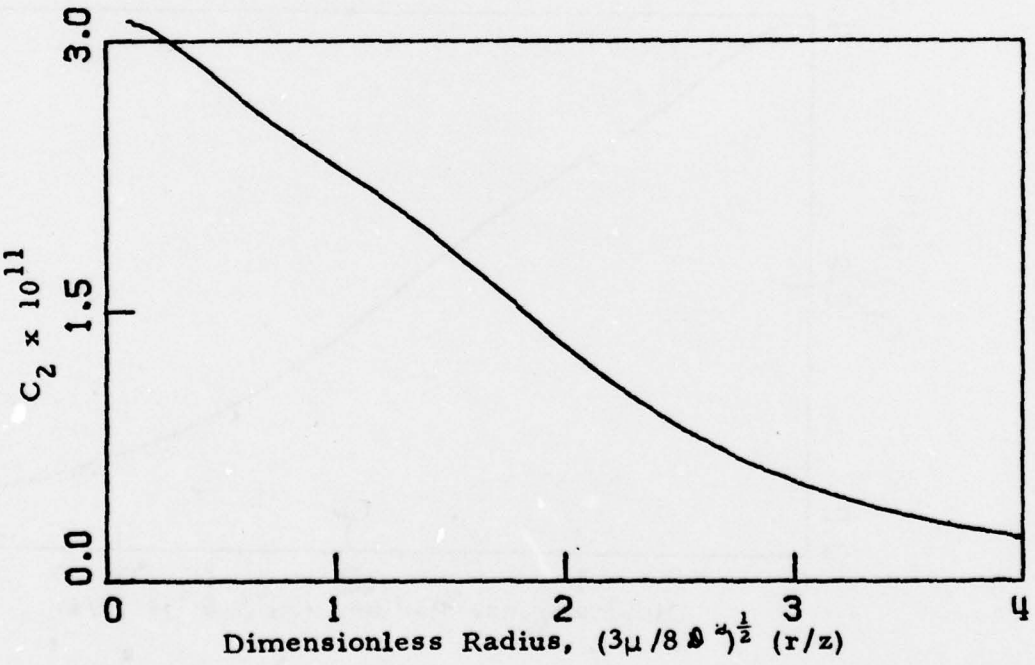

Figure 5. Population of HF Vibrational Level;
$\tau = 5$, $\zeta = 2$.
c) Second Vibrational Level

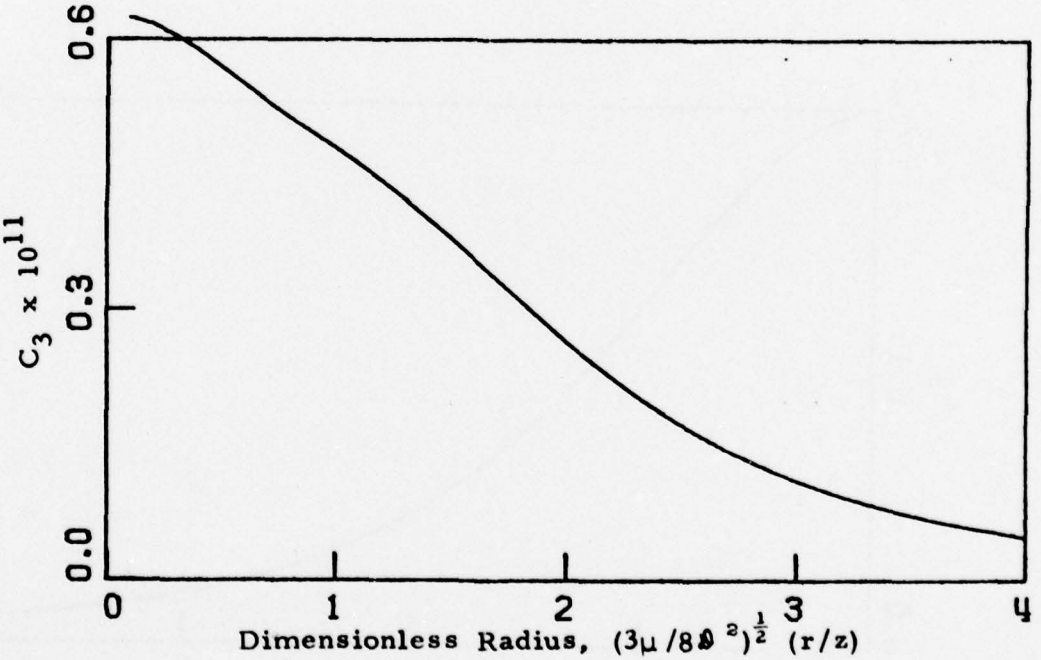

Figure 5. Population of HF Vibrational Level;
$\tau = 5$, $\zeta = 2$.
d) Third Vibrational Level

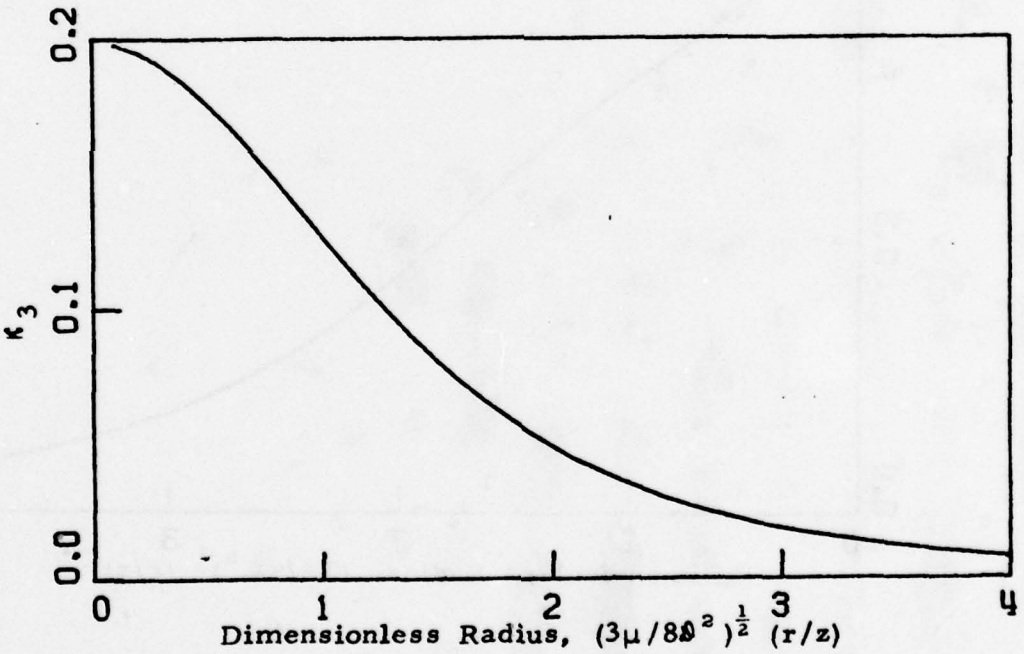

Figure 6. Distribution of HF Mass Fraction;
$\tau = 5$, $\zeta = 7$.

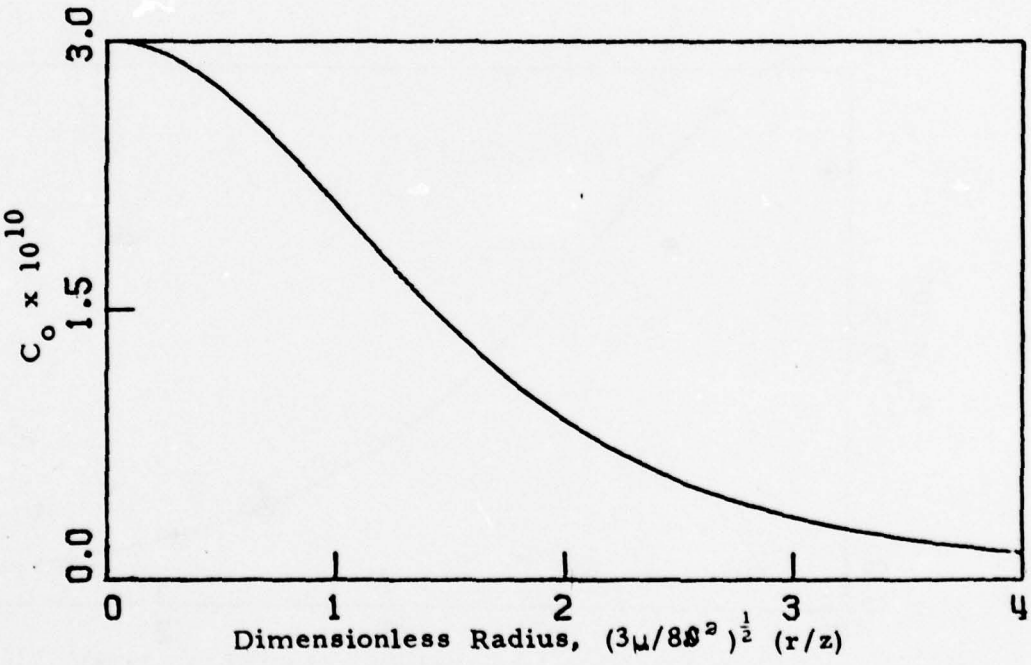

Figure 7. Population of HF Vibrational Levels;
$\tau = 5$, $\zeta \simeq 7$.
a) Ground State

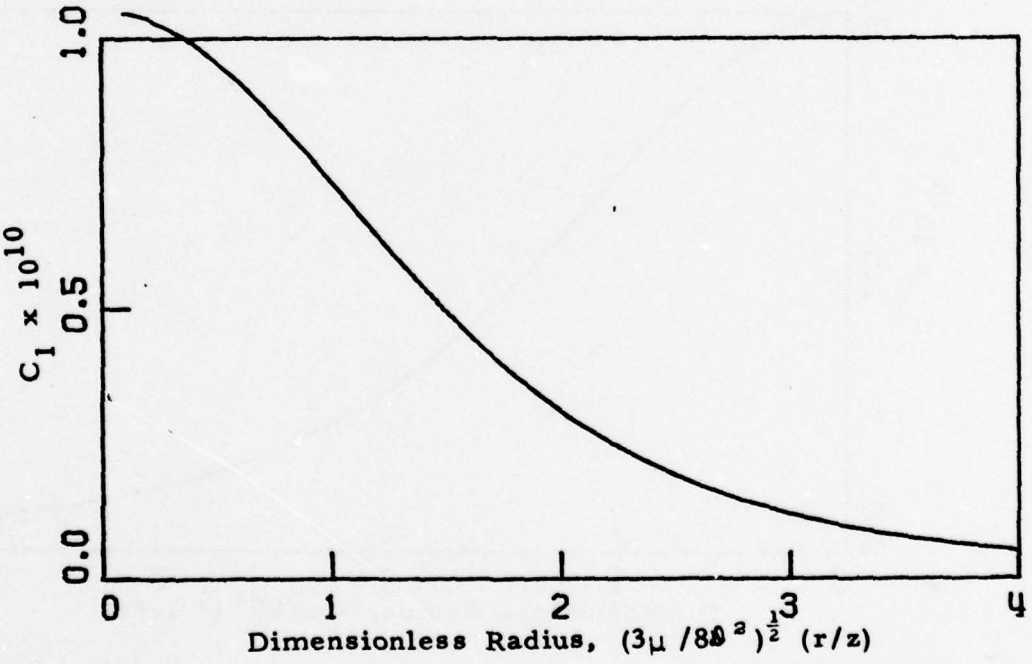

Figure 7. Population of HF Vibrational Levels;
$\tau = 5$, $\zeta = 7$.
b) First Vibrational Level

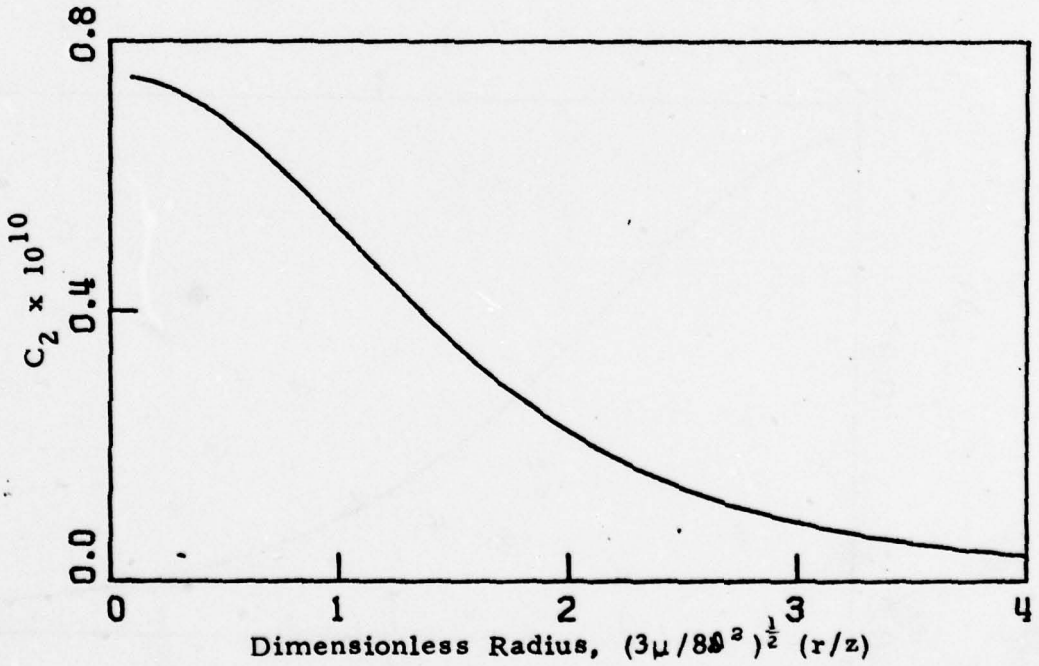

Figure 7. Population of HF Vibrational Levels;
$\tau = 5$, $\zeta = 7$.
c) Second Vibrational Level

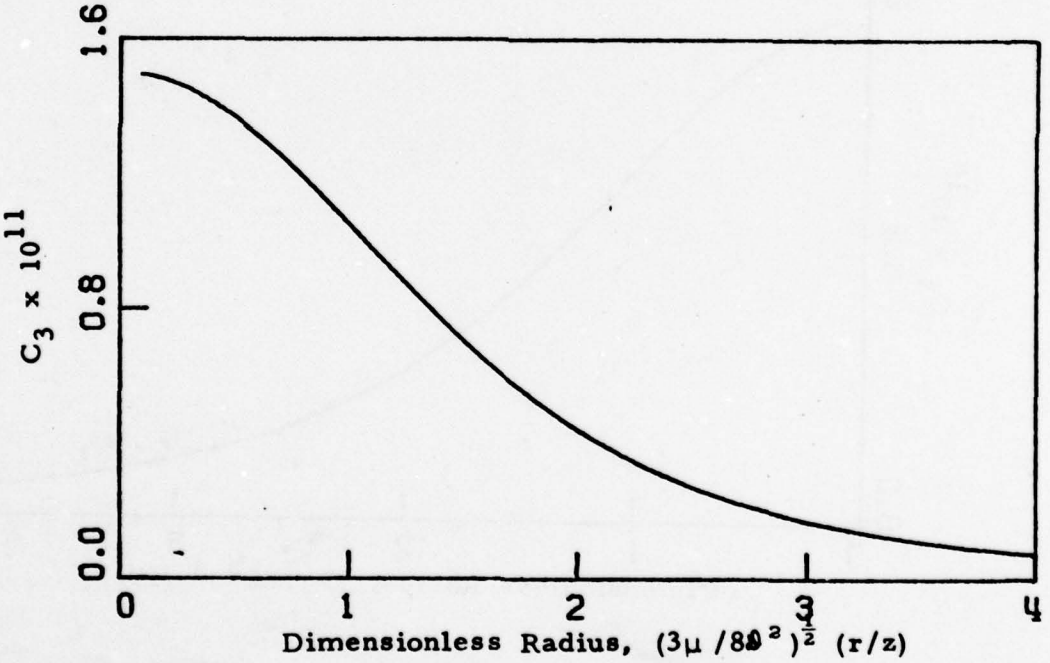

Figure 7. Population of HF Vibrational Levels; $\tau = 5$, $\zeta = 7$.
d) Third Vibrational Level

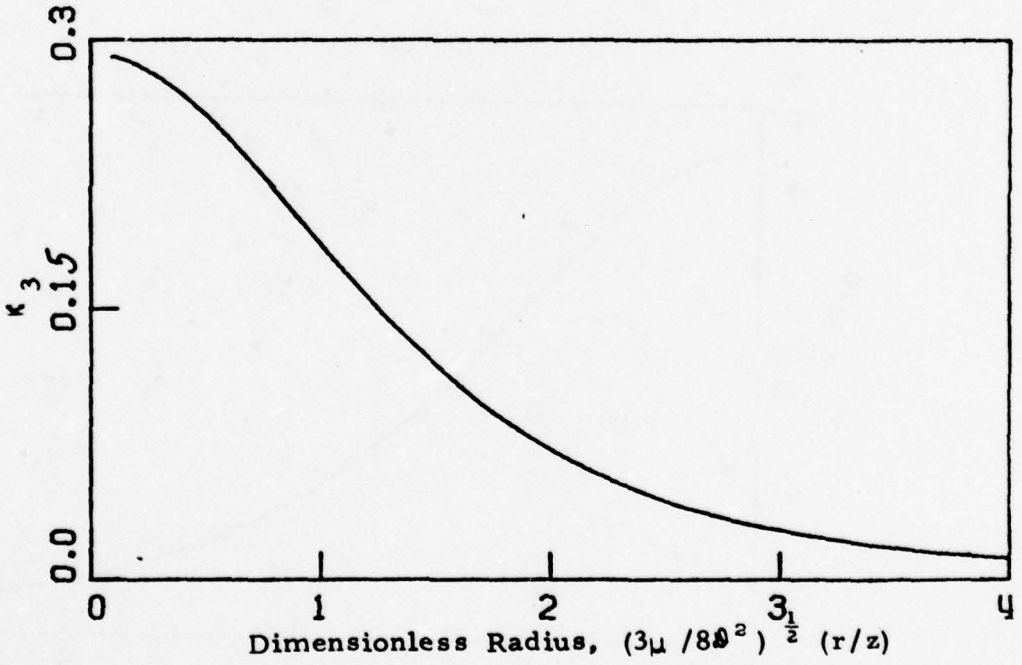

Figure 8. Distribution of HF Mass Fraction; $\tau = 5$, $\zeta = 15$

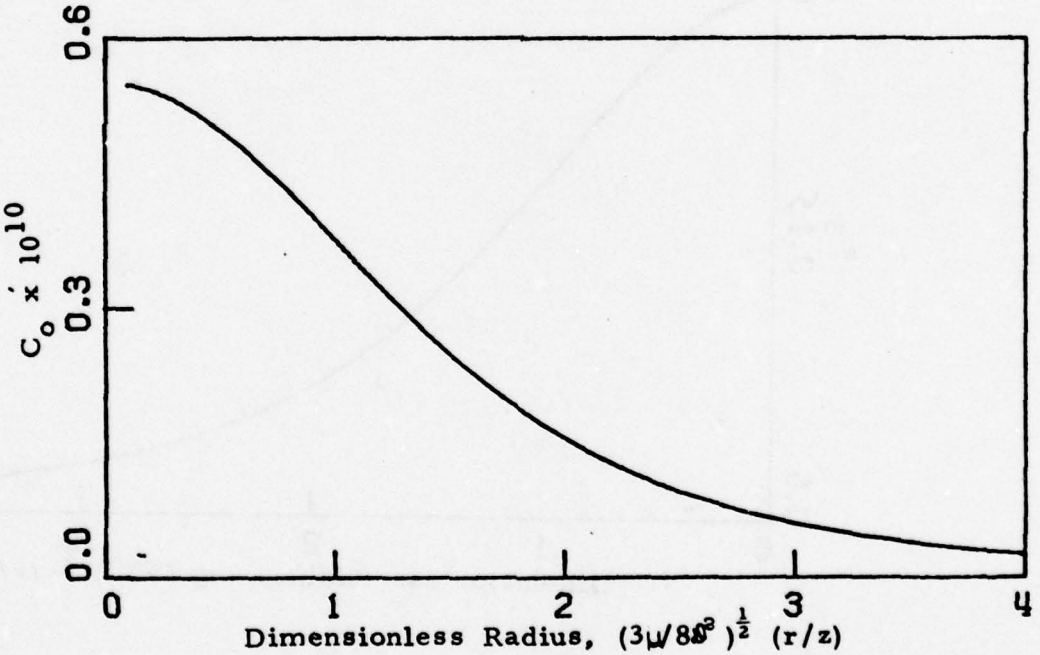

Figure 9. Population of HF Vibrational Levels;
$\tau = 5$, $\zeta = 15$
a) Ground State

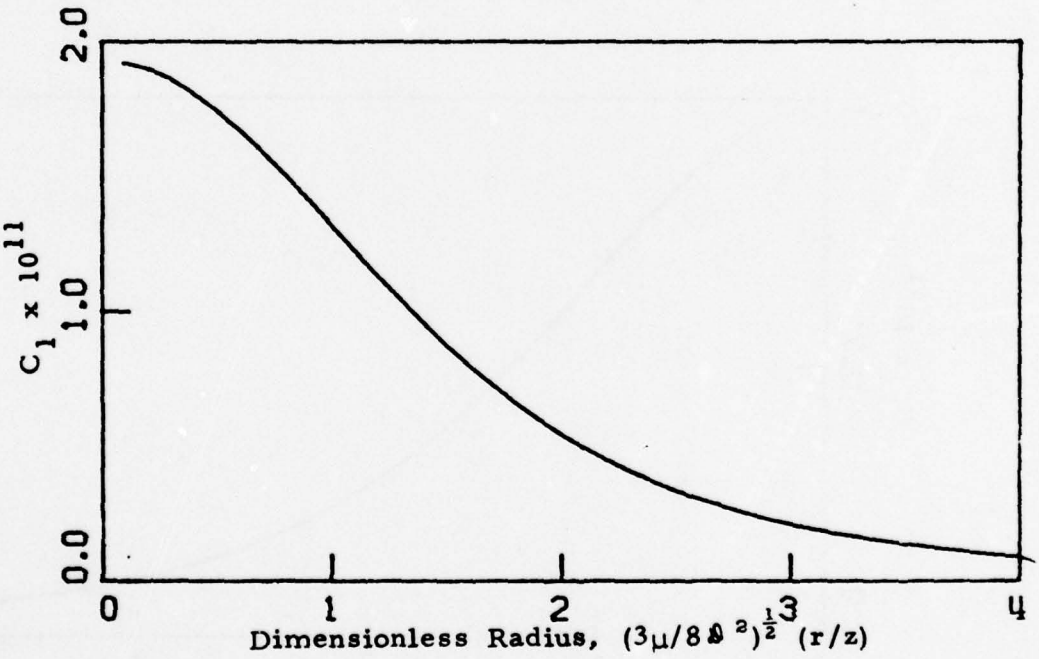

Figure 9. Population of HF Vibrational Levels;
$\tau = 5$, $\zeta = 15$
b) First Vibrational Level

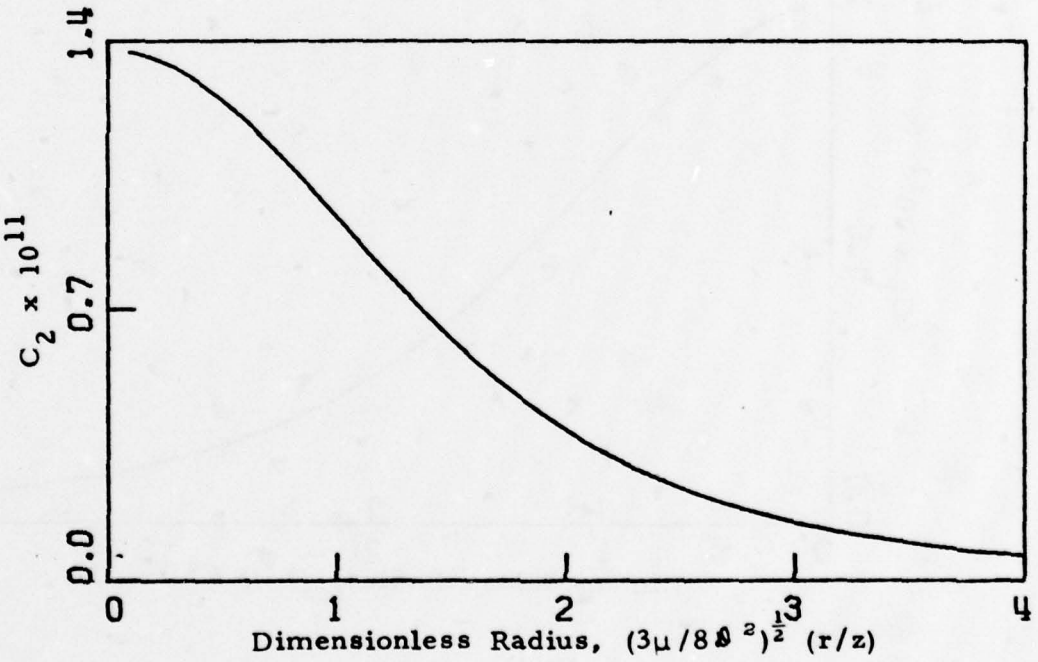

Figure 9. Population of HF Vibrational Levels;
$\tau = 5$, $\zeta = 15$
c) Second Vibrational Level

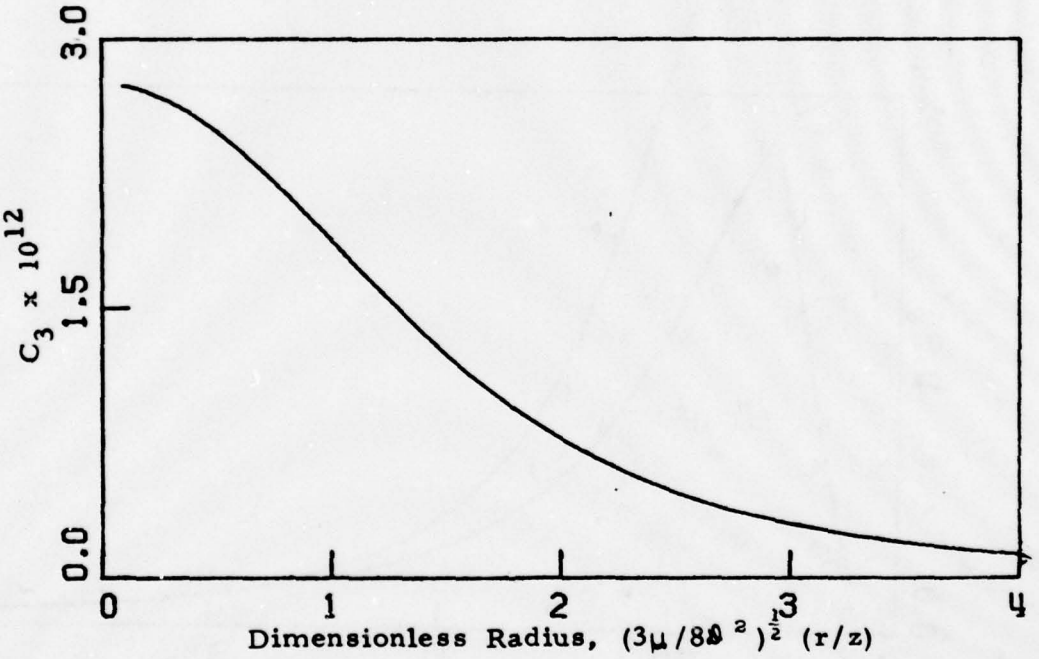

Figure 9. Population of HF Vibrational Levels;
$\tau = 5$, $\zeta = 15$
d) Third Vibrational Level

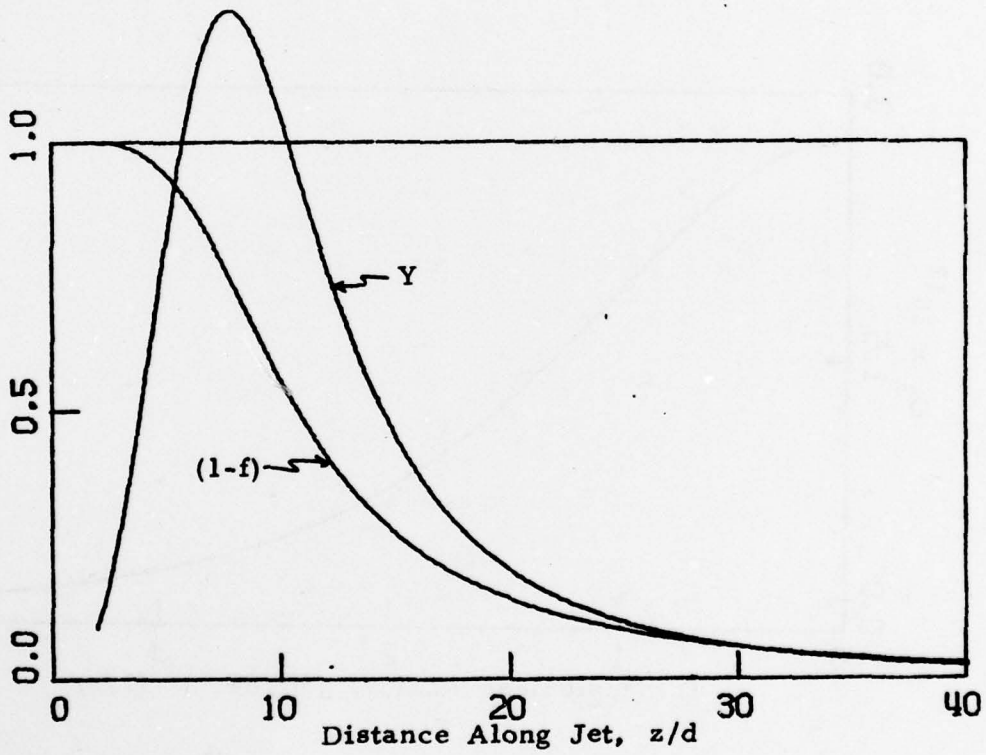

Figure 10. Hydrogen Concentration (1-f) and Flame Density (Y) Along Axis of Hydrogen Jet in Fluorine, $\varphi = 2$, $\alpha\sqrt{\mu}/\beta = 5$, $\lambda = 2$, $\tau = 20$.

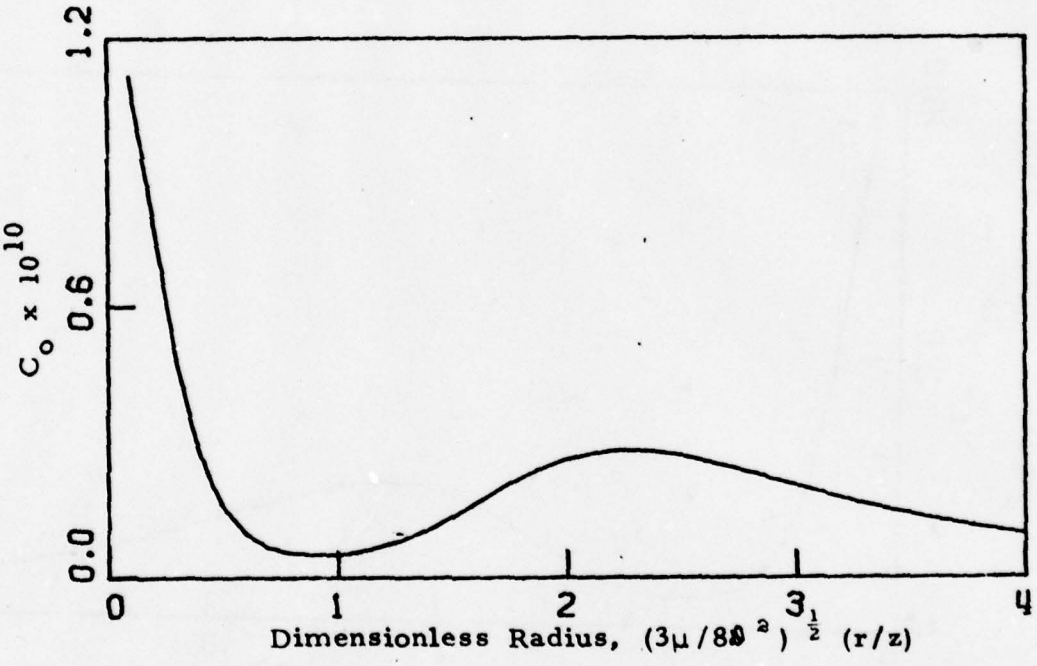

Figure 11. Distribution of HF Vibrational Levels; $\tau = 20$, $\zeta = 2$.
a) Ground State

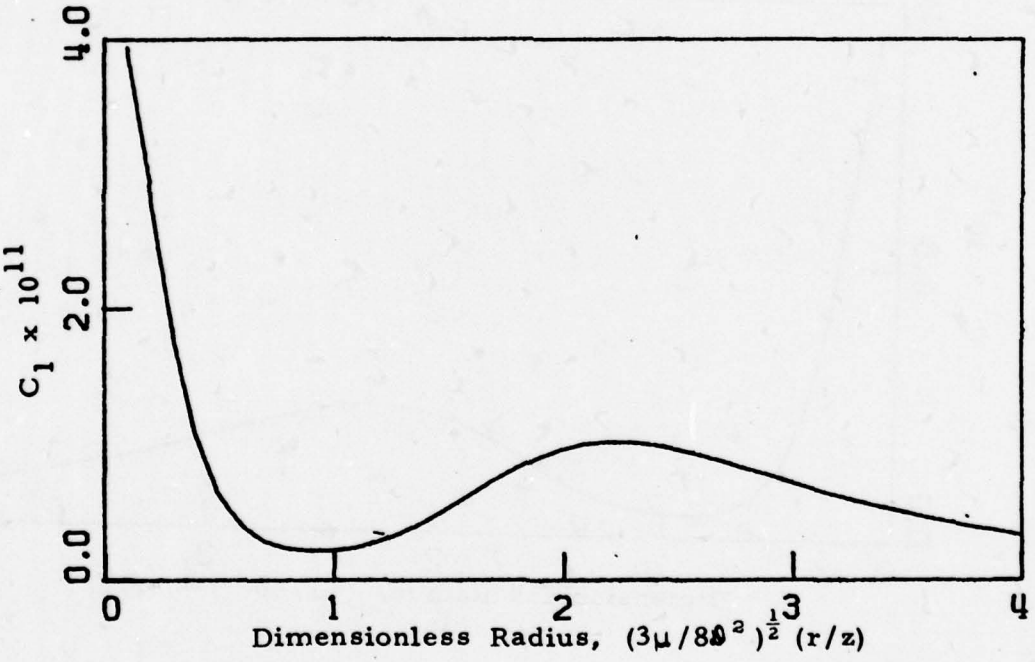

Figure 11. Distribution of HF Vibrational Levels;
$\tau = 20$, $\zeta = 2$.
b) First Vibrational Level

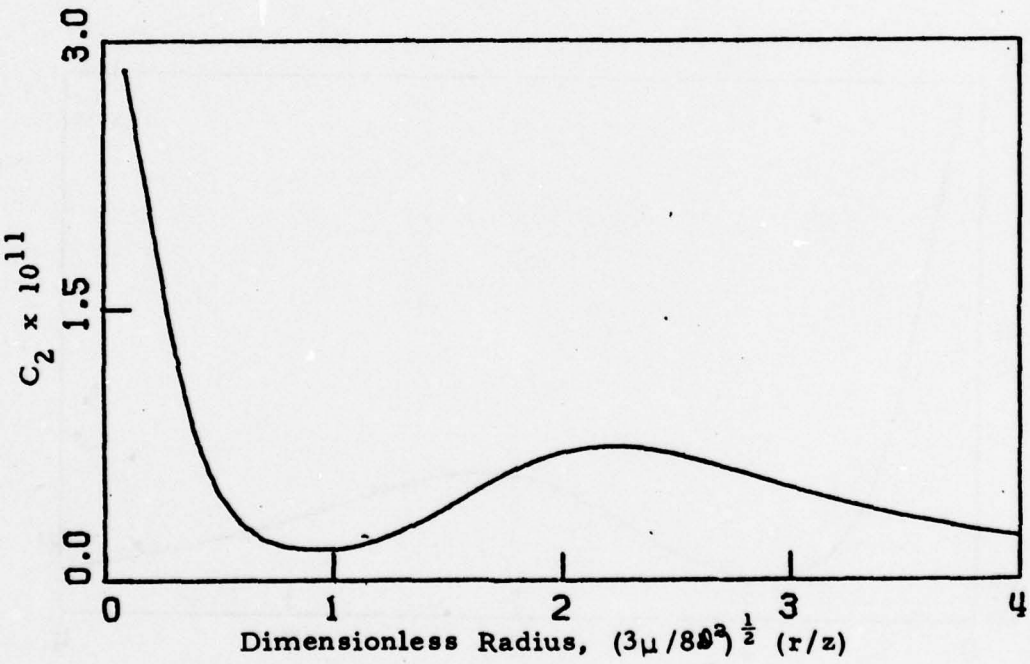

Figure 11. Distribution of HF Vibrational Levels;
$\tau = 20$, $\zeta = 2$.
c) Second Vibrational Level

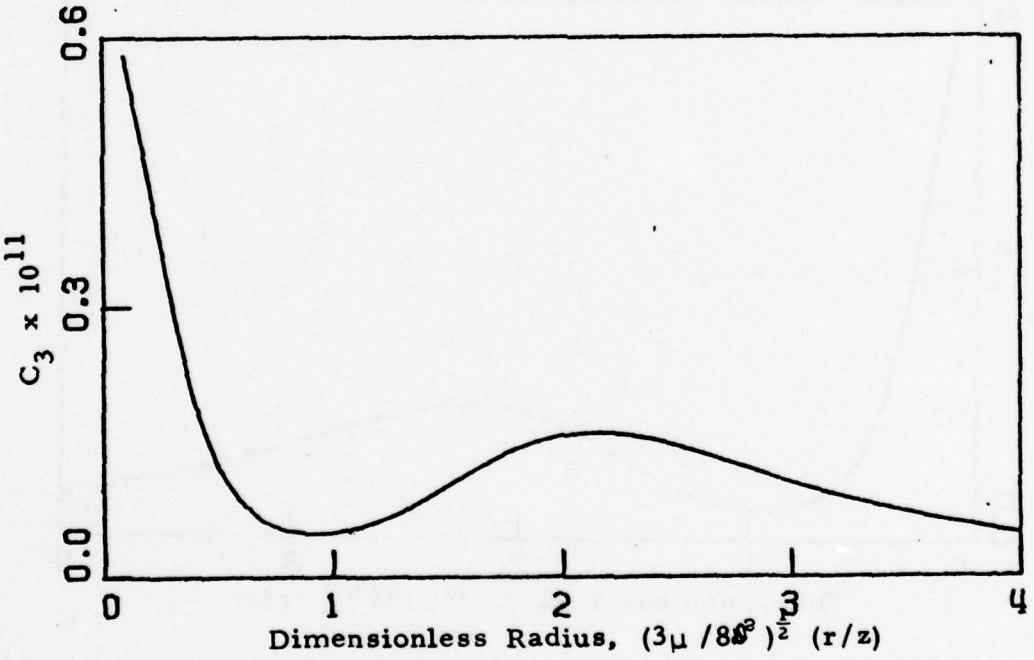

Figure 11. Distribution of HF Vibrational Levels;
$\tau = 20$, $\zeta = 2$.
d) Third Vibrational Level

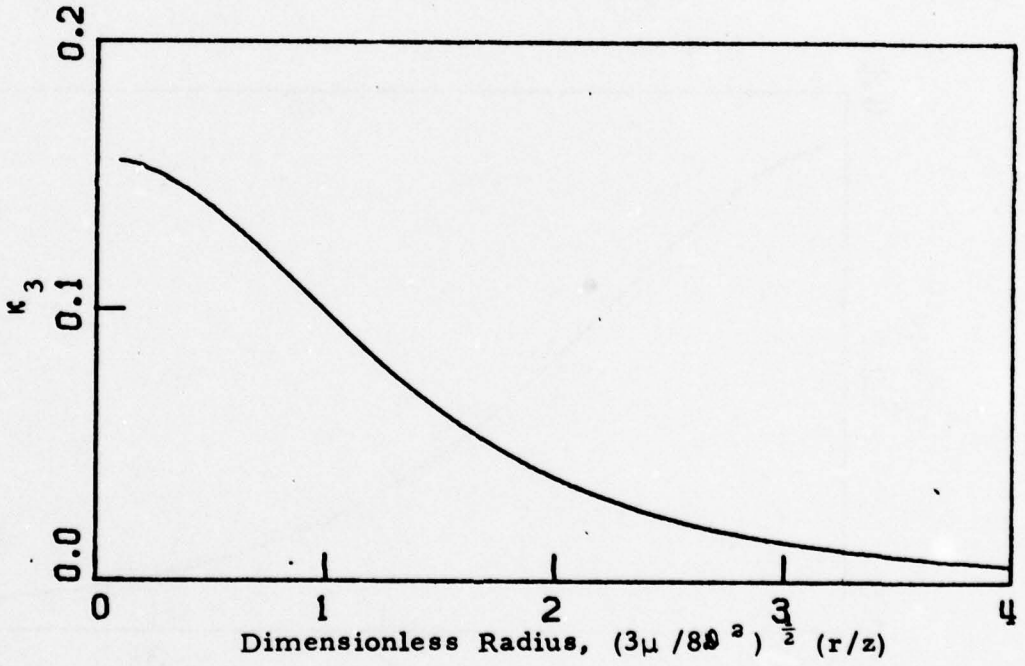

Figure 12. Distribution of HF Mass Fraction; $\tau = 20$, $\zeta = 7$.

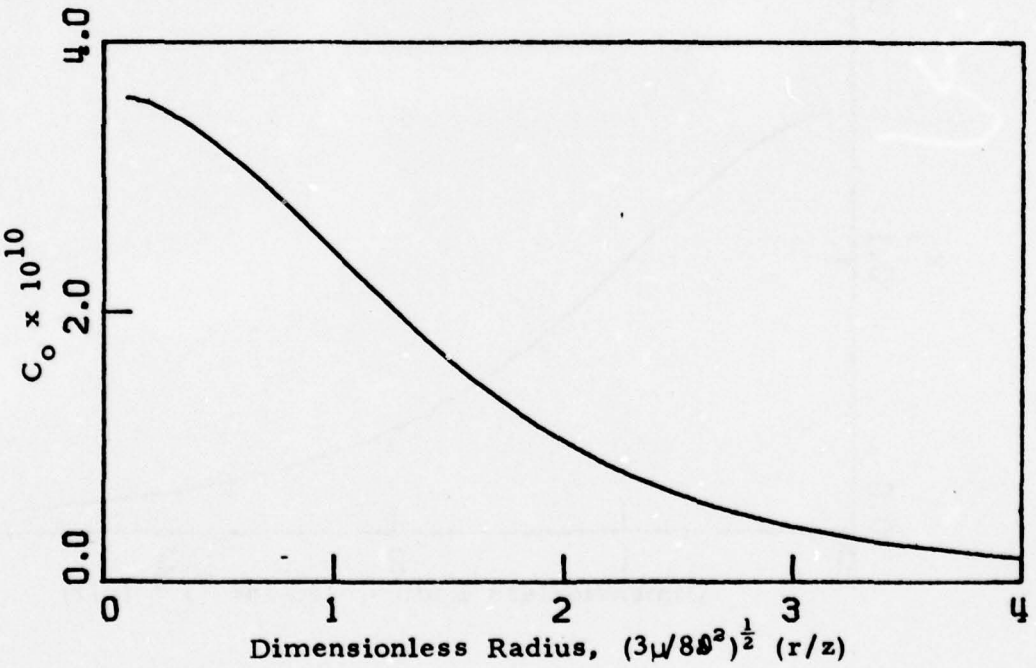

Figure 13. Distribution of HF Vibrational Levels;
$\tau = 20$, $\zeta = 7$.
a) Ground State

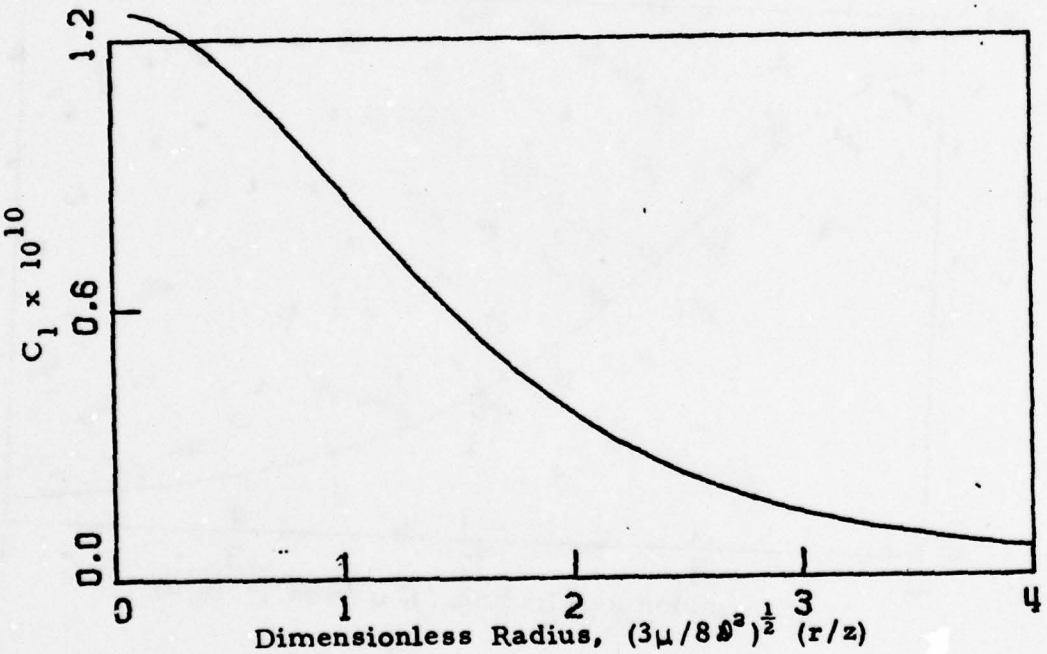

Figure 13. Distribution of HF Vibrational Levels;
τ = 20, ζ = 7.
b) First Vibrational Level

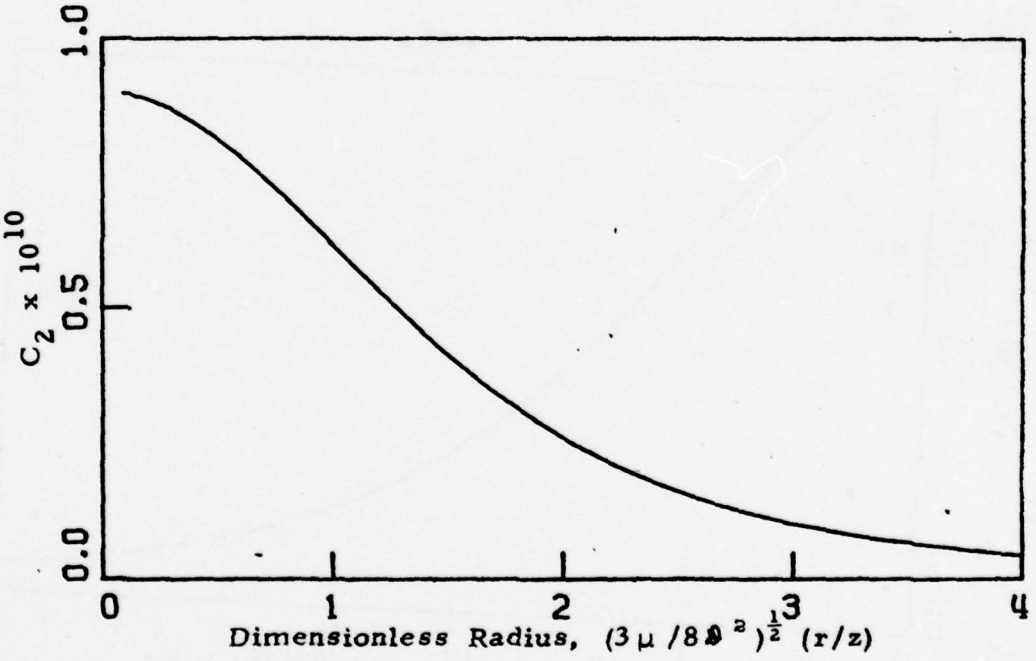

Figure 13. Distribution of HF Vibrational Levels;
$\tau = 20$, $\zeta = 7$.
c) Second Vibrational Level

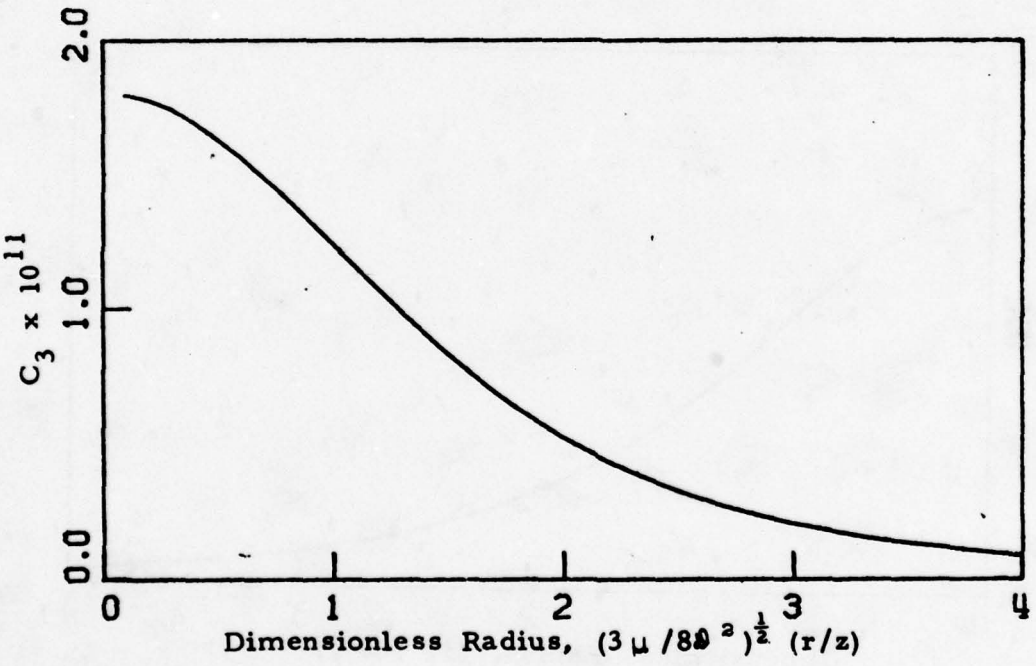

Figure 13. Distribution of HF Vibrational Levels; $\tau = 20$, $\zeta = 7$.
d) Third Vibrational Level

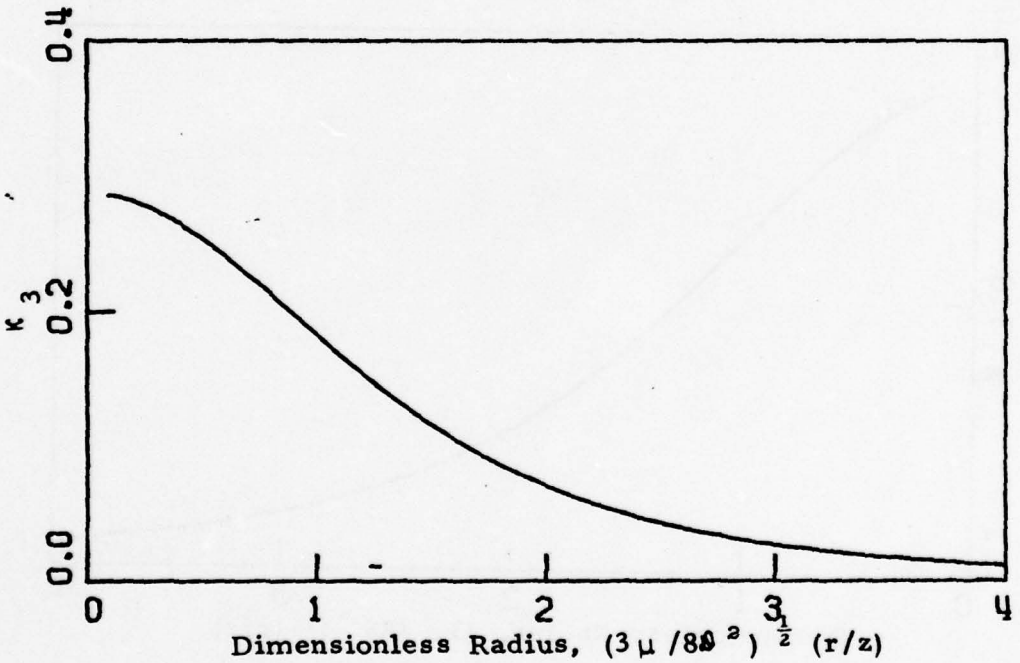

Figure 14. Distribution of HF Mass Fraction; $\tau = 20$, $\zeta = 15$.

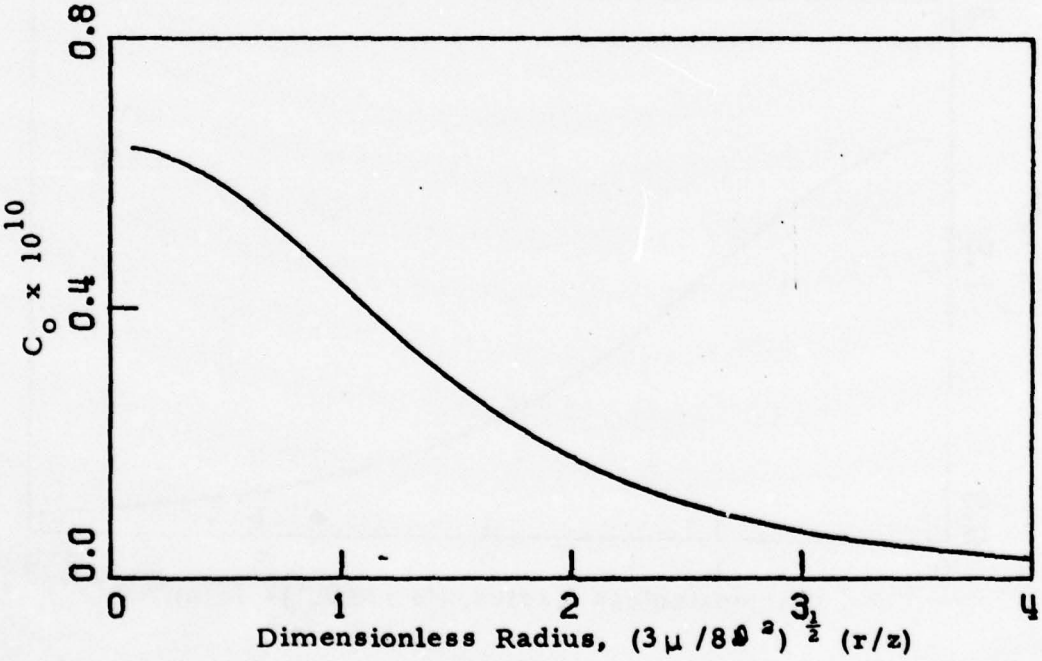

Figure 15. Distribution of HF Vibrational Levels;
$\tau = 20$, $\zeta = 15$.
a) Ground Level

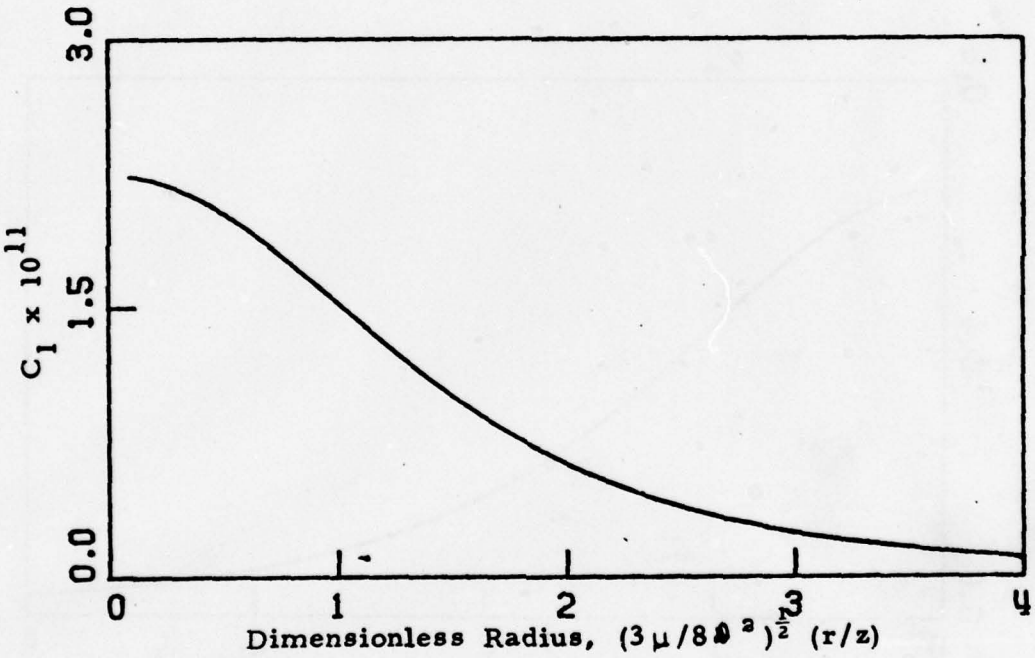

Figure 15. Distribution of HF Vibrational Levels; $\tau = 20$, $\zeta = 15$.
b) First Vibrational Level

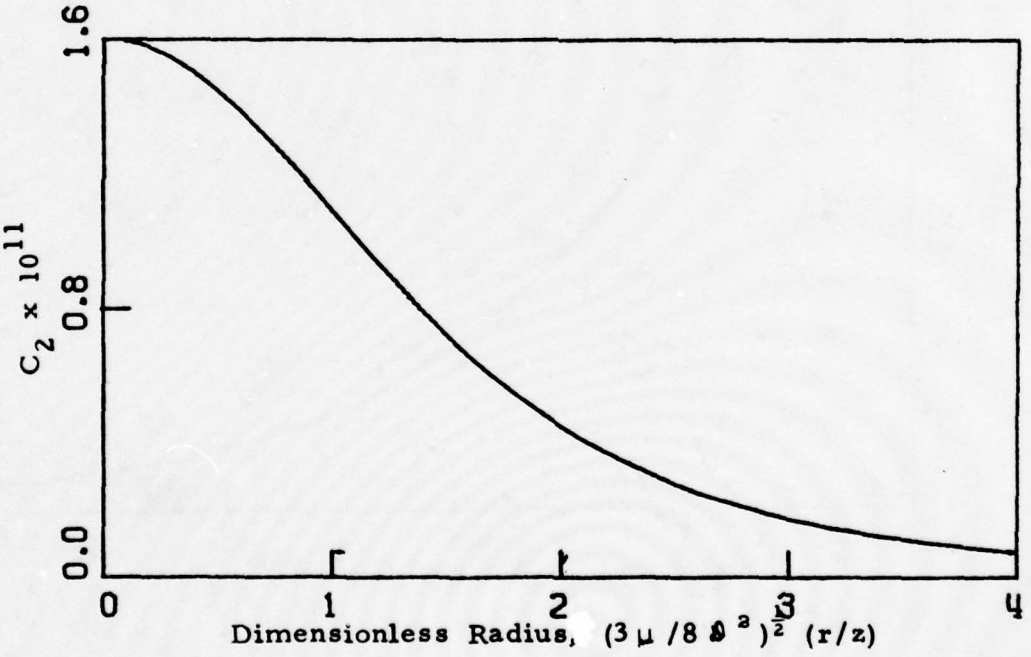

Figure 15. Distribution of HF Vibrational Levels; $\tau = 20$, $\zeta = 15$.
c) Second Vibrational Level

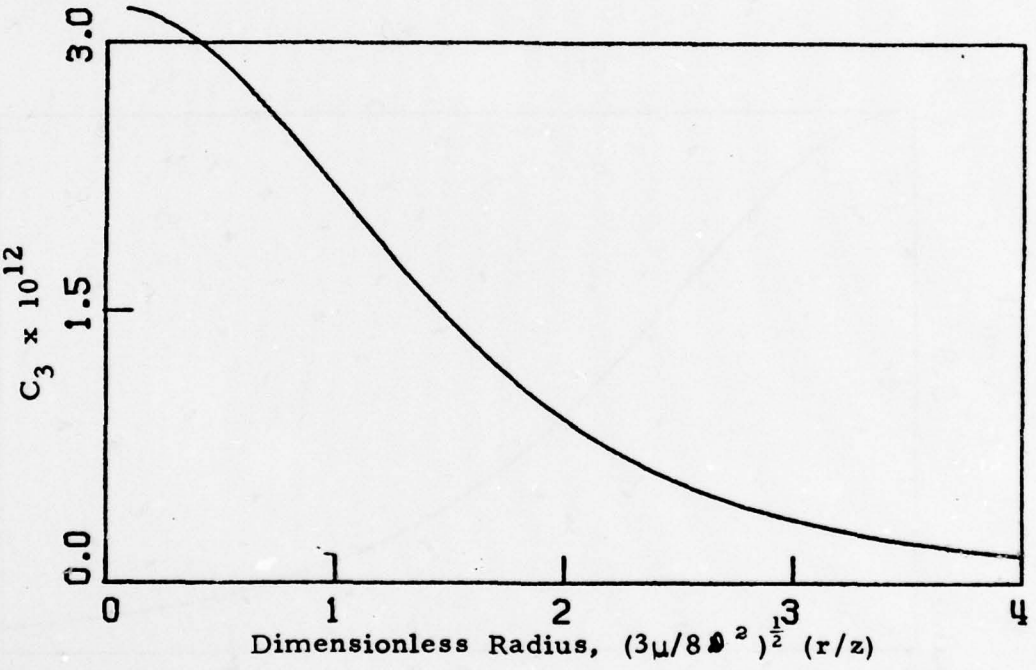

Figure 15. Distribution of HF Vibrational Levels; τ = 20, ζ = 15.
d) Third Vibrational Level

Presented at the Third International Workshop on
Laser Velocimetry, Purdue University, July 11-13, 1978

preprint

LASER DOPPLER VELOCITY MEASUREMENTS IN SUBSONIC, TRANSONIC AND SUPERSONIC TURBULENT BOUNDARY LAYERS

by

Paul E. Dimotakis,

Donald J. Collins,†

and

Daniel B. Lang

California Institute of Technology
Pasadena, California 91125

July 1978

---

†Jet Propulsion Laboratory

LASER DOPPLER VELOCITY MEASUREMENTS IN SUBSONIC, TRANSONIC AND SUPERSONIC TURBULENT BOUNDARY LAYERS

PAUL E. DIMOTAKIS[1], DONALD J. COLLINS[2] and DANIEL B. LANG[1]
[1]California Institute of Technology, Pasadena, California 91125
[2]Jet Propulsion Laboratory, Pasadena, California 91103

1. Introduction

Recent measurements by Johnson and Rose (1973, 1975), Yanta and Lee (1974, 1976), and Abbiss (1976) have used laser Doppler velocimetry techniques to make direct measurements of the Reynolds stress in turbulent boundary layers in the Mach number range of 1.5 to 3.0. A serious anomaly, however, is exhibited by these measurements in that the maximum of $-\overline{u'v'}$ occurs much further from the wall than is reasonable for flow at constant pressure. The anomaly has been discussed by Sandborn (1974), who supports the conjecture by some of the authors cited that density fluctuations may contribute substantially to the turbulent stresses near the wall. This conjecture is in direct opposition to the conclusion by Morkovin (1961) that effects of density fluctuations should be small compared to effects of variations in mean density for Mach numbers up to 4 or 5.

The purpose of the present experiments is to obtain redundant data over a substantial range of Mach numbers ($M = 0.1$ to 2.2), in an effort to resolve the anomaly in turbulent shearing stress. The flow was documented by conventional means using a Pitot tube, which was traversed through the boundary layer, to measure the mean flow. In addition, surface-friction measurements were made using both a floating-element balance and a Preston tube. The mean-flow scaling suggested by Van Driest was applied to the data, to test the adequacy of a single similarity formulation for both compressible and incompressible flow. The shearing stress was then computed from the mean flow as part of the analysis. These results were documented by Collins, Coles and Hicks (1978).

In the work presented here, the instrumentation, data acquisition and analysis for laser Doppler velocity measurements in the same flow are discussed. Measurements of u, v, $\overline{u'^2}$, $\overline{v'^2}$ and the Reynolds stress $\overline{u'v'}$ were made over the full Mach number range.

The low speed ($M \sim 0.1$) measurements were carried out in the GALCIT* Merrill wind tunnel. The high speed measurements ($0.6 \lesssim M \lesssim 2.2$) were conducted in the JPL† 20-inch wind tunnel.

The present paper is a preliminary report of a more extensive discussion of this work to appear by Dimotakis, Collins and Lang (1978).

2. High speed laser Doppler velocimetry

The first obvious problem that arises in making high speed laser

*Graduate Aeronautical Laboratories of the California Institute of Technology
†Jet Propulsion Laboratory

Doppler velocity measurements is that the resulting signal frequencies are very high. In principle, it would appear that this problem could be controlled by increasing the fringe spacing. In practice, however, conflicting requirements of a minimum number of Doppler cycles needed by the processing electronics, coupled with the spatial resolution considerations inescapably dictate the higher frequencies.

The restrictions on signal frequencies, above and beyond the problem of handling the high frequencies per se, arise for several reasons. The relative accuracy $\delta u/u$, with which the velocity of a single particle can be measured, is never less than the ratio of the processor clock period τ_c, to the total flight time Δt that is used for the measurement, i.e.

$$\delta u/u \gtrsim \tau_c/\Delta t \ . \tag{1}$$

In addition to these considerations which limit the accuracy even if the measurement environment was noise free, other factors become important at high velocities which decrease the signal-to-noise ratio of a single reading. As the flow velocities become higher, we are forced to use smaller particles to minimize problems of particle lag with rapidly decreasing scattering cross-sections and resulting signal intensities. In addition, as the velocity increases, the scattering particle spends less time in the focal volume. Even though the number of scattered photons per second remains constant (proportional to scattering cross-section), fewer total photons are collected by the detecting optics.

The extent to which the measurement of particle velocity represents the fluid velocity is, of course, a separate issue. Small particles can generally be expected to track the flow quite well if the (Lagrangian) frequency of fluctuations in the fluid velocity is less than the reciprocal of a characteristic particle response time τ_p. If the flow relative to the particle can be described by Stokes flow we have

$$\tau_p = (d_p^2/18)(\rho_p/\mu) = (d_p^2/18\nu)(\rho_p/\rho_f), \tag{2}$$

where d_p is the particle diameter, ρ_p and ρ_f are the particle and fluid densities, respectively, and μ is the (absolute) viscosity. It can be argued, and substantiated from direct spectral measurements (Klebanoff 1955, Perry and Abell 1975, 1977), that the expected fluctuation frequency in the interior of the boundary layer should be given by

$$\langle\omega\rangle \simeq \text{const}[U(y)/y], \tag{3}$$

where $U(y)$ is the local streamwise mean velocity and where the constant is of the order of unity. Consequently, the requirement for good particle tracking in a turbulent boundary layer becomes

$$\tau_p[U(y)/y] \lesssim 1 \ . \tag{4}$$

By way of example, using a dibutyl phthalate aerosol, a flow of $M \sim 1$ requires particles $\lesssim 1.5$ μm diameter to track the fluctuations at $y/\delta \gtrsim 0.1$. For a more detailed discussion, see Dimotakis, Collins and Lang (1978).

3. Scattering particles

The particle generator for the present experiments utilized a Laskin nozzle type construction to generate a polydisperse aerosol of dibutyl phthalate. Particles greater than 1 μm in diameter were effectively removed by an impact plate incorporated in the design. The resulting particle size

distribution, measured using both a cascade impactor and a multichannel particle analyzer, is shown in figure 1.

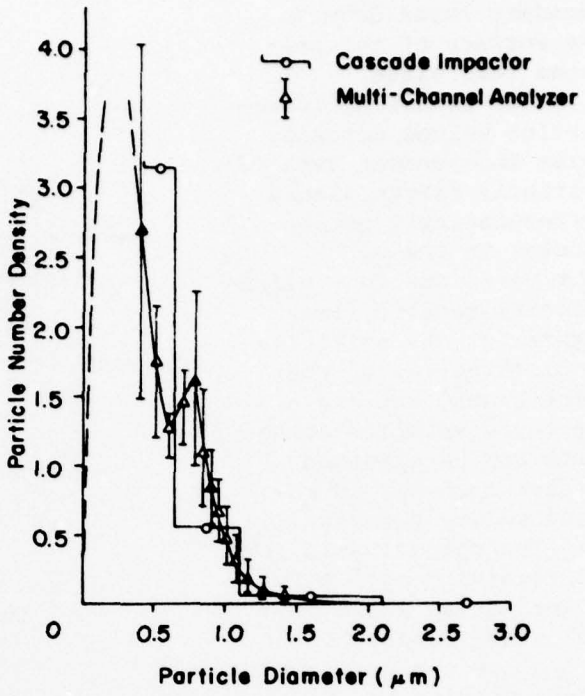

Fig. 1. Particle size distribution

Two different methods were used to introduce particles into the flow depending on the flow facility that was used. For the high speed measurements ($0.6 \leq M \leq 2.2$), which were conducted in the JPL 20" wind tunnel, it was necessary to seed the flow by introducing the particles into the settling chamber between the last turbulence screen and the contraction section. The particles were introduced through a tube which protruded 5 cm into the settling chamber. Holes were drilled into the tube along the stagnation line as well as the rear side at ±30° with respect to the flow vector.

For the low speed measurements in the Merrill wind tunnel ($M \simeq 0.1$), although some naturally occurring particles were present, the flow was seeded using the same aerosol generator in order to increase the data rate and to better control the scattering particle size distribution. For these measurements, the particles were injected through a tube spanning the test section located *downstream* of the boundary layer plate. The particles were convected around the wind tunnel circuit and over a period of a few minutes filled the whole tunnel. In practice, balancing the rate at which particles were introduced with the rate that they were lost, in order to keep the particle number density approximately constant in time, proved very difficult because the characteristic time lag was of the order of several tens of minutes. As a consequence, for the Merrill tunnel measurements the particle number density varied during the time required for the traverse through the boundary layer.

4. Optics and measurement geometry

The present experiments utilized the laser Doppler velocimeter in the single particle, dual (forward) scatter mode. For measurements in the JPL 20" wind tunnel, the instrument was mounted on a vibration isolated traversing mechanism on top of the wind tunnel test section, as depicted in figure 2. For measurements in the GALCIT Merrill wind tunnel, the traverse was suspended from the ceiling of the laboratory.

The light source for this instrument was a Coherent Radiation Model 52B, 4 watt Argon ion laser. The laser was operated single line at 0.5145 μm and etalon stabilized to provide a single mode beam. It was mounted on the tubular support structure for the optics as shown in figure 2.

The laser beam is directed into the transmitting optics cell where it is split into three parallel beams, of approximately equal intensity, which form a right isosceles triangle, whose base is nominally parallel to the wall. The three output beams are then focused in the center of the tunnel by a 1 m focal length lens, to a common intersection volume $\sim$ 0.8 mm in diameter. The optical axis intercepts the test plate from below at an angle of $\sim$ 1:100 in order to

permit measurement of the boundary layer down to the surface of the polished test plate.

The resulting intersection volume contains three independent sets of (virtual) fringe planes correspondingly perpendicular to the $\underline{u}$, $(\underline{u} + \underline{v})/\sqrt{2}$ and $(\underline{u} - \underline{v})/\sqrt{2}$ velocity vectors (see figure 3). By selectively blocking one of the three beams, any one of the three velocity components can be examined without a change in the focal volume geometry.

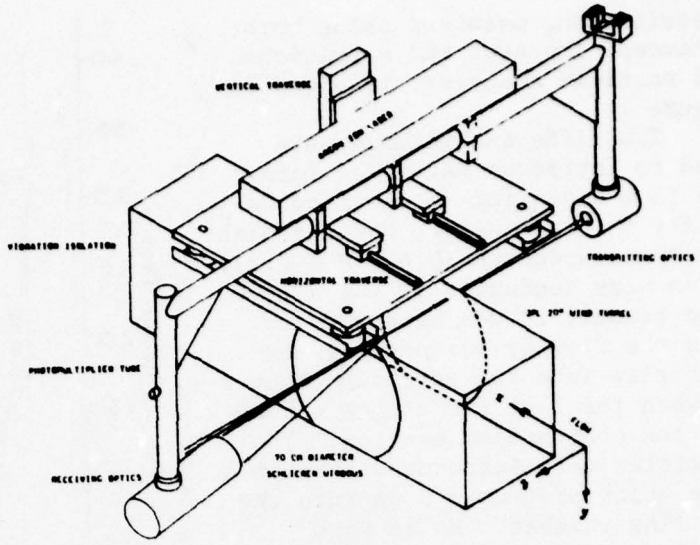

Fig. 2. Measurement assembly

The optical axis for the receiving optics is aligned at an angle of $\sim$ 7.5° with respect to the test plate surface. This allows viewing the focal volume down to the test plate surface and, recalling that the transmitting optics axis is in turn inclined with respect to the test plate, reducing the spanwise extent of the focal volume. The collected light cone is focused by a 1:1 imaging system into a 0.05 cm diameter pinhole which spatially filters the collected light accepted by the photomultiplier receiving optical assembly. The effective measurement volume diameter is defined by the pinhole in the receiving optics and therefore is equal to $\sim$ 0.05 cm.

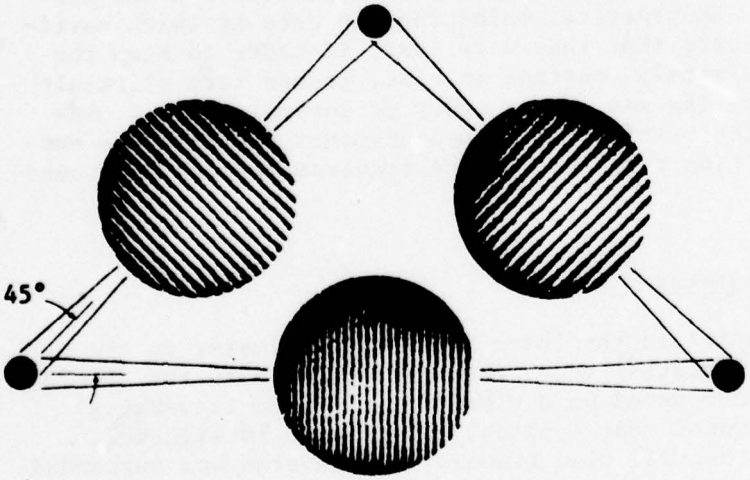

Fig. 3. Measurement fringes

5. Signal processing and data acquisition

The output of the photomultiplier was amplified by a direct coupled amplifier installed at the base of the photomultiplier housing. That output was in turn amplified by a low-noise, wide bandwidth, AC coupled preamplifier. The resulting signal was low-pass filtered to remove the substantial shot noise above the Doppler frequencies in each case. *Note that the pedestal, resulting from the dual scatter optics, is not removed by this processing scheme.*

The filtered signal is fed into a counter type processor (Dimotakis and Lang 1974, 1977, and Dimotakis, Collins and Lang 1978).

The processor uses a four level comparison scheme on every cycle of the Doppler burst. A TTL signal DIN is defined whose negative slope is driven by the crossing of the reference level V_o from above by the analog input (see figure 4a). DIN can be prescaled by m = 1,2,4,8 to yield DIN' which is used by the timing circuitry. DIN' is subsequently checked to ensure that every period is between two limits, τ_1 and $\tau_1 + \tau_2$. If τ was the period of the Doppler signal, we must have, as a consequence,

$$\tau_1 < m\tau < \tau_1 + \tau_2 \ . \qquad (5)$$

The time intervals τ_1 and τ_2 are front panel selectable and cover the range 60 nsec < τ_1, τ_2 < 3 msec. The processor updates the flight time register with the time between the first negative slope of DIN' and every successive acceptable negative slope of DIN' using a 100 MHz (τ_c = 10 ns) crystal. Every negative slope is also recorded in the cycle counter.

The data were recorded in two different modes. In the first mode (fixed fringe mode), the output corresponds to the (truncated) flight time for a fixed number of fringes. All the data for M ≥ 0.6 (JPL 20" wind tunnel) were recorded in this mode. Eight cycles were counted for the beam pair at 0° (u_1 data) with the prescaler m set to 2. Four cycles were counted for the ±45° (u_2, u_3 data) beam pairs with the prescaler set to unity.

In the second mode (free fringe mode), the processor only requires that a fixed number of cycles be *reached or exceeded by the burst* but records the flight time and number of cycles (fringes) *of the whole* burst. Both n and (the truncated) Δt were recorded in this mode and the velocity is

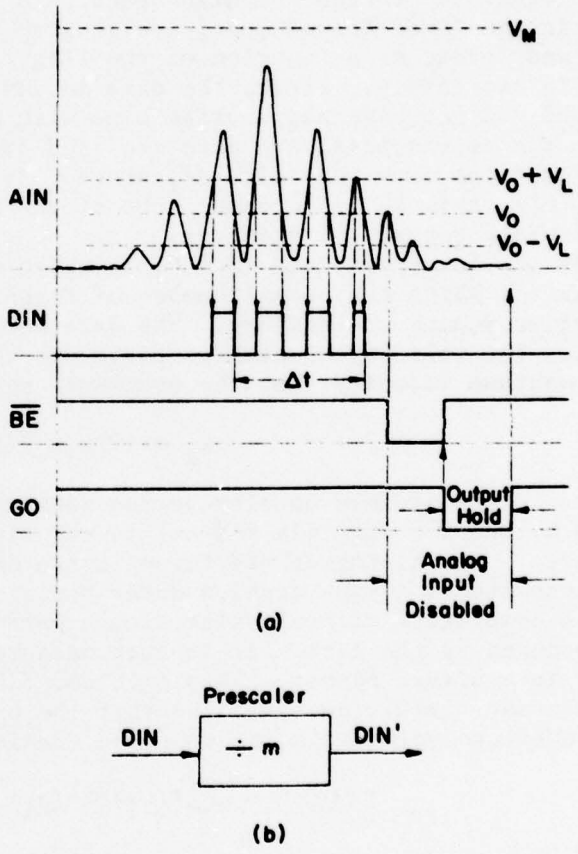

Fig. 4. Signal burst processing

$$u_1 = ns/\Delta t, \qquad (6)$$

where s is the fringe spacing. The data recorded at M ∿ 0.1 (GALCIT Merrill wind tunnel) were acquired in this mode requiring at least four fringes for the ±45° data (u_2, u_3) and at least eight for the 0° data (u_1) with the prescaler m set to 2. Thus, in both modes, the same (minimum) number of fringes had to be crossed.

There are several important differences between the two modes. First, using the facility of the processor to recognize the end of the burst while retaining the previous valid measurement, the total flight time can be used, instead of an arbitrary fraction, in determining the velocity component of in-

terest. This improves the measurement accuracy in an obvious way. Second, using the whole burst cancels the phase errors that are made in assigning equal phase to the crossings of the reference level V_o by the signal. Third, the sampling statistics are different between the two modes. In the first mode (fixed number of fringes), all we know is that the particle crossed *at least* that many. In the second mode (number of fringes unrestricted provided it exceeds a certain minimum) we know that the particle crossed *exactly* that many. That alters the sampling bias, as will be discussed later on.

The data were formatted into records of 1,024 particle measurements each and written on a Kennedy 9100 digital tape deck. Several records were recorded at each measurement location. Data rates up to 50 KHz were observed in the high speed flow.

6. Data processing

In order to process the high speed data ($0.6 \leq M \leq 2.2$), which were recorded in the fixed fringe mode, a histogram *of each record* (1,024 measurements) was formed as a function of the flight time Δt. The histograms were pruned in two passes. First, the data in any bin that contained only one count and did not have neighboring bins with more than one count were discarded. In the second pass, any data isolated from the main body of the histogram by at least one zero were also discarded. If, as a result of these two operations, more than 24 measurements out of the total of 1,024 had to be rejected, the whole record was rejected.

For the low speed data ($M \simeq 0.1$), which were recorded in the free fringe mode and for which the actual number of flight time clock counts was large, an alternative scheme was devised. The data were sorted in velocity bins as follows. The velocity of each particle was computed as an integer percentage of the maximum velocity that the processor settings admitted, i.e.

$$I_i = 100\tau_1 n_i/\Delta t_i, \tag{7}$$

where τ_1 is the minimum Doppler period setting, n_i is the number of fringes crossed by the i^{th} particle and Δt_i is the time of flight corresponding to the n_i fringes. The histogram was formed based on the velocity index I_i and each record was pruned in the fashion described above.

The complexity of processing single particle laser Doppler velocity data is compounded by the fact that in such measurements the fluid velocity is sampled in a biased manner. This problem, first pointed out by McLaughlin and Tiederman (1973), necessitates that the unbiased expectation value of any function of the velocity u, be computed consistently with this bias, i.e.

$$\langle f(\underline{u}) \rangle = \sum_i f(\underline{u}_i) B^{-1}(\underline{u}_i) \; / \sum_i B^{-1}(\underline{u}_i) \tag{8}$$

where $B(\underline{u})$ is proportional to the probability per unit time of making the particular measurement. The dependence of the sampling bias function B on the local velocity vector $\underline{u}$, as well as the shape of the measurement volume and the minimum number of fringe crossings required by the processing electronics, has been derived elsewhere (Dimotakis 1976). If the angle θ between the intersecting beams is small then, for the fixed fringe mode measurements, the expression for $B(\underline{u})$ simplifies to

$$B_{\text{fixed}}(\underline{u};\varepsilon) \simeq u_\perp (1 + u_\parallel^2/u_\perp^2)^{\frac{1}{2}} [1 - \varepsilon^2 (1 + u_\parallel^2/u_\perp^2)], \tag{9}$$

where $u_\perp$ is the velocity component perpendicular to the fringe planes, $u_\parallel$ is the velocity component parallel to the fringe planes and perpendicular to the

long axis of the measurement volume (beam bisector), and ε is the ratio n_{min}/n_T of the minimum number of fringe crossings (Doppler cycles) required by the processor to the total number (maximum) in the measurement volume. If $(u_\parallel/u_\perp)^2 \ll 1$ equation 9 reduces to the familiar form

$$B^{-1}_{fixed}(\underline{u}) \propto u_\perp^{-1} \propto (k + \tfrac{1}{2}), \tag{10}$$

where k is the (integer) output of the flight counter.

In the free fringe mode, the bias function is given by

$$B_{free}(\underline{u};n) \propto u_\perp^{-2}(u_\perp^2 + u_\parallel^2)^{3/2}(n + \tfrac{1}{2}), \tag{11}$$

or, equivalently,

$$B^{-1}_{free}(k;n) \propto (k + \tfrac{1}{2})n^2/(n + \tfrac{1}{2}). \tag{12}$$

See Dimotakis (1976) and Dimotakis, Collins and Lang (1978) for derivations and a more extensive discussion. Note that equation 12 is in disagreement with the predictions of Hoesel and Rodi (1977) who suggest that $B^{-1}_{free} \propto \Delta t \propto (k + \tfrac{1}{2})$.

7. Results and discussion

The mean streamwise velocity profiles are compared to the corresponding Pitot tube measurements in figures 5 and 6. The agreement can be seen to be quite good. The momentum thickness θ for the profiles was computed from the laser Doppler measurements. In figure 5 four profiles in the Mach number range $0.6 \leq M \leq 2.2$ are plotted as indicated. The agreement for the lower speed

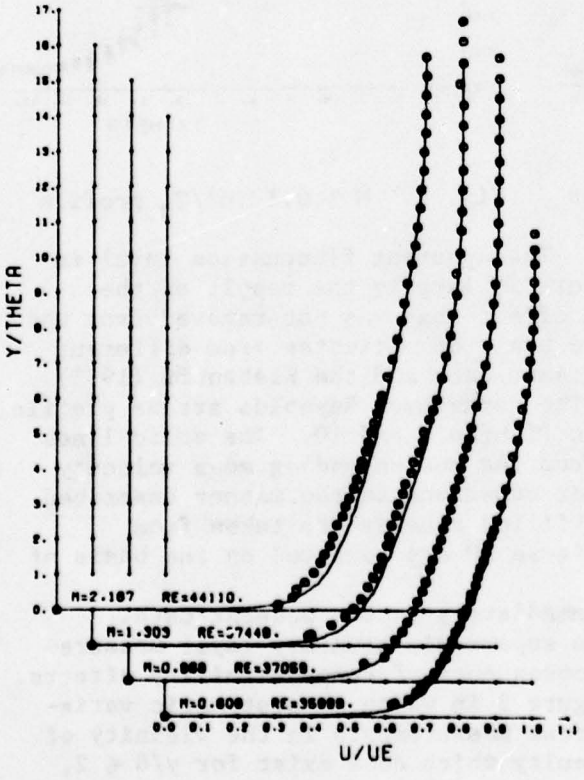

Fig. 5. $0.6 \leq M \leq 2.2$ velocity profiles

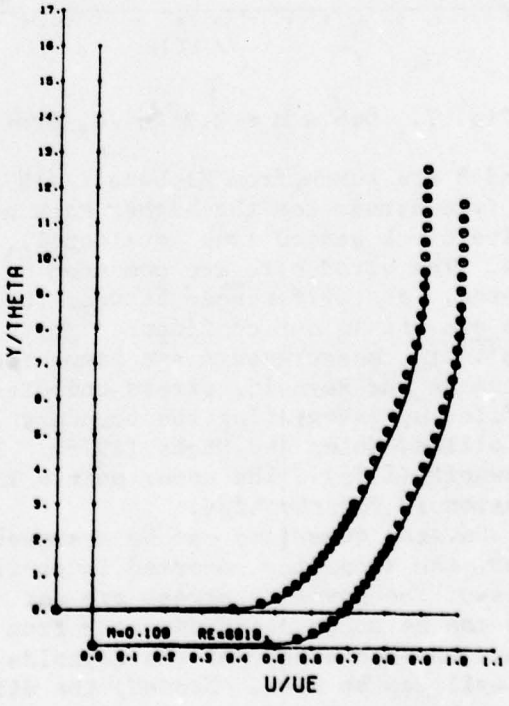

Fig. 6. $M \sim 0.1$ velocity profile

profiles is very good. We do not have an explanation for the small discrepancies that can be seen in the higher Mach number profiles. The top data points in figure 6 correspond to a computation of the mean velocities using the harmonic mean (bias function of equation 10), the bottom points correspond to the more exact bias compensation of equation 12. The differences are small as are also the differences between these and mean values computed with no compensation for the bias (not plotted). In figures 7 and 8 the root mean square fluctuations, normalized by the edge velocity, are plotted for the same flow. The upper set of points in figure 8 are computed using equation 10 for the bias. Again the differences between the two are small. The filled squares in figures

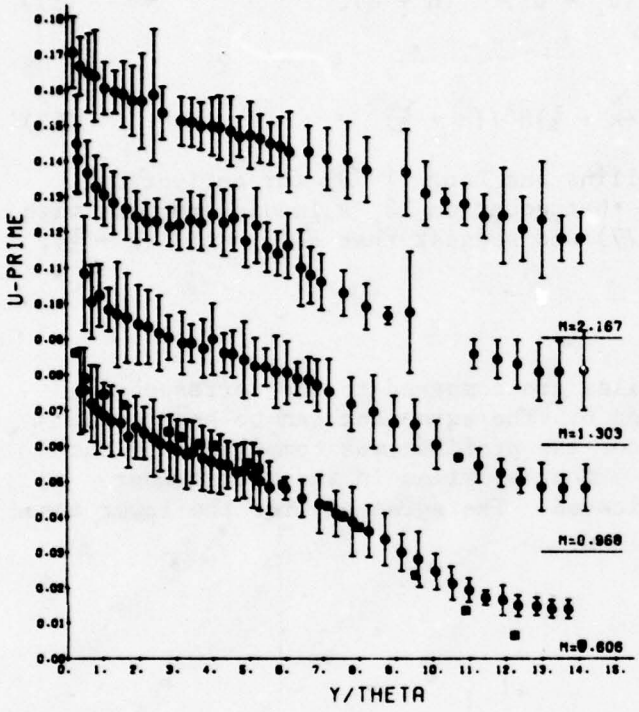

Fig. 7. $0.6 \leq M \leq 2.2$ u'/U_e profiles

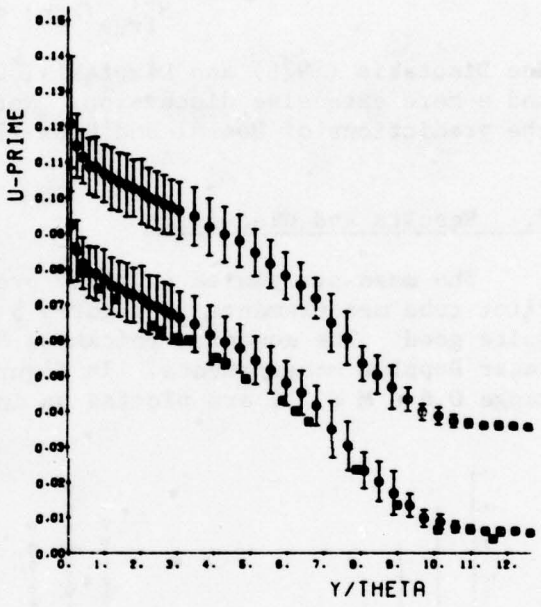

Fig. 8. $M \sim 0.1$ u'/U_e profile

7 and 8 are taken from Klebanoff (1955). The apparent fluctuation level in the free stream for the higher Mach numbers is largely the result of the finite clock period (see equation 1), an effect that was not removed from the data. The error bars are computed on the basis of estimates from different records. The differences between the present data and the Klebanoff (1955) data are within our confidence limits. The normalized Reynolds stress profile, $-\rho_w \overline{u'v'}/\tau_w$, measurements are presented in figures 9 and 10. The solid lines represent the Reynolds stress computed from the corresponding mean velocity profiles by integrating the boundary layer equations in the manner described in Collins, Coles and Hicks (1978). The filled squares are taken from Klebanoff (1955). The upper points in figure 10 are computed on the basis of equation 10 for the bias.

Several questions can be answered immediately by the present data. *First,* the anomalies reported in previous supersonic boundary layer measurements of the Reynolds stress are not a consequence of compressibility effects. This can be ascertained directly from figure 9 in which no systematic variation with Mach number of the Reynolds stress measurements in the vicinity of the wall can be seen. *Second,* the difficulty which does exist for $y/\theta \leq 2$, cannot be associated with local particle lag, in the context of equation 4,

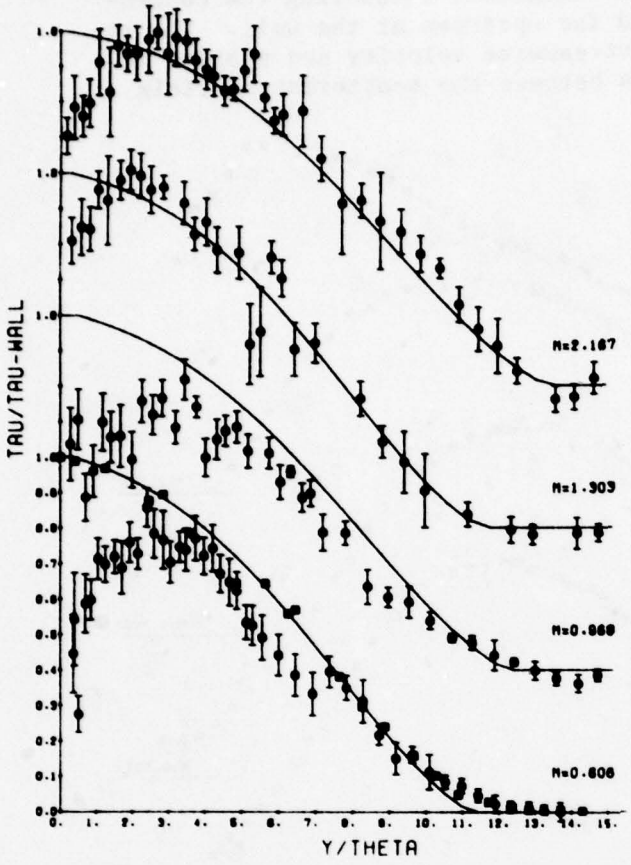

Fig. 9. $0.6 \lesssim M \lesssim 2.2$ $-\overline{u'v'}$ profiles

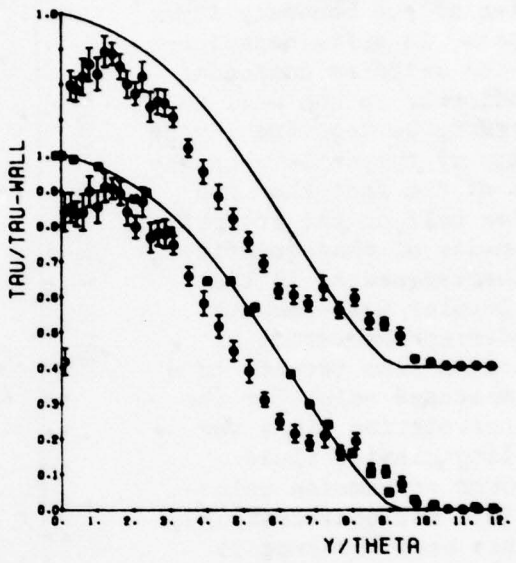

Fig. 10. $M \sim 0.1$ $-\overline{u'v'}$ profile

since the deviation from the expected behavior would have occurred at increasing distances from the wall as the Mach number increased (the boundary layer thickness was roughly 2.5 cm for all the measured profiles). *Third,* the previously reported anomalies cannot be attributed to the sampling bias. The differences between the correctly computed Reynolds stress data (lower data points of figure 10) and the simpler compensation by means of equation 10 are small, even though the bias function of equation 12 yields results that are closer to the expected values.

Except for the $M \sim 0.1$ stress measurements, the agreement between the computed stress profiles and the directly measured values is quite good, for $y/\theta \gtrsim 2$. The discrepancy near the wall, however, remains an open question as of this writing. The problem, we feel, is related to the behavior of the stress producing flow in the neighborhood of the wall. It is a common observation that the walls of the tunnel become coated with a thin film of the aerosol used for seeding. This indicates that the flow inside the viscous sublayer is such that a particle that enters the sublayer has a very low probability of leaving. The scaling law for particle behavior in a turbulent boundary layer, as expressed by equation 4, is not applicable in the viscous sublayer. A particle entering the viscous sublayer becomes caught in the motion of the longitudinal vortices, whose transverse extent is approximately $20\ \nu/u_\tau$, and ends up on the wall. Consequently, a fluid element coming *from* the wall is less likely to carry particles than a fluid element moving *towards* the wall. This causes several problems that show up in different measurements.

The scattering particle number density profile for the JPL data ($0.6 \leq M \leq 2.2$) should look approximately like a half Gaussian, resembling the concentration of a passive contaminant introduced far upstream at the wall. The recorded data rate was divided by the local streamwise velocity and plotted in figure 11. To the extent that correlations between the scattering particle number density fluctuations and the *streamwise* velocity can be neglected, the ratio is proportional to the local particle number density. The decrease as the wall is approached, extending to a large fraction of the boundary layer thickness, is quite conspicuous. The velocity component perpendicular to the wall is measured to be *negative* in the vicinity of the wall, a consequence of the fact that the positive half of the probability density of that quantity is underrepresented in the laser Doppler measurements. The underrepresentation of that motion also results in a lower measured value for the $-\overline{u'v'}$ correlation since the *upswelling* carries fluid with *lower* streamwise velocity. This motion (bursting), which has been observed to be intermittent and quite violent, is held responsible for a very large fraction of the total stress near the wall (Blackwelder and Kaplan 1976).

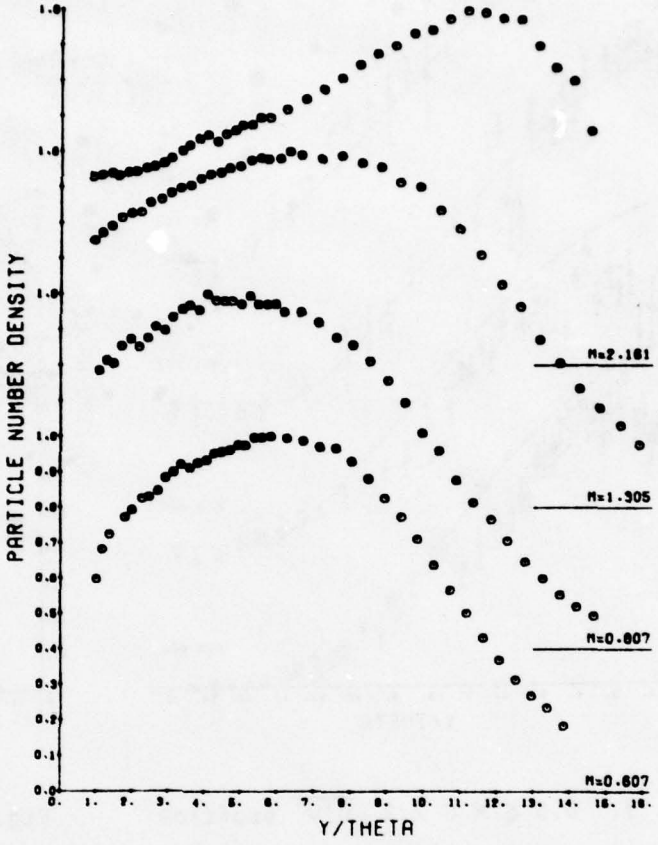

Fig. 11. Particle number density profiles

It appears that the particle transport to the wall via the viscous layer is so effective, even at the lower velocities, as to make the wall look like an infinite sink for particles. *The conclusion is then that the discrepancy in the measured Reynolds stress near the wall arises because the scattering particle number density is very strongly correlated with the instantaneous stress and not as a result of any local failure of the particles to track the flow.*

8. Acknowledgements

We are indebted to Professor Donald Coles of the California Institute of Technology for his assistance in this project. We would also like to acknowledge the early participation of Professor Steven Barker, presently at UCLA, who contributed substantially to the final optics design.

This paper presents the results of one phase of research carried out at the Jet Propulsion Laboratory under Contract NAS 7-100 and at the Merrill Wind Tunnel of the California Institute of Technology. The work was supported by the United States Air Force, Office of Scientific Research, under contracts F44620-75-C-0007 and F44620-76-C-0046; by the Arnold Engineering Development Center, under contracts EY 7483-76-0003 and EY 7483-76-0009; and by the

California Institute of Technology, President's Fund, under Grant PF-075.

9. References

ABBISS, J. B. (1976) *Development of photon correlation anemometry for application to supersonic flow.* AGARD CP-193, Applications of Non-Intrusive Instrumentation in Fluid Flow Research, 11.1 - 11.11.

BLACKWELDER, R. F. and KAPLAN, R. E. (1976) *On the wall structure of the turbulent boundary layer.* J. Fluid Mech. 76, 89-112.

COLLINS, D. J., COLES, D. E. and HICKS, J. W. (1978) *Measurements in the turbulent boundary layer at constant pressure in subsonic and supersonic flow. Part I. Mean flow.* AEDC-TR-78-21.

DIMOTAKIS, P. E. (1976) *Single scattering particle laser-Doppler measurements of turbulence.* AGARD CP-193, Applications of Non-Intrusive Instrumentation in Fluid Flow Research, 10.1 - 10.14.

DIMOTAKIS, P. E., COLLINS, D. J. and LANG, D. B. (1978) *Measurements in the turbulent boundary layer at constant pressure in subsonic and supersonic flow. Part II. Laser Doppler velocity measurements.* To appear as an AEDC report.

DIMOTAKIS, P. E. and LANG, D. B. (1974) *Single scattering particle laser Doppler velocimetry.* Bull. Am. Phys. Soc. (II) 19, 1145.

DIMOTAKIS, P. E. and LANG, D. B. (1977) *Signal responsive burst period timer and counter for laser Doppler velocimetry and the like.* U.S. Patent 4,051,433 (September 27, 1977).

HOESEL, W. and RODI, W. (1977) *New biasing elimination method for laser-Doppler velocimeter counter processing.* Rev. Sci. Instrum. 48(7), 910-919.

JOHNSON, D. A. and ROSE, W. C. (1973) *Measurement of turbulence transport properties in a supersonic boundary-layer flow using laser velocimeter and hot-wire anemometer techniques.* AIAA Paper 73-1045.

JOHNSON, D. A. and ROSE, W. C. (1975) *Laser velocimeter and hot wire anemometer comparison in a supersonic boundary layer.* AIAA J. 13(4), 512-515.

KLEBANOFF, P. S. (1955) *Characteristics of turbulence in a boundary layer with zero pressure gradient.* NACA Report 1247.

MCLAUGHLIN, D. K. and TIEDERMAN, W. G. (1973) *Biasing correction for individual realization of laser anemometer measurements in turbulent flows.* Phys. Fluids 16, 2082-2088.

MORKOVIN, M. V. (1961) *Effects of compressibility on turbulent flows.* Proc. Colloq. Mechanique de la Turbulence, CNRS (1962), 367-380. (Proc. reprinted as Mechanics of Turbulence, Gordon & Breach 1964).

PERRY, A. E. and ABELL, C. J. (1975) *Scaling laws for pipe flow turbulence.* J. Fluid Mech. 67, 257-271.

PERRY, A. E. and ABELL, C. J. (1977) *Asymptotic similarity of turbulence structures in smooth- and rough-walled pipes.* J. Fluid Mech. 79(4), 785-799.

SANDBORN, V. A. (1974) *A review of turbulence measurements in compressible flow.* NASA TM X-62, 337.

YANTA, W. J. and LEE, R. E. (1974) *Determination of turbulence transport properties with laser Doppler velocimeter and conventional time-averaged mean flow measurements at Mach 3.* AIAA Paper 74-575.

YANTA, W. J. and LEE, R. E. (1976) *Measurements of Mach 3 turbulence transport properties on a nozzle wall.* AIAA J. 14(6), 725-729.

Appendix E

MEASUREMENTS IN THE TURBULENT BOUNDARY LAYER AT CONSTANT PRESSURE IN SUBSONIC AND SUPERSONIC FLOW

Part II. Laser-Doppler Velocity Measurements

Paul E. Dimotakis, Donald J. Collins, and Daniel B. Lang

Jet Propulsion Laboratory
California Institute of Technology
Pasadena, California 91103

March 1979

Summary

Experiments have been carried out using laser-Doppler velocimetry in conjunction with Pitot and surface-friction instrumentation for the measurement of the mean flow, the velocity fluctuations, and the Reynolds stresses in turbulent boundary layers at constant pressure in subsonic and supersonic flows. Two facilities were used for these studies. In one facility, data were obtained on a flat plate at $M_e = 0.1$, with $Re_\theta = 6600$. In the other, data were obtained on an adiabatic nozzle wall at $M_e = 0.6$, 0.8, 1.0, 1.3, 2.2 with $Re_\theta = 23{,}000$ and 40,000.

Part I of this report is a detailed analysis of the mean flow as observed using Pitot-tube, Preston-tube, and floating-element balance instrumentation. The emphasis in Part I is on the use of similarity laws with Van Driest scaling and on the inference of the distribution of shearing stress and of the normal velocity component from the equations of mean motion. These data serve as a background for the analysis of the laser-Doppler data reported herein.

The present Part II of this report is a description of both the mean and the fluctuating components of the flow, and of the Reynolds stress as observed using a dual forward-scattering laser-Doppler velocimeter. A detailed description of the instrument, and of the data analysis techniques, have been included in order to fully document the data. A detailed comparison is made between the laser-Doppler results and those presented in Part I, and an assessment is made of the ability of the laser-Doppler velocimeter to measure the details of the flows involved.

Preface

This report represents the results of one phase of research carried out at the Jet Propulsion Laboratory of the California Institute of Technology, under Contract NAS 7-100. The work described in this report was supported by the United States Air Force, Office of Scientific Research, under Contracts F 44620-75-C-0007 and F 44620-76-C-0046; by the Arnold Engineering Development Center, under MIPR EY 7483-76-0003 and EY 7483-76-0009, Program Element No. 65807F; and by the California Institute of Technology, President's Fund, under Grant PF-075.

The authors are indebted to Professor Donald Coles for his continued assistance in this project and to Dr. Steven Barker, whose early participation contributed substantially to the final optics design. We would also like to acknowledge the assistance of Mr. George Tennant in assembling the optical system, and of Mr. Harold Holway and the crew of the J.P.L. 20-inch wind tunnel for their assistance in what may have been the final test to be conducted in that facility.

Contents

Part II. Laser-Doppler Velocity Measurements

Contents (Cont.)

I. Introduction

The turbulent boundary layer at constant pressure has been the subject of experimental and theoretical investigations for many years, and provides a well documented flow for the assessment of experimental techniques. These investigations have shown that for the incompressible turbulent boundary layer, the turbulent shearing stress can be measured directly or can be calculated from the distribution of mean velocity with the aid of well-established similarity laws. For compressible flows, however, measurements of the Reynolds stresses are rare, and interpretation of the results is difficult. Recent measurements by Johnson and Rose (1973), Yanta and Lee (1974), and by Abbiss (1976) have used laser-Doppler velocimetry techniques to make direct measurements of the Reynolds stress in turbulent boundary layers with free-stream Mach numbers in the range 1.5 to 3.0. However, a serious anomaly is exhibited by these measurements in that the maximum value of $-\rho\overline{u'v'}$ occurs much further from the wall than is reasonable for flow at constant pressure. This anomaly has been discussed by Sandborn (1974), who supports the conjecture by some of the authors cited that density fluctuations may contribute substantially to the turbulent stresses near the wall. This conjecture is in direct opposition to the conclusion by Morkovin (1961) that effects of density fluctuations should be small compared to effects of variations in mean density for Mach numbers up to 4 or 5.

The purpose of the present experiments is to obtain redundant data over a substantial range of Mach numbers (M_e = 0.1 to 2.2), in an effort to resolve the anomaly in turbulent shearing stress. The low-speed experiments were performed in the boundary layer on a flat plate model in the GALCIT* Merrill

*Graduate Aeronautical Laboratories of the California Institute of Technology.

wind tunnel at a free-stream Mach number $M_e \approx 0.1$. The high-speed experiments were performed in the ceiling boundary layer of the J.P.L.† 20-inch wind tunnel at Mach numbers $0.6 \leq M_e \leq 2.2$.

The flow was documented by conventional means using a Pitot tube, which was traversed through the boundary layer, to measure the mean flow. In addition, surface-friction measurements were made using both a floating-element balance and a Preston tube. The mean-flow scaling suggested by Van Driest (1955) was applied to the data, to test the adequacy of a single similarity formulation for both compressible and incompressible flow. The shearing stress was computed from the mean flow as part of the analysis. The details of these experiments have been discussed in Part I of this report by Collins, Coles and Hicks (1978).

In the present report, the instrumentation, data acquisition and analysis for laser-Doppler velocity measurements in the same flows are described. Measurements of $\bar{u}$, $\bar{v}$, $\overline{u'^2}$, $\overline{v'^2}$ and the Reynolds stress $-\rho\overline{u'v'}$ were made over the full Mach number range. These measurements are discussed and compared to the results for the mean flow presented in Part I of this work.

II. Measurement Considerations at High Speeds

The use of laser-Doppler velocimetry techniques in high-speed flows unavoidably results in very high frequency signals. Figure 1 is a plot of the Doppler frequency

$$\nu_D = \frac{2 \sin\theta/2}{\lambda} u_\perp , \qquad (1)$$

†Jet Propulsion Laboratory

as a function of the flow velocity $u_\perp$ with the beam separation angle θ as a parameter. For these computations, the wavelength has been assumed to be $\lambda = 0.5145$ μm, corresponding to an argon-ion laser.

A reduction in the beam separation angle θ, in order to achieve a reduction in the signal frequency, results in a reduction in the number of fringes within the measurement ellipsoid, and a consequent reduction in the measurement accuracy. The interesting beam pair produces a set of virtual fringes whose spacing is given by

$$s = \frac{\lambda}{2 \sin\theta/2} \quad . \tag{2}$$

Because the (TEM_{oo}) Gaussian beam radius at the focus is given by

$$w_o = \frac{\lambda R}{\pi w} \quad , \tag{3}$$

where R is the beam wavefront radius of curvature after the focusing lens ($R \sim f$ = lens focal length), and w is the $1/e^2$ intensity envelope radius at the focusing lens, the resulting number of fringes is then given by (e.g., Dimotakis (1976))

$$N_f = 4 \frac{w_o}{\lambda} \tan\theta/2 \quad . \tag{4}$$

The number of fringes, N_f, is plotted in Figure 2 as a function of the focal volume diameter $2 w_o$ with the angle θ as a parameter for a wavelength $\lambda = 0.5145$ μm. As can be seen from Figure 2, spatial resolution considerations place a lower bound on the angle θ, presenting a criterion which

conflicts with the requirement to keep the resulting Doppler frequencies small.

Other difficulties arise if the Doppler frequencies are permitted to be large. In addition to the problems of handling high frequencies per se, the relative accuracy $\delta u/u$ with which the velocity of a single particle can be measured is never less than the ratio of the processor clock period, τ_c, to the total flight time Δt that is used for the measurement, i.e.,

$$\frac{\delta u}{u} > \frac{\tau_c}{\Delta t} \quad . \tag{5}$$

By way of example, a processor with a clock frequency of 100 MHz ($\tau_c = 10^{-8}$ sec) can measure the velocity of a Mach ~ 2 particle in air ($u_\perp \sim 530$ m/sec) in a 800 μm diameter focal volume to about $\sim 0.7\%$.

In addition to these considerations, which would limit the accuracy even if the measurement environment was noise free, other factors become important at high velocities by decreasing the signal-to-noise ratio of a single reading. As the flow velocities become higher, smaller particles are required to minimize problems of particle lag. This results in rapidly decreasing scattering cross-sections (Born and Wolf (1975)) and consequent signal intensities. In addition, as the velocity increases, the scattering particle spends less time in the focal volume. As a result, even though the number of scattered photons per second remains constant, proportional to the scattering cross-section, fewer total photons are collected by the detecting optics. An equivalent way of analyzing this problem is to consider the noise bandwidth that must be utilized as the velocities, and resulting

Doppler frequencies, increase. For a shot-noise limited detection process, the noise power increases proportionally to the bandwidth that is accepted by the processing electronics. Consequently, using the same particles, the signal-to-noise ratio will decrease as the velocity increases.

III. Scattering Particles

A. Particle Lag

The extent to which the measurement of particle velocity represents the fluid velocity is, of course, a separate issue. If the Lagrangian fluctuation frequencies in the fluid are small compared to the reciprocal of a characteristic particle response time, τ_p, the particles are expected to follow those fluctuations.

For small solid particles in gas flows, the equation of motion in a Lagrangian frame can be approximated by

$$\frac{d}{dt} u_p + \frac{1}{\tau_p} u_p = \frac{1}{\tau_p} u_f \quad . \tag{6}$$

If the particle Reynolds number

$$Re_p \equiv \frac{|u_p - u_f|}{\nu} d_p \quad , \tag{7}$$

is small, and the flow can be described by the continuum equations, we have the classical Stokes flow for a spherical particle for which the drag coefficient is $C_D = 24/Re_p$. The particle response time is then given by

$$\tau_p = \frac{d_p^2}{18} \left(\frac{\rho_p}{\mu}\right) = \frac{d_p^2}{18\nu} \left(\frac{\rho_p}{\rho_f}\right) \quad , \tag{8}$$

which is independent of the fluid density. A plot of the particle response time as a function of the particle diameter is given in Figure 3 for dibutyl phthalate aerosol particles in air.

In order to estimate the fluctuation frequencies to which a particle will be subjected, it is useful to examine the Eulerian fluid motions in the turbulent boundary layer. From the measurements of Klebanoff (1954) in a boundary layer at constant pressure, and from the measurements of Perry and Abell (1975; 1977) in pipes, the behavior of the Eulerian velocity fluctuation spectrum can be inferred. These results give spectra which can be described by

$$\frac{S_{uu}(\omega,y)}{\overline{u'^2}(y)} \simeq \frac{\pi\delta}{u(y)} f_o\left[\frac{\omega\delta}{u(y)}\right] , \tag{9}$$

for the wake region, and

$$\frac{S_{uu}(\omega,y)}{\overline{u'^2}(y)} = \frac{\pi y}{u(y)} f_1\left[\frac{\omega y}{u(y)}\right] , \tag{10}$$

in the inner portion of the boundary layer, but outside the sublayer. These spectra then result in expected frequencies given by

$$\langle\omega\rangle_\delta = \text{const.} \frac{u(y)}{\delta} , \tag{11}$$

in the wake region, and

$$\langle\omega\rangle_y = \text{const.} \frac{u(y)}{y} , \tag{12}$$

in the boundary layer interior. Consequently, particles above the sublayer should track the flow well, provided that

$$\frac{\tau_p u(y)}{y} \lesssim 1 \quad , \tag{13}$$

or

$$\frac{\tau_p a_e}{\delta} \lesssim \frac{1}{M_e} \left[\frac{y/\delta}{u(y)/u_e}\right] . \tag{14}$$

Substituting Equation (8) for τ_p, we obtain an upper bound on the particle diameter for the particles to track the flow,

$$d_p < d_{p_{max}} \approx \frac{4.83}{M_e^{\frac{1}{2}}} \mu m \quad , \tag{15}$$

for di-butyl phthalate aerosol in air at 25°C.

A prediction of Equation (12) is that the turbulent wavenumbers $k \sim \omega/u$ increase as the wall is approached,

$$k \sim \frac{const.}{y} \quad . \tag{16}$$

This result is confirmed qualitatively by the photograph in Figure 4 in which the turbulent boundary layer on the surface of a water channel has been made visible using a thick suspension of aluminum flakes which preferentially align with the local strain field. The photograph was taken in the GALCIT low-speed water channel by Brian Cantwell and is reproduced here with his permission. The Reynolds number for this photograph, based on x,

was 10^6. The monotonic decrease in scale size as the wall is approached is quite evident. These observations, and the results of Equation (12) are consistent with the usual mixing-length hypotheses made for the outer layer by Prandtl (1942), and are consistent with the hypothesis for the region closer to the wall, but outside the viscous layer by von Kármán (1930).

In the interior of the boundary layer, the quantity in the brackets in Equation (14) is bounded by the relation

$$\frac{y/\delta}{u(y)/u_e} > \frac{u_e/u_\tau}{\delta u_\tau/\nu_w} \equiv \frac{u_e^+}{\delta^+} , \tag{17}$$

where u_τ is the friction velocity defined as

$$u_\tau \equiv (\tau_w/\rho_w)^{\frac{1}{2}} . \tag{18}$$

The ratio u_e^+/δ^+ has been shown by Coles (1968) to be a function of Re_θ for incompressible flows with zero pressure gradient. The square root of this quantity is plotted in Figure 5, for the range of Re_θ covered by the present measurements ($8 \times 10^3 < Re_\theta < 4 \times 10^4$). The data for this figure are taken from Table 4 of Collins, Coles and Hicks (1978). These data are compared in Figure 5 to a straight line fit given by the emperical relation

$$\sqrt{u_e^+/\delta^+} \simeq f(Re_\theta) = 5.01\ Re_\theta^{-0.435} . \tag{19}$$

In writing the lower bound in Equation (17), effects of compressibility have been ignored. Using the numerical result of Equations (15) and (19), we then have

$$d_p < d_{p_{max}} \simeq \begin{cases} \dfrac{4.83}{M_e^{\frac{1}{2}}} \left(\dfrac{y}{\delta}\right)^{\frac{1}{2}} (\mu m) & ; \quad \text{far from the sublayer} \\ \dfrac{24.2}{M_e^{\frac{1}{2}} Re_\theta^{0.435}} & ; \quad \text{near but outside the sublayer .} \end{cases} \tag{20}$$

By way of example, a flow of $M_e \sim 1$ requires particles less than 1.5 μm in diameter to track the fluctuations at $y/\delta \sim 0.1$.

B. Techniques for Seeding the Flow

The particle generator for the present experiments used a Laskin nozzle type construction to generate a poly-dispersed aerosol of di-butyl phthalate. Particles greater than 1 μm in diameter were effectively removed by an impact plate incorporated in the design. The resulting particle size distribution, measured using both a cascade impactor and a multi-channel particle analyzer, is shown in Figure 6. These results indicate little contribution to the number density for sizes greater than 1 μm. While little is known about the distribution below 0.4 μm, it was possible to ascertain that no particles with a diameter less than 0.1 μm were present.

Two different methods were used to introduce particles into the flow depending on the flow facility that was used. For the high-speed measurements ($0.6 \lesssim M_e \lesssim 2.2$), which were conducted in the JPL 20-inch wind tunnel, it was necessary to seed the flow by introducing the particles into the settling chamber between the last turbulence screen and the contraction section. The particles were introduced through a tube which protruded 5 cm vertically into the settling chamber from above. Holes were drilled into the tube along

the stagnation line as well as the rear side at $\pm 30^{o}$ with respect to the flow vector. Using this technique, data rates in excess of 50,000 samples per second were achieved. Preston-tube measurements obtained with and without particles indicate no detectable influence of the introduction of particles on the surface friction and therefore, probably, on the mean flow.

For the low-speed measurements in the Merrill wind tunnel ($M_e \sim 0.1$), although some naturally occurring particles were present, the flow was seeded using the same aerosol generator in order to increase the data rate and to control the scattering particle size distribution. For these measurements the particles were injected through a tube spanning the test section located downstream of the boundary-layer plate, providing a uniform distribution of particles throughout the test section. In practice, the adjustment of the rate at which particles were introduced proved difficult because the characteristic time was of the order of several minutes for equilibrium with particle losses. As a consequence, the particle number density changed during the time required for a traverse through the boundary layer. Using this seeding technique, data rates in excess of 2,000 samples/sec were achieved at low speeds.

C. The Distribution of Particles

The particle number density was measured by counting the average frequency of occurrence of valid data from the processing electronics. These data are a measure of the mean particle flux $\langle nu \rangle$. Assuming that correlations between the scattering particle number density and the streamwise velocity are small, then

$$\langle n \rangle = \frac{\langle nu \rangle}{\langle u \rangle} , \qquad (21)$$

gives the mean value of the particle number density.

It is an unfortunate consequence of this measurement technique that the measured value of the particle flux $\langle nu \rangle$ decreases with the signal-to-noise ratio of the experiment. The most common cause of a decrease in the signal-to-noise ratio in the high-speed flow experiments has been attributed to the random occurrence of oil filaments on the windows through which the observations were made. Imperfections in the lucite windows in the Merrill wind tunnel had a similar effect on the measured particle flux. In addition, a more serious problem arose in the low-speed measurements, where the particle flux was a slowly-varying function of time.

The resulting distribution of particle number density through the boundary layer is shown in Figures 7, 8 and 9, in which the particle number density has been normalized by the local fluid density in order to account for the effects of compressibility. These data are further normalized by their maximum value in the boundary layer to eliminate the effects of differing injection rates.

The loss mechanisms of the scattering particles from the boundary layer are important in understanding the resulting laser-Doppler observations. For the high-speed experiments, the particle distribution was initially both spatially and temporally approximately uniform over a restricted volume of fluid in the settling chamber. The particle distribution in the outer portion of the boundary layer is then determined by the diffusion of the passive scalar into the outer flow. In addition to diffusion, the entrainment of fluid into the boundary layer from the free stream by the mechanism of large-scale eddy engulfment contributes substantially to the structure of the particle number density profiles. Because the entrained fluid contains no particles,

the measured distributions shown in Figures 7 and 8 exhibit a rapid decay away from the wall, with the particle number density falling to zero in the outer portion of the boundary layer. This entrained fluid is under-represented in the Doppler measurements because of the loss of statistical weight.

As the wall is approached, the particle number density, normalized by the local fluid density, decays more rapidly than the velocity as a result of the loss of particles to the wall. This loss to the wall is evident from the observation of an oil film on the test surface.

IV. Optics and Measurement Geometry

A. Position Measurement

The present experiments utilized the laser-Doppler velocimeter in the single particle, dual forward-scatter mode. The instrument was mounted on a vibration isolated, two-axis traverse which permitted surveys up to 75 cm in the streamwise direction, and 20 cm in the direction normal to the test plate. For measurements in the JPL 20-inch wind tunnel, the instrument was mounted on top of the wind tunnel test section, as depicted in Figure 10. For measurements in the GALCIT Merrill wind tunnel, the traverse was suspended from the ceiling of the laboratory, and was not fixed relative to the test plate.

The vertical position was sensed by means of a helipot mounted on the vertical traverse and was repeatable to better than 0.005 cm. The origin for the vertical position measurements was estimated by placing a razor blade of known width normal to the test surface at the location of the focal volume. The origin was then measured by determining the half intensity of transmission as a function of position of one of the beams.

In practice, establishing the origin, to within the accuracy warranted by the data, by direct measurement proved difficult for a variety of reasons. These inherent difficulties in measuring the position of the wall, relative to the LDV traversing mechanism necessitated establishing the origin in y using the data for the mean-velocity profile. This was accomplished by a least-squares fit of the mean-velocity data to the law of the wall and the law of the wake in the form

$$u^+ = \frac{1}{\kappa} \ln y^+ + c + \frac{2\Pi}{\kappa} \sin^2 Y \ , \tag{22}$$

where

$$u^+ = u/u_\tau \ , \tag{23}$$

$$y^+ = (y - y_o) \frac{u_\tau}{\nu} \ , \tag{24}$$

$$Y = (y - y_o) \frac{\pi}{2\delta} \ , \tag{25}$$

and where y_o is the small offset of the position of the wall required to establish the proper origin.

For this purpose, a least-squares analysis was performed to determine the parameters u_τ, Π and y_o with $\kappa = 0.41$ and $c = 5.0$ given, and δ was computed as a constraint imposed by the local friction law,

$$u_e^+ = \frac{1}{\kappa} \ln \delta^+ + c + \frac{2\Pi}{\kappa} \ . \tag{26}$$

The technique for this analysis is outlined in Part I of this work by Collins, Coles and Hicks (1978) in conjunction with the mean-flow data

presented there. The results of this procedure lead to corrections y_o of the order of the focal volume diameter. In particular, the maximum correction was 0.18 cm for one case of the high-speed data and 0.075 cm for the low-speed flow measurements.

B. Transmitting Optics

The light source for this instrument was a Coherent Radiation Model 52B, 4-watt argon-ion laser. The laser was operated single line at 0.5145 μm and used an oven stabilized etalon to provide a single-mode beam. It was mounted on the tubular support structure for the optics as shown in Figure 10. This configuration ensures that the focal volume remains unchanged as the assembly is traversed and also that the relative alignment between the transmitting and receiving optics is preserved to within a few percent of the focal-volume diameter.

The laser output beam was directed into the vertical support tube for the transmitting optics by means of two separate mirrors in order to preserve the proper polarization of the beam. The transmitting optics cell contains a fixed mirror to direct the beam into the horizontal plane maintaining a vertical polarization vector. The beam is then split into two beams of unequal intensity by reflection from the front and rear surfaces of the first of two multiply-coated beam splitters. The resulting beam pair is then transmitted through a second multiply-coated beam splitter which divides the stronger beam into two beams of equal intensity. This arrangement results in three parallel beams of approximately equal intensity which form a right isosceles triangle whose base is nominally parallel to the test surface. The three output beams are then focused in the center of the tunnel by a 1.0 meter focal length, antireflection coated lens, to a common focal volume ~ 0.8 mm in

diameter. The optical axis intercepts the test plate from below at an angle of ~ 1:100 in order to permit measurement of the boundary layer close to the surface of the polished test plate.

The resulting focal volume contains three independent sets of virtual fringe planes correspondingly perpendicular to the $\underline{u}$, $(\underline{u} + \underline{v})/\sqrt{2}$ and $(\underline{u} - \underline{v})/\sqrt{2}$ velocity vectors. The geometry of the three beam pairs, and actual photographs of the fringes formed by each beam pair, are shown in Figure 11. By selectively blocking one of the three beams, any one of the three velocity components can be examined without a change in the focal-volume geometry. This method we consider superior to the more common one of rotating a single beam pair in the desired orientation which, in our experience, cannot easily be done with sufficient reproducibility and without slight displacements of the focal volume.

C. Geometry of the Intersection Volume

The three intersecting beams, taken in pairs, define three planes, along which the measurements were taken. Even though considerable care was taken to orient these planes at 0° and $\pm 45^\circ$ with respect to the wall, the small deviations that were measured were taken into account in the data analysis.

The subtended angles between the beam pairs were measured by two different methods on two different occasions and found to be within ~ 0.3% of the values:

$$\begin{aligned} \theta_1 \left\{ \underline{u} \text{ measurement} \right\} &= 0.02112 \text{ rad} \\ \theta_2 \left\{ \frac{1}{\sqrt{2}} (\underline{u} + \underline{v}) \text{ measurement} \right\} &= 0.01490 \text{ rad} \\ \theta_3 \left\{ \frac{1}{\sqrt{2}} (\underline{u} - \underline{v}) \text{ measurement} \right\} &= 0.01424 \text{ rad}. \end{aligned} \tag{27}$$

Thus, $\theta_2 \simeq \theta_3 \simeq \theta_1/\sqrt{2}$ define a nearly isosceles triangle as illustrated in Figure 11.

As a consequence of the requirement to isolate the traversing mechanism from vibrations, the relative orientation between the hypotenuse of the triangle and the wall (angle ϕ, Figure 12) had to be determined by a separate measurement for each profile. This was accomplished by permanently mounting a second razor blade to one side of the test plate with its edge aligned with the surface of the plate. The relative orientation for the optics could then be determined by measuring the offset between the two beams forming the triangle hypotenuse. This angle ϕ is small in every case but must be accurately known to estimate any quantities that involve v, the velocity component normal to the wall.

Using the geometry as defined in Figure 12, we have from the law of cosines,

$$\left.\begin{aligned} \cos\alpha &= \frac{\theta_2^2 + \theta_3^2 - \theta_1^2}{2\,\theta_2\theta_3}\,, \\ \cos\beta &= \frac{\theta_3^2 + \theta_1^2 - \theta_2^2}{2\,\theta_3\theta_1}\,, \\ \text{and}\quad \cos\gamma &= \frac{\theta_1^2 + \theta_2^2 - \theta_3^2}{2\,\theta_1\theta_2}\,. \end{aligned}\right\} \tag{28}$$

Assuming now that the velocity vector in two dimensions can be defined by its components in the three directions defined in Figure 12, we have that the three measured components are given by

$$\left.\begin{aligned} u_1 &= b_{11}u + b_{12}v \\ u_2 &= b_{21}u + b_{22}v \\ u_3 &= b_{31}u + b_{32}v \end{aligned}\right\} , \tag{29}$$

where

$$\left.\begin{aligned} b_{11} &= \cos\phi & b_{12} &= \sin\phi \\ b_{21} &= \cos(\gamma + \phi) & b_{22} &= \sin(\gamma + \phi) \\ b_{31} &= \cos(\beta - \phi) & b_{32} &= -\sin(\beta - \phi) \end{aligned}\right\} . \tag{30}$$

Equations (29) form a redundant set, and can be used to check the validity of the data. In particular, since $\sin(\beta + \gamma) = \sin\alpha$, we must have

$$\langle u_1 \rangle \sin\alpha = \langle u_2 \rangle \sin\beta + \langle u_3 \rangle \sin\gamma . \tag{31}$$

Recall from Equation (1) that

$$\nu_{D_i} = \frac{2 \sin\theta_i/2}{\lambda} u_i \simeq \frac{\theta_i}{\lambda} u_i , \tag{32}$$

so that the consistency Equation (31) becomes

$$\langle \nu_{D_1} \rangle = \langle \nu_{D_2} \rangle + \langle \nu_{D_3} \rangle . \tag{33}$$

Alternatively, Equations (29) can be solved in pairs to obtain two independent estimates of $\langle u \rangle$ and $\langle v \rangle$ at each location,

$$\begin{pmatrix} b_{11} & b_{12} \\ b_{21} & b_{21} \end{pmatrix} \times \begin{pmatrix} \langle u_I \rangle \\ \langle v_I \rangle \end{pmatrix} = \begin{pmatrix} \langle u_1 \rangle \\ \langle u_2 \rangle \end{pmatrix} , \tag{34}$$

and

$$\begin{pmatrix} b_{11} & b_{12} \\ b_{31} & b_{32} \end{pmatrix} \times \begin{pmatrix} \langle u_{II} \rangle \\ \langle v_{II} \rangle \end{pmatrix} = \begin{pmatrix} \langle u_1 \rangle \\ \langle u_3 \rangle \end{pmatrix} . \tag{35}$$

Inverting Equations (34) and (35), we then have

$$\left.\begin{aligned} \langle u_I \rangle &= \frac{\langle u_1 \rangle \sin(\gamma + \phi) - \langle u_2 \rangle \sin\phi}{\sin\gamma} \\ \langle v_I \rangle &= \frac{\langle u_2 \rangle \cos(\phi) - \langle u_1 \rangle \cos(\gamma + \phi)}{\sin\gamma} \end{aligned}\right\} , \tag{36}$$

and

$$\left.\begin{aligned} \langle u_{II} \rangle &= \frac{\langle u_1 \rangle \sin(\beta - \phi) + \langle u_3 \rangle \sin\phi}{\sin\beta} \\ \langle v_{II} \rangle &= \frac{\langle u_1 \rangle \cos(\beta - \phi) - \langle u_3 \rangle \cos\phi}{\sin\beta} \end{aligned}\right\} . \tag{37}$$

The final values for $\langle u \rangle$ and $\langle v \rangle$ were then estimated by averaging the two independent estimates,

$$\left.\begin{aligned} \langle u \rangle &= \frac{1}{2} \left(\langle u_I \rangle + \langle u_{II} \rangle \right) \\ \langle v \rangle &= \frac{1}{2} \left(\langle v_I \rangle + \langle v_{II} \rangle \right) \end{aligned}\right\} . \tag{38}$$

Using Equations (29), we can also relate the mean-square fluctuations of the measured velocity components, to $\langle u'^2 \rangle$, $\langle v'^2 \rangle$ and $\langle u'v' \rangle$. In

particular, we have

$$\left.\begin{aligned} \langle u'^2_1 \rangle &= b_{11}^2 \langle u'^2 \rangle + b_{12}^2 \langle v'^2 \rangle + 2\, b_{11} b_{12} \langle u'v' \rangle \\ \langle u'^2_2 \rangle &= b_{21}^2 \langle u'^2 \rangle + b_{22}^2 \langle v'^2 \rangle + 2\, b_{21} b_{22} \langle u'v' \rangle \\ \langle u'^2_3 \rangle &= b_{31}^2 \langle u'^2 \rangle + b_{32}^2 \langle v'^2 \rangle + 2\, b_{31} b_{32} \langle u'v' \rangle \end{aligned}\right\} . \tag{39}$$

Note that while Equations (29) are redundant, Equations (39) are not, except for special choices of β, γ and ϕ. Inverting Equations (39), we then have

$$\left.\begin{aligned} \langle u'^2 \rangle &= C_{11} \langle u'^2_1 \rangle + C_{12} \langle u'^2_2 \rangle + C_{13} \langle u'^2_3 \rangle \\ \langle v'^2 \rangle &= C_{21} \langle u'^2_1 \rangle + C_{22} \langle u'^2_2 \rangle + C_{23} \langle u'^2_3 \rangle \\ \langle u'v' \rangle &= C_{31} \langle u'^2_1 \rangle + C_{32} \langle u'^2_2 \rangle + C_{33} \langle u'^2_3 \rangle \end{aligned}\right\} , \tag{40}$$

where the C_{ij} matrix is given by,

$$\left.\begin{aligned} C_{11} &= \sin(\beta+\gamma)\sin(\beta-\phi)\sin(\gamma+\phi)/\Delta \\ C_{12} &= -\sin\beta \sin(\beta-\phi)\sin\phi/\Delta \\ C_{13} &= \sin\gamma \sin(\gamma+\phi)\sin\phi/\Delta \end{aligned}\right\} \left.\begin{aligned} \\ \\ \\ \end{aligned}\right.$$

$$\left.\begin{aligned} C_{21} &= -\sin(\beta+\gamma)\cos(\beta-\phi)\cos(\gamma+\phi)/\Delta \\ C_{22} &= \sin\beta \cos(\beta-\phi)\cos\phi/\Delta \\ C_{23} &= \sin\gamma \cos(\gamma+\phi)\cos\phi/\Delta \end{aligned}\right\} \left.\begin{aligned} \\ \\ \\ \end{aligned}\right\} \tag{41}$$

$$\left.\begin{aligned} C_{31} &= -\frac{1}{2}\sin(\beta+\gamma)\sin(\beta-\gamma-2\phi)/\Delta \\ C_{32} &= \frac{1}{2}\sin\beta\sin(\beta-2\phi)/\Delta \\ C_{33} &= -\frac{1}{2}\sin\gamma\sin(\gamma+2\phi)/\Delta \end{aligned}\right\}\Bigg|\Bigg| \quad ,$$

and where

$$\Delta = \sin\beta \cdot \sin\gamma \cdot \sin(\beta+\gamma) \quad . \tag{42}$$

D. Receiving Optics

The optical axis for the receiving optics is aligned at an angle of $\sim 7.5^{\circ}$ with respect to the test-plate surface, thus permitting a full view of the focal volume throughout the boundary layer. This inclination of both the transmitting and the receiving optics with respect to the test surface results in a reduction of the spanwise extent of the focal volume. The collecting lenses consist of a pair of 15.24 cm diameter, f/5 achromats which have been anti-reflection coated and are mounted back-to-back in a common cell. This configuration provides a 1:1 imaging system that was measured to be approximately twice diffraction limited. The collected light cone is directed by a 10 cm diameter multi-layer dielectric coated mirror into a 0.05 cm diameter pinhole which spatially filters the collected light that is accepted by the photomultiplier assembly. The photomultiplier assembly consists of a focusing mount with a 20 mm focal length, f/5 coated lens, a 30Å wide 0.5145 μm filter and magnetic lensing to restrict the photocathode of an EMI 9813B photomultiplier tube. The photomultiplier tube output is coupled directly to a low-noise fast rise-time preamplifier, constructed inside the tube housing at the base of the photomultiplier tube. The photodetection system was designed with a frequency response in excess of 50 MHz.

The effective focal-volume diameter is defined by the pinhole in the receiving optics and is therefore equal to ~ 0.05 cm.

Oscilloscope traces of raw signals from the output of the preamplifier at the base of the photomultiplier are included in Figure 13. These photographs are multiple exposures taken of particle bursts at the highest recorded velocities of $M_e \sim 2.2$ ($Re_\theta \sim 4 \times 10^4$) at the edge of the boundary layer. The frequency of the $\underline{u}$-component signal is about 26 MHz. The frequency of the $(\underline{u} + \underline{v})$-component signal is almost exactly one-half the $\underline{u}$-component frequency. This feature, which will be discussed later, is exploited by the processing scheme. Typical signal-to-noise ratios of 15-20 db were measured at these velocities.

V. Signal Processing and Data Acquisition

The output of the photomultiplier, coupled through the integral preamplifier, was monitored on a HP 8553B/8552B wave analyzer which was also used to align the optics and tune the entire system by maximizing the signal-to-noise ratio of the Doppler signal. This signal was filtered by a two-pole low-pass filter in order to eliminate the substantial shot noise above the Doppler frequencies. The pedestal, resulting from the dual-scatter optics, is not removed by this processing scheme.

A. The LDV Processor

The filtered output signal is fed into the LDV processor (Dimotakis and Lang (1977)) depicted in block diagram in Figure 14. The various components of this processor are described in the following paragraphs.

1. The Analog Input Processor

The Analog Input Processor defines a reference level V_0 and two symmetric levels $V_0 - V_L$, $V_0 + V_L$ about V_0 as shown in Figure 15a. In addition, a fourth

level V_M can also be defined which must be higher than $V_O + V_L$. The amplitudes V_O, V_L and V_M, as well as the polarity, are independently selectable. The filtered Analog INput (AIN) must cross $V_O - V_L$ from below and then $V_O + V_L$ from below, in that order, before the Digital INput (DIN) is raised. A subsequent crossing of V_O from above will cause DIN to go low. This test sequence must be passed by the analog input AIN on every cycle, otherwise the burst is rejected, the logic is reset, and the processor waits for the next burst. If the analog input AIN exceeds V_M at any time during the burst, the burst is rejected, the logic is reset, and the processor waits for the next burst (cf. Figure 15a). Thus the amplitudes V_O, V_L and V_M specify the range of particle sizes accepted by the processor for the measurement. The frequency of the signal DIN can be prescaled (cf. Figure 15b) to produce the signal DIN′ which has one negative slope for every m negative slope of DIN. The constant m is front panel selectable and can be set to 1, 2, 4 or 8. The Analog Input Processor is designed with high-speed ECL circuitry and stripline technology with a maximum Doppler frequency of 170 MHz.

2. The Digital Input Processor

The prescaled digital input DIN′ is subsequently processed by the Digital Input Processor. The negative slope of DIN′ fires a resettable one-shot T1 of duration τ_1, as illustrated in Figure 16. The negative slope of T1 fires a resettable one-shot of duration τ_2. The first negative slope of DIN′ also raises a signal G, which gates a 100 MHz crystal clock into the Flight Time (FT) counter, as illustrated in Figure 17. The next negative slope of DIN′, refires the one-shot T1, resets the T2 one-shot and generates a short TRansfer Pulse (TRP) which stores the FT buffer and increments the cycle counter (cf. Figures 16 and 17). If the T2 one-shot times out before it is reset, an error

flag is raised, the logic is reset and the processor waits for the next burst. As a consequence, the logic checks that every period of the prescaled digital input falls within predetermined limits. If τ is the period of the Doppler signal, we must have, as a consequence,

$$\tau_1 < m\tau < \tau_1 + \tau_2 \quad , \tag{43}$$

where m = 1, 2, 4, 8. The time intervals τ_1 and τ_2 are front panel selectable and cover the range 60 nsec $< \tau_1, \tau_2 <$ 3 msec. The maximum Doppler frequency that can be handled by the Analog and Digital Processors working in tandem is given by,

$$(\nu_D)_{max} = \frac{max(m)}{min(\tau_1)} = \frac{8}{60 \times 10^{-9}} = 130 \text{ MHz} \quad . \tag{44}$$

3. The Timer

The 100 MHz crystal clock is divided by 10 to form a 10 MHz time standard which is used as the clock for the timer, as illustrated in Figure 17. The timer, in turn, has a $\div 10^N$ prescaler which sets the time base. This increments a free running 32-bit counter which can be reset if required but is normally allowed to overflow. The gate signal G is inverted to form $\overline{G}$ and is used to latch the contents of the timer counter into the timer buffer, as illustrated in Figure 18. The purpose of this information is to record the real time of each scattering event, to permit the reconstruction of the velocity fluctuations in time (cf. Dimotakis and Brown (1975)). While the present data rate was often high enough ($\sim$ 50 kHz) to warrant an examination of the velocity fluctuations in time, it was decided not to include such data in the present report.

4. Performance and Operating Modes

The LDV processor operates at the theoretical performance of ± 1/2 clock count (10 nsec) in determining the flight time Δt_i of the i^{th} scattering particle. The overall measurement accuracy is of course limited by a variety of other factors such as optical precision, signal-to-noise of the signal at the processor input, etc. In all the high-speed cases ($M_e \gtrsim 0.8$), the finite frequency of the processor clock was the limiting factor in the velocity measurement accuracy of a single particle. The highest frequency that occurred was 27 MHz in the $M_e \simeq 2.2$ flow. This frequency was measured with an overall accuracy for a single particle of ~ 2%. A histogram from a 1,024 particle record taken in the free stream ($M_e \simeq 2.2$) of the flight time for 8 Doppler cycles, is depicted in Figure 19. It can be seen that ~ 2/3 of all the counts fall in one 10 nsec bin. At the lower velocities the limitations arose as a result of the combined effect of all the other sources of error. For the $M_e \sim 0.1$ measurements an accuracy of 0.5% for a single particle was achieved. It should be emphasized that while the accuracy for a single particle velocity measurement does not limit the accuracy with which mean velocities can be determined, it contaminates the measurement of the rms fluctuation levels.

The processor is capable of operating in a variety of modes. Two of the modes that were used in this work will be discussed.

In the first mode, a fixed number of cycles is stored in the Mode Logic circuitry and compared with the contents of the Cycle Counter after each TRP pulse (cf. Figures 16 and 17). When the two numbers match, the Count End (CEND) flag is raised which in turn lowers the GO disabling the system (cf. Figures 17 and 15a). The output is then read and the processor is

reset and waits for the next burst (dead time ~ 60 nsec). All the data for $M_e > 0.6$ (JPL 20-inch Wind Tunnel) were recorded in this mode. Eight cycles were counted for the beam pair at 0^o (u_1 data) with the prescaler m set to 2. Four cycles were counted for the $\pm 45^o$ (u_2, u_3 data) beam pairs with the prescaler set to unity. The advantage of this scheme was that the digital processor saw the same frequencies and numbers of cycles for all configurations. This occurs for the present measurements because the projection of the velocity vector along the $\pm 45^o$ directions is approximately given by

$$u_2 \simeq u_3 \simeq \frac{u_1}{2^{\frac{1}{2}}} \quad , \tag{45}$$

and hence the resulting Doppler frequencies are given by

$$\nu_{D_2} \simeq \nu_{D_3} \simeq \frac{1}{2} \nu_{D_1} \quad . \tag{46}$$

This uniformity in the processing, allows all the signals to be processed with identical settings except for a change in the prescaler from 1 to 2. The particle velocity is then determined by reading the output of the FT counter which corresponds to the flight time of the particle for the fixed number of fringes specified.

In the second mode, the processor requires that a fixed number of cycles be reached or exceeded by the burst and records the flight time and number of cycles of the entire burst. The sequence depicted in Figure 15a represents such a mode where, assuming that each period of DIN passed the τ_1, τ_2 test, the end of the burst was determined by the Analog Input Processor. The flight time Δt that would have resulted from

such a burst is indicated on the figure while the output of the cycle counter would have been n = 3 (number of TRP pulses and also number of fringe plane intervals). Both n and Δt would be recorded in this mode and the velocity would be

$$u_{\perp} = \frac{ns}{\Delta t} \quad . \tag{47}$$

The data recorded at $M_e \sim 0.1$ (GALCIT Merrill Wind Tunnel) were acquired in this mode requiring at least four fringes for the $\pm 45^{\circ}$ data (u_2, u_3) and at least eight for the 0° data (u_1). Thus, in both modes, the same minimum number of fringes had to be crossed.

There are several important differences between the two modes. First, using the facility of the processor to recognize the end of the burst while retaining the previous valid measurement allows the total flight time to be used, instead of an arbitrary fraction, in determining the velocity component of interest. This improves the measurement accuracy in an obvious way. Second, the phase errors that are made in assigning equal phase to the crossings of the reference level V_0 by the signal are cancelled when the entire burst is used. Third, the sampling statistics are different between the two modes. In the first mode (fixed number of fringes), all we know is that the particle crossed at least that many. In the second mode (number of fringes unrestricted provided it exceeds a certain minimum) we know that the particle crossed exactly that many. The sampling bias is different for these two cases, as will be discussed in Section VI-B.

B. Output Formatting

The (i) flight time, (ii) total number of validated cycles and (iii) the real time are encoded by the processor into three 32-bit words as binary

coded decimals (BDC). These data serve as input to the subsequent formatting electronics which selected the four least significant decades of the flight time to form a sixteen-bit word and, depending on the fringe mode, either the sixteen bits of the real time for the fixed-fringe mode, or the number of fringe crossings, in the free-fringe mode. These data were then combined to form a single 32-bit word.

The asynchronous data from the processor were recorded in dual 1024 X 32-bit buffers. One buffer was filled asynchronously with the processor output while the second was clocked synchronously, as a sequence of 4 bits/word on a Kennedy Model 9100 digital tape deck. Each 1024 X 32-bit buffer constituted a 4K-bit record on tape. Several records were recorded at each station depending on the turbulence level and average data rate.

VI. Data Processing

In computing the Reynolds stress $-\rho\overline{u'v'}$ from the measured velocity data, it is necessary to estimate both the first and second moments of the data, and to extract relatively small differences between two large numbers. This necessitates a careful accounting of all random and systematic errors that result from spurious measurements. In the present experiments, such errors are caused by a finite signal-to-noise ratio, and appear as isolated counts when the measurements are treated in histogram form. Errors are also caused by LDV sampling bias and by both the finite clock period and by noise in the processing electronics and in the optics. Errors which arise as a result of the finite measurement volume have been found to only be important in the immediate vicinity of the wall, and have not been corrected in the present analysis. The correction of such errors would result in a correction of at most the first two data points adjacent to the wall, for which we have the least confidence, and would not affect the conclusions presented.

A. Histogram Pruning

The data from the present experiments were recorded as multiple records of 1024 individual realizations of the three instantaneous velocity components $\underline{u}$, $\underline{u} + \underline{v}$, $\underline{u} - \underline{v}$. These data were processed by forming a separate histogram for each record, and subsequently performing the statistical computations using the resulting histograms. For the high-speed flow experiments, the data were recorded in the fixed-fringe mode and the histograms were formed as a function of the integer flight time Δt_i. The low-speed measurements were recorded in the free-fringe mode for which the flight time was large and covered a much wider range. For these data, the histogram was formed as a function of the velocity of the particles, computed as an integer percentage of the maximum velocity that the processor would admit, i.e.,

$$I_i = 100 \, \tau_1 \frac{n_i}{\Delta t_i} \quad , \tag{48}$$

where τ_1 is the minimum Doppler period and n_i is the number of fringes crossed by the i^{th} particle in time Δt_i.

The pruning was performed in two passes. First, data in any bin that contained only one count, and did not have neighboring bins with more than one count, were discarded. In the second pass, any data isolated from the main body of the histogram by at least one zero were also discarded. If, as a result of these two operations, more than 24 measurements out of the total of 1024 were rejected, the entire record was rejected. This scheme was preferred to the more usual one of rejecting data outside a certain number of standard deviations from the mean. By way of example, the few

counts in bin 40 of the histogram in Figure 19 would be discarded by this scheme.

The histograms which result from the data in the present investigations are illustrated in Figures 20 and 21. In these figures, the histograms at several locations through the boundary layer are superimposed on the mean-velocity profiles for that case. For both flows represented here, the histogram for the free-stream flow encompasses only four bins. Near the wall, the histogram is spread over more than forty bins.

B. Sampling Bias

The complexity of processing single particle laser-Doppler velocity data is compounded by the fact that the fluid velocity is sampled in a biased manner. This problem, first pointed out by McLaughlin and Tiederman (1973), is a consequence of the fact that the particle flux through the measurement volume, and the resulting measurement probability per unit time, is higher when the local fluid velocity is high than when it is low. The fact that the measurement probability is a function of the measured quantity gives rise to the sampling bias $\beta(\underline{u})$, where $\underline{u}$ is the three-dimensional velocity vector. Consequently, to compute the expectation value of a particular function of the measurements we must remove this bias, i.e.,

$$\langle f(\underline{u}) \rangle = \frac{\sum_i f(\underline{u}_i)\beta^{-1}(\underline{u}_i)}{\sum_i \beta^{-1}(\underline{u}_i)} \quad . \tag{49}$$

The dependence of the sampling bias function β on the local velocity vector $\underline{u}$, on the shape of the measurement volume, and on the minimum number of fringe crossings required by the processing electronics, has been derived

by Dimotakis (1976). For data recorded in the fixed-fringe mode, if the angle between the intersecting beams is small, the expression for $\beta(\underline{u})$ simplifies to

$$\beta(\underline{u};\epsilon) \simeq u_{\perp}(1 + u_{\parallel}^2/u_{\perp}^2)^{1/2} [1 - \epsilon^2(1 + u_{\parallel}^2/u_{\perp}^2)] \quad , \tag{50}$$

where $u_{\perp}$ is the velocity component perpendicular to the fringe planes, $u_{\parallel}$ is the velocity component parallel to the fringe planes and perpendicular to the beam bisector, and ϵ is the ratio n_{min}/n_T of the minimum number of fringe crossings required by the processor to the total number in the focal volume. Note that recording the flight time for a fixed number of fringes in fact requires that <u>at least</u> that many were crossed. Consequently, the fixed number of fringes is equal to n_{min} in the context in which ϵ was defined for Equation (50).

Evaluating $\beta(\underline{u};\epsilon)$ for the u_1 data in the boundary layer, which were acquired using the fixed-fringe mode ($0.6 \lesssim M_e \lesssim 2.2$), we note that $u_{\parallel}^2/u_{\perp}^2 = v^2/u^2 \ll 1$ so that, in this case,

$$\beta(\underline{u};\epsilon) \simeq u_{\perp}\cdot(1 - \epsilon^2) \quad , \tag{51}$$

or,

$$\beta(\underline{u};\epsilon) \propto u_{\perp} \quad . \tag{52}$$

In going from Equation (51) to Equation (52), an additional assumption has been made. Even though n_{min} is fixed by the signal processing electronics, the total number of fringes crossed, n_T, is unfortunately a complicated function of the particle size. This is a consequence of the fact that the amplitude levels V_0 and V_L are absolute. A large particle,

with a correspondingly large scattering cross-section, will yield a burst which is expected to result in more validated cycles. Thus, the ratio ϵ is a function of the particle size. In the context of Equation (49), the transition from Equation (51) to (52) is valid only if the local velocity vector is uncorrelated with particle size. This requirement will be satisfied if the particles track the flow.

With this proviso we then have from Equations (49) and (52), for the u_1 data in the fixed-fringe mode,

$$\langle f(\underline{u}) \rangle = \frac{\sum_i f(\underline{u}_i) u_{\perp_i}^{-1}}{\sum_i u_{\perp_i}^{-1}} \quad . \tag{53}$$

In particular, the mean velocity is given by

$$\langle u_\perp \rangle = \frac{N}{\sum_i u_{\perp_i}^{-1}} \quad , \tag{54}$$

where N is the total number of data points, as originally proposed by McLaughlin and Tiederman (1973). Similarly the mean square is given by,

$$\langle u_\perp^2 \rangle = \frac{\sum_i u_{\perp_i}}{\sum_i u_{\perp_i}^{-1}} \quad . \tag{55}$$

The mean-square fluctuations can then be computed by means of

$$\langle u'^2_\perp \rangle = \langle u_\perp^2 \rangle - \langle u_\perp \rangle^2 \quad . \tag{56}$$

or

$$\langle u'^{2}_{\perp} \rangle = \frac{\sum_i (u_{\perp i} - \langle u_{\perp} \rangle)^2 \, u_{\perp i}^{-1}}{\sum_i u_{\perp i}^{-1}} \quad . \tag{57}$$

The latter form is preferable in avoiding finite precision problems in the computer, at the expense, however, of substantially more computing time.

In evaluating Equations (54) and (55), note that the i^{th} measured velocity component is given by Equation (47), or

$$u_{\perp i} = \frac{ns}{\tau_c} \left(\frac{1}{k_i + \frac{1}{2} + x} \right) \quad , \tag{58}$$

where n is equal to the number of fringes, s is the fringe spacing, τ_c is the clock period (10 nsec), k_i is the (integer) output of the flight time counter and x is a random variable representing the collective uncertainty in the determination of the flight time Δt and resulting from (i) the finite clock period τ_c , and (ii) the uncertainty with which the equal phase points are determined by the comparators from the signal burst as a result of finite signal-to-noise ratio. The 1/2 is added to k_i to remove the systematic truncation error of the digital counter.

Using Equations (54) and (55) and correcting for the finite variance of the random variable x, we have

$$\langle u_{\perp} \rangle_{fixed} = \left(\frac{ns}{\tau_c} \right) \frac{N}{J_{-1}} \quad , \tag{59}$$

and

$$\langle u_{\perp}^{2} \rangle_{fixed} \simeq \left(\frac{ns}{\tau_c} \right)^2 \left(\frac{J_2 - \sigma^2 J_3}{J_{-1}} \right) \quad , \tag{60}$$

where

$$J_\ell \equiv \sum_i (k_i + \tfrac{1}{2})^{-\ell} \quad , \tag{61}$$

and

$$\sigma^2 \equiv \frac{\int x^2 p(x)dx}{\int p(x)dx} \quad , \tag{62}$$

is the variance of x.

Unfortunately, the situation is less well defined for the $\pm 45^\circ$ data recorded in the fixed-fringe mode. In that case, the two relevant velocities, $u_\perp$ and $u_{/\!/}$, are of the same order of magnitude. Nevertheless, since only one velocity component was measured at a time, we use Equation (52) for the bias and reduce the $\pm 45^\circ$ data using Equations (59) and (60). While this is clearly not correct, it is better than ignoring the bias altogether.

Note that the expression for the sampling bias β given by Equation (52) is not appropriate for data acquired in the free-fringe mode because this equation was derived using the assumption that the probability of measurement is determined by the fact that the particle has crossed at least the fixed number of fringes. In the free-fringe mode, the measurement of the number of fringes crossed and of the flight time in units of τ_c corresponds to a particle crossing of <u>exactly</u> n_i fringes. The probability for this event can be determined from Equation (50). Since $\beta\ (\underline{u};\ n_i/n_T)$ is proportional to the probability of crossing at least n_i fringes, i.e.,

$$\beta_{\text{fixed}}\ (\underline{u};n_i/n_T) \propto \dot{p}\ \{n < n_i \,|\, \underline{u}\} \quad , \tag{63}$$

we have that

$$\dot{p}\{n = n_i | \underline{u}\} = \dot{p}\{n < n_i | \underline{u}\} - \dot{p}\{n < (n_i + 1) | \underline{u}\} \quad , \tag{64}$$

where $\dot{p}\{\ \}$ denotes the probability per unit time of observing the event in the braces. Consequently,

$$\beta_{free}(\underline{u}; n_i/n_T) \propto \beta_{fixed}(\underline{u}; n_i/n_T) - \beta_{fixed}[\underline{u}; (n_i + 1)/n_T] \quad , \tag{65}$$

or

$$\beta_{free}(\underline{u}; n_i/n_T) \propto u_\perp^{-2}(u_\perp^2 + u_{/\!/}^2)^{3/2}(n_i + 1/2) \quad , \tag{66}$$

where, in the context of Equation (49), the assumption has been made that the particle size is uncorrelated with the local velocity. In the context of Equation (49), note that

$$u_\perp \propto \frac{n_i}{\Delta t_i} \quad , \tag{67}$$

whereas

$$(u_\perp^2 + u_{/\!/}^2) \propto \frac{1}{\Delta t_i} \quad , \tag{68}$$

where Δt_i is the time of flight for the measured n_i fringes. Substituting these equations in Equation (66), we have

$$\beta_{free}^{-1}(\underline{u}; n_i/n_T) \propto \frac{(k_i + 1/2 + x)n_i^2}{n_i + 1/2} \quad , \tag{69}$$

where, as before, k_i is the integer output of the flight time counter and x is a random variable representing the uncertainty in the measurement of

the flight time. Using this bias function, we thus have

$$\langle u_\perp \rangle_{free} = \left(\frac{ns}{\tau_c}\right) \frac{K_{0,3}}{K_{-1,2}} \quad , \tag{70}$$

and

$$\langle u_\perp^2 \rangle_{free} = \left(\frac{ns}{\tau_c}\right)^2 \left(\frac{K_{1,4} - \sigma^2 K_{3,4}}{K_{-1,2}}\right) \quad , \tag{71}$$

where

$$K_{\ell,m} \equiv \sum_i \frac{n_i^m}{(k_i + \frac{1}{2})^\ell (n_i + \frac{1}{2})} \quad , \tag{72}$$

and σ^2 is the variance of x. Note that Equations (70) and (71) are equally valid for the 0^o data as for the $\pm 45^o$ data. The data recorded at $M_e \simeq 0.1$ in the free-fringe mode were analyzed using Equations (70) and (71). In order to compare them to the previous data, Equations (54) and (55) were also used, which in this case reduce to

$$\langle u_\perp \rangle = \left(\frac{s}{\tau_c}\right) \frac{L_{0,1}}{L_{-1,-1}} \quad , \tag{73}$$

and

$$\langle u_\perp^2 \rangle = \left(\frac{s}{\tau_c}\right)^2 \left(\frac{L_{1,1} - \sigma^2 L_{3,1}}{L_{-1,-1}}\right) \quad , \tag{74}$$

where

$$L_{\ell,m} = \sum_i \frac{n_i^m}{(k_i + \frac{1}{2})^\ell} \quad . \tag{75}$$

Note also that Equation (69) for the sampling bias in the free-fringe mode is in disagreement with the results of Hoesel and Rodi (1977) and Buchhave, George and Lumley (1979), who claim that $\beta_{free}^{-1} \propto \Delta t_i \propto (k_i + \frac{1}{2})$. If that were true, Equations (59) and (60) would be valid for the free-fringe mode as well, with the three summations as defined in Equation (61).

The variance σ^2 of x was estimated from the mean-square fluctuations in the free stream where $\langle u'^2 \rangle \simeq 0$.

The results of this analysis have been applied to the data obtained in these experiments. The bias correction is most important in the region near the wall, where the fluctuation levels are highest. These calculations indicate at most a 2% correction for the low-speed flow data in this region, and a 3.3% correction for the high-speed flow data.

VII. Results and Discussion

A. Data Reduction

Following the computation of the proper statistical averages, the data were reduced to a form appropriate for boundary layer flows by utilizing the scheme outlined in Part I of this report by Collins, Coles and Hicks (1978). For this purpose, the Van Driest (1955) scaled mean streamwise velocity data were fitted to the law of the wall and the law of the wake using a three-parameter nonlinear least-squares fit with a single constraint equation based on the local friction law. The profile parameters u_τ, Π and δ, determined by this analysis, were then used to infer both the distribution of shear stress, and of the normal velocity, from the data by an integration of the equations for the conservation of mass and momentum from the wall to the free stream, using the formulation by Spalding (1961) to describe the flow in the viscous sublayer. The details of these computations are given in Part I.

One significant difference between the present LDV data and the data obtained using standard Pitot instrumentation (cf. Part I) is the ability of the Pitot to obtain valid data in the region adjacent to the wall. Because of noise considerations, the present data are limited to a distance of approximately one focal-volume diameter from the wall. This fact requires that the boundary-layer scale parameters δ^* and θ be computed directly from the law of the wall and the law of the wake representations rather than from a direct integration of the data, as in the results discussed in Part I.

The scale parameters are defined as

$$\delta^* = \int_o^\delta \left[1 - \frac{\rho u}{\rho_e u_e}\right] dy \quad , \tag{76}$$

and

$$\theta = \int_o^\delta \frac{\rho u}{\rho_e u_e} \left[1 - \frac{u}{u_e}\right] dy \quad . \tag{77}$$

In terms of the Van Driest (1955) scaled velocity U,

$$\frac{\rho u}{\rho_e u_e} = \frac{1}{m} \frac{T_e}{T_w} \frac{\sin U}{\cos^2 U} \quad , \tag{78}$$

and

$$\frac{\rho u^2}{\rho_e u_e^2} = \frac{1}{m^2} \frac{T_e}{T_w} \frac{\sin^2 U}{\cos^2 U} \quad , \tag{79}$$

where

$$m = \left(\frac{T_w - T_e}{T_w}\right)^{1/2} \quad , \tag{80}$$

and U is defined by the Van Driest scaling

$$m \frac{u}{u_e} = \sin U \quad . \tag{81}$$

AD-A073 746 CALIFORNIA INST OF TECH PASADENA GRADUATE AERONAUTIC--ETC F/G 20/4
CHEMICAL REACTIONS IN TURBULENT MIXING.(U)
JUL 79 H W LIEPMANN, G L BROWN, P E DIMOTAKIS F44620-76-C-0046
UNCLASSIFIED GALCIT-151 AFOSR-TR-79-0952 NL

3 OF 4
AD A073 746

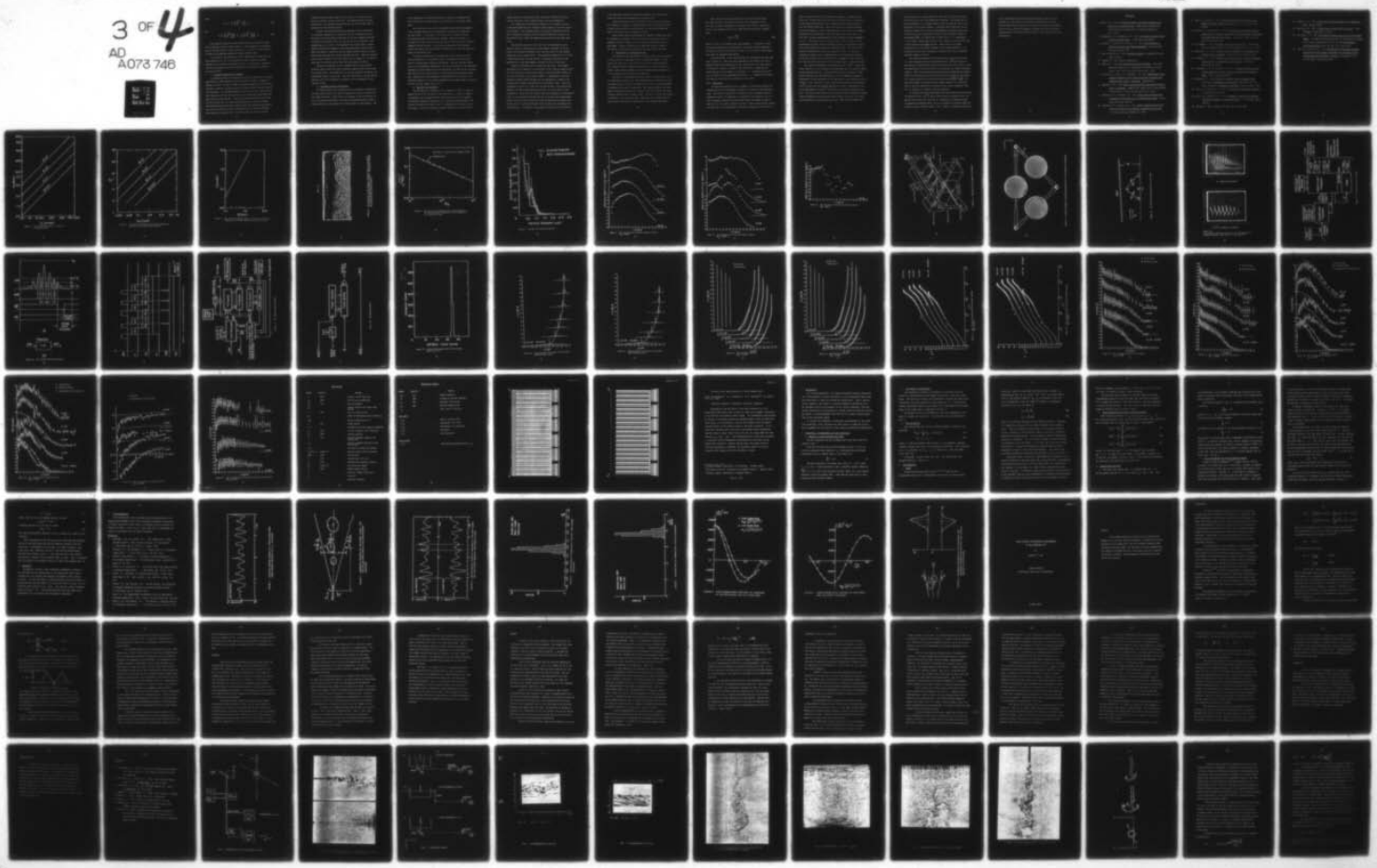

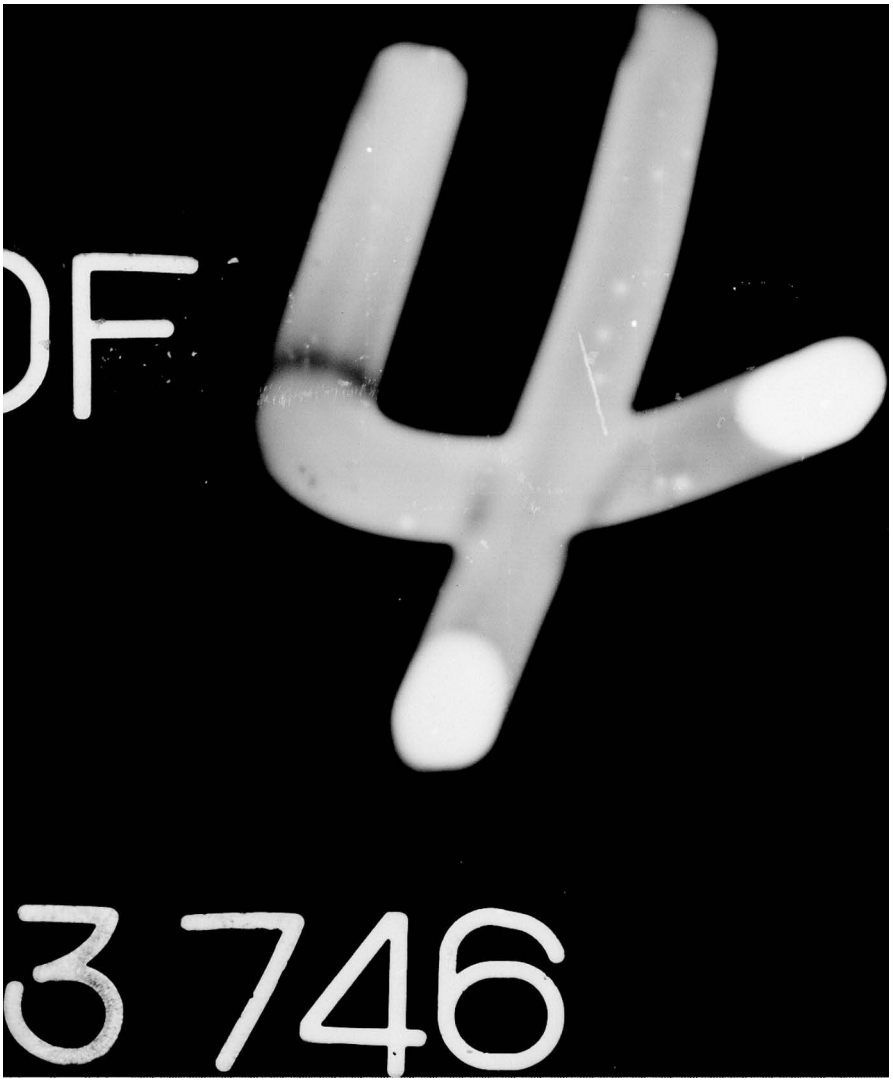
OF
4
3 746

Thus,

$$\delta^* = \delta - \frac{1}{m} \frac{T_e}{T_w} \int_o^\delta \frac{\sin U}{\cos^2 U} \, dy \quad , \tag{82}$$

and

$$\theta = \frac{1}{m} \frac{T_e}{T_w} \int_o^\delta \frac{\sin U}{\cos^2 U} \, dy - \frac{1}{m^2} \frac{T_e}{T_w} \int_o^\delta \frac{\sin^2 U}{\cos^2 U} \, dy \, . \tag{83}$$

The integrals involved in these expressions were evaluated in terms of the integrals P and Q defined in Part I. These integrals are functions only of the mean-velocity profile parameters u_τ, Π and δ, and are evaluated in terms of the Spalding formulation for the boundary layer.

As a result of the differences in the computational procedure for the scale parameters δ^* and θ, these quantities differ slightly from those computed for the identical flows given in Part I of this work. Corrections for these discrepancies have been included where comparisons are made to the previous work.

B. Streamwise Mean-Velocity Profiles

A comparison between the mean-velocity profiles obtained in the present experiments and those obtained from the Pitot data of Part I is given in Figures 22 and 23. In order to make a consistent comparison, the Pitot data from Part I have been replotted using the integral scale θ obtained from the LDV experiments. At high Mach numbers, the results exhibit a small discrepancy between the LDV and the Pitot data, with the LDV data exhibiting lower mean velocities near the wall. The cause of this discrepancy is not clear at this writing, nor is it clear which measurement is the more reliable. The low-speed flow mean-velocity profiles have been computed using both the exact bias correction, according to Equation (70) and using the harmonic mean according to Equation (59). The differences are small as are the

differences between these results and the results of the mean value of these data without any bias correction. The comparisons have not been plotted here. The agreement between the LDV data and the Pitot data is excellent for the low-speed results.

The data obtained from the present experiments have been plotted in coordinates appropriate to the law of the wall in Figures 24 and 25. The solid line associated with each data set has been computed using the formulation by Spalding (1961), and illustrates the fit obtained in the computation of u_τ, Π and δ. The high-speed flow results shown in these figures illustrate the problem of obtaining measurements near the wall. These data exhibit a departure from the computed profile because of noise which occurs when the focal volume intercepts the wall. This fact required that the data included in the least-squares fit be limited to $y^+ \geq 200$ for these data, as was the case for the Pitot data reported in Part I.

The profile parameters u_τ and δ computed from the least-squares procedure agree closely with those parameters computed from the Pitot data for the same flows. The computations of the wake parameter Π, however, are considerably higher in every case. The self-consistency of the LDV results indicates that this discrepancy is probably not the consequence of data reduction errors.

C. Streamwise Velocity Fluctuations

The fluctuations of the streamwise velocity component, normalized by the free-stream velocity, are shown in Figures 26 and 27 as a function of the normal coordinate. These results are compared to the distribution of the u' fluctuations obtained at low speeds by Klebanoff (1954) in flow at constant pressure, represented by the solid squares in these figures. For

these comparisons, the normal coordinate for the data by Klebanoff have been scaled with the boundary-layer scale obtained in the present experiments.

The error bars in each of the subsequent figures have been computed as the standard deviation of the ensemble of records used in computing the mean values. In each case, a few data points for which the error bars exceed the mean value have been excluded. From these results, it is clear that, near the free-stream, the velocity fluctuations are properly computed from the LDV data. As the wall is approached, the deviations between the present results and those of Kelbanoff are within the confidence limits in the present data.

It can be concluded from these data that, within the error in the present experiments, no measurable effects of compressibility have been found on the mean-square velocity fluctuations. The data for Mach numbers up to 2.2 are adequately represented by the data of Klebanoff. The differences exhibited in these figures between the high-speed flow data and the low-speed flow data arise from the differences in the boundary-layer Reynolds number, Re_θ. These results confirm Morkovin's (1961) hypothesis that there is no essential difference in the dynamic behavior of the boundary layer at constant pressure for Mach numbers up to 4 or 5.

D. Reynolds Stress Profiles

The distribution of Reynolds stress, computed as $-\rho\overline{u'v'}$, is shown in Figures 28 and 29 for the data of these experiments. In order to compare the Reynolds stress deduced from the experimental data with the expected distribution through the boundary layer, a second computation based on the integral formulation outlined in Part I is displayed as the solid curve in each figure. The results from the integral formulation coincide with the

results obtained using the Pitot data, with minor differences arising from the difference in the computed value of the wake parameter Π.

For comparison with the expected behavior at low speeds, the data of Klebanoff (1954) has been included in these figures as the dark squares on each figure. The agreement between the integral formulation and the data of Klebanoff indicates that the integral formulation, based on the mean-velocity data, yields the expected distribution for the total shear stress.

The dominant feature of the results for the distribution of the Reynolds stress, as measured by the laser-Doppler technique, is the departure of the measured Reynolds stress from the results of the integral computation in the region $y/\delta \lesssim 3$. This departure represents a major error in these measurements and may indicate a fundamental limitation on the applicability of the laser-Doppler technique in flows of this type.

Several conclusions can be reached from these data. The anomaly represented by the departure of the Reynolds stress from the expected value near the wall has been reported previously by Johnson and Rose (1973), by Yanta and Lee (1974), and by Abbiss (1976). An explanation of this phenomenon by Sandborn (1974) assumed that the phenomenon is related to the contributions of density fluctuations to the Reynolds stress. That this assumption is incorrect is clear from the present data. The observed phenomenon is not Mach number dependent and hence is not an effect of compressibility. These data also indicate that the discrepancy in the Reynolds stress is not associated with particle lag at the position of measurement, because for this to be the case the results of Equation (13) require that the lag occur at increasing distances from the wall with increasing free-stream velocity. In addition, the agreement obtained in the distribution

of the mean-square velocity fluctuations indicates that the particles follow the flow locally throughout the boundary layer.

Similar distributions for the Reynolds stress, measured using hot-wire anemometer techniques by Laderman (1978), have recently been shown to agree with the present results given by the integral distributions shown by the solid curves in Figures 28 and 29.

These results again confirm Morkovin's hypothesis (1961) and refute the hypothesis by Sandborn (1974) that density fluctuations may be responsible for major changes in the distribution of Reynolds stress at high speeds. Similar conclusions were expressed in Part I, based on the results of the Pitot measurements of the mean-velocity profiles.

E. The Problem of the Normal Velocity

The results for the distribution of normal velocity are illustrated in Figure 30 for the high-speed flow at low Reynolds number. In this figure, the solid line is the result for the correct distribution of v/u, computed from the integral representation of the data outlined by Collins, Coles and Hicks (1978), using the boundary-layer parameters u_τ, Π and δ derived from the least-squares analysis.

The errors in estimating the normal velocity from the present data are substantial in every case. The principal feature of the data is that the normal velocity is large and negative at the wall, increasing sharply in magnitude as the wall is approached. The disparity between the large negative value and the error bars indicates that the particles are being convected toward the wall in this region. In the free stream, the velocity is positive in most cases, but with a magnitude that is larger than the correct free-stream value as represented by the integral formulation.

These data illustrate the difficulty in accurately representing the normal velocity. This difficulty arises as a consequence of the fact that any small misalignment of the optics will result in substantial errors in the computed value of the normal velocity, which has a maximum value

$$(v/u) \lesssim \frac{HC_f}{2} \quad , \tag{84}$$

where $H = \delta^*/\theta$ is the boundary layer form parameter. In addition, because of the non-uniform particle distributions, the normal velocity components of both the flow near the wall and the flow in the vicinity of the boundary-layer edge are improperly represented.

The fluctuations in the normal velocity are represented for these same data in Figure 31. These data have approximately the value of the data of Klebanoff (1954) for incompressible flow, represented by the solid squares in the figure. However, in light of the difficulties in measuring the normal velocity, this agreement is fortuitous. The magnitude of the error bars for these data are approximately one-half of the magnitude of the data, and indicate a low degree of confidence in the results.

VIII. Conclusions

The present experiments lead to a number of conclusions regarding the applicability of the laser-Doppler technique to the study of boundary-layer flows. The results presented for the behavior of the streamwise velocity components indicate the importance of including in the analysis of the raw data an adequate technique for pruning the initial histograms in order to remove errors in the data introduced by noise. These results further indicate the importance of including proper statistical averaging in the analysis in

order to account for the bias introduced by sampling. In addition, the effects of a finite clock period and noise have been shown to be important in the proper determination of the streamwise velocity fluctuations, u', near the boundary-layer edge. When these effects are properly included in the data analysis, a direct comparison between the present laser-Doppler measurements and measurements in the same flows, presented in Part I of this work, indicates good agreement for the streamwise velocity components u and u'. The present results, when properly scaled to account for compressibility using the ideas of Van Driest (1955), are also shown to agree with the low-speed data presented by Kelbanoff (1954). This observation further corroborates the conclusions expressed in Part I of this work regarding the proper role of compressibility in determining the behavior of the mean velocity, and confirms Morkovin's hypothesis (1961) regarding the role of density fluctuations in the boundary layer at constant pressure.

The present measurements of the Reynolds stress, $-\rho\overline{u'v'}$, and for the normal velocity, v, are in substantial disagreement with the expected results derived from the mean flow. These observations seem to indicate a fundamental difficulty with the application of the laser-Doppler technique as implemented in these experiments to the measurement of the detailed structure of flows in the vicinity of a wall. The measured Reynolds stress profiles, $-\rho\overline{u'v'}$, deviate from the expected behavior for $y/\theta \lesssim 3$, indicating an error in the measurement for the $\overline{u'v'}$ correlation in the region adjacent to the wall. This error arises because of the strong correlation between the normal velocity component and the particle number density that occurs as a result of the depletion of particles near the wall. These results indicate that

the flow inside the viscous sublayer is such that a particle that enters the sublayer has a very low probability of leaving. The scaling law for particle behavior in a turbulent boundary layer (cf. Equation (13)) is not applicable in the viscous sublayer. A particle which enters the viscous sublayer is subjected to the very high Lagrangian frequencies which occur in the motion of the longitudinal vorticies, whose transverse extent is approximately $\frac{20\nu}{u_\tau}$, and lags the flow in this region. As a consequence, a fluid element coming <u>from</u> the wall is less likely to carry particles than a fluid element moving <u>toward</u> the wall. This results in an under-representation of the positive component of the normal velocity, v, in the region near the wall, resulting in a negative value for the measured component normal to the wall.

This under-representation of the motion near the wall also results in a lower measured value for the Reynolds stress, $-\overline{\rho u'v'}$, than would be expected by an analysis based on the mean flow as described in Part I, since the upswelling of fluid from the wall is associated with a lower streamwise velocity. This bursting motion has been observed by Blackwelder and Kaplan (1976) to be intermittent and quite violent, and is held to be responsible for a large fraction of the total stress near the wall $\left(\frac{yu_\tau}{\nu} \lesssim 100\right)$. The particle transport to the wall via the viscous sublayer is so effective, even at the lower velocities of the Merrill wind tunnel experiments, that the wall appears as an infinite sink for particles.

We conclude from these observations that the measured disparity between the Reynolds stress, $-\overline{\rho u'v'}$, and the total stress, as defined by the integration of the mean flow, arise not as a consequence of compressibility, as suggested by Sandborn (1974), but as a consequence of particle depletion which is unique to boundary layers in air. This is a fundamental limitation

of the techniques for particle seeding which must be solved if this technique is to be useful for detailed measurements near the wall. For free-shear flows, because of the absence of the wall, this problem does not arise, and the laser-Doppler technique will give an accurate representation of the mean and fluctuating velocity components and their correlations.

References

1. Abbiss, J. B. 1976 Development of photon correlation anemometry for application to supersonic flow. AGARD CP-193, "Applications of Non-Intrusive Instrumentation in Fluid Flow Research," 11.1 - 11.11.

2. Blackwelder, R. F. and Kaplan, R. E. 1976 On the wall structure of the turbulent boundary layer. J. Fluid Mech. 76, 89-112.

3. Buchhave, P., George, W. K, Lumley, J. L. 1979 The measurement of turbulence with the laser-Doppler anemometer. Ann. Rev. Fluid Mech. 11, 443-503, 1979.

4. Born, M. and Wolf, E. 1975 Principles of optics. Pergamon Press, New York, p. 633 ff.

5. Cantwell, B. 1978 Private communication.

6. Coles, D. E. 1968 The young person's guide to the data. Proc. 1968 AFOSR-IFP-Stanford Conf., "Computation of Turbulent Boundary Layers," Vol. II (D. Coles and E. Hirst, eds.), 1-45.

7. Collins, D. J., Coles, D. E. and Hicks, J. W. 1978 Measurements in the turbulent boundary layer at constant pressure in subsonic and supersonic flow. Part I. Mean flow. AEDC-TR-78-21.

8. Dimotakis, P. E. 1976 Single scattering particle laser-Doppler measurements of turbulence. AGARD CP-193, "Applications of Non-Intrusive Instrumentation in Fluid Flow Research," 10.1 - 10.14.

9. Dimotakis, P. E. and Brown, G. L. 1975 Large structure dynamics and entrainment in the mixing layer at high Reynolds number. Project Squid Tech. Rept. CIT-7-PU.

10. Dimotakis, P. E. and Lang, D. B. 1977 Signal responsive burst period timer and counter for laser-Doppler velocimetry and the like. U.S. Patent 4,051,433 (September 27, 1977).

11. Hoesel, W. and Rodi, W. 1977 New biasing elimination method for laser-Doppler velocimeter counter processing. Rev. Sci. Instrum. 48(7), 910-919.

12. Johnson, D. A. and Rose, W. C. 1973 Measurement of turbulence transport properties in a supersonic boundary-layer flow using laser velocimeter and hot-wire anemometer techniques. AIAA Paper 73-1045; see also AIAA J. 13, 512-515, 1975.

13. von Kármán, T. 1930 Mechanische ahnlichkeit und turbulenz. Proceedings 3rd International Congress for Applied Mechanics, Vol. 1, pp. 85-92.

14. Klebanoff, P. S. 1954 Characteristics of turbulence in a boundary layer with zero pressure gradient. NACA TN 3178; also TR 1247, 1955.

15. Laderman, A. J. 1978 Effects of Mach number and heat transfer on Reynolds shear stresses in compressible boundary layers. Aeronutronic Publication No. U-6412.

16. McLaughlin, D. K. and Tiederman, W. G. 1973 Biasing correction for individual realization of laser anemometer measurements in turbulent flows. Phys. Fluids 16, 2082-2088.

17. Morkovin, M. V. 1961 Effects of compressibility on turbulent flows. Proc. Colloq. Mechanique de la Turbulence, CNRS (1962), 367-380. (Proc. reprinted as Mechanics of Turbulence, Gordon & Breach 1964).

18. Perry, A. E. and Abell, C. J. 1975 Scaling laws for pipe flow turbulence. J. Fluid Mech. 67, 257-271.

19. Perry, A. E. and Abell, C. J. 1977 Asymptotic similarity of turbulence structures in smooth- and rough-walled pipes. J. Fluid Mech. 79(4), 785-799.

20. Prandtl, L. 1942 Z. Angew. Math. Mech. 22, 241-243, 1942.

21. Sandborn, V. A. 1974 A review of turbulence measurements in compressible flow. NASA TM X-62337.

22. Spalding, D. B. 1961 A single formula for the "law of the wall". Trans. ASME 28E (J. Appl. Mech.), 455-457.

23. Van Driest, E. R. 1955 The turbulent boundary layer with variable Prandtl number. "50 Jahre Grenzschichtforschung" (H. Görtler and W. Tollmien, eds.), Vieweg, Braunschweig, 257-271; see also The problem of aerodynamic heating, Aeron. Eng. Rev., Oct. 1956, 26-41.

24. Yanta, W. J. and Lee, R. E. 1974 Determination of turbulence transport properties with laser-Doppler velocimeter and conventional time-averaged mean flow measurements at Mach 3. AIAA Paper 74-575; see also AIAA J. 14, 725-729, 1976.

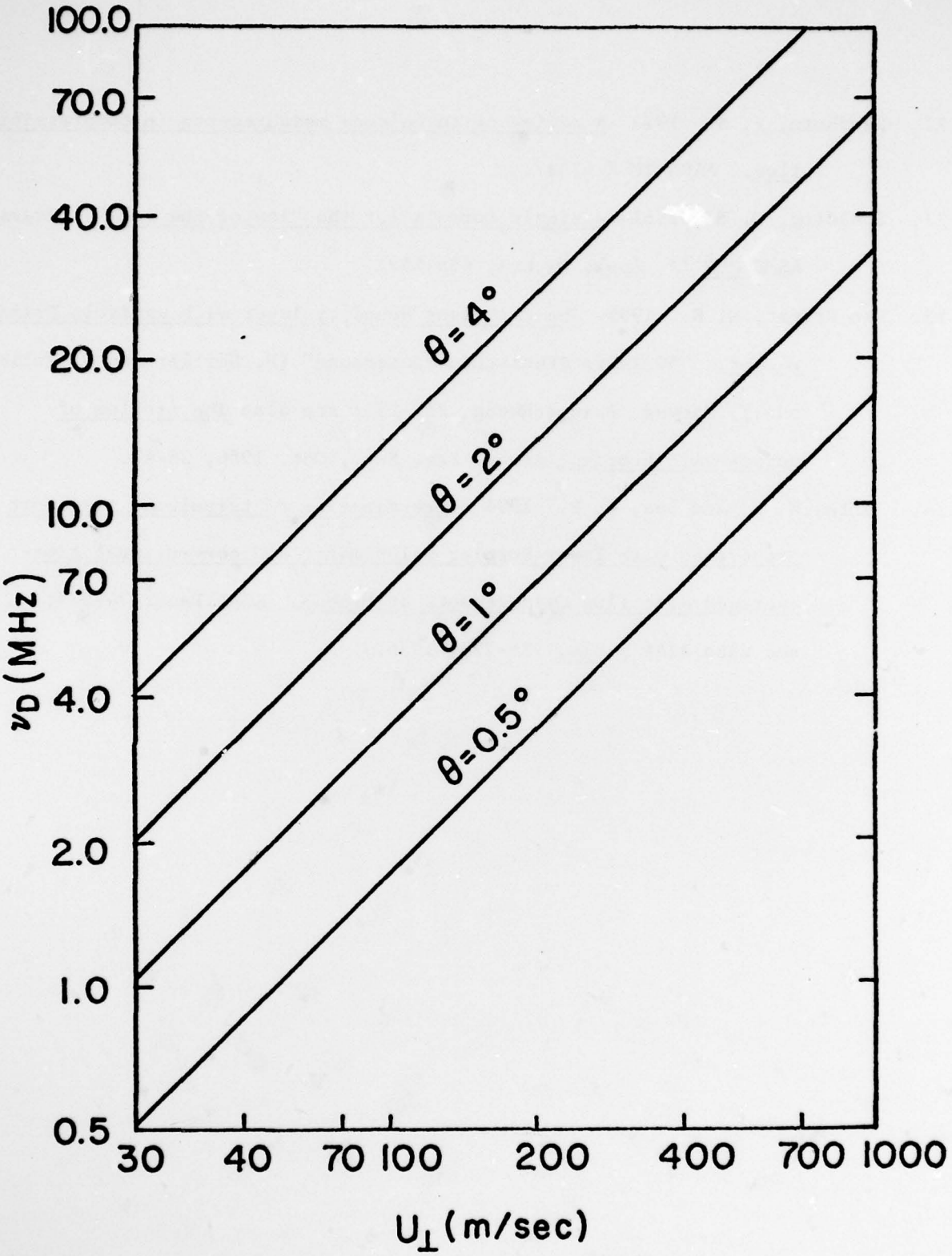

Figure 1. The Doppler Frequency as a Function of Flow Velocity

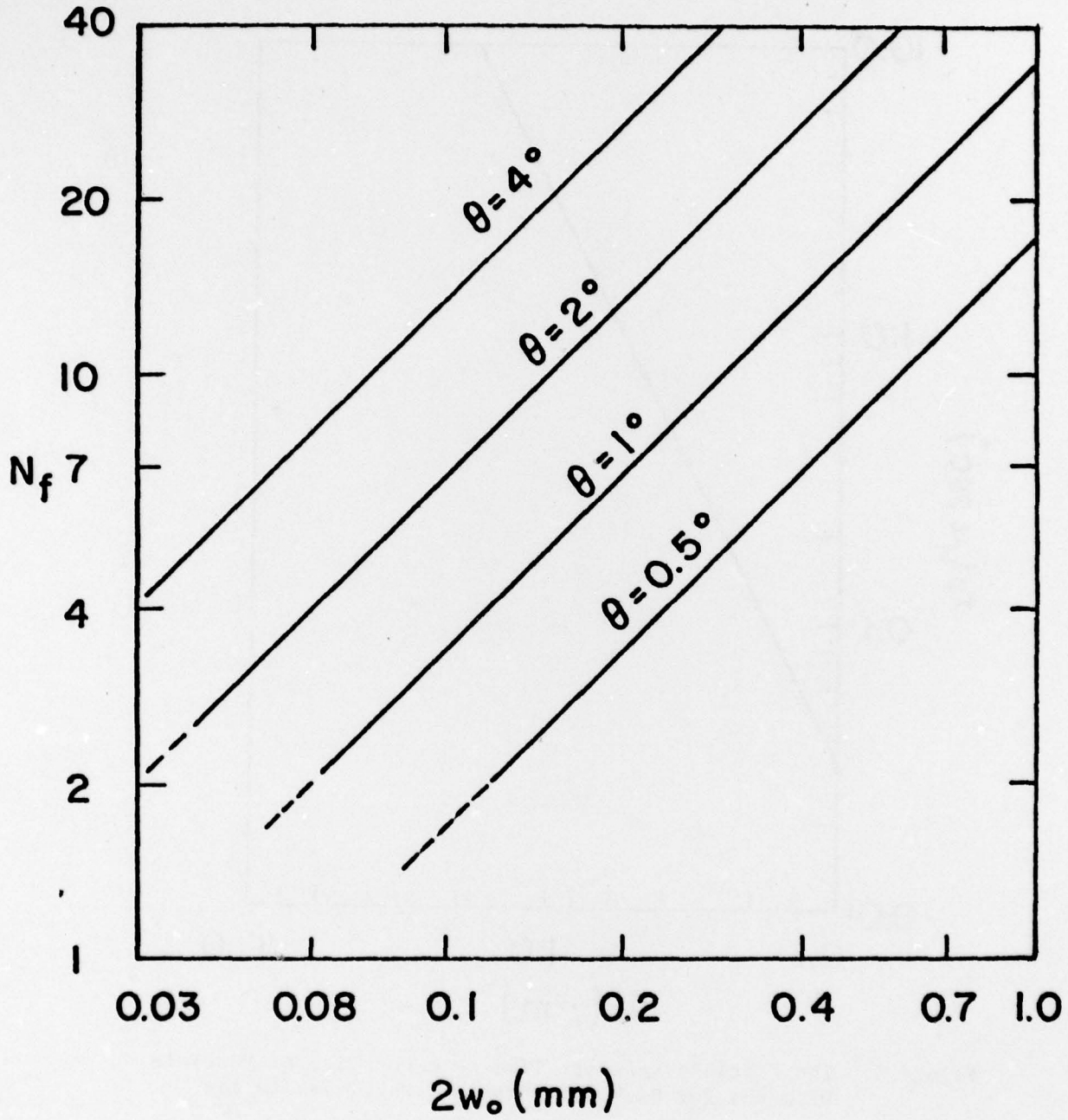

Figure 2. The Number of Fringes in the Focal Volume as a Function of the Focal Volume Diameter

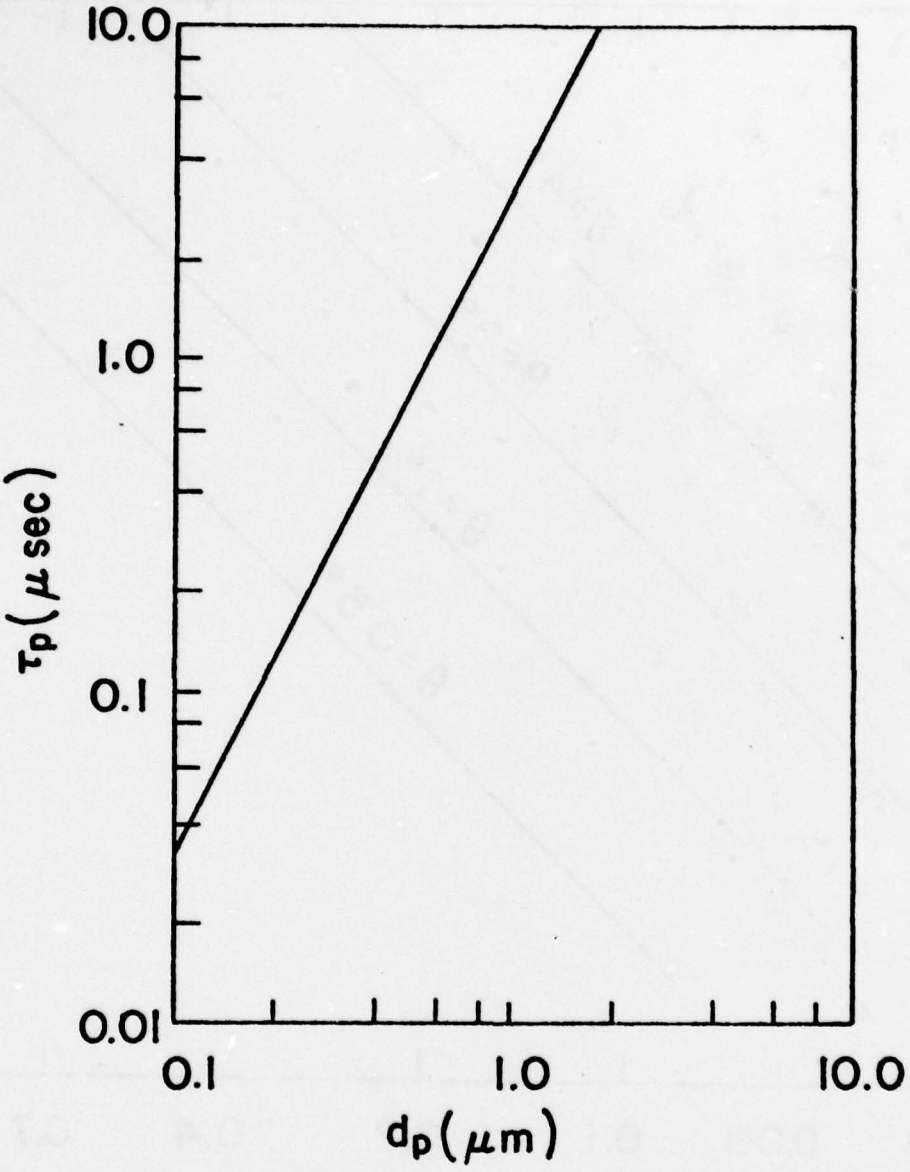

Figure 3. The Particle Response Time as a Function of Particle Diameter for Di-butyl Phthalate Particles in Air

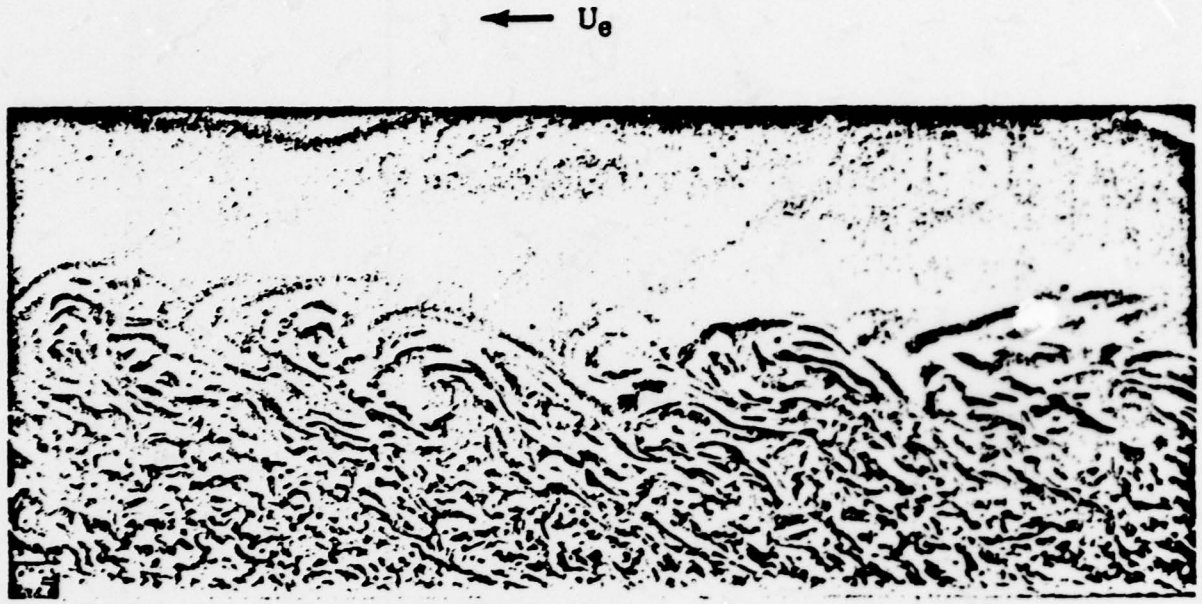

Figure 4. The Structure of the Turbulent Boundary Layer as Visualized by the Use of Aluminum Flakes in Water. Photograph courtesy of Brian Cantwell, Caltech (1978).

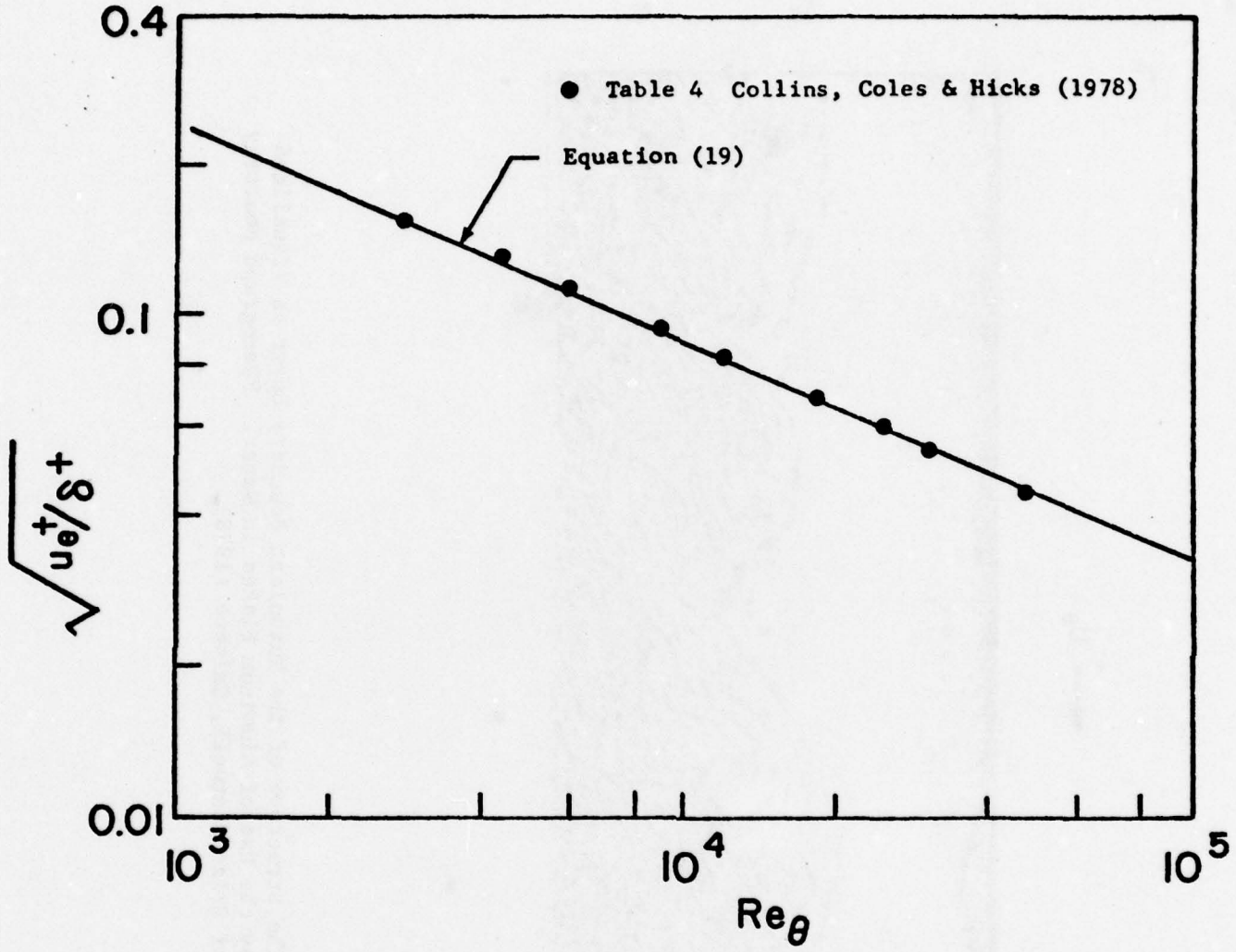

Figure 5. The Ratio of the Boundary-Layer Edge Velocity to the Boundary-Layer Thickness in Wall Coordinates as a Function of Re_θ.

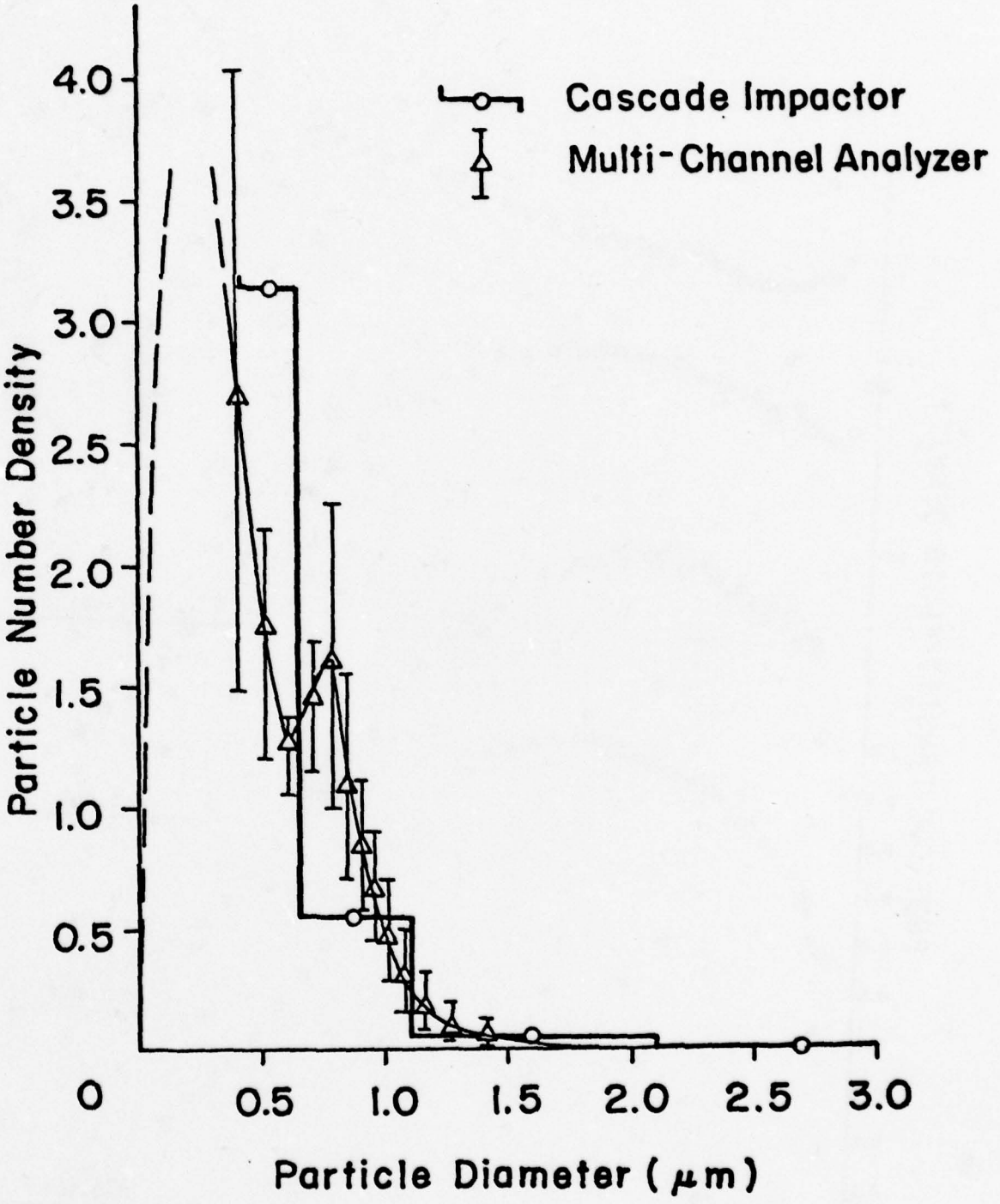

Figure 6. The Particle Size Distribution.

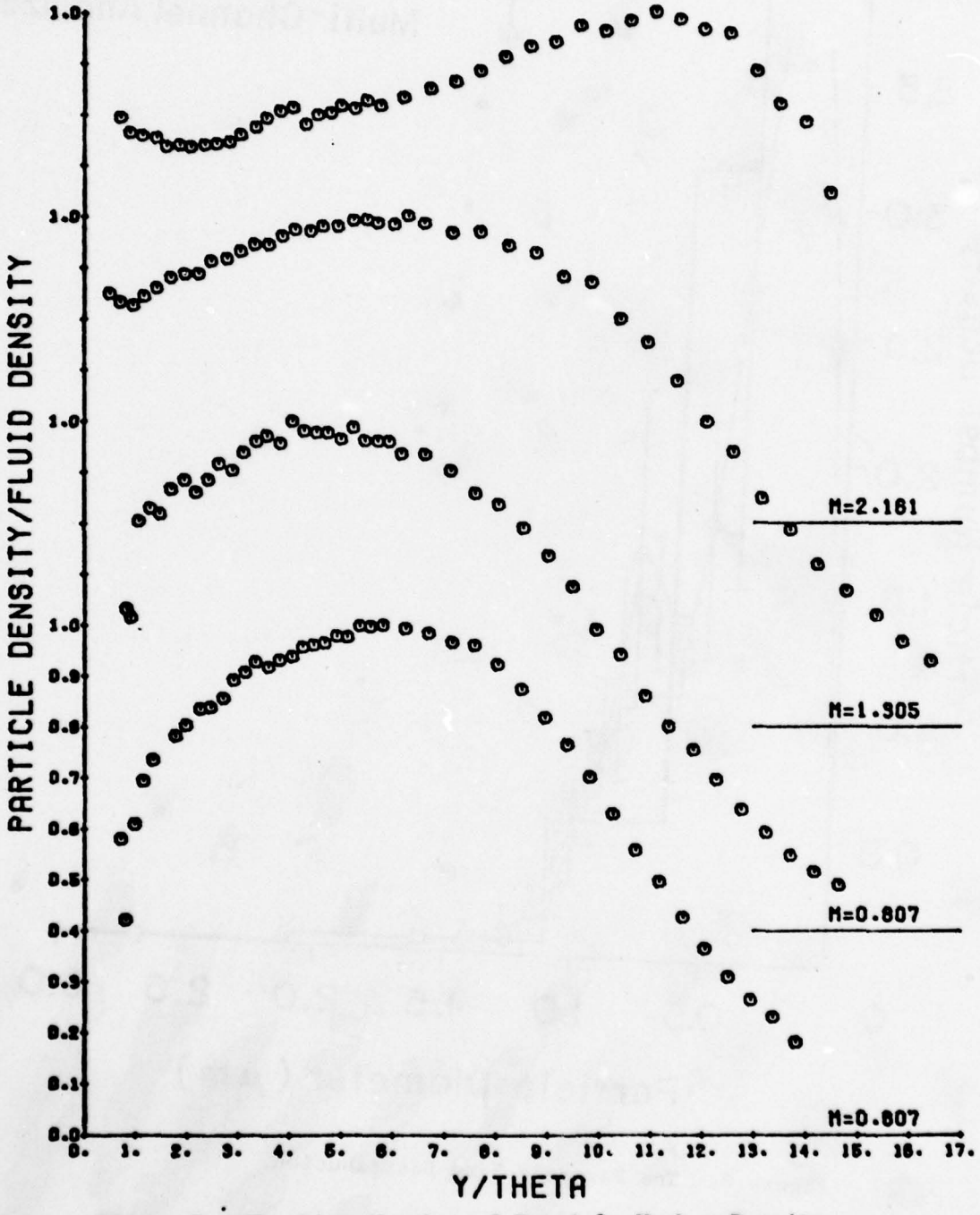

Figure 7. The Distribution of Particle Number Density. $Re_\theta \simeq 23000$.

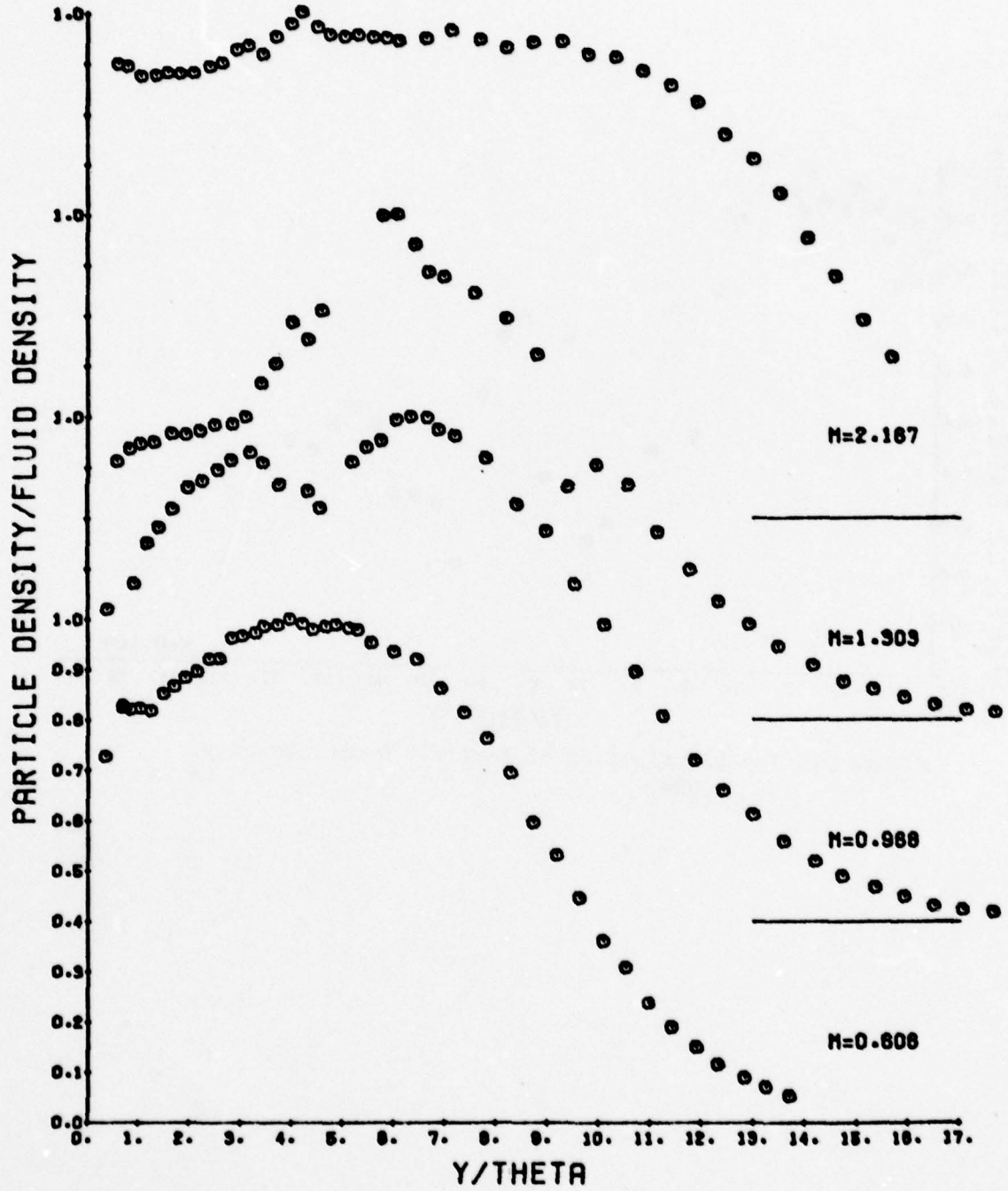

Figure 8. The Distribution of Particle Number Density. $Re_\theta \simeq 40000$.

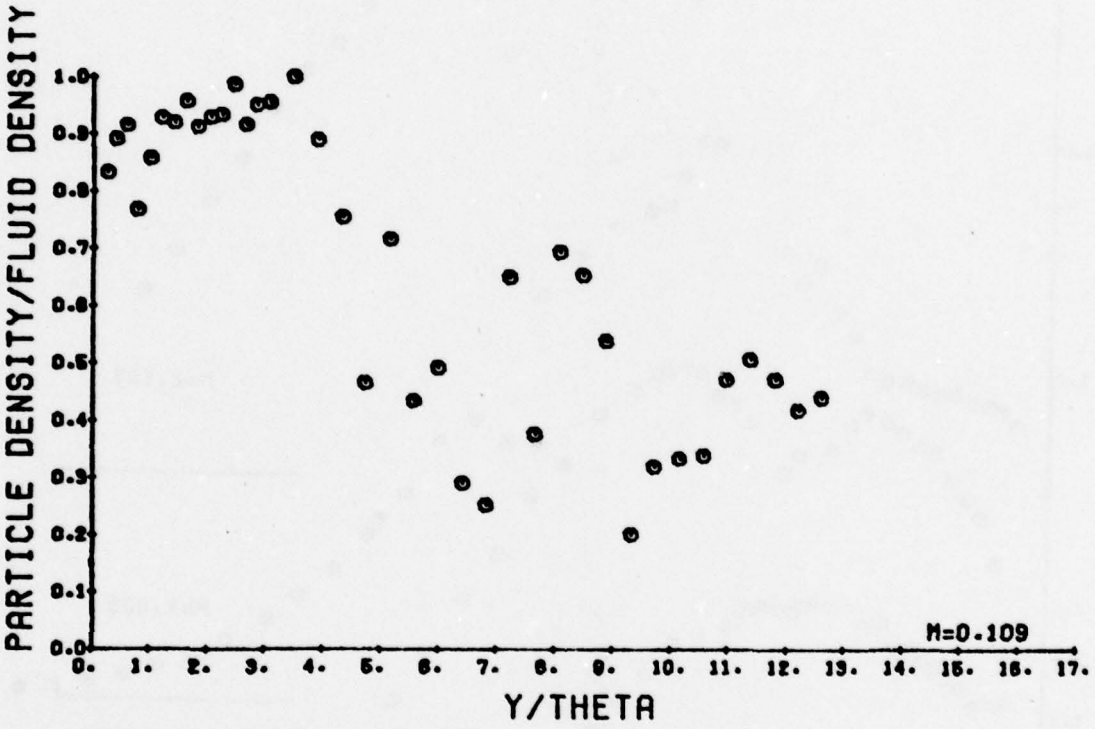

Figure 9. The Distribution of Particle Number Density. Re_θ = 6900.

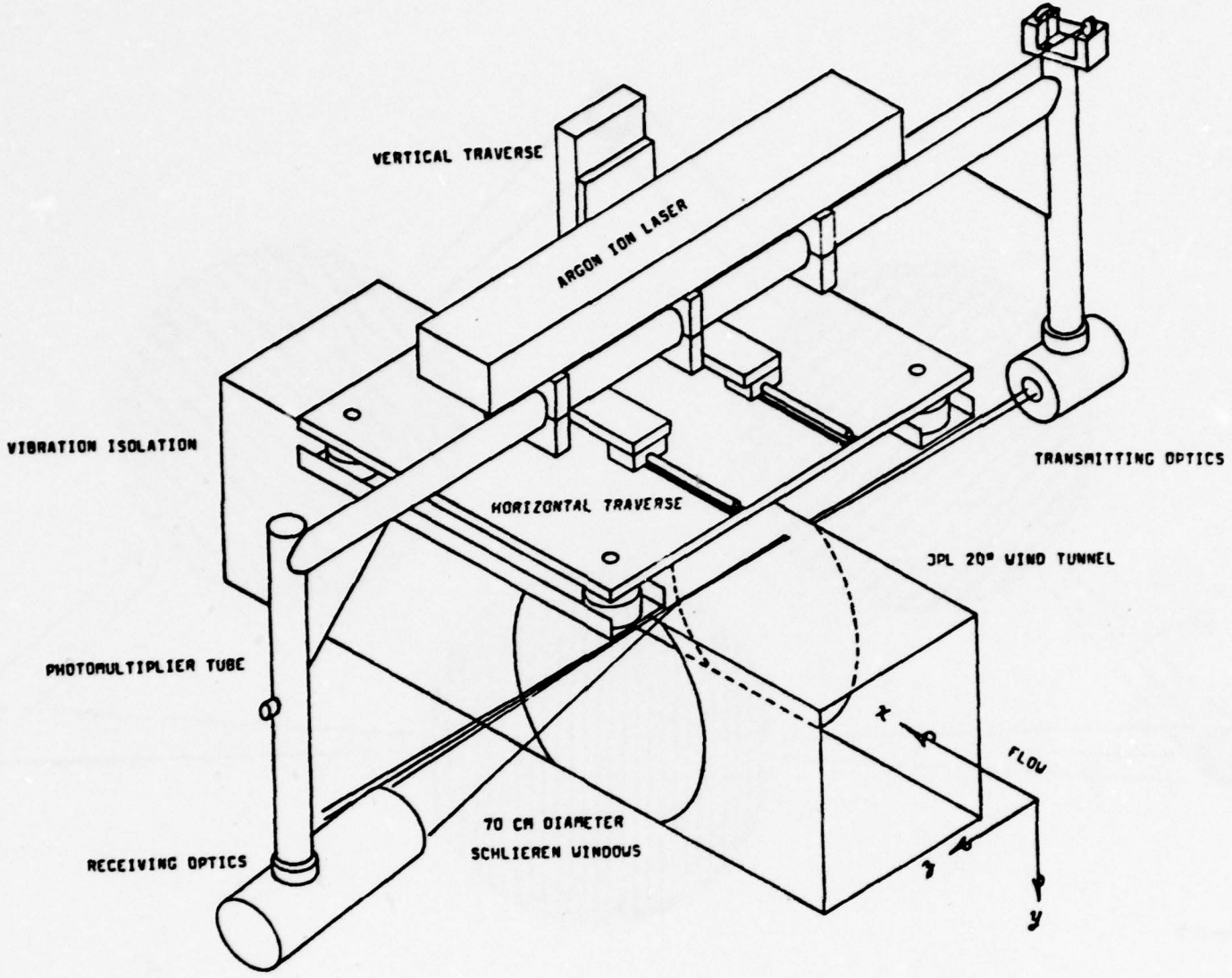

Figure 10. High-Speed Laser-Doppler Velocimeter.

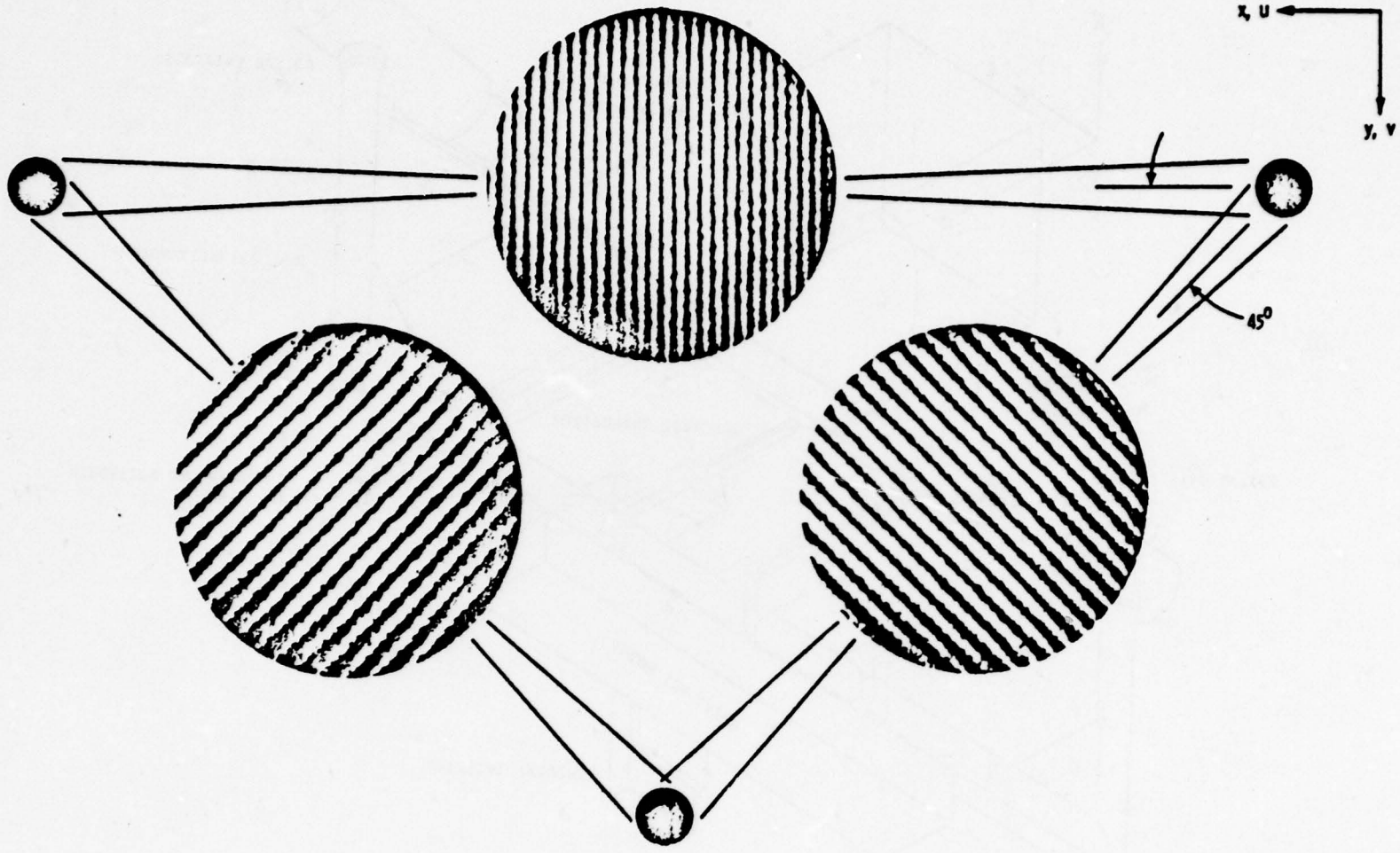

Figure 11. Optical Geometry and Fringe Patterns for Laser-Doppler Anemometer

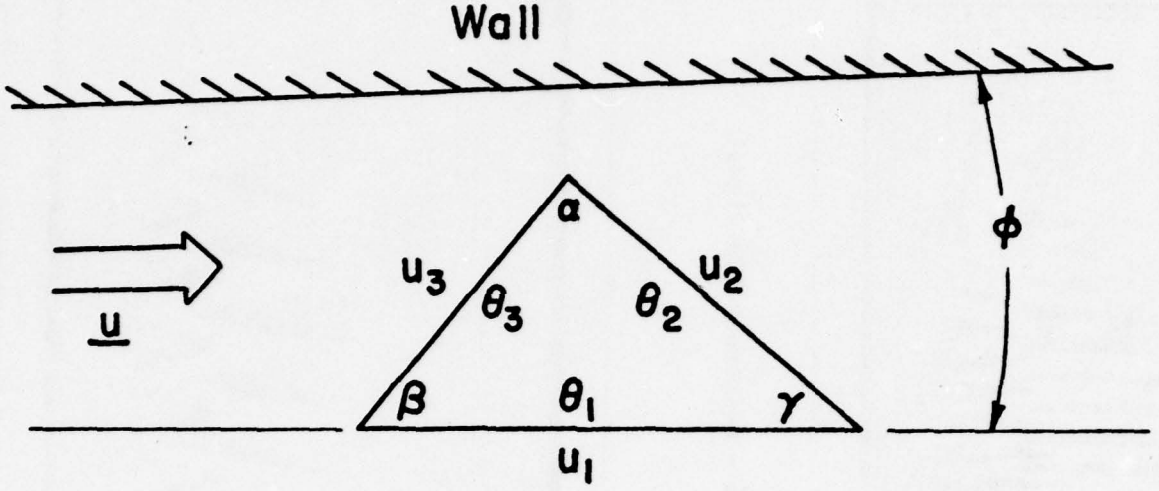

Figure 12. The Optical Geometry Relative to the Wall.

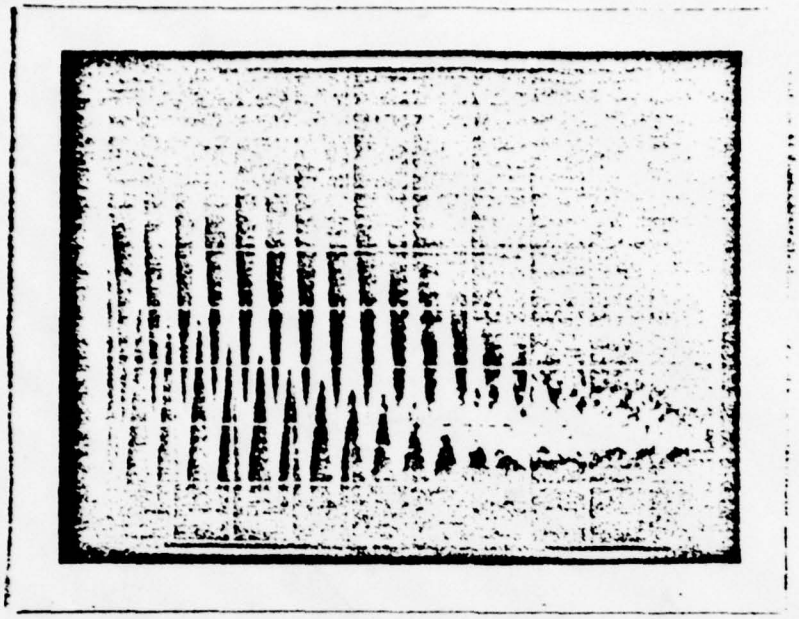

$\vec{u}$ - Component LDA Signal

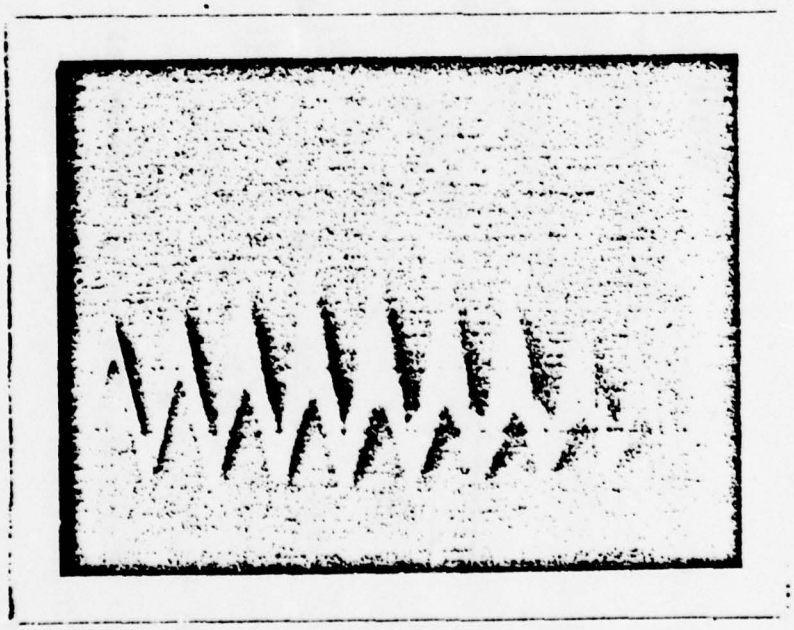

$\overrightarrow{(u + v)}$ - Component LDA Signal

Figure 13.
Laser-Doppler Anemometer Signals at the Outer Edge of a Turbulent Boundary Layer $M_\infty = 2.2$, $Re_\theta = 40{,}000$

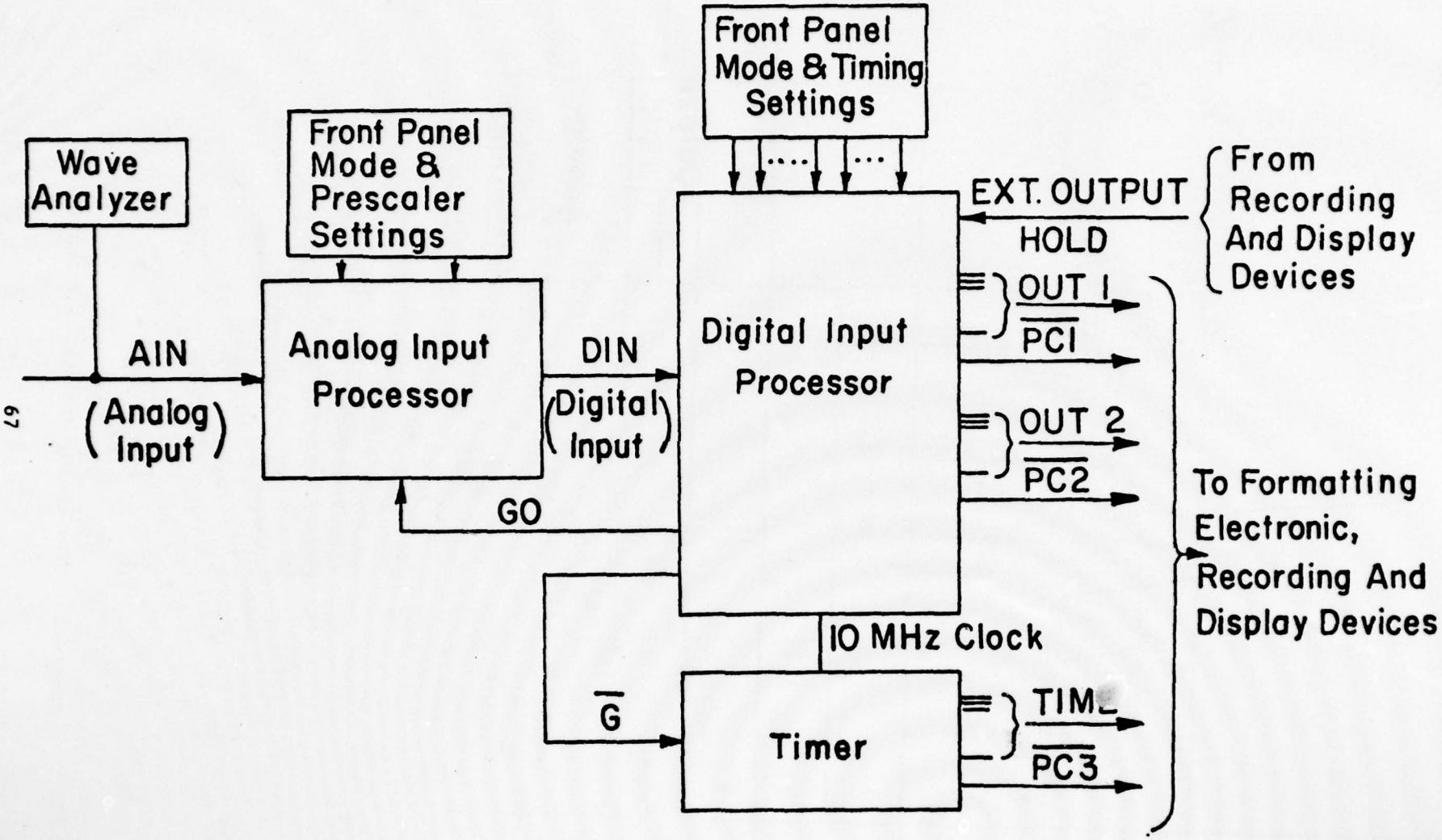

Figure 14. LDV Processor Block Diagram.

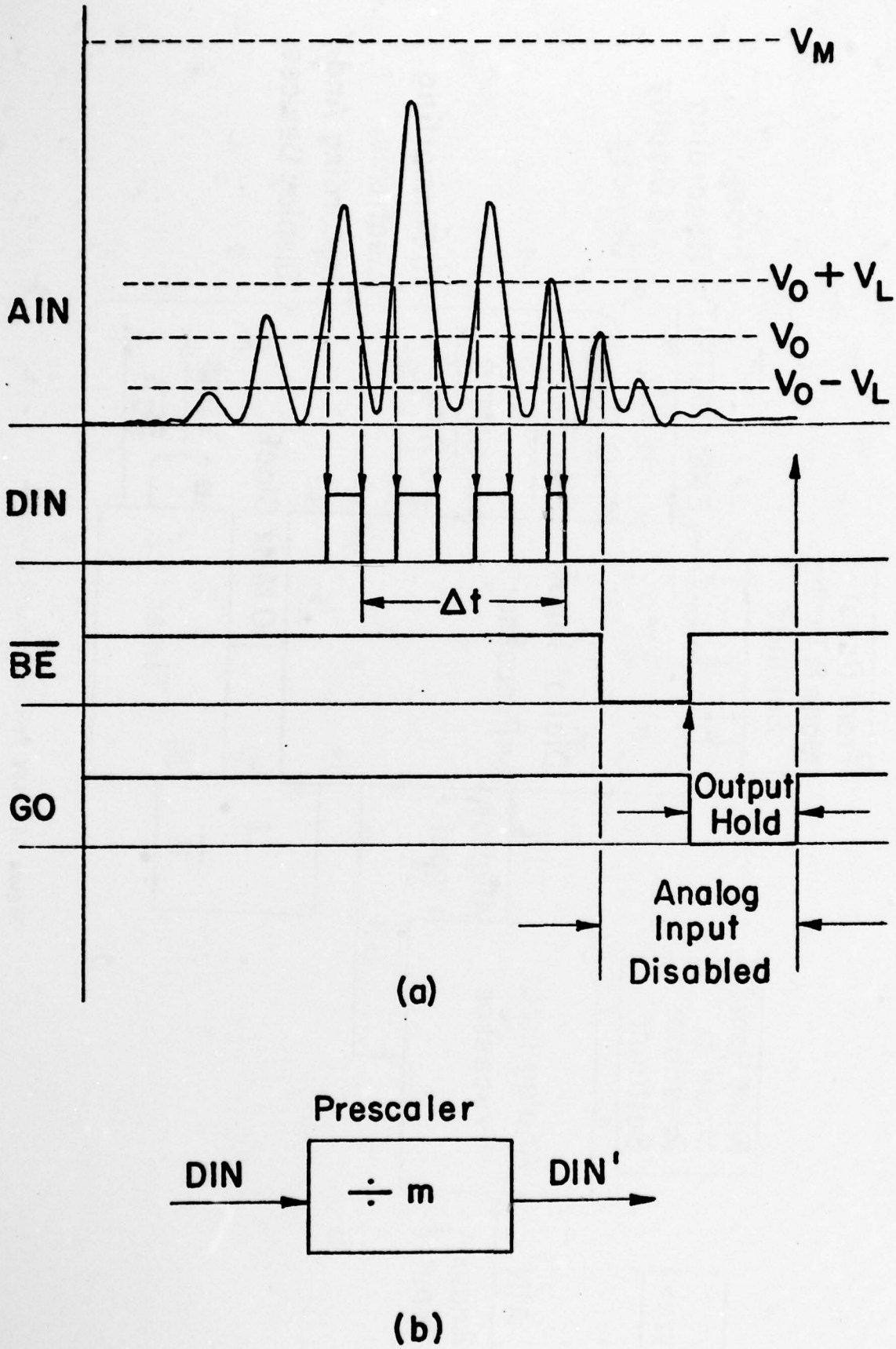

Figure 15. The Analog Processing Technique.

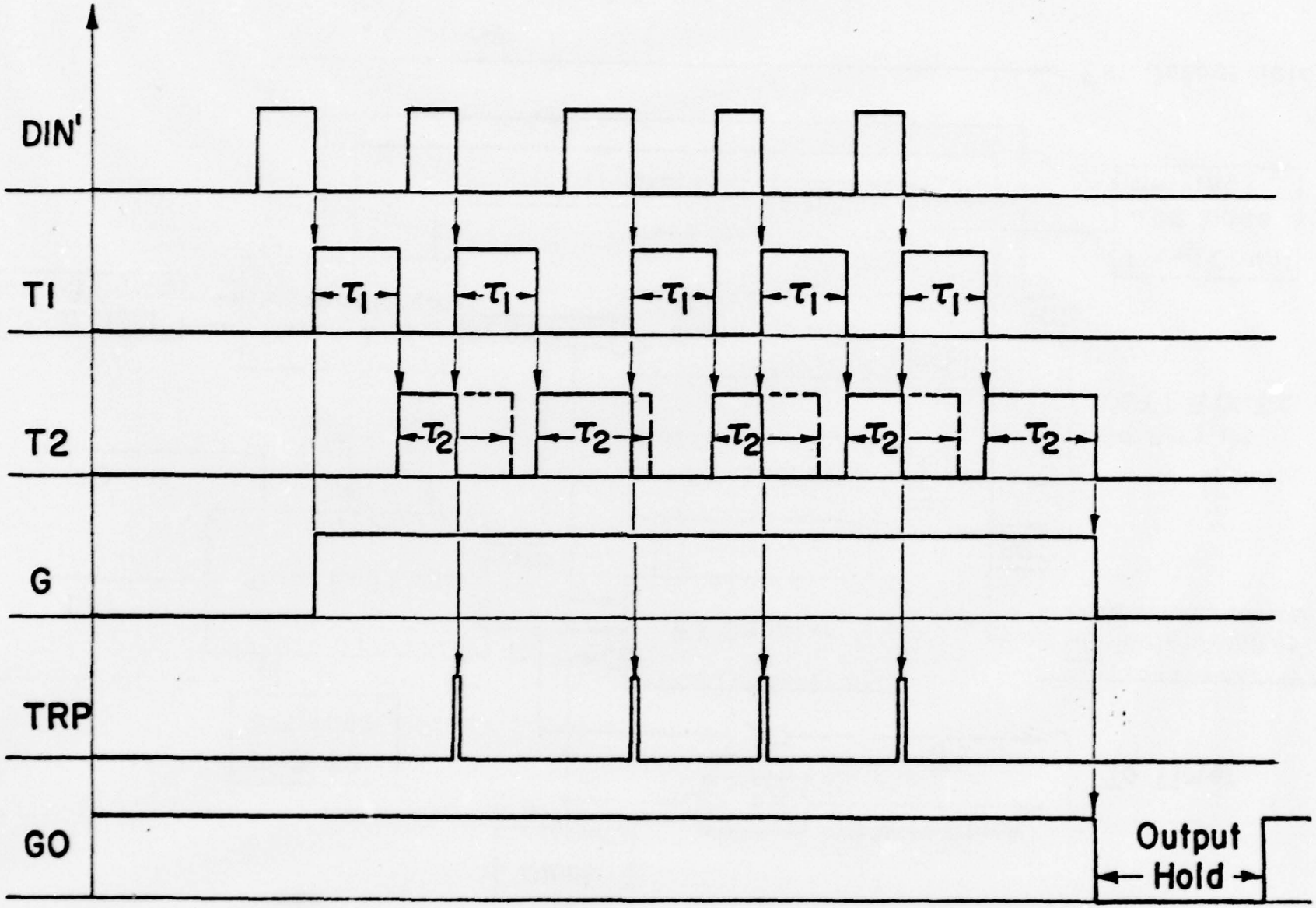

Figure 16. The Logic Associated with the Digital Input Processor.

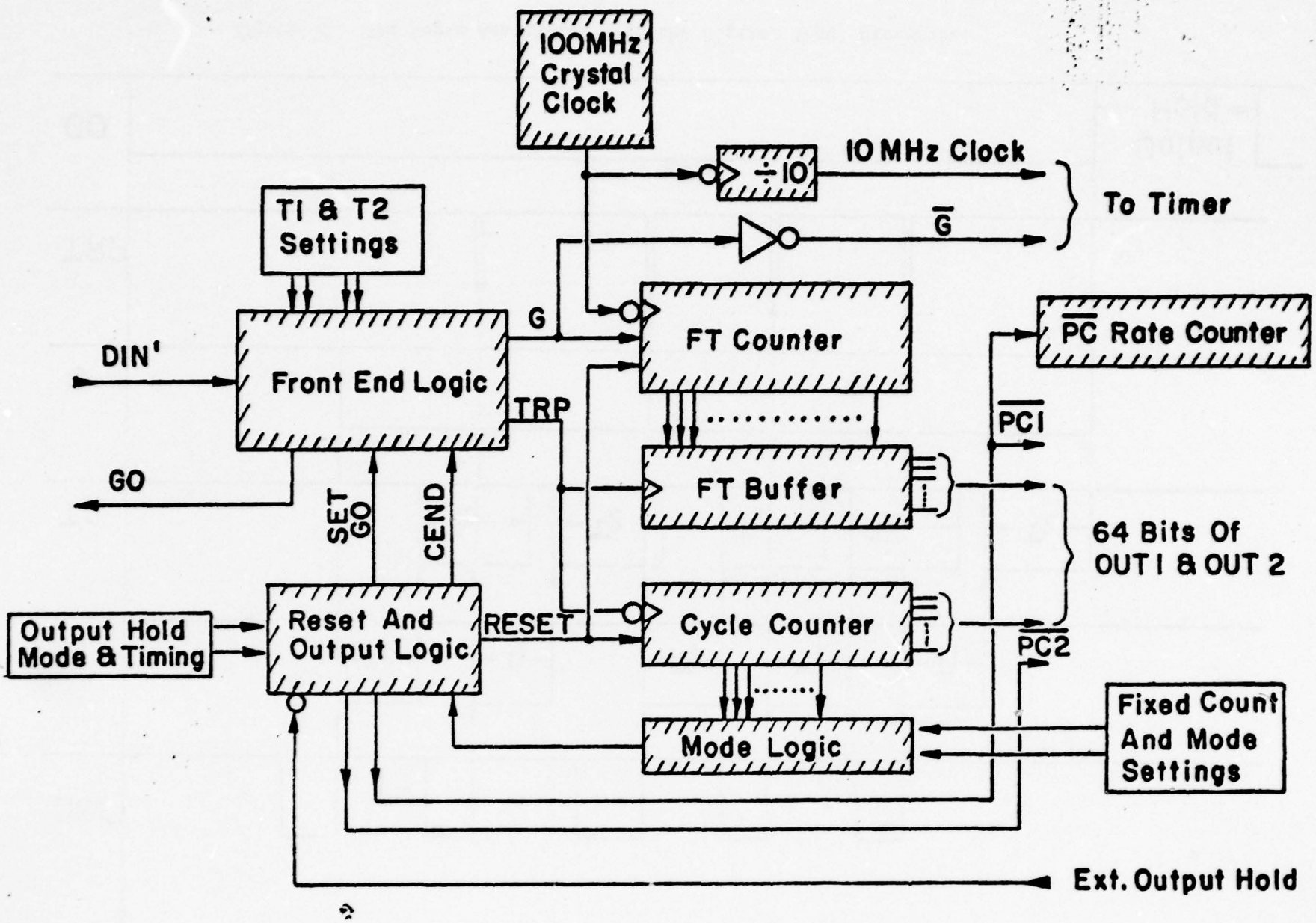

Figure 17. The Digital Input Processor.

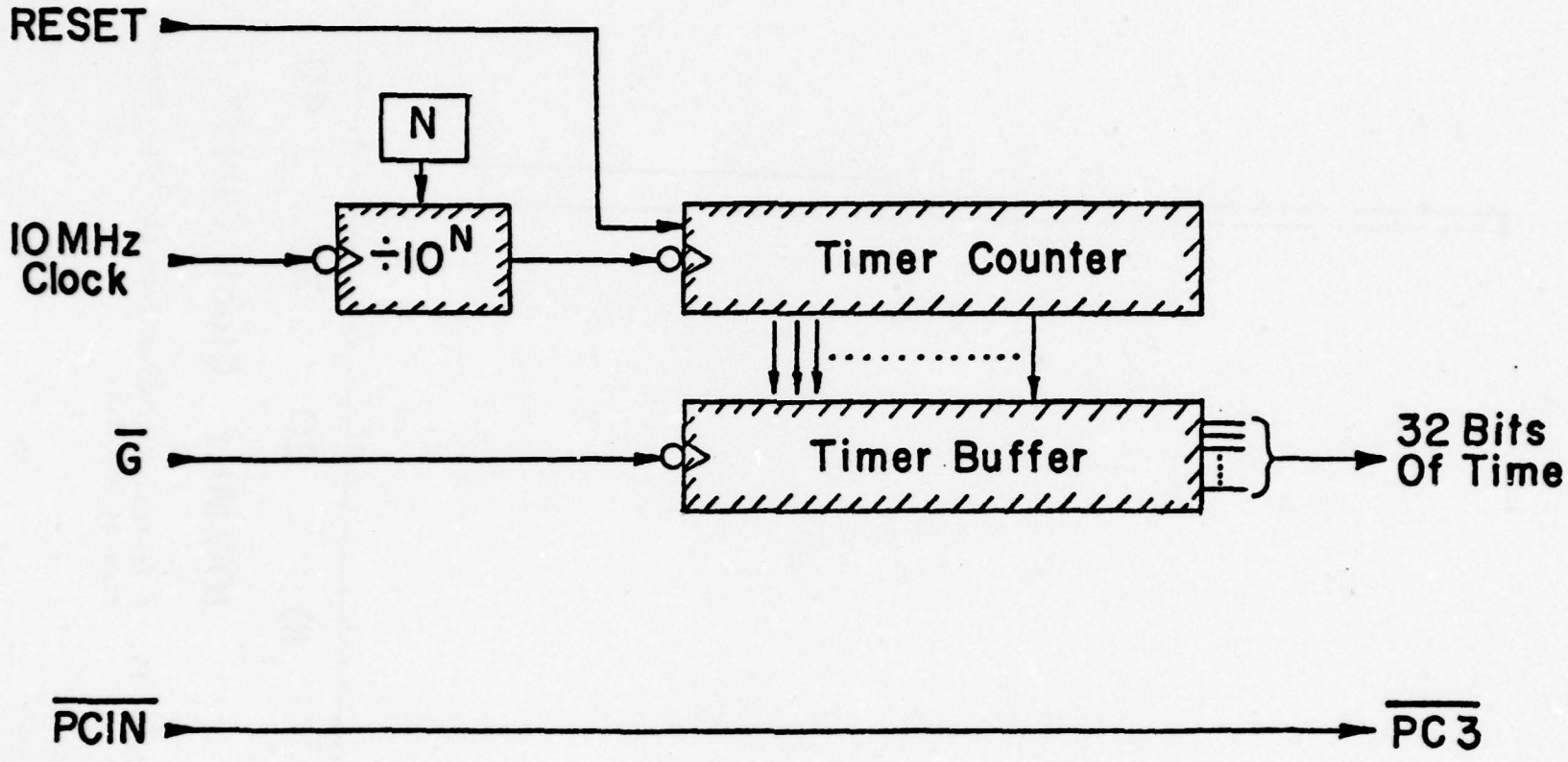

Figure 18. The Timing Circuit.

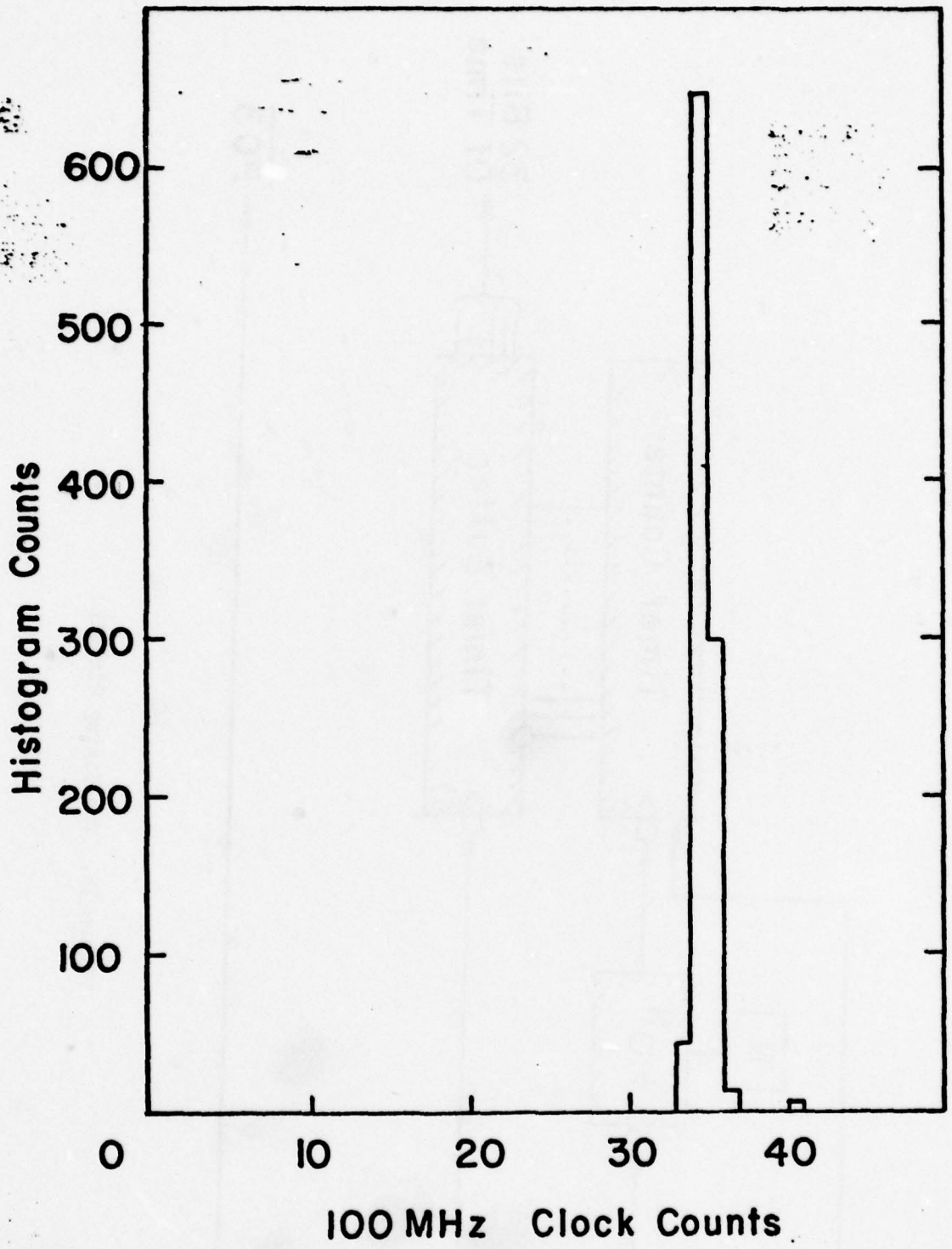

Figure 19. A Typical Histogram from the Free-Stream Flow at M ≃ 2.2.

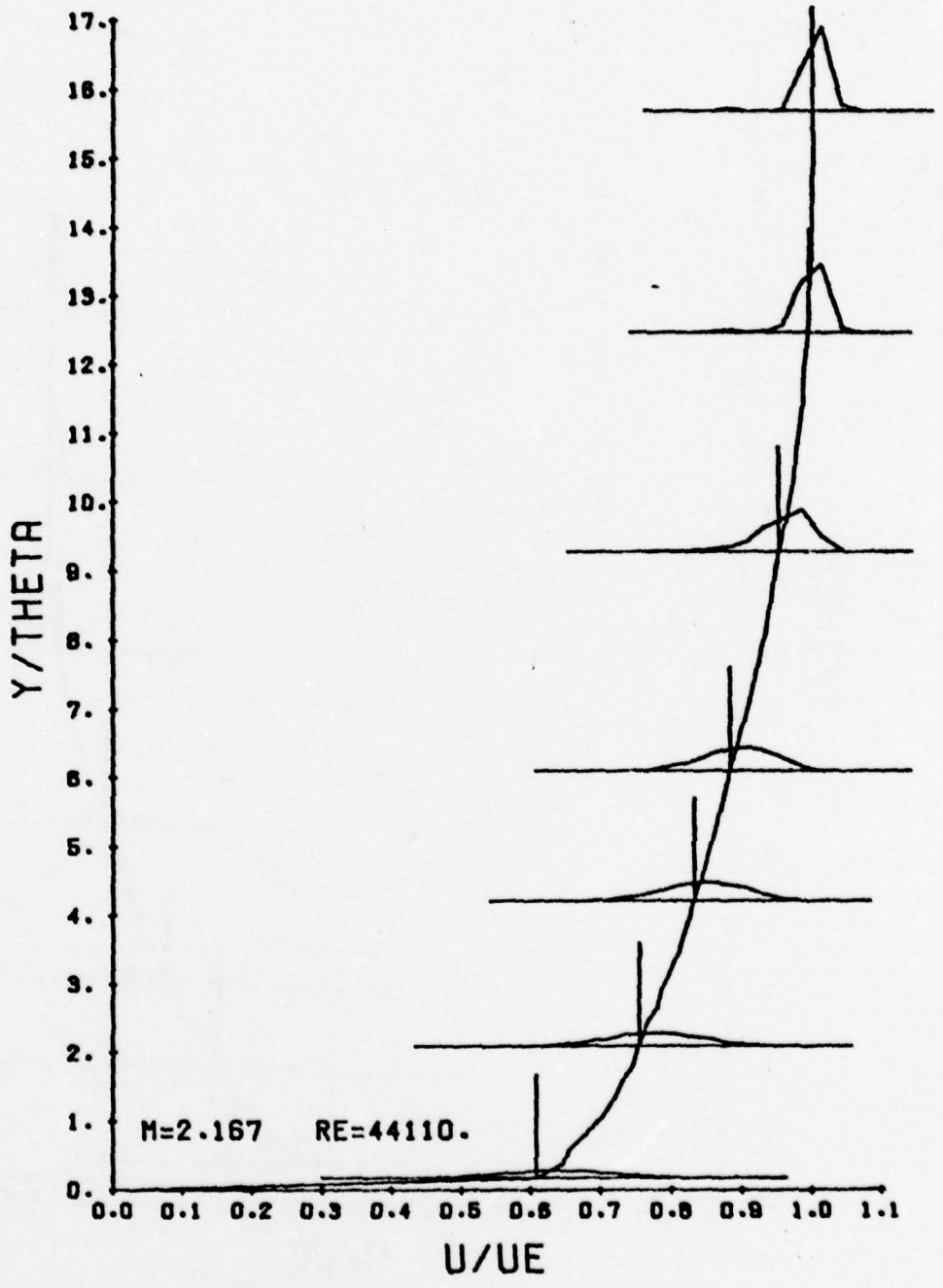

Figure 20. Representative Histograms from the High-Speed Boundary Layer.

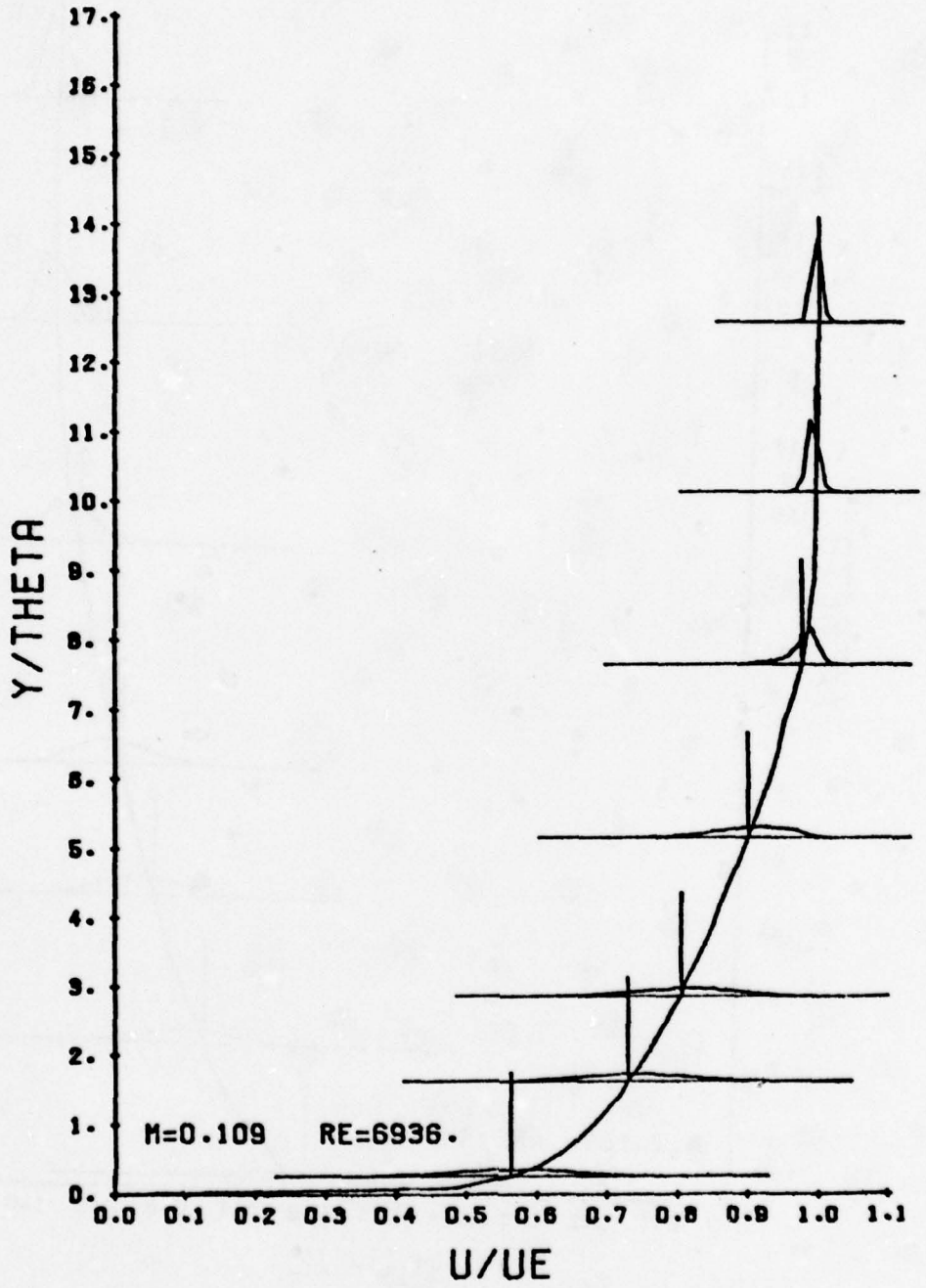

Figure 21. Representative Histograms from the Low-Speed Boundary Layer.

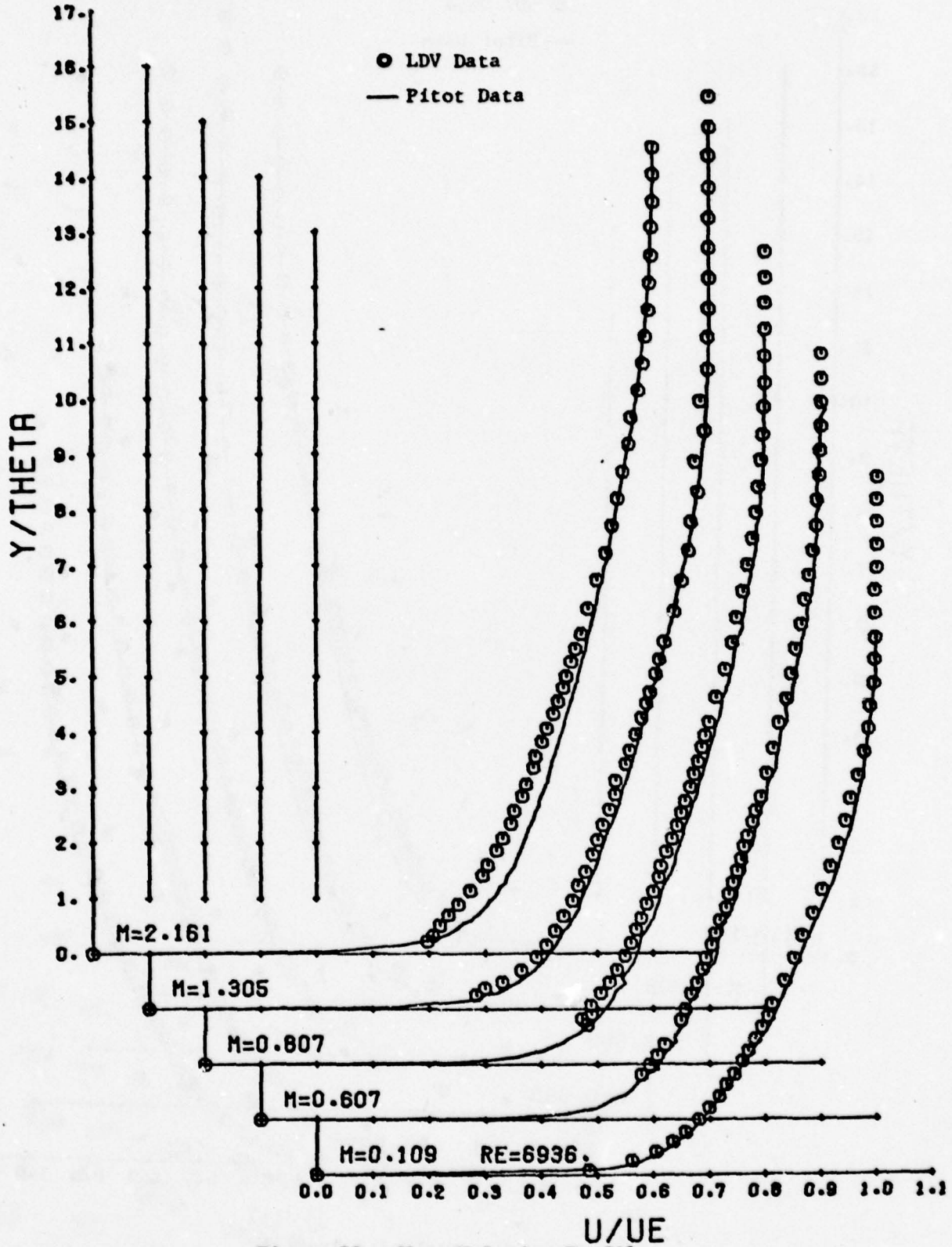

Figure 22. Mean Velocity Profiles.
Re_θ = 23,000

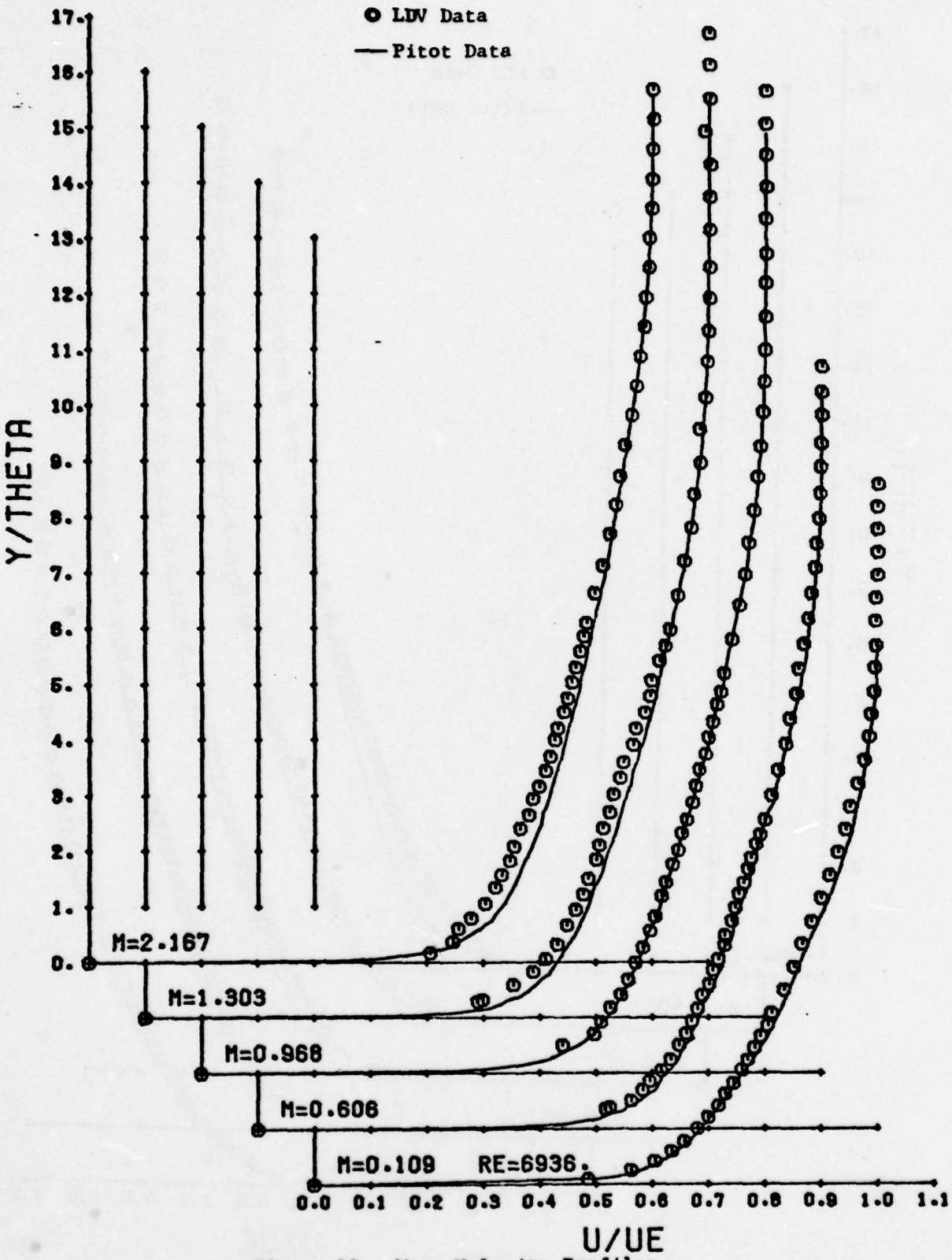

Figure 23. Mean Velocity Profiles
Re_θ = 40,000

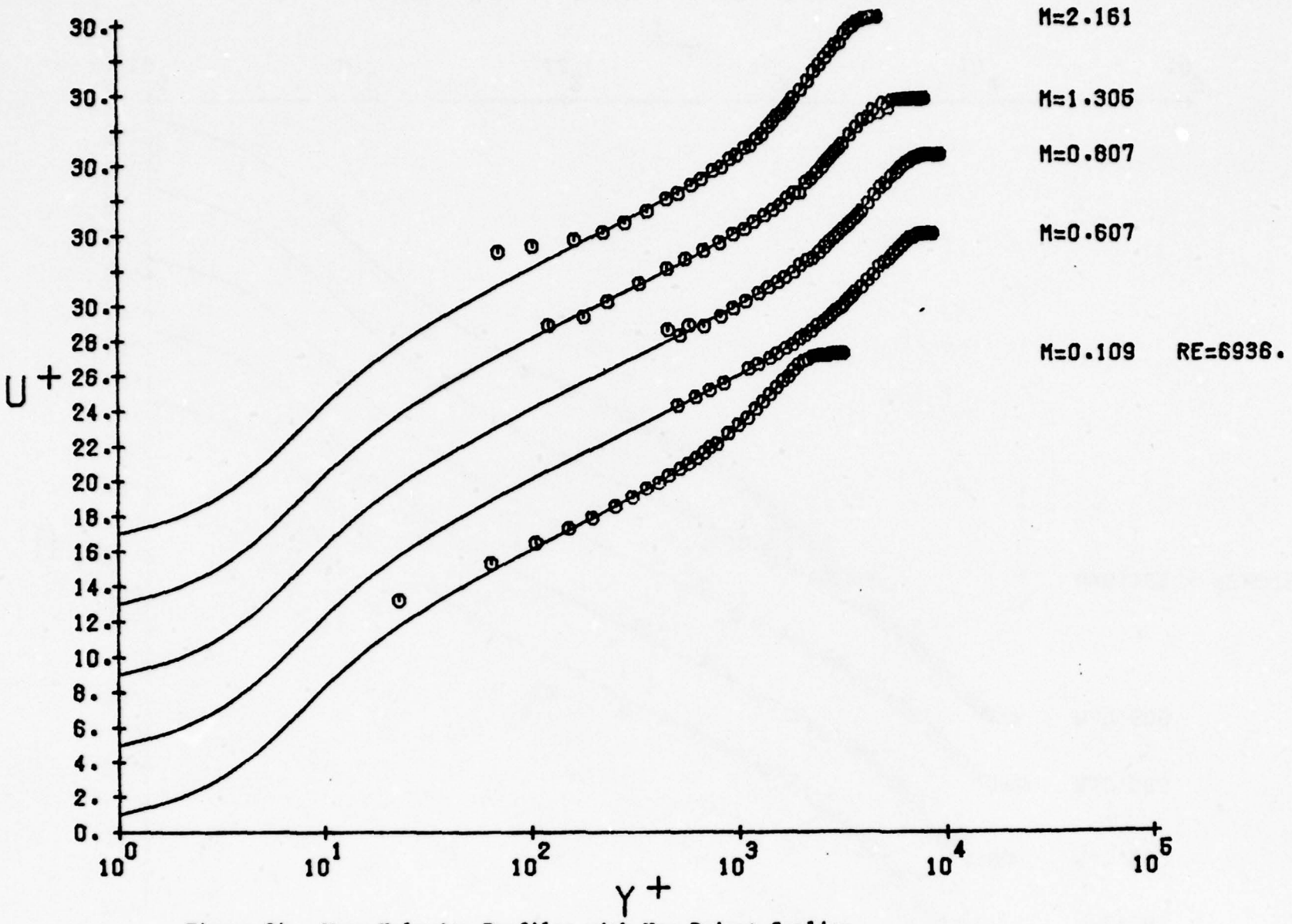

Figure 24. Mean Velocity Profiles with Van Driest Scaling
Re_θ = 23,000

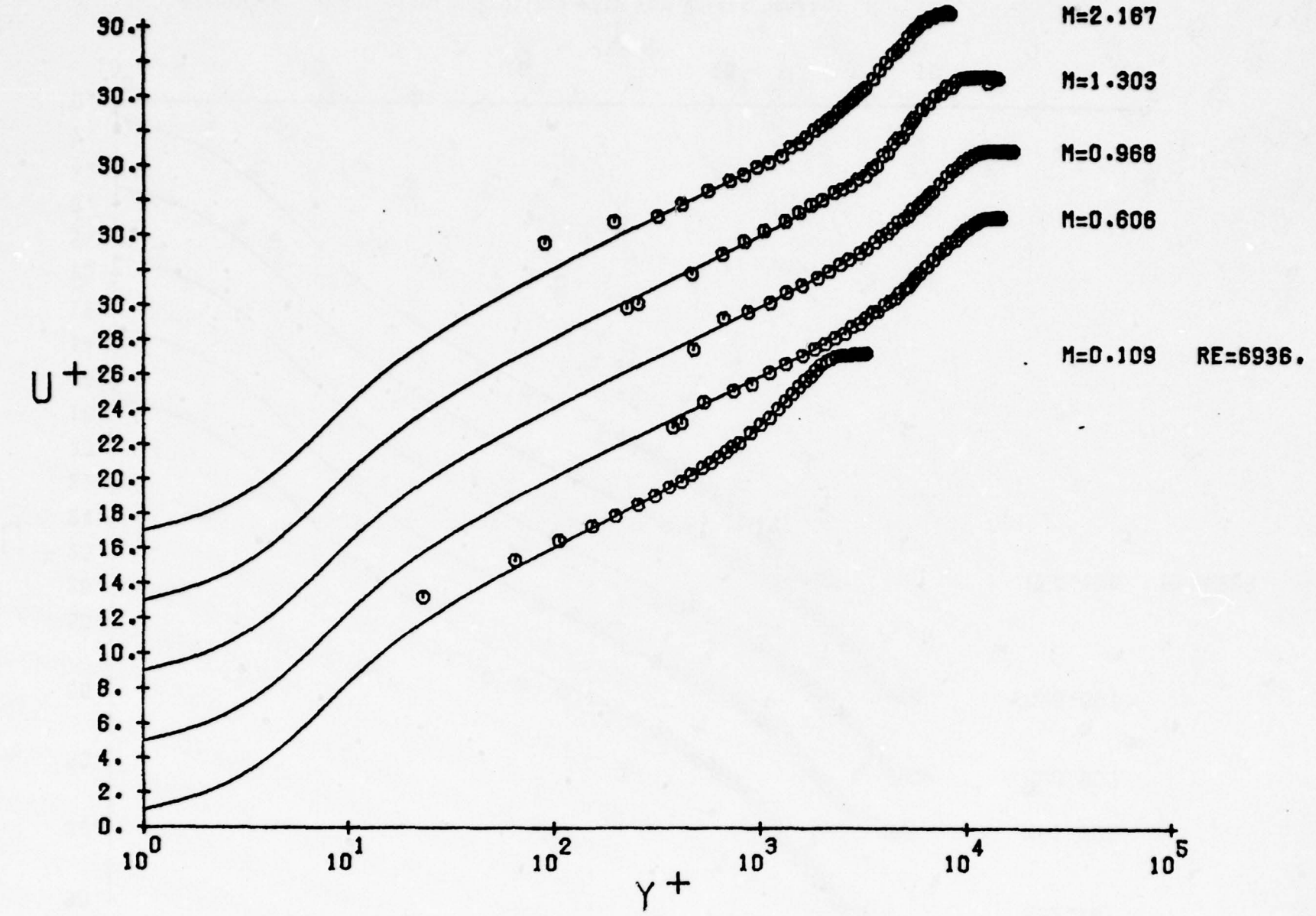

Figure 25. Mean Velocity Profiles with Van Driest Scaling.
Re_θ = 40,000

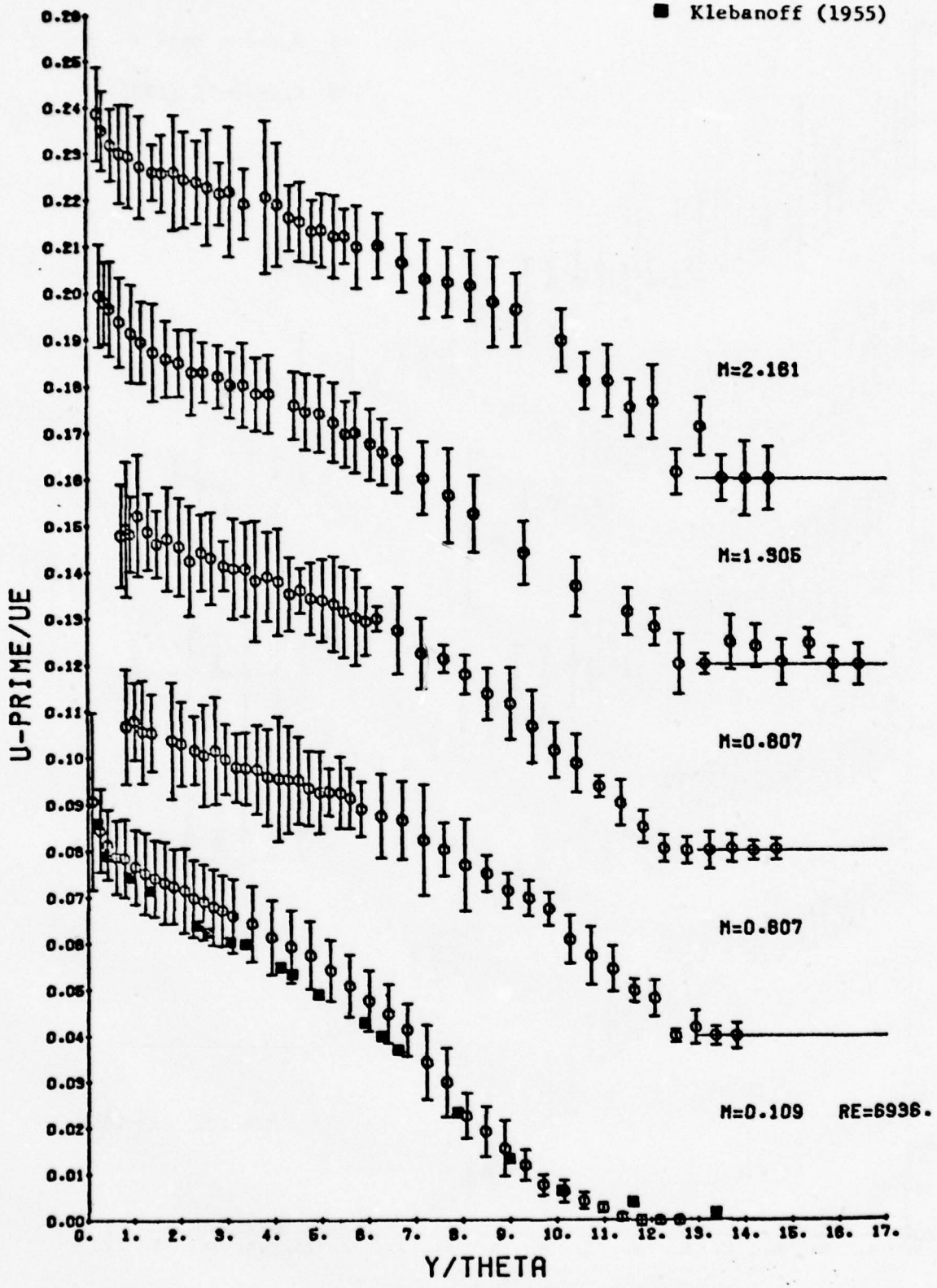

Figure 26. The Streamwise Velocity Fluctuations
Re_θ = 23,000

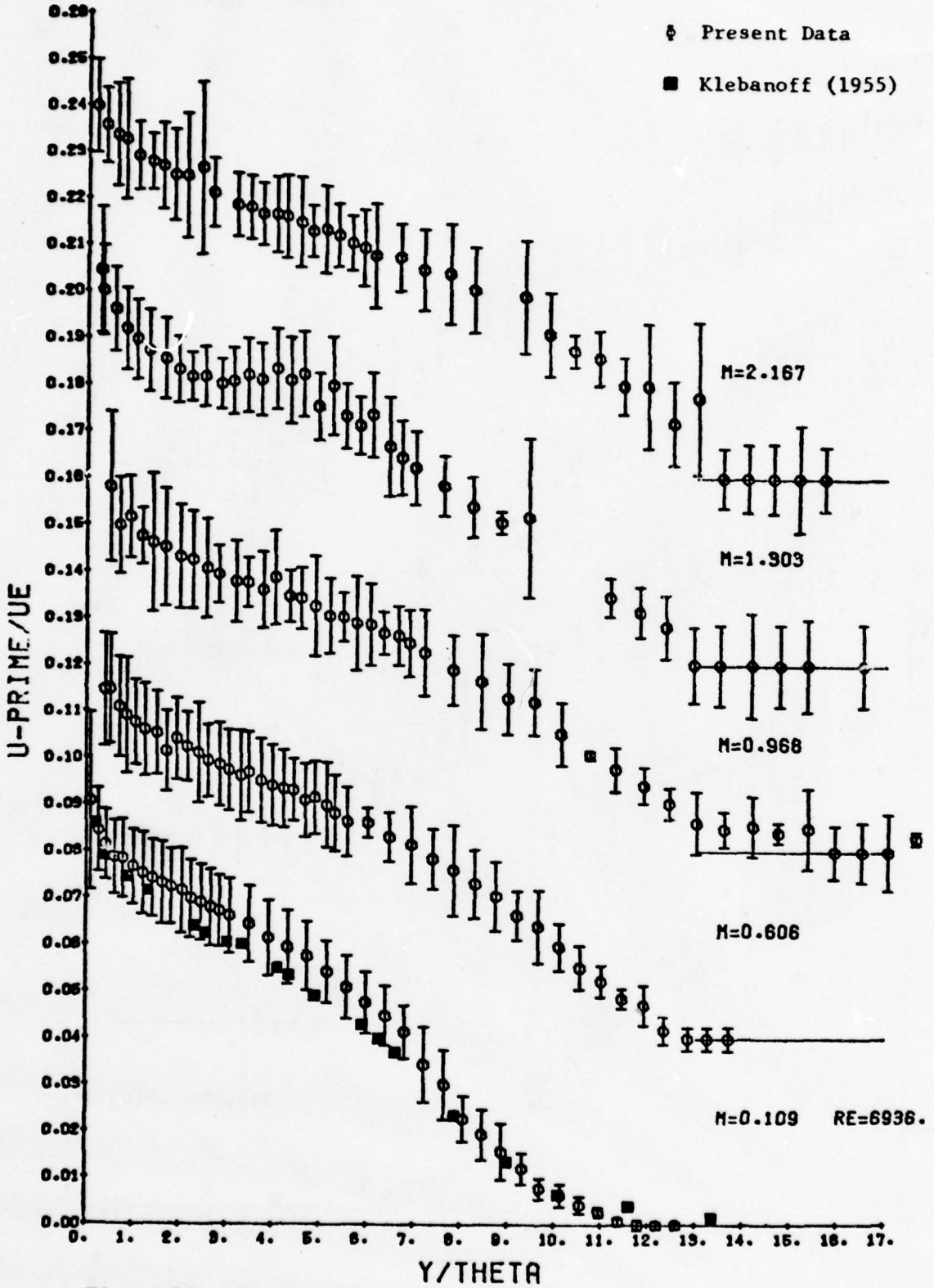

Figure 27. The Streamwise Velocity Fluctuations
Re_θ = 40,000

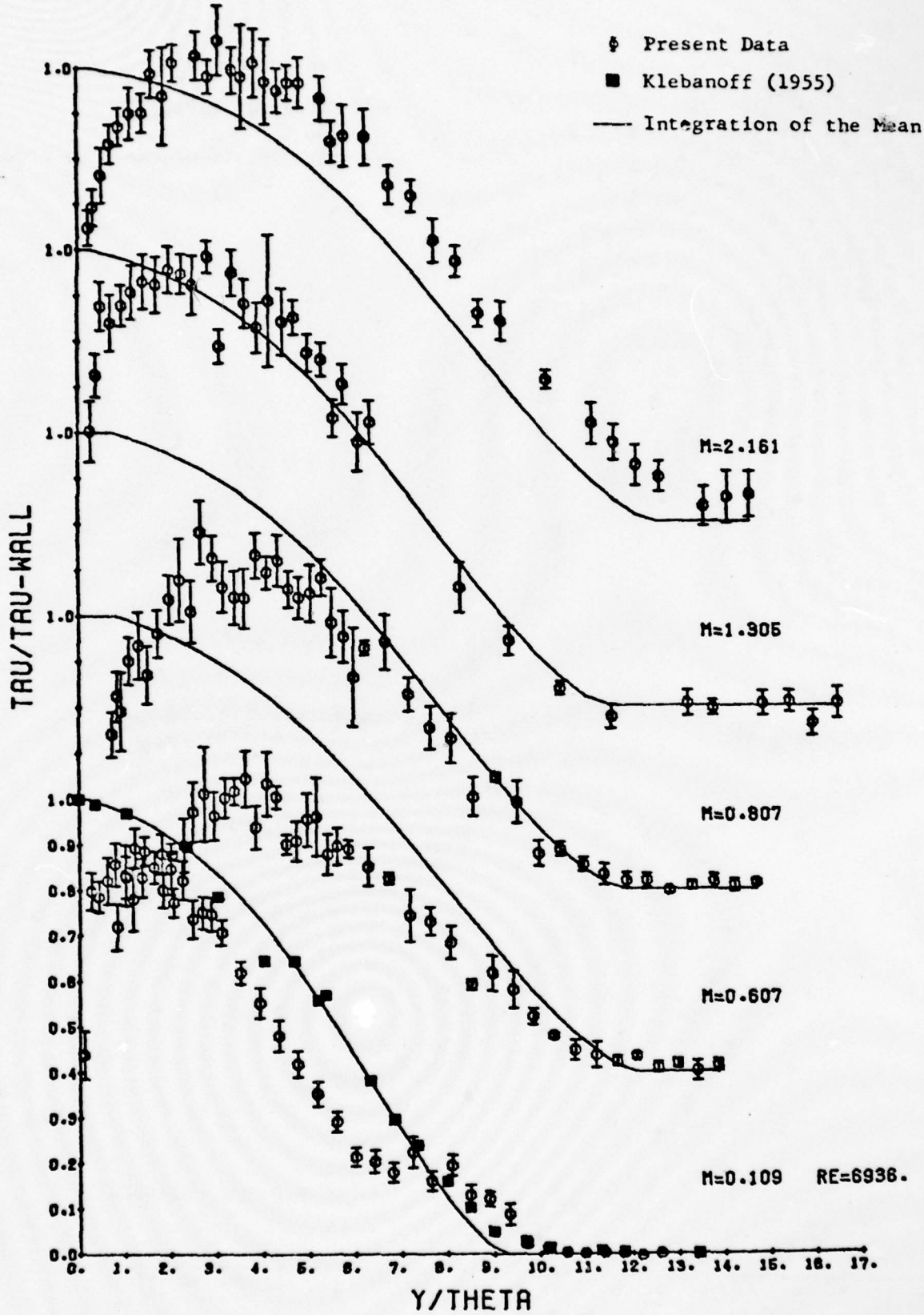

Figure 28. The Distribution of Reynolds Stress
Re_θ = 23,000

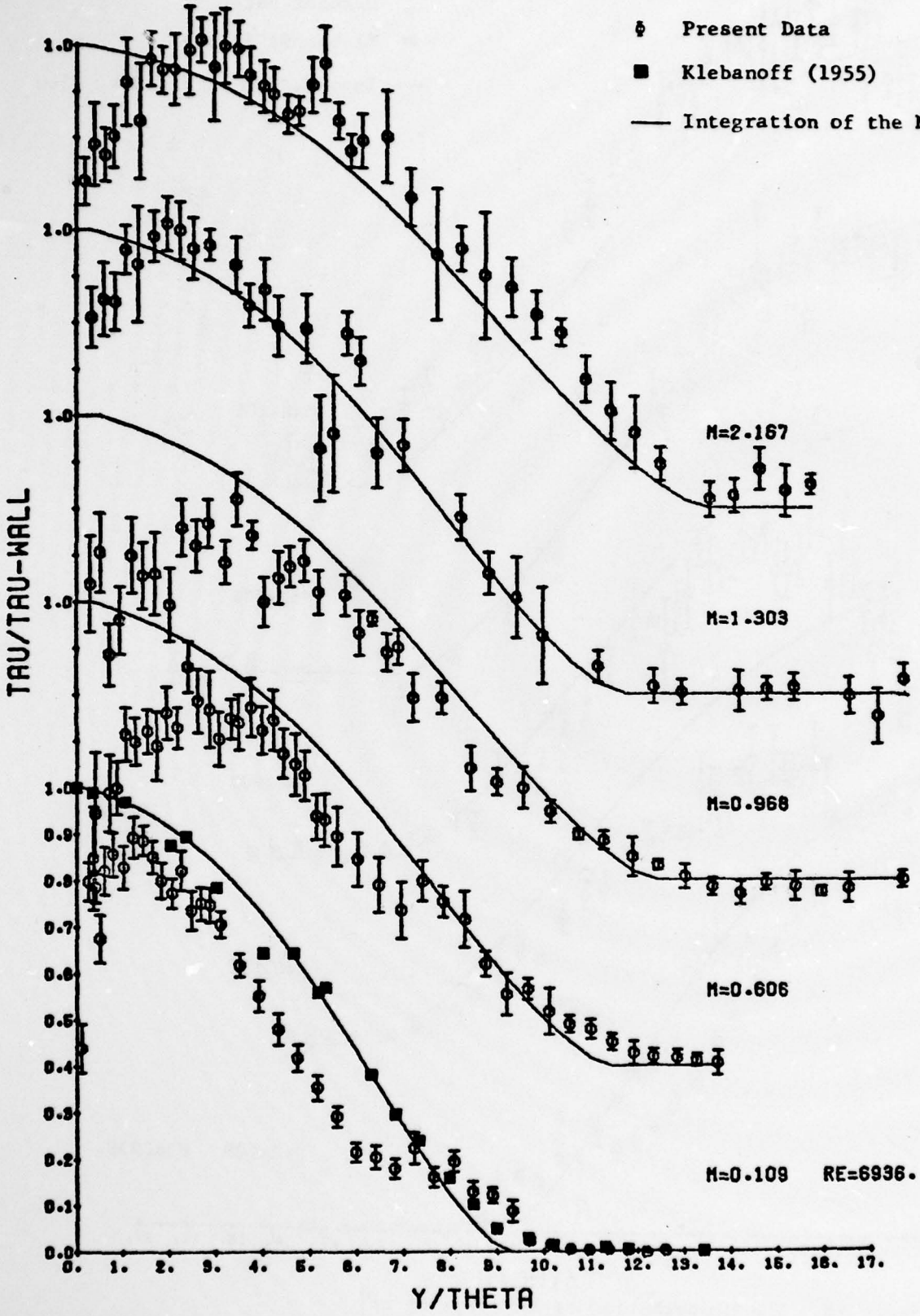

Figure 29. The Distribution of Reynolds Stress
Re_θ = 40,000

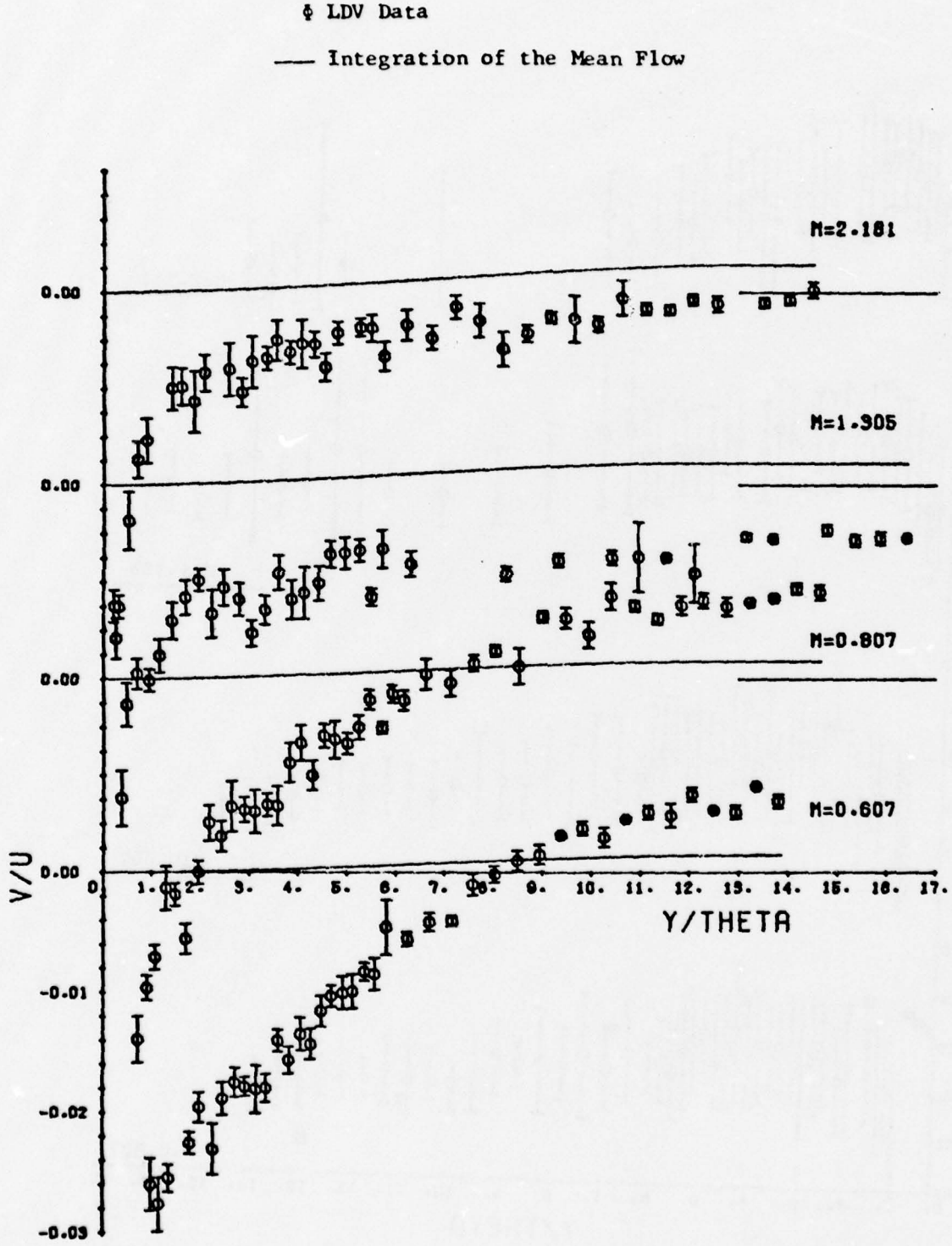

Figure 30. The Distribution of Normal Velocity. Re_θ = 23,000.

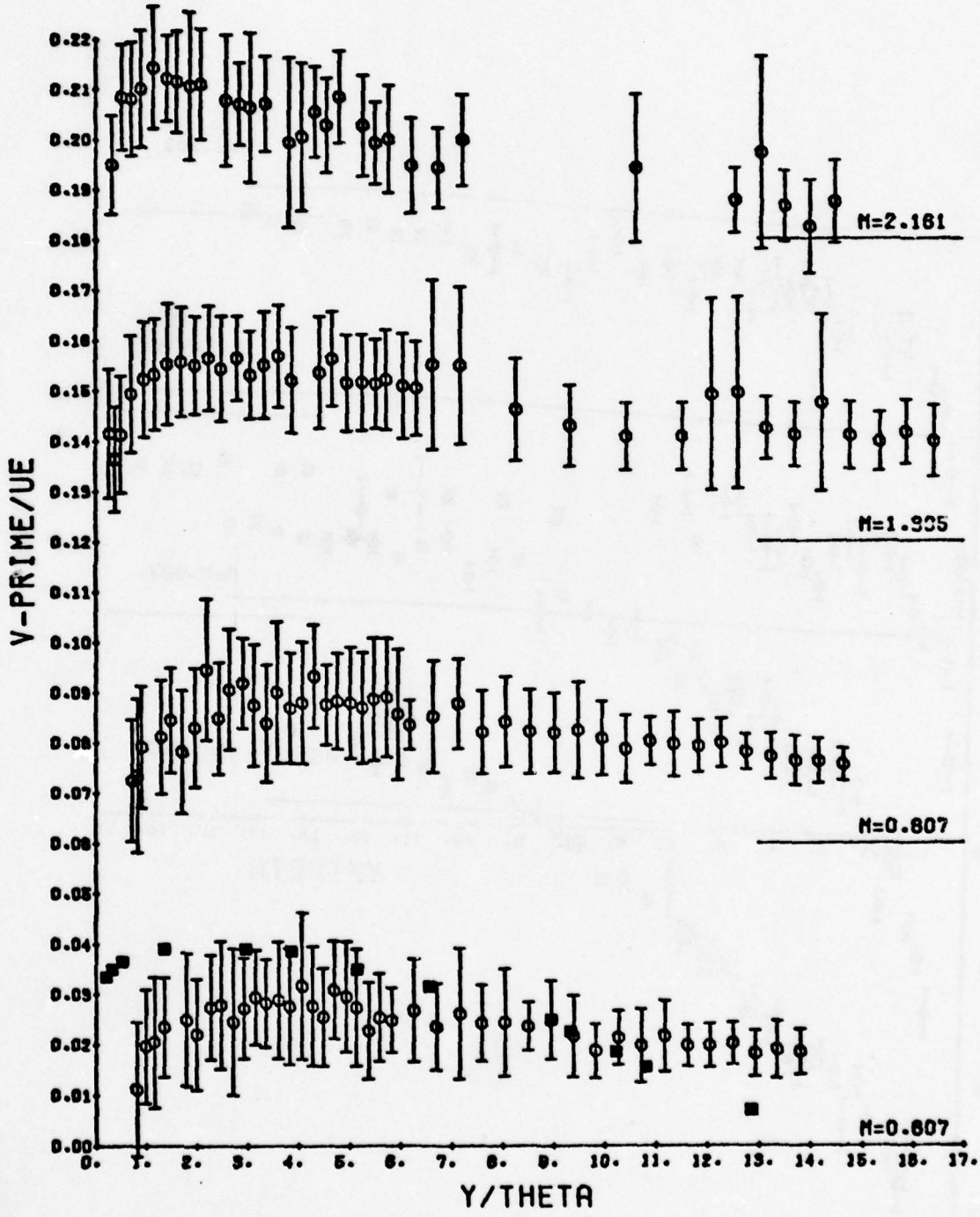

Figure 31. The Distribution of the Normal-Velocity Fluctuations. Re_θ = 23,000.

Nomenclature

Symbol	Equation	Meaning
c	(22)	constant in wall law (5.0)
C_f	(84)	local friction coefficient
d_p	(7)	particle diameter
k_i		integer output of the flight time counter
n	(21)	particle number density
n_i		number of observations with velocity u_i
Re_θ		Reynolds number based on θ
s	(2)	fringe spacing
u, v		streamwise and normal velocity components
u_i	(29)	velocity component in i^{th} direction
u_τ	(18)	friction velocity
$u_\perp$	(1)	velocity component normal to the fringe plane
$u_\parallel$		velocity component parallel to the fringe plane
x, y		streamwise and normal coordinates
α, β, γ, ϕ	Figure 12	angles defined by the beam planes
$\beta(u)$	(49)	bias function
δ	(26)	boundary-layer thickness
θ	(77)	boundary-layer momentum thickness
θ_i	Figure 12	beam separation angles
$\varkappa$	(22)	Kármán constant (0.41)
λ		laser wave length (0.5145 μm)
μ		viscosity
ν		kinematic viscosity

Nomenclature (Cont.)

Symbol	Equation	Meaning
ν_D	(1)	Doppler frequency
Π	(22)	strength of the wake component
τ_c	(5)	processor clock period
τ_p	(8)	particle response time
τ_w		shear stress at the wall

Subscripts

$( )_e$	edge or external value
$( )_f$	pertaining to the fluid
$( )_p$	pertaining to the particles
$( )_w$	wall value
$( )'$	*rms* fluctuations

Superscripts

$( )^+$	value made dimensionless with u_τ, ν_w

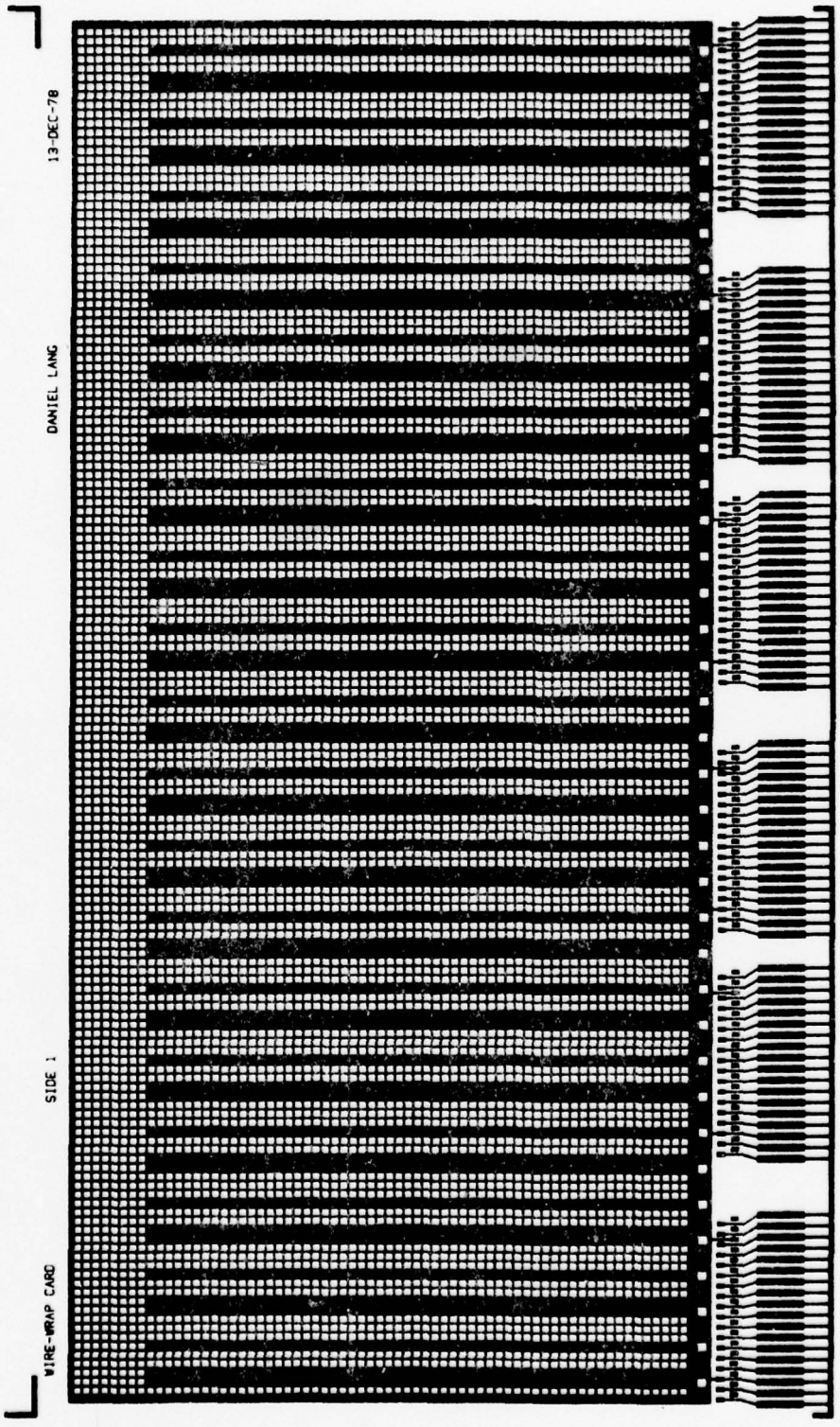
WIRE-WRAP CARD
SIDE 1
DANIEL LANG
13-DEC-78

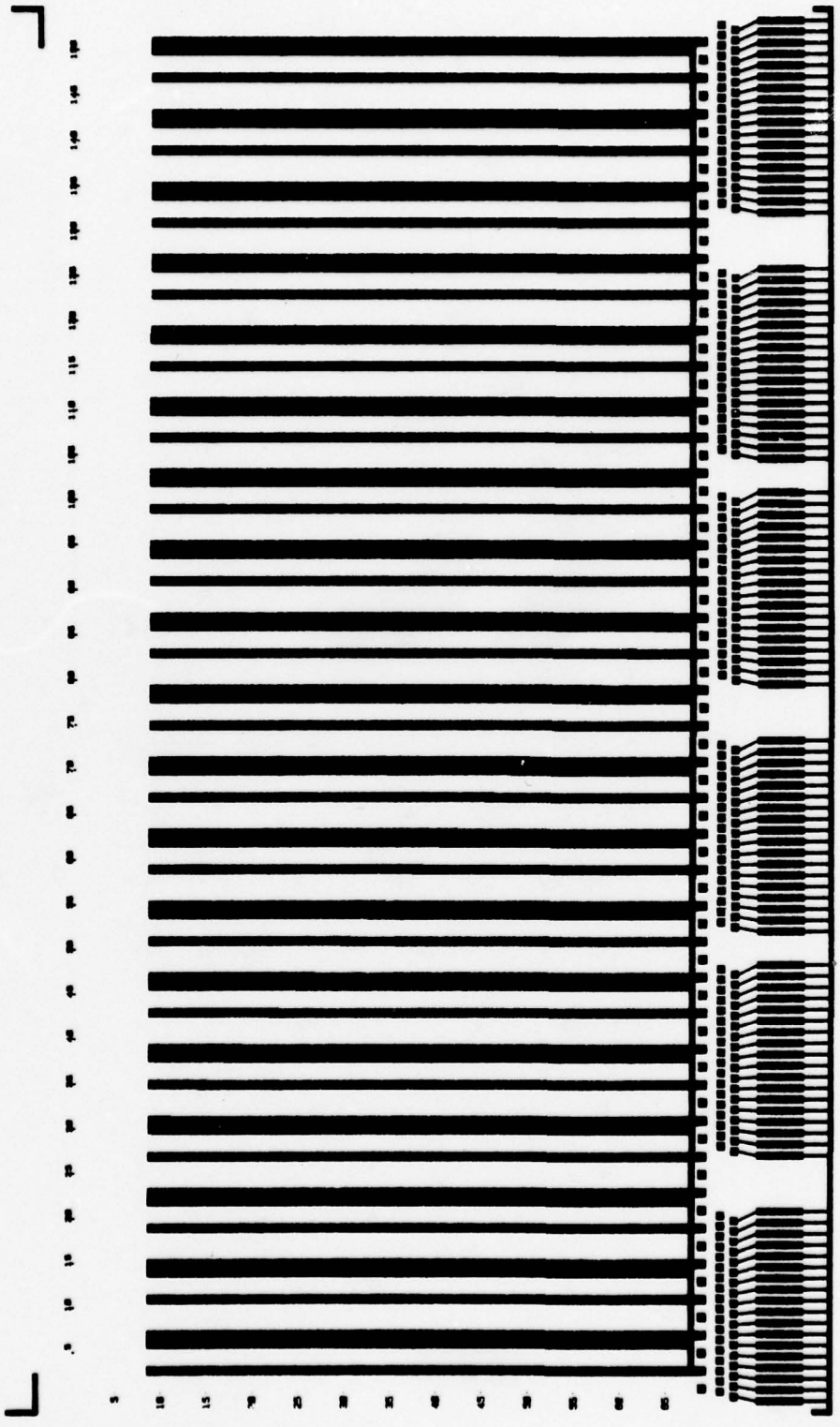

Two-Point LDV Measurements in a Plane Mixing Layer

M. M. Koochesfahani*, C. J. Catherasoo*, P. E. Dimotakis**, M. Gharib* and D. B. Lang†

California Institute of Technology, Pasadena, California

Investigations into the nature of the large structures in a two-dimensional shear layer were carried out using Laser Doppler velocimetry in the GALCIT Free Surface Water Tunnel. By simultaneous measurements of velocity at two points outside the turbulent region, above and below the shear layer, it was possible to measure the strength (total circulation) and the location of the vorticity center of the large structures. It was found that structures not in the process of pairing convect downstream with the center of their cores close to the ray y/x along which the mean velocity $U_m = \frac{1}{2}(U_1 + U_2)$. The determined value of the mean circulation is consistent with the independent measurements of the mean spacing between the structures. Results indicate that if the large structure vorticity distribution is elliptical, the inclination angle of its axis of symmetry with respect to the flow direction is small.

---

*Graduate Student, Department of Aeronautics. Member AIAA.

**Assistant Professor, Aeronautics and Applied Physics. Member AIAA.

†Graduate Student, Department of Applied Physics

June 27, 1979

1. Introduction

In a recent experiment[1], the induced streamwise velocity fluctuations due to the passage of vortical structures in a two dimensional shear layer were measured at a point just outside the mixing layer. Such a velocity record, however, (see figure 1), provides ambiguous information about the strengths and the core positions of the vortical structures, since the induced velocity due to the passage of a strong vortex far from the measuring station, is indistinguishable from that due to a weaker vortex passing close to the measuring station.

To resolve this ambiguity, simultaneous measurements at two points were performed, above and below the shear layer, to allow the circulations (strength) and core position of the vortical structures to be determined.

2. Apparatus, instrumentation and data processing

a. Apparatus and the resulting flow field

The flow apparatus and the resulting shear layer have been documented in Ref. 1.

From the measured mean velocity profiles ($U_s/U_1 \simeq 0.19$), the vorticity (maximum slope) thickness δ_ω, normalized with the distance downstream from the splitter plate x, was found to be

$$\frac{\delta_\omega}{x} \simeq 0.10 \ . \qquad (1)$$

The data presented in this paper were taken at x = 30 cm with U_1 = 56 cm/s. These parameters yield a Reynolds number, defined by $\frac{\Delta U \delta_\omega}{\nu}$, of 1.4×10^4 at the measuring location, where ΔU is the velocity difference across the mixing layer. Note that the shear layer is fully turbulent at this Reynolds number.

b. LDV optics and electronics

The streamwise component of velocity was measured at the two points by a single-particle Laser-Doppler velocimeter in the dual scatter mode. The two pairs of beams were generated by passing the laser beam through two cube beam-splitters at right angles (fig. 2). The two focal volumes (measuring stations) were located at the high-speed and low-speed edges of the mixing layer, respectively (see fig. 3).

The outputs of the two photodetectors were time-multiplexed at the input of a single LDV processor. The processor has been described in Ref. 1.

c. Data processing

The velocity data were low-pass filtered digitally according to the algorithm

$$\tilde{U}(t_m) = \sum_n h(t_m - t_n)\, U(t_n)\, \delta t_n \qquad (2a)$$

$$\delta t_n = t_n - t_{n-1}\,, \qquad (2b)$$

where h is the (normalized) filter function, U the unfiltered, randomly sampled, velocity data and $\tilde{U}$ is the filtered velocity data. The summation over n is such that $-T_f \le t_m - t_n \le T_f$ where $2T_f$ is the total width of the filter $h(t)$.

A Gaussian, low-pass filter was used. The filtered data were sampled uniformly. See fig. 4.

3. Data Reduction

a. Model

Recent measurements have shown[1,2,3,4,5,6] that the two-dimensional shear layer is characterized by an array of large vortical

structures, which are convected downstream with a velocity U_c, approximately given by $U_c \simeq \frac{1}{2}(U_1 + U_2)$. Now, in a frame moving with U_c, the induced velocities u_H, u_L, at the points (x, b) and $(x, -b)$ respectively, when the center of vorticity of a particular structure is at (x, c), are given by

$$u_H = \frac{\Gamma}{2\pi} \frac{1}{b-c} \tag{3a}$$

$$u_L = -\frac{\Gamma}{2\pi} \frac{1}{b+c} \tag{3b}$$

where Γ is the total circulation of the vortical structure. Note that Γ is defined to be positive for an induced velocity in the clockwise sense. Note also that the absolute values of the induced velocities reach a maximum at the instant the center of vorticity is on the line joining the measuring points. In this model the effect of neighboring structures is neglected. It can be shown, however, that the resulting overestimation of the circulation Γ is of the same order as the underestimation of Γ caused by neglecting the expected higher moments (quadrupole moment) of the vorticity distribution. The effect of the quadrupole moment was estimated using the data in Fig. 6a of Ref. 2.

Using this model, an isolated, well-defined local maximum in the velocity measured on the high-speed side, associated with a corresponding well-defined local minimum on the low-speed side, was interpreted as the signature of the passage of a single vortical structure not in the process of pairing. If additional significant disturbances were discernible in the maximum-minimum pair (interpreted as resulting from the presence of additional vortical structures), the pair was not included in the data.

By way of example, only the data at t = 0.65, 0.98, 1.33, 1.65, 2.35, 2.63 and 3.35 seconds in figure 5 were considered.

The maximum induced velocity on the high-speed side and the corresponding minimum on the low-speed side were used in equations (3) to compute the position of the vortex center c and total circulation Γ of each vortical structure. The results for 350 structures are presented in histogram form in figures 6 and 7.

b. Cross-correlation and Auto-correlation functions

The correlation functions of $u_H' = u_H - \bar{u}_H$ and $u_L' = u_L - \bar{u}_L$, the velocity fluctuations on the high-speed and low-speed sides, respectively, were computed from the filtered data by means of the equations

$$R_{HL}(\tau) = \frac{1}{M} \sum_{m=1}^{M} u_H'(t_m) u_L'(t_m + \tau) \tag{4a}$$

$$R_{HH}(\tau) = \frac{1}{M} \sum_{m=1}^{M} u_H'(t_m) u_H'(t_m + \tau) \tag{4b}$$

$$R_{LL}(\tau) = \frac{1}{M} \sum_{m=1}^{M} u_L'(t_m) u_L'(t_m + \tau) \tag{4c}$$

where, for each time shift τ, M is the largest index such that $t_M + \tau \leq T$, T being the record length. The results, averaged over 30 records, are plotted in figures 8 and 9. The smooth curves through the data points have been drawn to aid the eye.

4. Results and Discussion

a. The mean core position (fig. 6) is slightly below (i.e., on the low-speed side) the ray c = 0 on which $U_m = \frac{1}{2}(U_1 + U_2)$. The

small dispersion in the histogram indicates that structures not in the process of pairing convect downstream with their cores closely spaced about a single ray.

The mean circulation $\overline{\Gamma}$ (fig. 7), normalized by the product $\delta_\omega \Delta U$, is given by

$$\frac{\overline{\Gamma}}{\delta_\omega \Delta U} \simeq 3.9 \tag{5}$$

where $\Delta U = U_1 - U_2$ is the velocity difference across the shear layer. Note that from the boundary condition

$$\frac{\overline{\Gamma}}{\overline{\ell}} \simeq \Delta U \ , \tag{6}$$

and equation (5) we estimate $\overline{\ell}$, the spacing between structures, to be

$$\frac{\overline{\ell}}{\delta_\omega} \simeq 3.9 \ . \tag{7}$$

This result is consistent with earlier independent measurements of this ratio[1,4]. It should be mentioned that, strictly speaking, the boundary condition given by equation (6) should be written instead as $(\overline{\Gamma/\ell}) = \Delta U$. The use of the ratio of the mean quantities is justified a posteriori in this case, since the distribution of Γ is narrowly peaked about its mean value. See fig. 7.

b. Cross-correlation and Auto-correlation results

Results of other investigators[2,4,5] suggest that the vortical structures in a mixing layer are, by and large, cylinders of elliptical cross-section whose major axes may be inclined with respect to the streamwise direction. (See fig. 3). If the angle of inclination is positive, the velocity on the high-speed side will reach its maximum before the low-speed side velocity reaches its minimum. This would

cause the minimum of the cross-correlation function of the high-speed and low-speed velocity fluctuations to occur at a positive time shift. It should be noted, however, that the minimum of the cross-correlation function has occurred at a negative time shift. See fig. 9. We believe that pairing is responsible for this result.

In pairing, neighboring vortices rotate around each other and coalesce to form a larger one. Using fig. 3 of Ref. 5, a schematic diagram of this process and the resulting induced velocity fluctuations are sketched on fig. 10. It can be seen that, in the process of pairing, a pair of vortices taken together can be assigned an effective negative angle of inclination.

The pairing process also affects the auto-correlation functions of the velocities on each side of the mixing layer (fig. 8). The auto-correlation function of the high-speed side data gives a smaller characteristic time, τ_H, (twice the time to the first minimum), than that for the low-speed side (i.e., τ_L). This becomes clear when one considers the fact that, in the process of pairing, the vortex on the high-speed side must be accelerating, while the vortex on the low-speed side is decelerating. Note that this is consistent with the results of Ref. 7. It should also be noted that the data support the relation

$$\tau_{HL} \simeq \tfrac{1}{2}(\tau_H + \tau_L) , \qquad (8)$$

where τ_{HL} is the characteristic time determined from the cross-correlation function (twice the time interval between the minimum and maximum).

If we use the characteristic time τ_{HL} derived from the cross-correlation function as a measure of the mean time between the passage of the large structures, the mean spacing would then be given by

$$\overline{\ell} \simeq \tau_{HL} U_c \ , \tag{9}$$

where, from the cross-correlation function, we have

$$\tau_{HL} U_c / x \simeq 0.40 \ . \tag{10}$$

Combining equations (1), (9) and (10) yields

$$\overline{\ell}/\delta_\omega \simeq 4.0 \ . \tag{11}$$

Note that the independent estimates of $\overline{\ell}/\delta_\omega$ as given by (7) and (11) are consistent.

Direct examination of the velocity records shows that the maximum velocity on the high-speed side and the minimum velocity of the low-speed side, corresponding to the passage of a single structure, occur at the same time, within the accuracy of the present measurements. Note the time markers on fig. 5. This indicates that if the vorticity distribution is elliptical, the inclination angle is small. This is consistent with the findings of the stability analysis by Moore and Saffman (Ref. 8).

6. Conclusion

Simultaneous records of the streamwise component of velocity at the high-speed and low-speed edges of the mixing layer were used to calculate the core position and strengths (circulation) of the vortical structures. It was found that an isolated structure (not in the process of pairing) travels with the center of its core very close to the [redacted] y/x on which the mean velocity is $U_m = \frac{1}{2}(U_1 + U_2)$ and has a mean circulation given by $\overline{\Gamma}/\delta_\omega \Delta U \simeq 3.9$. The small dispersion about the mean of the distributions of core position and circulation is noteworthy.

7. Acknowledgments

The measurements were conducted under the sponsorship of the Experimental Methods course of the Graduate Aeronautical Laboratories at Caltech and the Air Force Office of Scientific Research Contract No. F44620-76-C-0046. One of us (D. Lang) would like to acknowledge the support of the Fannie and John Hertz Foundation.

References

1. Dimotakis, P. E. and Brown, G. L., "The mixing layer at high Reynolds number: large structure dynamics and entrainment". J. Fluid Mech. 78 (3), 535-560 + 2 plates, 1976.
2. Browand, F. K. and Weidman, P. E. "Large scales in the developing mixing layer". J. Fluid Mech. 76 (1), 127-144, 1976.
3. Brown G. and Roshko, A., "The effect of density differences on the turbulent mixing layer". Turbulent Shear Flows, AGARD-CP-93, paper no. 23, 1971.
4. Brown, G. L. and Roshko, A., "On density effects and large structure in turbulent mixing layers". J. Fluid Mech. 64, 775-816, 1974.
5. Roshko, A., "Structure of Turbulent Shear Flows: A New Look". AIAA paper 76-78. Also in AIAA J. 14, 1348-1357 and 15, 768, 1976.
6. Winant, C. D. and Browand, F. K., "Vortex pairing: the mechanism of turbulent mixing-layer growth at moderate Reynolds number". J. Fluid Mech. 63 (2), 232-255, 1974.
7. Oster, D., "An experimental investigation of the two dimensional turbulent mixing layer", M. Sc. Thesis, Tel-Aviv University, July 1976.
8. Moore, D. W. and Saffman, P. G., "The density of organized vortices in a turbulent mixing layer". J. Fluid Mech. 69 (3), 465-473, 1975.

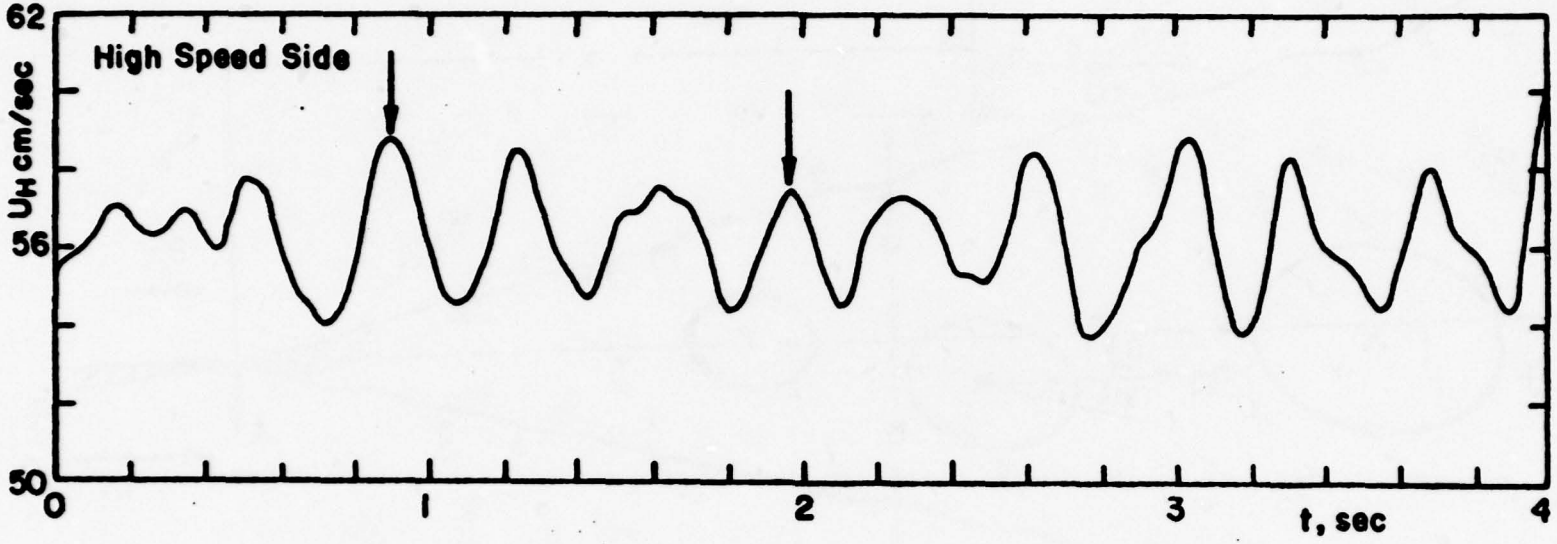

FIGURE 1. VELOCITY RECORD TAKEN AT A MEAN HIGH SPEED FREE STREAM VELOCITY OF U_1 = 56 CM/SEC

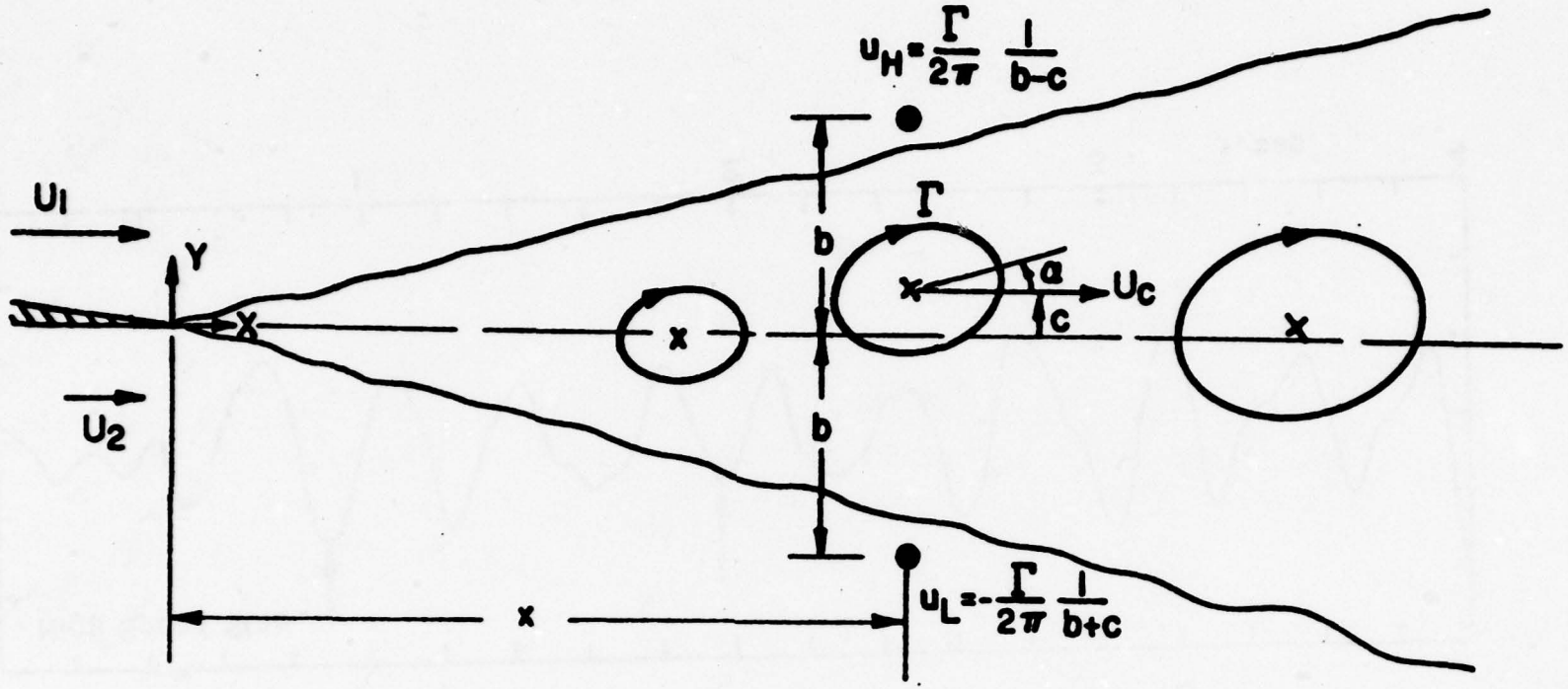

FIGURE 3. SCHEMATIC DIAGRAM OF THE MIXING LAYER. THE TWO FILLED DOTS DENOTE THE MEASUREMENT LOCATIONS.

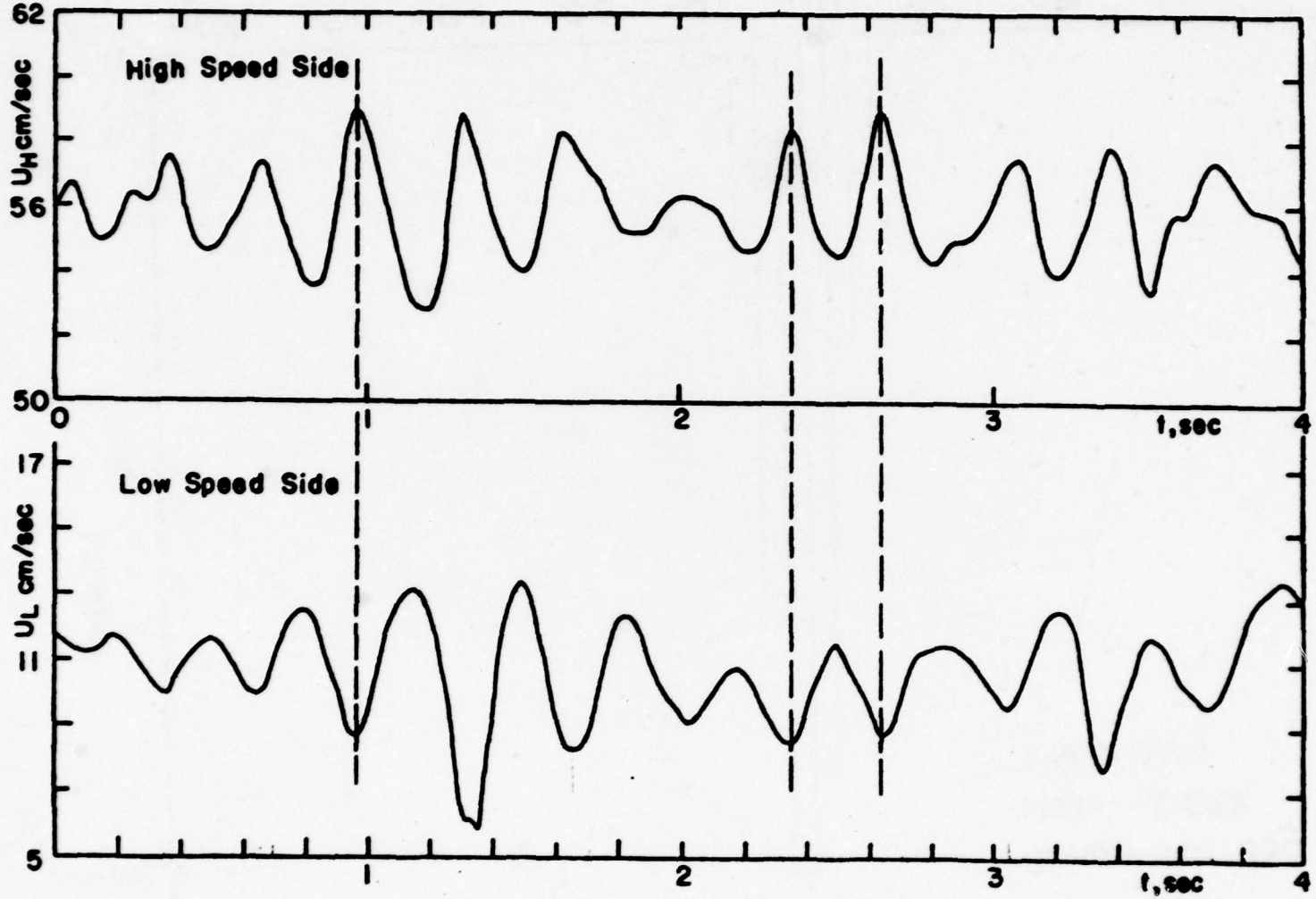

FIGURE 5. SIMULTANEOUS VELOCITY RECORDS AT THE HIGH SPEED AND LOW SPEED EDGES OF THE SHEAR LAYER

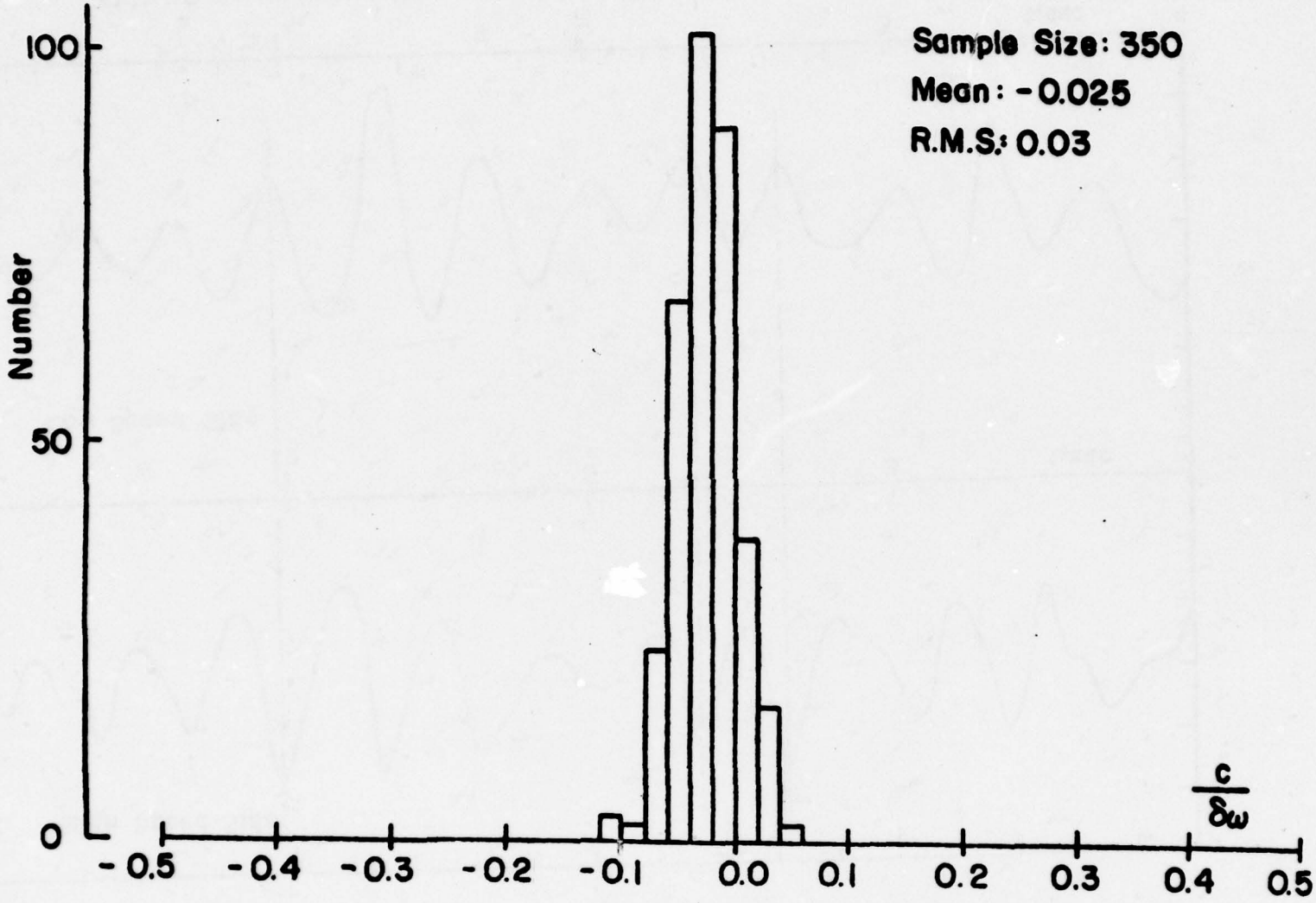

FIGURE 6. DISTRIBUTION OF NORMALIZED VORTEX CORE OFFSET DISTANCES

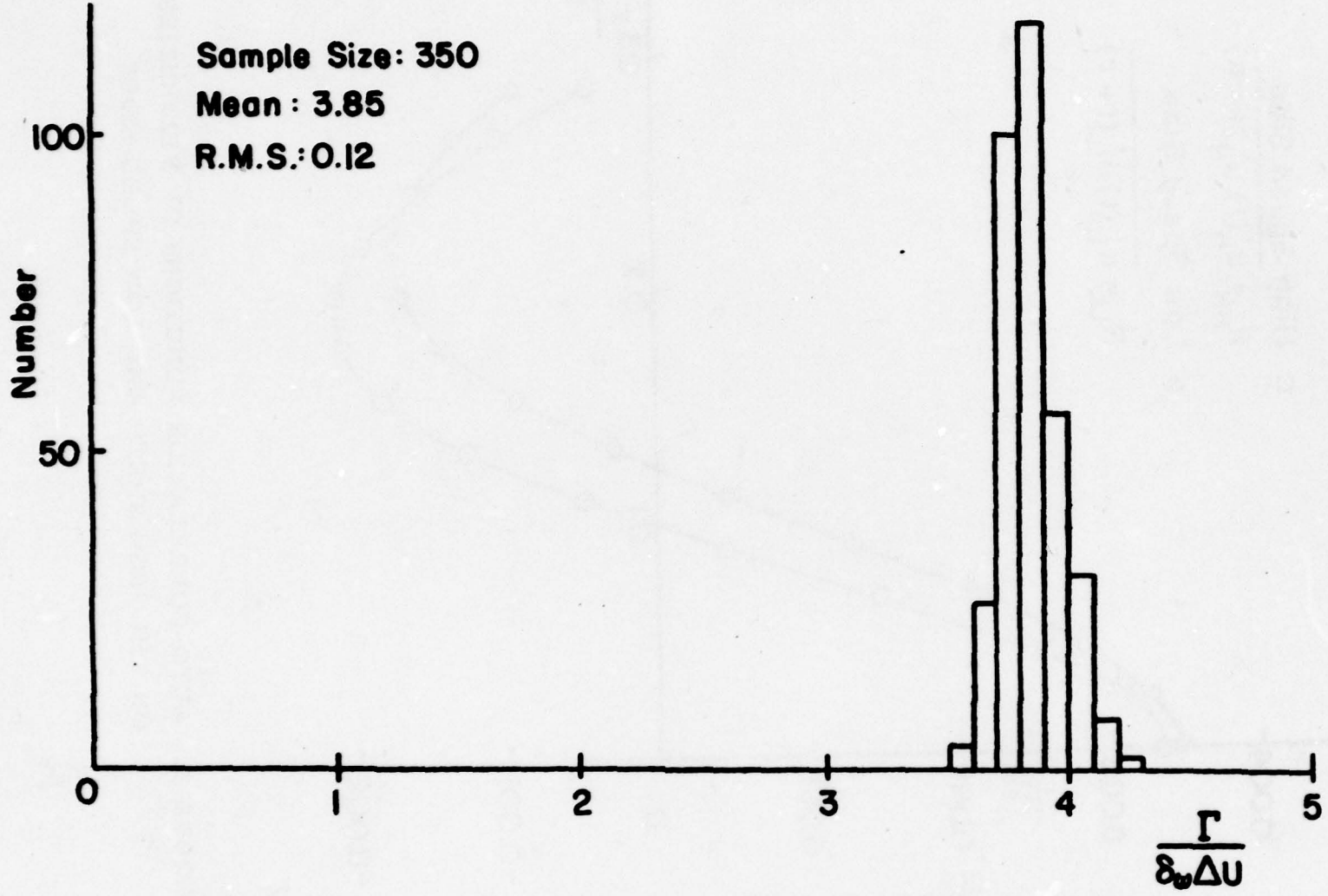

FIGURE 7. DISTRIBUTION OF NORMALIZED VORTEX STRENGTHS

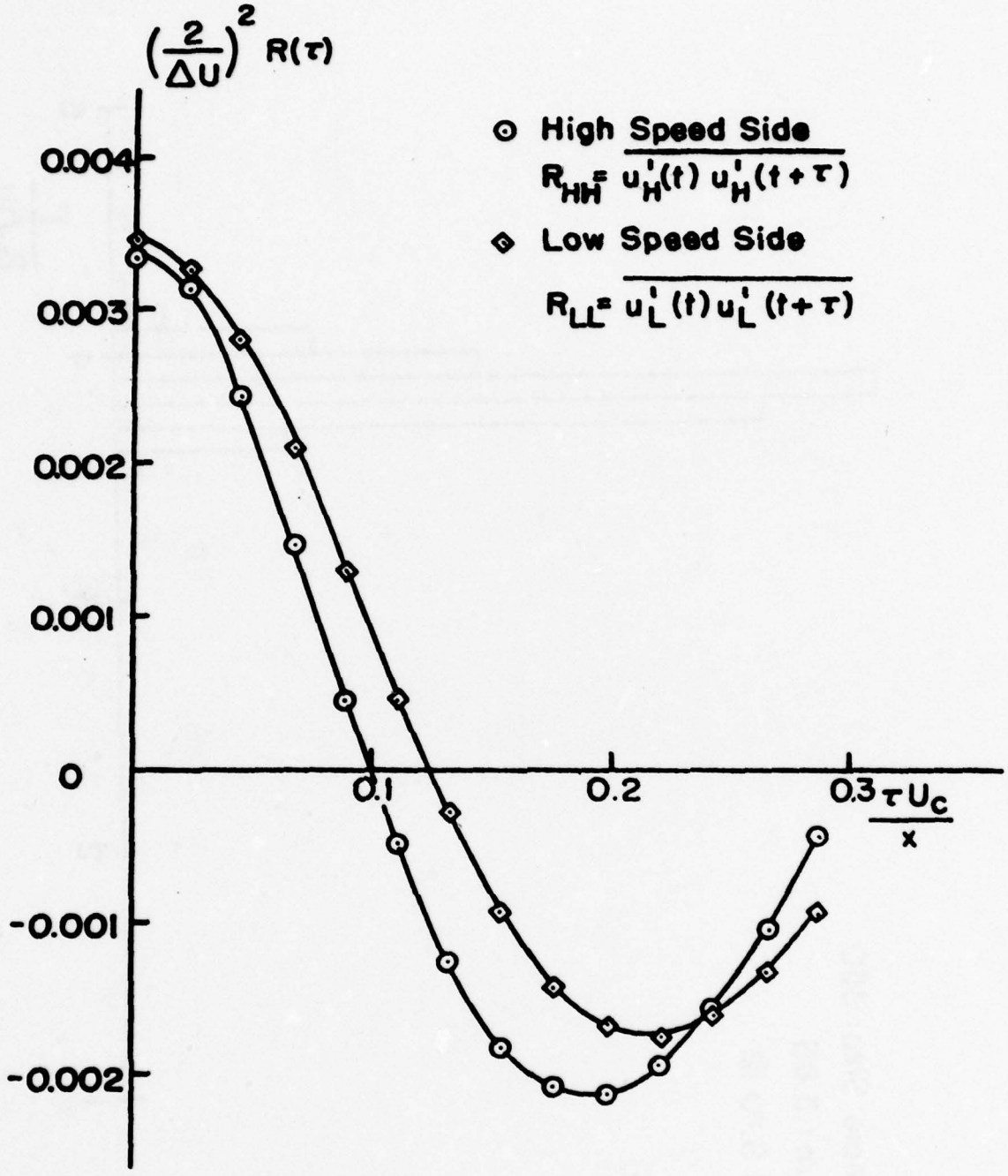

FIGURE 8. AUTO-CORRELATION FUNCTIONS OF VELOCITIES ON THE HIGH SPEED AND LOW SPEED SIDES

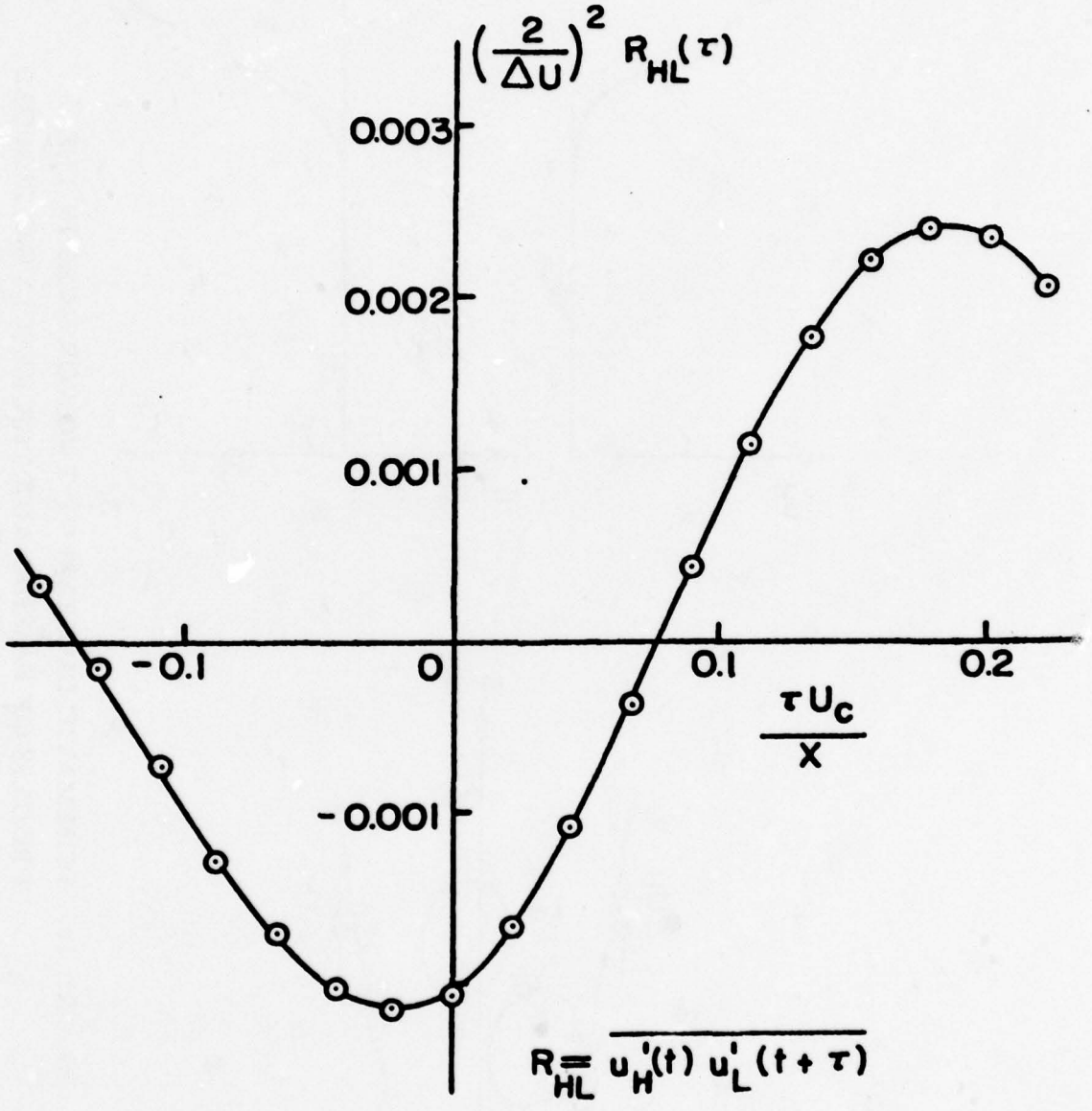

FIGURE 9. CROSS-CORRELATION FUNCTION OF HIGH SPEED AND LOW SPEED VELOCITIES.

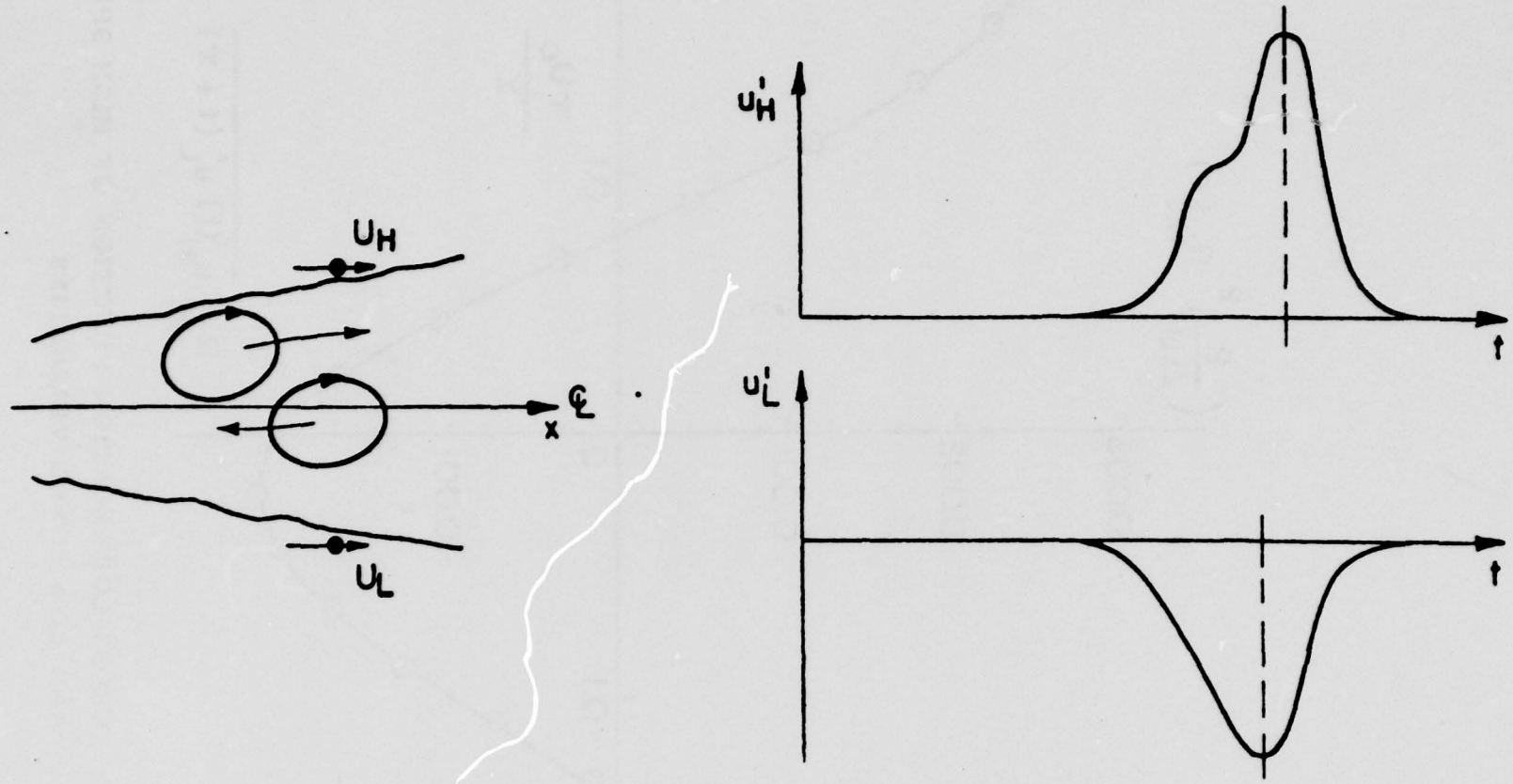

FIGURE 10. SCHEMATIC DIAGRAM OF TWO VORTICES IN THE PROCESS OF PAIRING AND THE RESULTING INDUCED VELOCITY FLUCTUATIONS

Appendix H

LASER INDUCED FLUORESCENCE MEASUREMENTS IN THE TURBULENT JET

by

Richard C. Lye

Senior Thesis

California Institute of Technology

26 May 1978

ABSTRACT

The turbulent stuctures in the flow of a jet were studied through the use of laser induced fluorescence. The fluid to be issued from the jet was labelled with a dye that fluoresced resonantly when illuminated with laser light. The linearity of the dye, combined with the freedom to illuminate the flow in many ways, makes this a powerful and versatile technique. Some preliminary observations made in this fashion are discussed.

INTRODUCTION

The study of turbulent flows has been carried out primarily by qualitative flow visualization techniques and by quantitative single point measurements. The difficulties encountered in correlating the single point measurements in space and time, and interpreting the results if the correlations are carried out, have limited most observations to be time averaged descriptions of the flow. Such a description necessarily contains little information concerning the turbulent structures themselves. Consequently, a detailed description of the nature of turbulent structures has not yet evolved due to the lack of adequate measurement techniques.

A detailed picture of the structures is necessary for a working knowlege of the processes that involve turbulence. Such information would contribute to the understanding of energy loss due to turbulence and especially to the understanding of turbulent dissipation and mixing, as for chemical reactions. In chemical reactions, such as combustion, the reaction occurs at the interface of the mixing substances and this interface is defined by the shape of the turbulent structures.

Kotsovinos[1,2,3] and List[2] have constructed a comprehensive description of the properties of plane (two dimensional) turbulent jets, including bouyancy effects. Their description includes integral properties of the flow, such as mass flux and momentum flux, and fluctuation properties, such as velocity fluctuations and jet/ambient fluid interface crossings.

From similarity arguments, which are supported by experiments, the momentum flux through any plane perpendicular to the flow is equal to a constant. Thus: (Fig.1)

(1) a. $J = \int \rho \bar{u}^2 dy = \text{constant}$, $\bar{u}^2_{max}(x)\, b(x) = \text{const.}$ (2 dim)

b. $J = \int \rho \bar{u}^2 dy dx = \text{const.}$, $\bar{u}^2_{max}(x)\, b^2(x) = \text{const.}$ (3 dim)

where J is the momentum flux, $\bar{u}$ is the time averaged velocity which has its maximum on the jet axis, and b(x) is the local jet flow width. Dimensional analysis gives (Landau and Lifshitz [4])

(2) $b(x) \sim x$

so, substitution into (1) gives:

(3) a. $\bar{u}_{max} \sim \frac{1}{x^{\frac{1}{2}}}$ (2 dim)

b. $\bar{u}_{max} \sim \frac{1}{x}$ (3 dim)

This is not a strictly accurate description of the flow in that the entrainment flow can introduce a net momentum flux that invalidates equation (1), as Kotsovinos [1] noticed. However the sign of the correction due to the entrained flow is dependent upon the jet's environment and since the correction to the momentum flux is ~17% at an x/D of 100, the effect can generally be ignored. The change in the flow due to the nonconstant J is that the growth of the jet width, b(x), becomes nonlinear, a decrease in the momentum flux resulting in a greater spreading rate.

Goertler's solutions [5] for the velocity profile of the turbulent

jet are given by:

$$(4)\quad a.\quad \frac{\bar{u}(x,y)}{\bar{u}(x)_{max}} = \operatorname{sech}^2\left(\frac{\sigma y}{x}\right) \qquad (2\ \text{dim})$$

$$b.\quad \frac{\bar{u}(x,y)}{\bar{u}(x)_{max}} = \left(1+\frac{\eta^2}{4}\right)^{-2} \quad \eta=\frac{\sigma y}{x} \qquad (3\ \text{dim})$$

The fluctuation and intermittency measurements performed by Kotsovinos indicate that for the two dimensional jet no ambient fluid reaches the centerline of the flow. They indicate that the mixing and fluctuations increase on each side of the centerline before going to zero again in the ambient fluid.

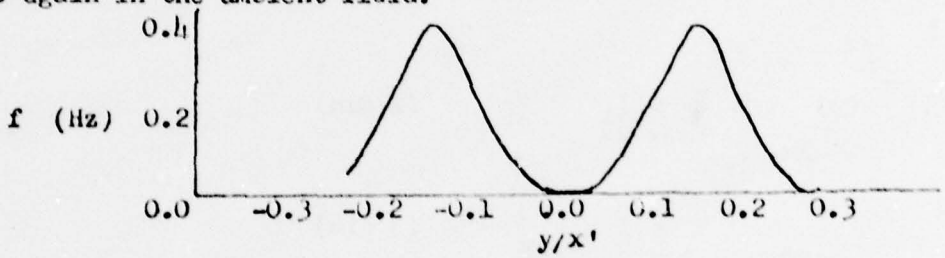

Profile of frequency of interface crossing

That ambient fluid does reach the jet axis will be born out by this investigation, previous measurements probably being limited by resolution considerations. In fact, part of this study was directed toward the structures of ambient fluid on the axis of a three dimensional jet and the presence of ambient fluid on the two dimensional jet axis was also observed.

What is missing from the description so far is data that is correlated, whether over space at a given time or over time at given spatial coordinates. Perry and Lim [6] have developed a technique similar

to that used in this investigation that enables them to make such observations of the entire flow. They use laser illumination of a flow labelled with a smoke tracer to visualize a turbulent flow in a gaseous medium.

The technique employed in this investigation also uses laser illumination, but here the jet fluid is labelled with a fluorescent dye. The dye is Rhodamine 6-G, which is used in dye lasers and fluoresces resonantly when illuminated with green light. The fluorescence is at a longer wavelength, in the yellow, and is excited strongly by the 5145 Å line of an argon ion laser. The laser light, when focused to a thin pencil or sheet, can be used to intersect the flow, causing the fluid that was issued from the jet to fluoresce while it simply passes through the ambient fluid. The fluorescence is unaffected by the flow (unlike light scattered by smoke particles which can be rescattered) so that observations of the center of a flow can be made. Any scattered laser light is easily removed by an appropriate optical filter.

Up to near saturation, the fluorescence of R6G is proportional to the incident intensity of the illuminating beam. Since the fluorescence is resonant and consequently quite strong, it is not necessary to even approach the point of saturation in practice, so the fluorescent light provides a quantitative representation of the jet fluid concentration in the flow.

The laser light, as described by gaussian optics, can be manipulated to provide illumination that is sufficiently precise to resolve the finest scale of turbulence with vitually infinite time resolution. In this way, the technique of laser induced fluorescence can be

used to retrieve nearly any information on the jet fluid concentration field as a function of time. By observing scattering from small particles in the flow for a short interval, it is also possible to characterize the velocity field, yielding a substantial amount of information on the flow.

APPARATUS

Both two and three dimensional jets were studied during this investigation, although the emphasis was on the flow from a 0.3" diameter three dimensional jet. This jet with its reservoir of dyed water was suspended above a glass aquarium (2'x 1' x 1½' deep) containing undyed water. The flow from the jet was regulated by metering the introduction of air into the jet reservoir. A wide range of jet exit velocities was realized by this arrangement, making Reynolds numbers of zero to several thousand accessible. This system was conceived and designed by Dimotakis. A two dimensional jet with a variable slit width (1-6 mm x 23.5 cm) designed by the author was also studied in the course of the investigation.

An argon ion laser, typically outputting several hundred milliwatts, was the illumination source. In the various methods of illumination used here, this was enough light intensity when used in conjunction with a 0.6 mg/liter concentration of R6G. This concentration was sufficiently small that the fluorescent losses did not attenuate the illuminating beam significantly in its traverse of the flow. In more quantitative experiments, it may be necessary to consider the attenuation

but a calibration of the fluorescence and the calculation of the losses is not difficult to carry out.

To observe a line intersecting the flow, a long focal length lens focused the beam to a waist, as described by gaussian optics. The waist diameter and the length over which the beam had not appreciably expanded permitted viewing of the smallest structures in the flows under consideration here. To observe a plane in the flow, diverging cylindrical lenses were placed in the beam, expanding the beam in one dimension perpendicular to its axis of propagation. The beam was manipulated with a mirror or prisms to direct it through the flow in the desired direction.

The resulting fluorescence was recorded in two different ways for these two observational schemes. One method consisted of illuminating the flow with the sheet of light and photographing the fluorescence with a conventional camera focused on the plane of the sheet. The second method used a pencil of light to illuminate the flow and the concentration pattern along this line was observed as a function of time. The data from the first method can be displayed as concentration as a function of x and y at a fixed time. The second methods results can be displayed as concentration as a function of x (or y) and t for a fixed y (or x).

To collect the concentration data along the line as a function of time, a linear optic array camera was used. (Fig. 1) This camera, designed by the author with Dimotakis for this use, consists of a reticon linear array of photodiodes and its associated electronics and an optical imaging system. A Nikon photographic lens images the illuminated line on the array of diodes.

Although there exist both 100 and 1000 element arrays that can be used in the camera, only the 1000 element array (each diode 25 um square, total length 1") was used for these measurements. With an external clock and power supply, the camera outputs sequentially a signal from each element that is proportional to the integrated intensity that element received since the last sampling. The camera could be clocked more quickly (200 samplings/sec) than the fastest fluctuations observed in the flows, permitting observations that were not time resolution limited.

The output of the camera, then, is a concentration versus position representation of the flow when the signal is viewed as a function of time on an oscilloscope for a single sampling of the array. The changes in this functional relationship give the desired time correlated information. To get a concentration versus position and time representation, Morrison designed an optic array scanner that synchronously sweeps an oscilloscope screen and modulates the beam intensity with the output of the camera. The resulting oscilloscope tube image, much like that of a radar screen, was recorded photographically, giving the desired concentration versus x (or y) and t representation.

METHODS

Industrial water passed through an inline 10 um filter was the fluid used throughout this investigation. Even though laser light scattered by particles could be optically filtered, it was deemed important to keep the water as clean as possible. A Hoya HMC O(G) filter was used to preferentially pass the fluorescent light while blocking the scattered light.

There was one arrangement where the particles remaining in the water were used to advantage. (Fig. 2 a.) Without any dye in the jet reservoir and with a sheet of light (xy plane) along the jet axis, a velocity field representation of the flow was recorded. This was accomplished by taking a short time lapse photograph of the light scattered by the uniformly distributed particles. The length and direction of the streaks recorded on the film amount to a two component (xy) vector velocity field for the flow.

As with all the fluorescence measurements, these velocity field measurements were recorded over a range of Reynolds numbers where the flow was turbulent (500-4000). Similarity of the flows was preserved over this range to the extent that it was investigated in this study. That is to say the growth of the jet width and growth of the turbulent structures was similar over this range. The importance of keeping the densities (i.e. temperatures) of the jet reservoir fluid and the ambient fluid the same was observed, the reason being that the effects of buoyancy can alter the flow considerably (Kotsovinos[1]).

Perhaps the most intuitively suggestive measurement is the sheet

illumination of the flow. The flow was illuminated with a sheet of light directed upward through the bottom of the tank (aquarium) as in the velocity measurement. (Fig. 3 a.) However the scattered light was blocked in this case and the jet fluid was dyed, yeiloing a concentration field representation of the flow. A conventional photographic camera using 400 ASA Tri X film recorded this representation at a fixed time value sometime after the flow had established itself. This means of viewing the flow was intended to show turbulent structures of all scales, their variations with x/D and x/y, and the spatial coherence and ordering of the structures. (Fig. 2 b.)

The time coherence of the structures is also of interest, as are the propagation velocities of the structures (in a structural sense as opposed to the vector velocity of points within the structures, as was previously discussed). Two different methods were employed to study time variations in the flow. The first consisted of viewing a line intersecting the axis of the jet perpendicularly. This is a concentration versus y and t representation of the flow at a given x value. (Figs. 3 b. and 4) The second scheme was to view the axis of the jet as a function of time; an xt at fixed y ($y \approx 0$) representation. If the commonly held idea that no ambient fluid reaches the jet axis were true, this would have been a singulatly uninteresting measurement. The opposite turned out to be the case. (Figs. 3 c. and 5)

Since the illuminating beam was made as small as possible to observe the finest structures and the linear array of photodiodes is only 25 um (1 mil) wide, the alignment of the system was not a simple task. (see APPENDIX) The width of the sheet or the diameter of the pencil can be calculated from:

$$(5) \quad w(r) = w_o \left(1 + \left(\frac{\lambda r}{\pi w_o} \right)^2 \right)^{\frac{1}{2}} \qquad w_o = \frac{\lambda f}{\pi R_o}$$

where R_o is the radius of the laser beam, f is converging lens focal length, and r is the distance along the beam axis from the focal point, being x or y in the two cases. So for $\lambda = 5145$ Å, f = 1 m, and $R_o \simeq 2$mm, the half width or radius of the illumination is 0.082 mm.

In the yt method, the beam was brought in through the end of the tank, intersecting the vertical jet axis horizontally. In the xt method, the beam was directed up through the bottom of the tank. In all of the measurements, the flow close to the bottom was not studied because of the interruption of the flow due to the bottom and its effects further upstream.

Some preliminary observations of a two dimensional jet designed and built for this investigation were also carried out. These observations consisted of the instantaneous concentration field in a plane. When the plane was aligned along the direction of the flow and perpendicular to the slit, a concentration pattern much like that of the xy photographs of the three dimensional jet was recorded. When the plane was aligned again along the direction of the flow, but along the slit instead, a means of determining the two dimensionality of the flow was realized. (Figs. 6 and 7)

EXPERIMENTAL RESULTS AND DISCUSSION

A comparison of the concentration field and the velocity field (Figs. 2 a. and b.) allow a number of observations. Where the flow is still laminar near the jet exit, the velocity field indicates that there is considerable entrainment of ambient fluid into the flow. (The bright spot in the photograph is a reflection of the jet exit from the back of the tank.) Apparently the simple presence of entrainment does not necessitate turbulence, although such a laminar flow with so considerable an entrainment may be a metastable state that eventually does become turbulent.

Townsend[7] describes a model for entrainment based on the diffusion of vorticity into the ambient fluid through the flow's boundary. The ambient fluid is considered to be irrotational outside the boundaries while the fluid just inside the boundary is gaining vorticity by a uniform (on the scale of the smallest structures present) diffusion process. Any large scale disturbances in this pattern, that might trap irrotational fluid in the flow for instance, are expected to be due to normal statistical fluctuations.

The entrainment and the acquisition of vorticity are not diffusion-like but rather have some definite large scale characteristics in this flow as can be seen in Fig. 2 a. Large scale vorticity extends deeply into the ambient fluid, setting up a flow that must have some deterministic nature. Clearly a model of uniform entrainment does not apply in the ambient fluid just outside the jet.

The instantaneous concentration fields for the three dimensional jet (Fig. 2 b.) and the two dimensional jet (Fig. 6) are qualitatively much the same. After an initial laminar region, the flow

becomes unstable and turbulent. The initial instability has a form that is similar in these two cases althogh it is simpler in the two dimensional jet. Because of the relative simplicity, which is due to the one less degree of freedom in two dimensions, the following descriptions are of the plane jet.

There are two distinctly different types of transition to turbulence. The abrupt change between the types occurs at a Reynolds number ($\sim$100) where the flow at the exit shows a stable periodic vorticity. The transition to turbulence for a slow jet seems to come about after a developing periodic wander attains a critical rotation, at which point a vortex is created. (Fig. 10 a.) In the case where the flow already has a periodic vortex structure; the faster flow; the large vortices appear where the wandering begins. (Fig. 10 b.) Apparently the flow already has sufficient vorticity to be turbulent and any asymmetry in the flow is enough to trigger the large vortices.

Once the large scale vortices appear in the flow, all the chaotic connotations of turbulence are realized. A general periodic wandering trend is still evident in the flow in many records, but its coherence is not especially great - the trend sometimes disappears. Compare, for example, Fig. 2 b., which is fairly typical, to Fig. 9 in which the meandering is quite pronounced. But beyond any shadow of doubt ambient fluid does reach the jet axis.

It should be noted here that when a ~~wider~~ thicker sheet of light was used to illuminate the flow, the ambient fluid on the jet axis was not evident at small x/D. This implies that the structures on the axis are fine scale, especially closer to the exit, and previous measurements may

have not found them due to a lack of resolution. Kotsovinos[1] reports that the region immune to ambient contamination narrows with x/D. This is consistent with the similarity result that the scale of the structures increases with x/D. Consequently the ability to resolve the structures improves until the finest structurs are observed and ambient fluid is noticed on the axis. The difficulties in observing the fine scale of the structures is aggravated by the fact that the velocity is at a maximum on the jet axis and so time resolution is important as well.

In checking the two dimensionality of the plane jet, striations in the flow were noticed along the length of the slit. (Fig. 8) Similar phenomena have been noticed before, in particular by Konrad[8] in a shear layer. He begins to explain their occurence in terms of a Rayleigh instability, which comes about when a structure is rotating in a sense opposite to that of the more general flow. This model turns out to fit in well with the Reynolds number dependence of the phenomenon, a dependence that appeared to be present to some degree in the jet as well. But by polishing the contraction surfaces of the jet and taking precautions to avoid their contamination with particles or bubbles, the striations were made to disappear. This effect might indicate that the instability is still triggered by imperfections in the flow.

Even without the striations, the two dimensionality of the flow is limited. (Fig. 7) The initial region shows good two dimensional behavior, but with the onset of large scale vorticity, three dimensional structure develops. There is still some overall two dimensional behavior, seen in the bands of turbulence, but this has the same sort of limited coherence that the wandering was seen to have had.

The increase of the turbulent scale with x/D as given by similarity is also evident in Figs. 2 b. and 6. The spreading of the jet, due to entrainment, is very nearly linear as previously noted ($b(x) \sim x$). Although the turbulence is not uniform within its boundaries, it does have linearly spreading edges. That the effects of the large vortices extends into the ambient fluid is consistent with the fact that the edges of the jet are not made up of uniform structures. The concept of a jet boundary is still valid, but the rotational influences of the flow are not restricted to be within those limits.

It may be somewhat surprising that the size of structures depends only on x/D, while there is considerable variation in the velocity across the flow, as a function of the y coordinate. This result implies that structures in different environments, moving at different velocities change their scale in the same way. Nevertheless, this is predicted by similarity and it is born out by this investigation. Observing yt records shows that structures at the edges of the flow are elongated in the t direction. (Fig. 4) Thus they are moving more slowly, yet the xy records show that in spatial coordinates the scale is preserved across the flow.

The remaining thechnique used to analyze the flow was the use of axial illumination. The signal was inverted for this technique so that the ambient fluid appears as bright regions. This was convenient because, although some ambient fluid does reach the axis, the greatest part of the flow was issued from the jet and a clearer record is made with fewer bright regions.

The average velocity along the three dimensional jet's axis

goes as the inverse of the distance along that axis. On an xt record, the velocity of a structure is the slope of its path. Thus we have:

$$(6) \qquad \frac{dx}{dt} \sim \frac{1}{x} \qquad \text{or} \qquad x^2 \sim t$$

so the paths should be parabolic, in an average sense. That this is roughly correct can be seen in Fig. 5., but a larger test section would be necessary to verify this observation.

This measurement turned out to be particularly revealing in that it permitted the observation of how the flow grows due to the interaction of the turbulent structures. The growth of the turbulent scale raises the question of the mechanism of this growth. Rather than each vortex expanding (which might wreak havoc with the velocity dependence) the flow causes vortices to combine, becoming part of larger structures. This can be seen in the anti-branching patterns that lie between converging parabolas. The complicated structure of the vortices sometimes give the impression of anomolous velocities; a round structure crossing a line obliquely can have both positive and negative apparent velocities. (Fig 11) An example of this effect is recorded in Fig. 5 with the nestled arches of a spiraled vortex 4 blocks from the left and 0.75 blocks from the bottom of the figure.

Some insight into the nature of the turbulent structures is provided by the the observation that their trajectories are basically straight lines on the xt record. The major exception to this rule is when several structures are close together, in the process of combining. The parabolas are made up of line segments which are parabolic only in

an average sense. This provides an analogy to a free vortex ring which travels with a constant velocity through the ambient fluid. It might be possible, then, to formulate an atomistic model of turbulence in which the structures behave like independent vortex rings that only interact when they are close together. This would not be a complete description though, because it could not explain the periodic wandering that is observed in the entire flow.

CONCLUSIONS

A method for studying the structures in a turbulent flow has been developed. It has been employed to make detailed qualitative measurements of the flow of a turbulent jet and has the potential to permit quantitative, as well as qualitative, studies of many flows.

In two and three dimensional jets, ambient fluid was observed to reach the jet axis. The nature of the onset of turbulence was studied and it appears to be due to an instability caused by the wandering of the flow. The growth of the jet was seen to be accomplished by the combination of turbulent structures as the jet width increases. These structures appear to travel with constant velocity like free vortex rings except while in the process of combining to form larger structures.

ACKNOWLEDGEMENTS

I would like to express with gratitude and appreciation my thanks to Dr. Paul Dimotakis for his advice, enthusiasm, and insight which were essential to this work. I also gratefully acknowledge the assistance of Robert Morrison for his construction of the optic array scanner and other work on the electronic systems employed in this work. The design advice and construction by the Aeronautics Shop were also greatly appreciated, as was the darkroom work of Harry Hamaguchi. Finally, I would like to thank the Physics Undergraduate Committee for allowing me to avoid taking another laboratory course in such an enlightening and rewarding way.

REFERENCES

1. KOTSOVINOS, N. E. 1975. A Study of the Entrainment and Turbulence in a Plane Buoyant Jet. Ph.D. Thesis, California Institute of Technology.

2. KOTSOVINOS, N. E. and LIST, E. J. 1977. Plane Turbulent Buoyant Jets. Part 1. J. Fluid Mech., Vol. 81, pp 25-44.

3. KOTSOVINOS, N. E. 1977. Plane Turbulent Buoyant Jets. Part 11. J. Fluid Mech., Vol. 81, pp 45-62.

4. LANDAU, L. D. and LIFSHITZ, E. M. 1959. Fluid Mechanics. Pergamon.

5. WHITE, F. M. 1974. Viscous Fluid Flow. McGraw-Hill.

6. PERRY, A. E. 1977. Topology of Coherent Eddies. Preprint.

7. TOWNSEND, A. A. 1976. The Structure of Turbulent Shear Flow. Cambridge University Press, second edition.

8. KONRAD, J. H. 1976. An Experimental Investigation of Mixing in Two Dimensional Turbulent Shear Flows with Applications to Diffusion-limited Chemical Reactions. Project Squid, Technical Report CIT-8-PU.

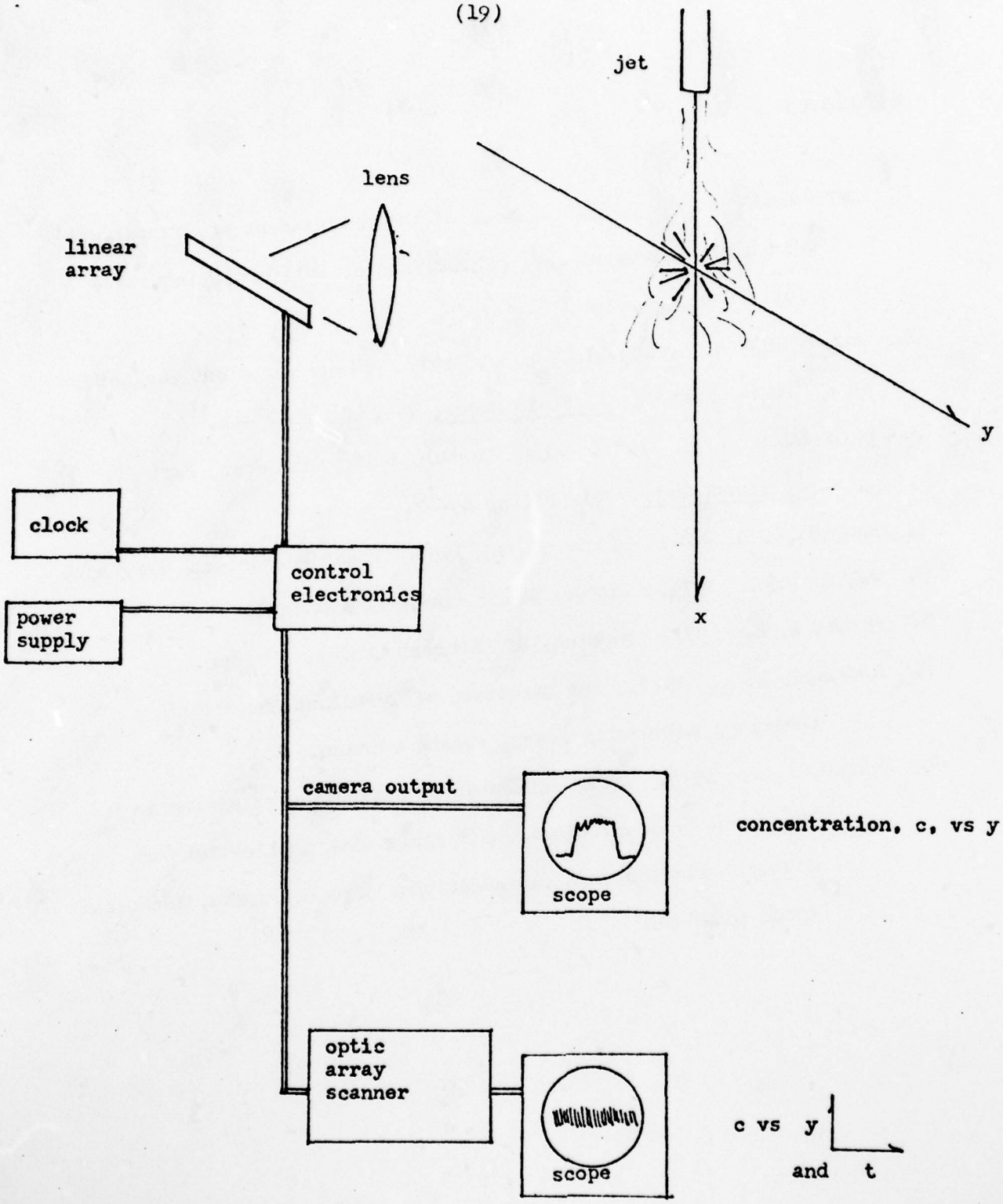

Fig. 1 Experimental set up and definition of axes

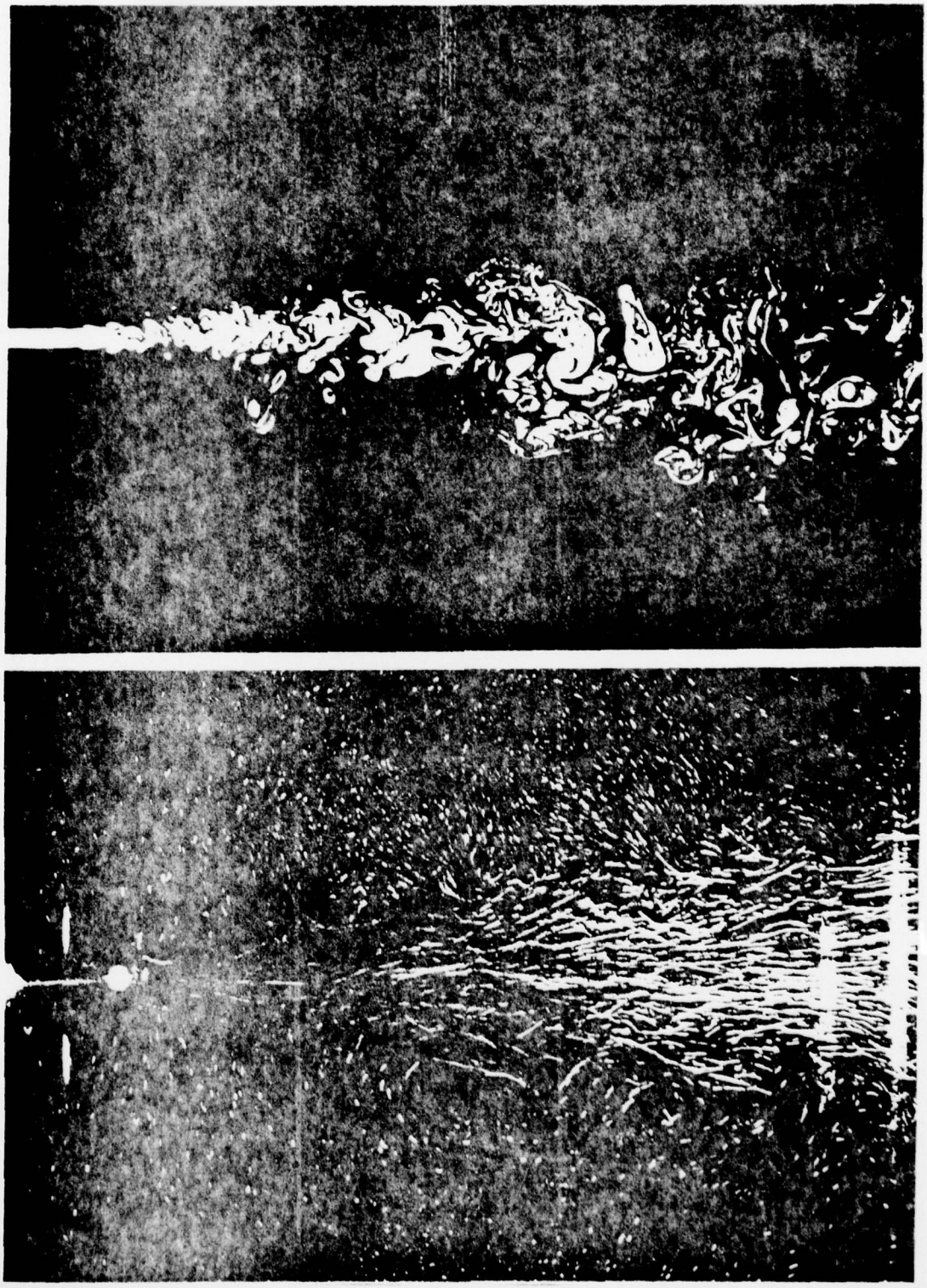

Fig. 2 a.(below) and b.(above) xy representation of the velocity and concentration, respectively. Re = 2,300. $x/L_{max} = 47$

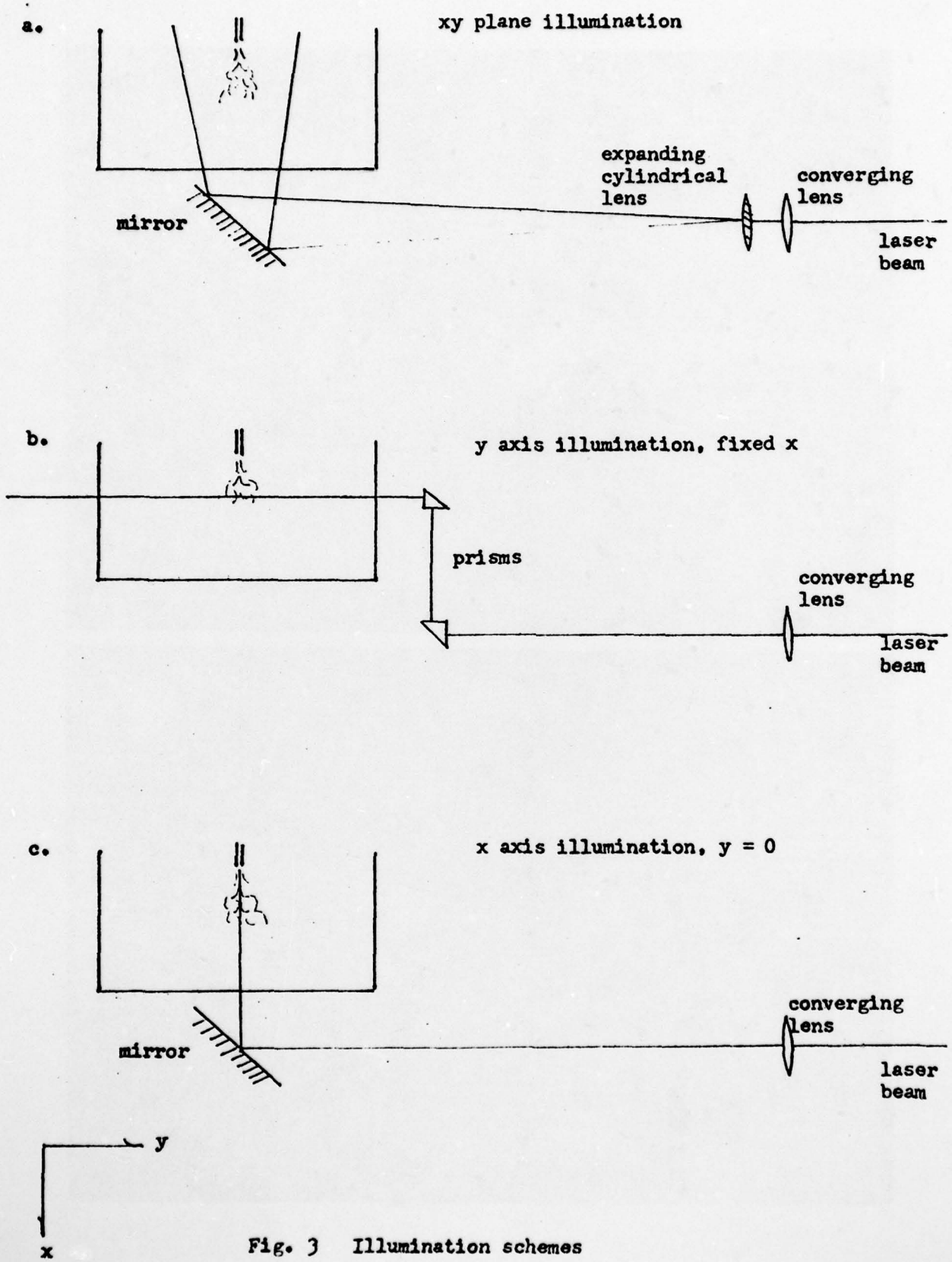

Fig. 3 Illumination schemes

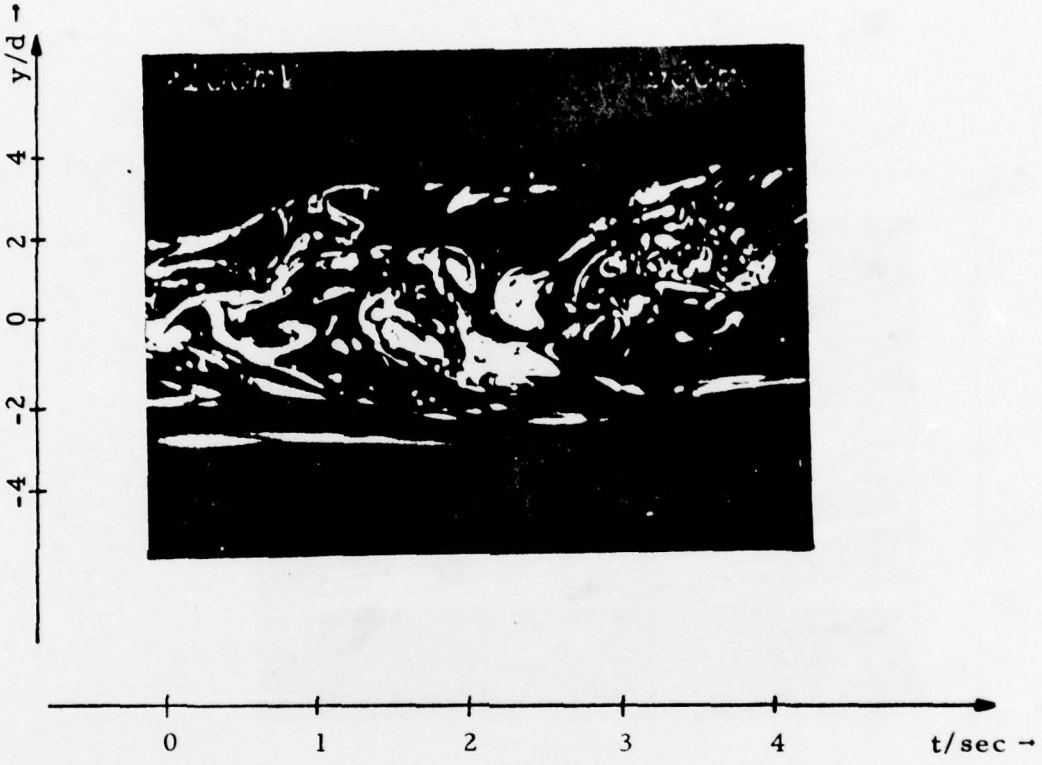

Re = 500 , d = 0.3" , x/d = 37.5 ,

Fig. 4 yt representation of the flow

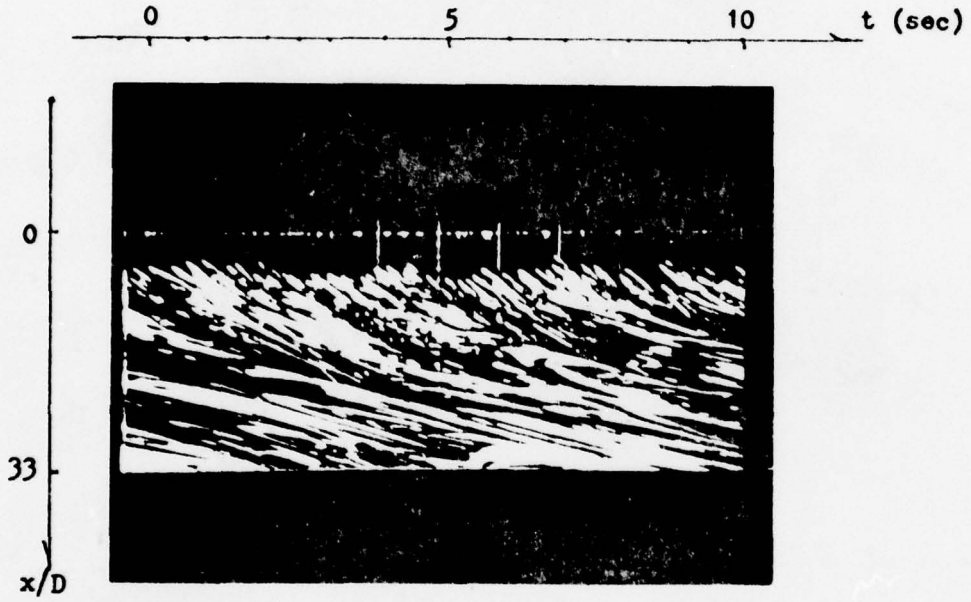

Re = 500 , D = 0.3" , y = 0

Fig. 5 xt representation of the flow

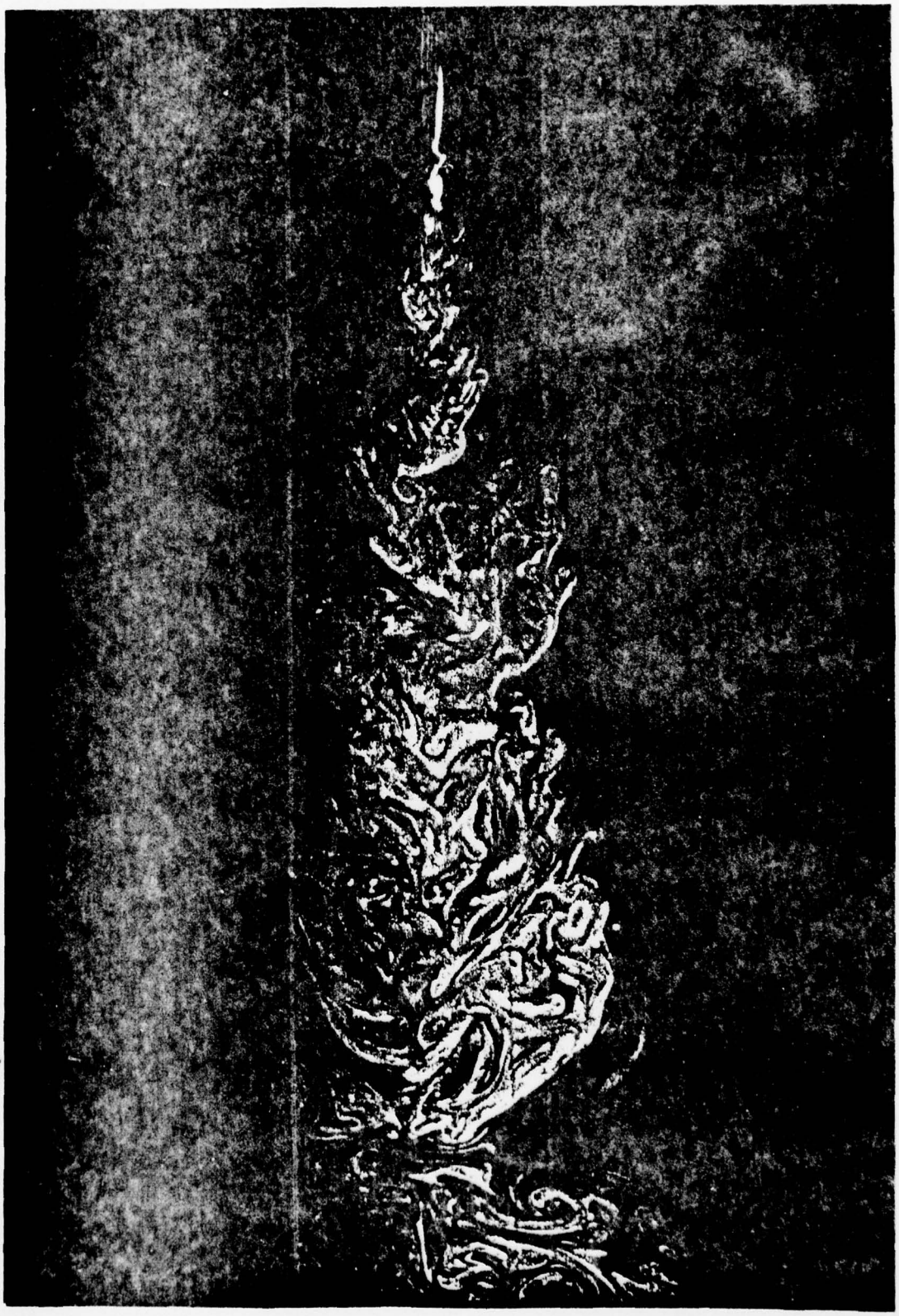

Fig. 6 xy representation of the two dimensional flow. $Re \approx 200$ at exit(grows as x). $x/U_{max} \cong 340$

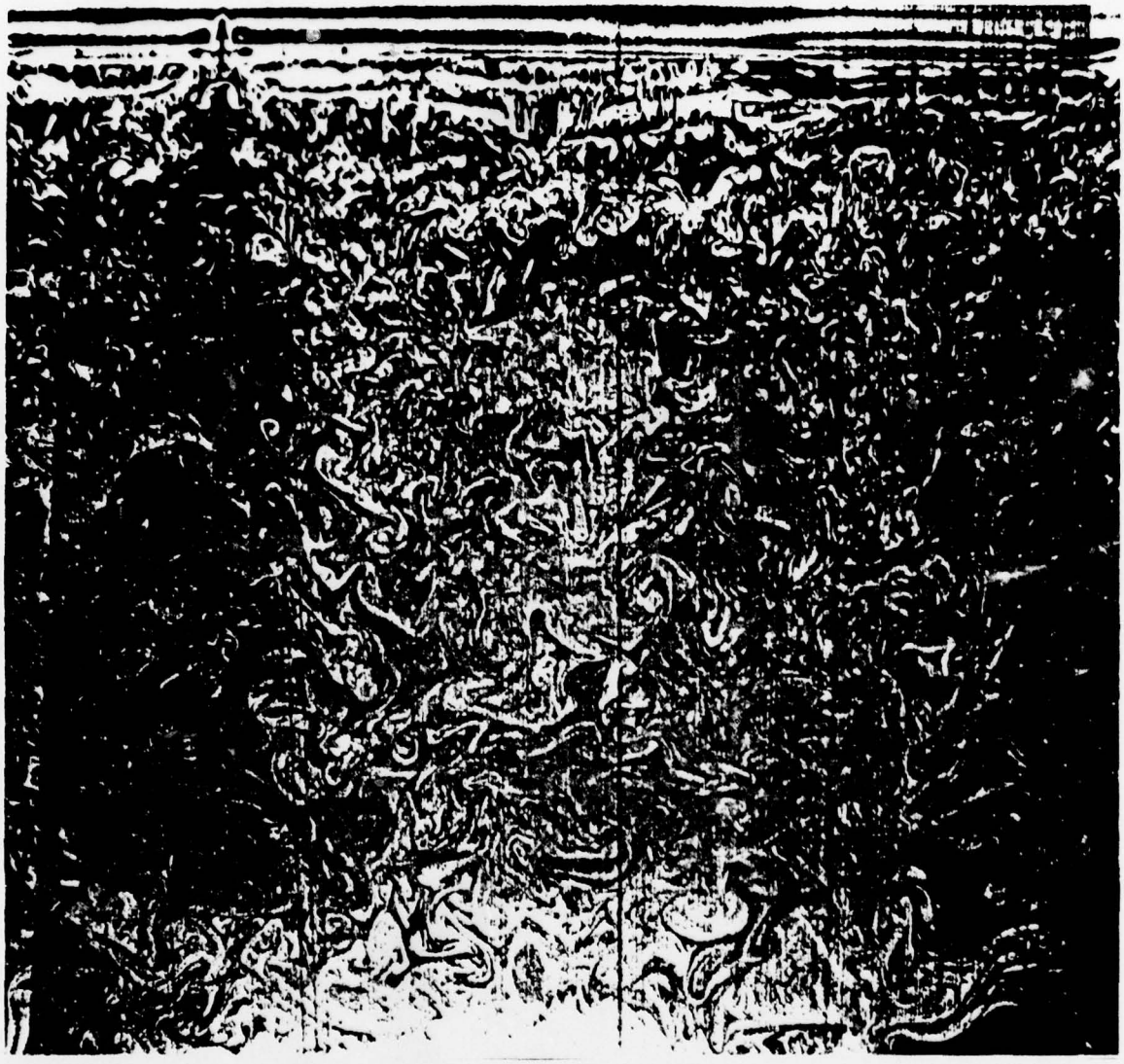

Fig. 7 Two dimensionality. Re $\sim$200. $x/D_{max} \simeq 340$

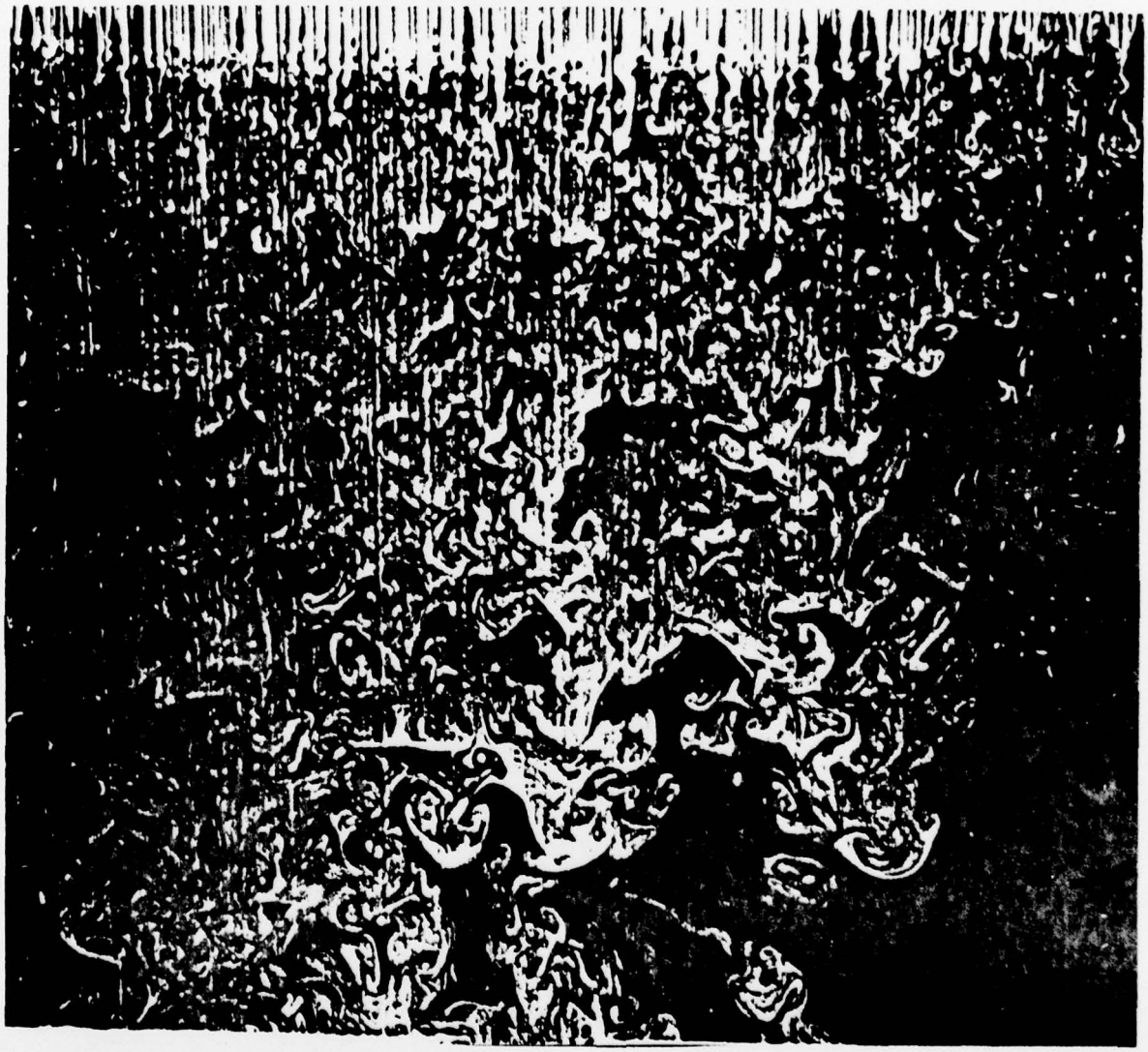

Fig. 8 Striations in two dim. jet. $Re \sim 200$. $x/D_{max} \sim 340$

Fig. 9 Pronounced wander (3 dim). $Re = 2,300$. $x/D_{max} = h/7$

a.

b.

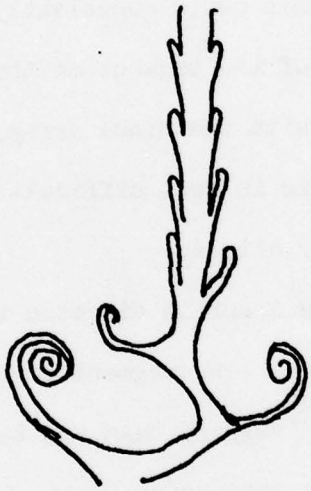

Fig. 10 Transition Region

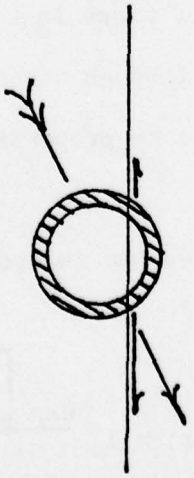

Fig. 11 Anomolous Velocities

APPENDIX

The linear optical system is an important part of the laser induced fluorescence experiment. The illuminating beam from the laser is directed through the fluid flow, exciting any of the fluorescent dye in its path. The fluorescent light is collected by a lens and focused upon an array of photodiodes for its measurement. (Fig. A1) The illuminating beam is a narrow pencil of light and the photodiode array is a line of small elements. This could conceivably cause some difficulty in trying to bring the image of the segment of the illuminated flow to be observed into coincidence with the diode array. Due to several properties of the optical system, it is in fact difficult to determine when the optical system is optimally aligned.

The beam from the laser is directed through a lens that focuses the beam at the center of the line segment in the fluid that is to be observed. The converging/diverging beam can be described accurately by Gaussian optics - so the intensity is gaussian in the distance from the axis of the beam and the intensity distribution becomes most peaked where the beam is focused. If there is a constant concentration of fluorescent dye in the fluid through which the beam is passing, the fluorescence at any point will be proportional to the light intensity at that point.

Gaussian optics gives the intensity of the beam as a function of position as;

$$A(1) \qquad I(x,y,z) = I_o \frac{\exp\left[\frac{-2(x^2 + z^2)}{w^2}\right]}{w^2(y)}$$

where, A(2) $$w(y) = w_o \left[1 + \left(\frac{\lambda y}{\pi w_o^2}\right)^2\right]^{\frac{1}{2}}$$

and w_o is the waist, the smallest radius of the beam, given by Eqn. (5).

The fluorescing dye removes some intensity from the beam, resulting in an exponentially decreasing total intensity. With very low dye concentrations these losses can be made small and in this case the amount of light scattered by fluorescence does not appreciably alter the intensity further along the beam. Thus the exponential decrease can be ignored and the fluorescence becomes proportional to $I(x,y,z)$.

The low concentration of dye provides a means of determining the intensity of the illuminating beam as a function of position. The fluorescence can be measured using a collecting lens and the photodiode array and the result can be compared with the following calculation to see if the array is aligned to be coincident with the image of the illuminated segment. Since the intensity of the fluorescence is known to a high degree of accuracy and the optics can be analyzed quantitatively, it should be possible to calculate the intensity distribution expected to reach the array.

To a good approximation, the collecting lens can be considered to be perfect. That is, any point in the object field will focus to a point in the image field according to Eqn. A(3)

A(3) $$\frac{1}{s_o} + \frac{1}{s_i} = \frac{1}{f}$$

and the two points will be conjugate with the center of the lens. The finite size of the lens can also be ignored for this purpose since this

AD-A073 746 CALIFORNIA INST OF TECH PASADENA GRADUATE AERONAUTIC--ETC F/G 20/4
CHEMICAL REACTIONS IN TURBULENT MIXING.(U)
JUL 79 H W LIEPMANN, G L BROWN, P E DIMOTAKIS F44620-76-C-0046
UNCLASSIFIED GALCIT-151 AFOSR-TR-79-0952 NL

4 OF 4
AD A073 746

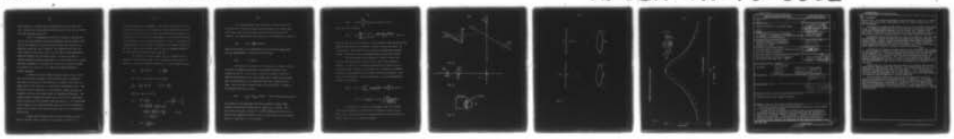

END
DATE FILMED
10-79
DDC

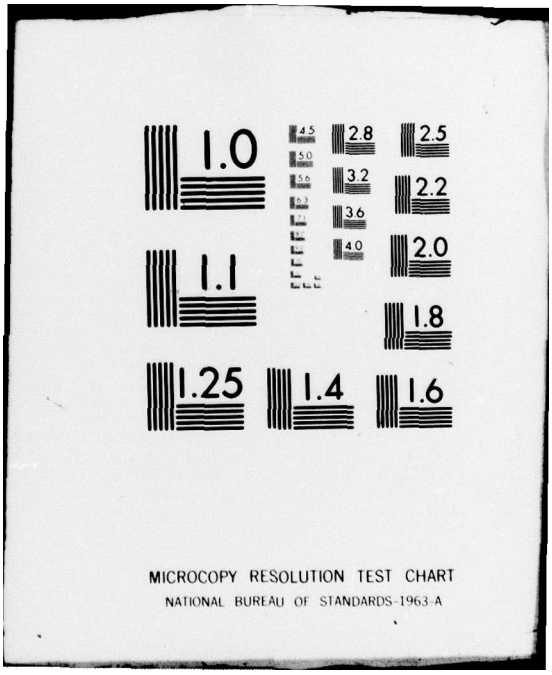
1.0
1.1
1.25
1.4
1.6
1.8
2.0
2.2
2.5
2.8
3.2
3.6
4.0
4.5
5.0
5.6
6.3
MICROCOPY RESOLUTION TEST CHART
NATIONAL BUREAU OF STANDARDS-1963-A

only introduces a constant factor proportional to the aperature size and a cosine factor due to oblique incidence that is very nearly constant for these purposes (within 2%).

Due to the changing cross section of the beam, even when the axis of the array coincides (in three dimensions) with the image of the axis of the illuminating beam, the light intensity that falls on the photodiode array will have a maximum. This maximum occurs where the cross section is most peaked, that is at the image of the origin where where the intensity has its maximum value. If the diode array is slightly skewed or otherwise misaligned, it is still likely that a peaked intensity profile will be observed, but it will have a different shape. In practice it is not easy to tell when the profile corresponds to optimal alignment.

To calculate how the collecting optics forms an image in the plane of the array, an impulse response function will be calculated. This relates the amount of light received at a point in the array, or image, plane to that emitted at a point in the illumination field. This function can then be multiplied by the intensity actually present and integrated over the volume where there is a significant intensity. The impulse response function will depend on the point in the illumination field, (x,y,z), and on the position along the array, y'. The integration of the product of the impulse response, $G(x,y,z;y')$ and the intensity, $I(x,y,z,)$ will yield a value for the signal, $S(y')$ that the photodiodes will measure.

A point source emitting equally in all directions, as does a point in the dyed fluid, illuminates an aperature of radius r at a

distance z_o uniformly if $P^2/2z_o^2 \ll 1$. The aperature of the lens defines a cone of light emitted from a point that is then focused to a point in the image field. (Fig. A2) The amount of light from this point that is received at a given detector is proportional to the fraction of light in the converging cone that is incident upon the detector. The fraction of light collected by the lens that is incident on the detector is given by the area of cone's cross section that overlaps the detector divided by the total area of the cross section. (Fig. A3)

The radius of the cross section, R_c, is a function of the z coordinate of the emitting point. Since any point in the xy plane is focused to a point in the plane defined by $z = z_o$ d_o the lens law gives:

$$A(4) \qquad \frac{1}{z_o} + \frac{1}{d_o} = \frac{1}{f} \qquad d_o = \frac{z_o f}{z_o - f}$$

If we take a point not in the xy plane,

$$A(5) \qquad \frac{1}{z_o - z} + \frac{1}{d} = \frac{1}{f} \qquad \frac{1}{d} = \frac{1}{f} - \frac{1}{z_o - z}$$

From Fig. A4, we can write,

$$A(6) \qquad \frac{P}{d} = \frac{R_c}{d_o - d} \qquad \text{or} \qquad R_c = P\left|\frac{d_o}{d} - 1\right|$$

$$\frac{d_o}{d} = \frac{z_o f}{z_o - f}\left(\frac{1}{f} - \frac{1}{z_o(1 - z/z_o)}\right)$$

$$\approx \frac{z_o}{z_o - f} - \frac{z_o f}{z_o - f}\left(\frac{1}{z_o} + \frac{z}{z_o^2}\right) \qquad z \ll z_o$$

$$= 1 - \frac{fz}{z_o(z_o - f)}$$

so $$R_c \approx P\,\frac{f|z|}{z_o(z_o - f)}$$

If h_c is much smaller than the size of a detector, the cone of light can be considered focused and the response of the system will have a sharp step when the focused point moves off the edge of the detector. The detectors are 25 um square, so the condition for a step is,

$$A(7) \qquad h_c \approx r \frac{f}{z_o} \frac{z}{} \ll 25 \text{ um}$$

Here we will define, as is conventional, $f\# = f/2P$ and $M = z_o/d_o$, where M is the magnification. So, for $M = 3$ and $f\# = 1.4$,

$$A(8) \qquad z \ll 840 \text{ um}$$

The question now arises if it is necessary to consider $z \sim 840$ um to include all regions where there is appreciable intensity in the integral for $S(y')$. We will have to consider the largest values of z when the cross section is the least peaked, that is where $w(y)$ is large. With a magnification of 3, the detectors will view a segment 7.62 cm long. Thus y can take on values between -3.81 and 3.81 cm. Looking at the expression for $w(y)$, we see,

$$A(9) \qquad w_{max} = w(y_{max}) = 244\text{um} \quad \text{using } \lambda = 514.5 \text{ nm}, \; w_o = 25 \text{ um}$$

The intensity at the point where the step condition no longer holds contains the term $\exp(-2z^2/w^2)$, where z 840 um and w 244 um. This term, then, introduces a factor of 4×10^{-11}, indicating that there is no light of any significance emitted where it is not valid to use a response that has a sharp step. We have defined,

$$A(10) \qquad S(y') = \int_{-\infty}^{\infty}\int\int G(x,y,z;y')\, I(x,y,z)\, dx\, dy\, dz$$

using the step condition,

$$A(11) \qquad S(y') = \int_{-\infty}^{\infty}\int_{y_o-a/2}^{y_o+a/2}\int_{a/2}^{a/2} I_o \frac{\exp(-2(x^2+z^2)/w^2)}{w(y)^2}\, dx\, dy\, dz$$

where $y_o = My'$ and $a = M\ 25\ \text{um} = 75\ \text{um}$. These parameters make the integration over the anti-image of the detector that lies in the object field. We can integrate z from $-\infty$ to ∞ since there is no appreciable intensity outside of $|z| < 340$ um and its inclusion will not affect the results.

The function w(y) varies slowly as y takes on values from -3.81 to 3.81 cm, separated by 76.2 um as y' moves from detector to detector. So w(y) can be considered constant on the interval $(y_o+a/2, y_o-a/2)$ and equal to $w(y_o)$. The integral over z introduces a constant, which can be incorporated into the overall constant, and cancels a term w(y) in the denominator. The integration over y also only introduces a constant. We now have,

$$A(12) \qquad S(y') = I_1\int_{-a/2}^{a/2} \frac{\exp(-2x^2/w^2)}{w}\, dx = I_2\int_0^{a/2} \exp(-2u^2)\, du$$

$$S(y') = I_3 \operatorname{erf}\frac{a}{\sqrt{2}\,w} = I_3 \operatorname{erf}\frac{2.121}{\left[1-\left(\frac{z\,y'\lambda}{a_o w_o \pi}\right)^2\right]^{\frac{1}{2}}}$$

To account for the index of refraction of the water through which the beam passes, it is convenient to define $y'' = y'/n = y'/1.33$. The measured intensity profile is slightly narrower than this calculated profile (Fig. A5) due to some misalignment.

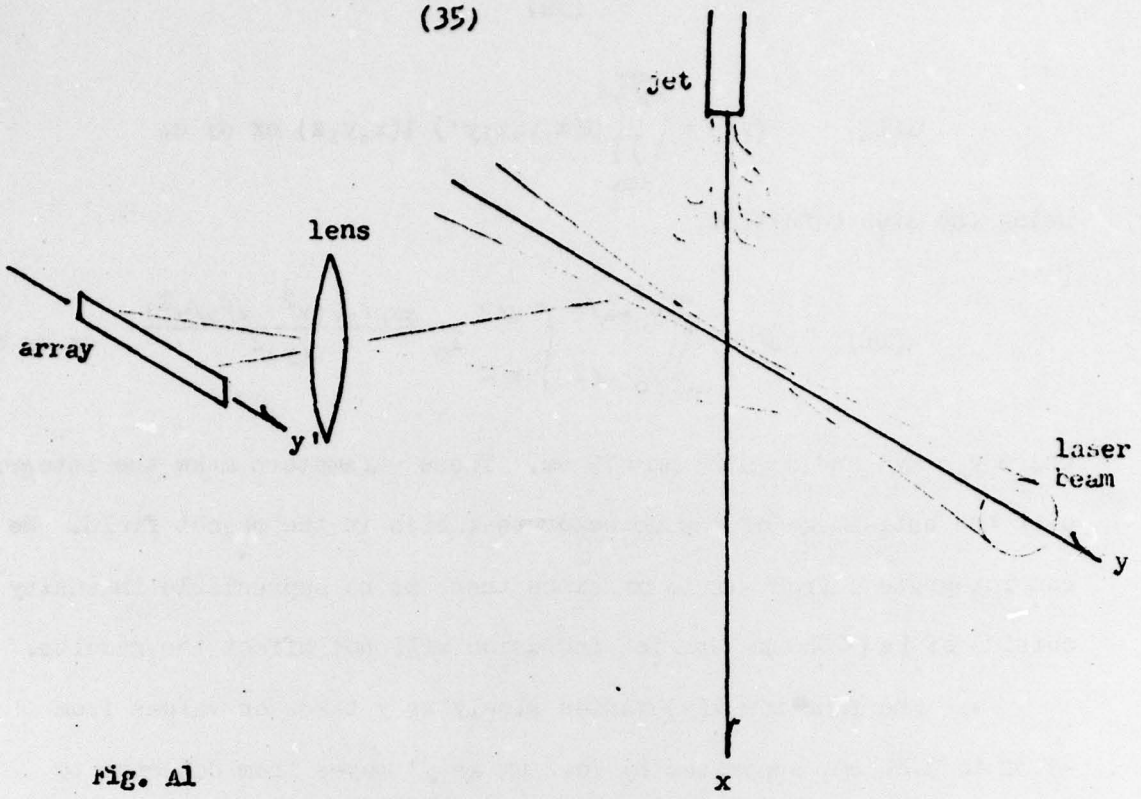

Fig. A1

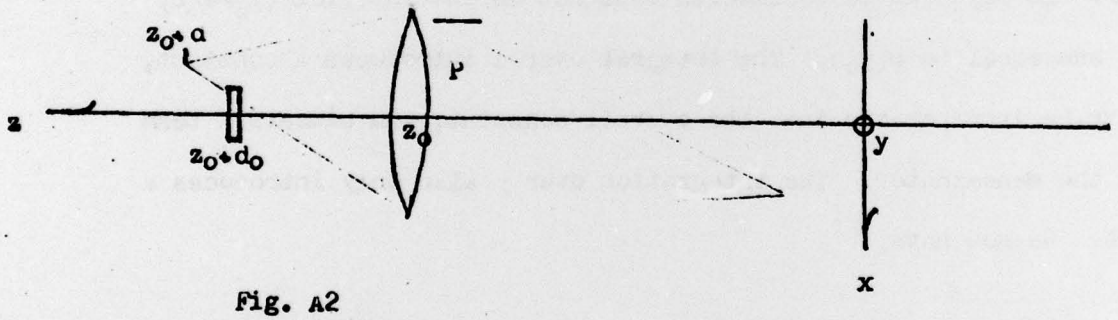

Fig. A2

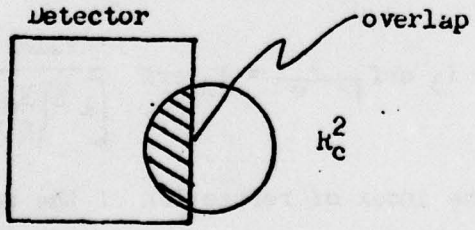

Fig. A3

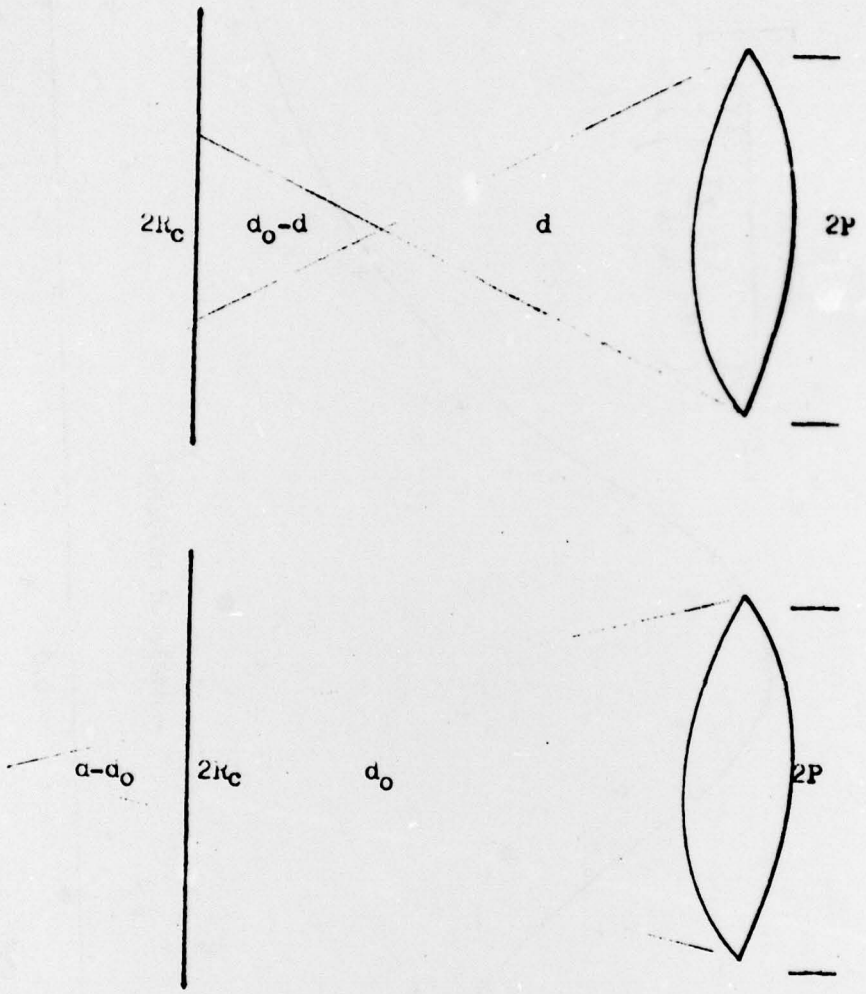

Fig. A4

Relative intensity vs. array position

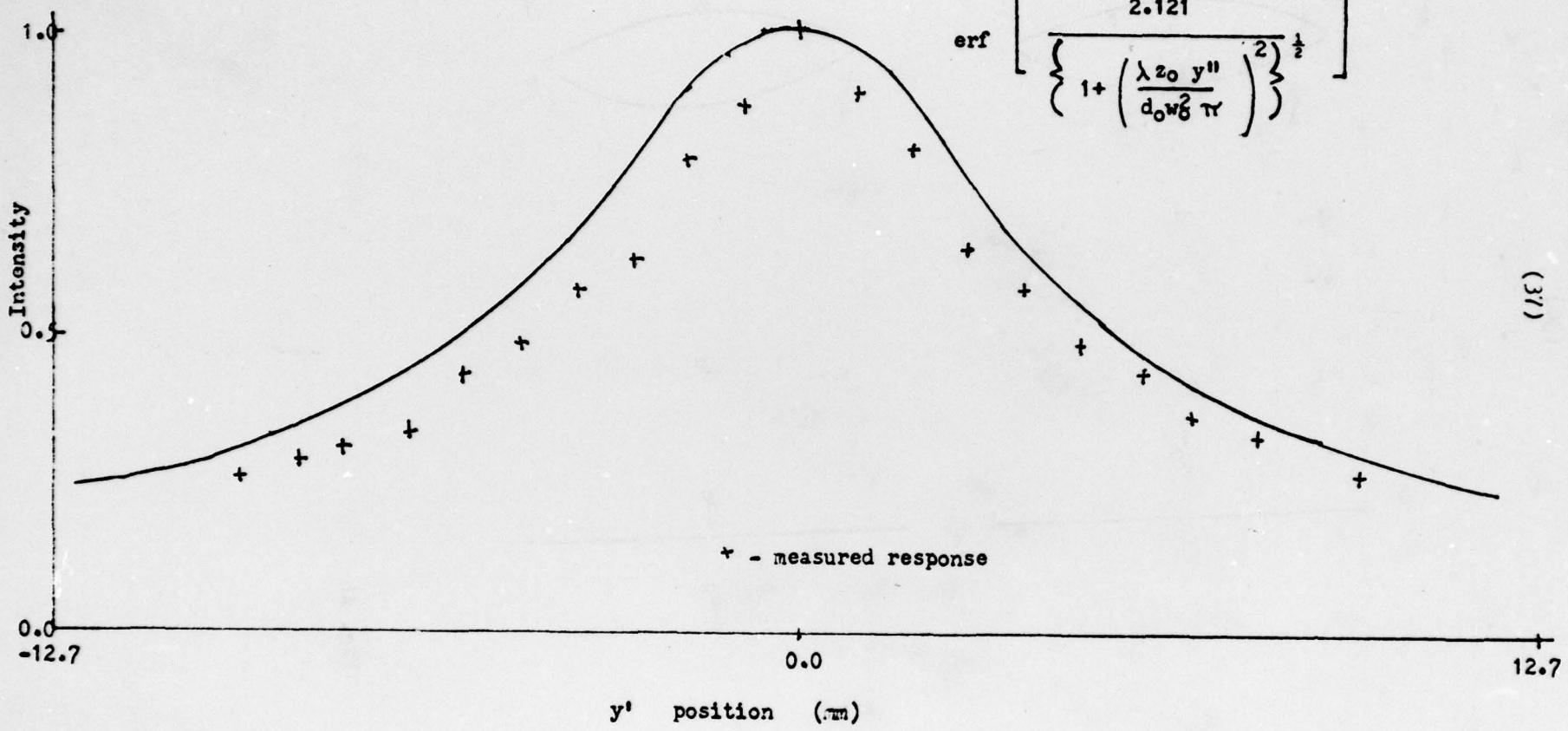

(37)

Unclassified

SECURITY CLASSIFICATION OF THIS PAGE (When Data Entered)

REPORT DOCUMENTATION PAGE

READ INSTRUCTIONS BEFORE COMPLETING FORM

1. REPORT NUMBER (6)	2. GOVT ACCESSION NO.
3. RECIPIENT'S CATALOG NUMBER (9)	
4. TITLE (and Subtitle) (10) CHEMICAL REACTIONS IN TURBULENT MIXING.	5. TYPE OF REPORT & PERIOD COVERED Final Technical Report. 1 Dec 1975 — 14 Apr. 1979
6. PERFORMING ORG. REPORT NUMBER (14) GALCIT-151	
7. AUTHOR(s) H.W. Liepmann (Principal Investigator), G.L. Brown, P.E. Dimotakis, F.E. Marble, A. Roshko, P.G. Saffman (Co-investigators)	8. CONTRACT OR GRANT NUMBER(s) (15) AFOSR Contract No. F44620-76-C-0046
9. PERFORMING ORGANIZATION NAME AND ADDRESS Graduate Aeronautical Laboratories, California Institute of Technology, Pasadena, CA 91125	10. PROGRAM ELEMENT, PROJECT, TASK AREA & WORK UNIT NUMBERS 2307A3 61102F
11. CONTROLLING OFFICE NAME AND ADDRESS Air Force Office of Scientific Research and Air Force Weapons Laboratory (11)	12. REPORT DATE (12) July 1979
	13. NUMBER OF PAGES (12) 290p
14. MONITORING AGENCY NAME & ADDRESS (if different from Controlling Office) Air Force Office of Scientific Research, Bolling Air Force Base, D.C. 20332	15. SECURITY CLASS. (of this report) Unclassified
	15a. DECLASSIFICATION/DOWNGRADING SCHEDULE

16. DISTRIBUTION STATEMENT (of this Report)

(16) 2307 (17) A3

Unlimited

This document has been approved for public release and sale; its distribution is unlimited.

17. DISTRIBUTION STATEMENT (of the abstract entered in Block 20, if different from Report) (18) AFOSR

18. SUPPLEMENTARY NOTES (19) TR-79-0952

19. KEY WORDS (Continue on reverse side if necessary and identify by block number)

Turbulent shear flows; chemical reactions

20. ABSTRACT (Continue on reverse side if necessary and identify by block number)

The more important results and developments achieved as a direct result of this contract are as follows:

A model for the calculation of turbulent flows was constructed which incorporates effects of Reynolds stress relaxation with the generation or destruction of turbulent energy by rotation. The model was verified by comparison with experiment. It was then used to predict the properties of isolated turbulent vortices and applied to the turbulent mixing layer, in particular to the formation and interaction of the organized structure in the

DD FORM 1 JAN 73 1473

Unclassified

SECURITY CLASSIFICATION OF THIS PAGE (When Data Entered)

157700

20. (continued)

mixing layer. An alternative approach to the mixing layer in which it is modelled by a rolling-up vortex sheet between fluids of different density has also been formulated.

Calculations of strained flame elements for use in the coherent flame model of H_2, F combustion showed that only at very high strain rates was sufficient vibrational nonequilibrium produced to be of interest for a chemical laser. This result is reflected in the fact that only in the early portion of the jet, where strain rates are a maximum, does this vibrational nonequilibrium occur.

Experimental results were obtained in a new facility and by a new technique for the amount of reaction product obtained between two chemically reacting aqueous streams. Results at high and low Reynolds number showed the dependence of the mixing on Reynolds number and Schmidt number. A transition Reynolds number region was found and the nature of the generation of small scale motions which dominate the formation of reaction product was explored.

A new facility to explore energetic reactions with substantial heat release has been designed, is being built, and should be used for the first measurements in the summer of 1979. The design problems were formidable but the facility is unique and offers the prospect of obtaining new and very important data with which to compare existing models. As a result of the design, the range of problems and parameters that can be studied in the facility and the possibilities for the development and application of new instrumentation and diagnostics are very great.

State-of-the-art, very high speed and precise laser Doppler velocity measurements were completed under this contract. The acquired experties will find application in the turbulent combustion experiments. It has already been applied with considerable success up to a Mach number of 2.2. The extension of two-point velocity measurements has now been made and a multipoint multichannel LDV system has been designed and is nearing completion.

A laser induced fluorescence technique was developed and successfully applied to the observation of turbulent mixing in a water jet. It allowed the direct observation of a concentration field to the smallest turbulent scales. Both direct photographic techniques and imaging of a line on a 1024 detector Recticon array have been used to obtain the data. Image processing will give quantitative measurements of the concentration field and potentially an inferred velocity field.